INFN
LNGS

Annual Report 2018
Laboratori Nazionali del Gran Sasso

Cover Image: BOREXINO Experiment

Annual Report 2018

Contents

BOREXINO

M. Agostini[p], K. Altenmüller[p], S. Appel[p], V. Atroshchenko[f], Z. Bagdasarian[v], D. Basilico[i],

G. Bellini[i], J. Benziger[m], D. Bick[1], G. Bonfini[h], D. Bravo[i,3], B. Caccianiga[i], F. Calaprice[l], A. Caminata[c], L. Cappelli[h], P. Cavalcante[o,5], F. Cavanna[c], A. Chepurnov[q], K. Choi[u], D. D'Angelo[i], S. Davini[c], A. Derbin[k], A. Di Giacinto[h], V. Di Marcello[h], X.F. Ding[r,h], A. Di Ludovico[l], L. Di Noto[c], I. Drachnev[k], K. Fomenko[b], A. Formozov[b,i,q], D. Franco[a], F. Gabriele[h], C. Galbiati[l], M. Gschwender[x], C. Ghiano[h], M. Giammarchi[i], A. Goretti[l,5], M. Gromov[q,b], D. Guffanti[r,h], C. Hagner[1], E. Hungerford[y], Aldo Ianni[h], Andrea Ianni[l], A. Jany[d], D. Jeschke[p], S. Kumaran[v,w], V. Kobychev[e], G. Korga[y,6], T. Lachenmaier[x], M. Laubenstein[h], E. Litvinovich[f,g], P. Lombardi[i], L. Ludhova[v,w], G. Lukyanchenko[f], L. Lukyanchenko[f], I. Machulin[f,g], G. Manuzio[c], S. Marcocci[r,4], J. Maricic[u], J. Martyn[t], E. Meroni[i], M. Meyer[s], L. Miramonti[i], M. Misiaszek[d], V. Muratova[k], B. Neumair[p], M. Nieslony[t], L. Oberauer[p], V. Orekhov[f], F. Ortica[j], M. Pallavicini[c], L. Papp[p], Ö. Penek[v,w], L. Pietrofaccia[l], N. Pilipenko[k], A. Pocar[n], G. Raikov[f], G. Ranucci[i], A. Razeto[h], A. Re[i], M. Redchuk[v,w], A. Romani[j], N. Rossi[h,1], S. Rottenanger[x], S. Schönert[p], D. Semenov[k], M. Skorokhvatov[f,g], O. Smirnov[b], A. Sotnikov[b], Y. Suvorov[h,f,2], R. Tartaglia[h], G. Testera[c], J. Thurn[s], E. Unzhakov[k], A. Vishneva[b], R.B. Vogelaar[1], F. von Feilitzsch[p], M. Wojcik[d], M. Wurm[t], O. Zaimidoroga[b], S. Zavatarelli[c], K. Zuber[s], G. Zuzel[d]

The Borexino Collaboration

[a]*AstroParticule et Cosmologie, Université Paris Diderot, CNRS/IN2P3, CEA/IRFU, Observatoire de Paris, Sorbonne Paris Cité, 75205 Paris Cedex 13, France*
[b]*Joint Institute for Nuclear Research, 141980 Dubna, Russia*
[c]*Dipartimento di Fisica, Università degli Studi e INFN, 16146 Genova, Italy*
[d]*M. Smoluchowski Institute of Physics, Jagiellonian University, 30348 Krakow, Poland*
[e]*Kiev Institute for Nuclear Research, 03680 Kiev, Ukraine*
[f]*National Research Centre Kurchatov Institute, 123182 Moscow, Russia*
[g]*National Research Nuclear University MEPhI (Moscow Engineering Physics Institute), 115409 Moscow, Russia*
[h]*INFN Laboratori Nazionali del Gran Sasso, 67010 Assergi (AQ), Italy*
[i]*Dipartimento di Fisica, Università degli Studi e INFN, 20133 Milano, Italy*
[j]*Dipartimento di Chimica, Biologia e Biotecnologie, Università degli Studi e INFN, 06123 Perugia, Italy*
[k]*St. Petersburg Nuclear Physics Institute NRC Kurchatov Institute, 188350 Gatchina, Russia*
[l]*Physics Department, Princeton University, Princeton, NJ 08544, USA*
[m]*Chemical Engineering Department, Princeton University, Princeton, NJ 08544, USA*
[n]*Amherst Center for Fundamental Interactions and Physics Department, University of Massachusetts, Amherst, MA 01003, USA*
[o]*Physics Department, Virginia Polytechnic Institute and State University, Blacksburg, VA 24061, USA*

---

[1]Present address: Dipartimento di Fisica, Sapienza Università di Roma e INFN, 00185 Roma, Italy

[2]Present address: Dipartimento di Fisica, Università degli Studi Federico II e INFN, 80126 Napoli, Italy

[3]Present address: Universidad Autnoma de Madrid, Ciudad Universitaria de Cantoblanco, 28049 Madrid, Spain

[4]Present address: Fermilab National Accelerato Laboratory (FNAL), Batavia, IL 60510, USA

[5]Present address: INFN Laboratori Nazionali del Gran Sasso, 67010 Assergi (AQ), Italy

[6]Also at: MTA-Wigner Research Centre for Physics, Department of Space Physics and Space Technology, Konkoly-Thege Mikls t 29-33, 1121 Budapest, Hungary

^{p}*Physik-Department and Excellence Cluster Universe, Technische Universität München, 85748 Garching, Germany*
^{q} *Lomonosov Moscow State University Skobeltsyn Institute of Nuclear Physics, 119234 Moscow, Russia*
^{r} *Gran Sasso Science Institute, 67100 L'Aquila, Italy*
^{s}*Department of Physics, Technische Universität Dresden, 01062 Dresden, Germany*
^{t}*Institute of Physics and Excellence Cluster PRISMA, Johannes Gutenberg-Universität Mainz, 55099 Mainz, Germany*
^{u}*Department of Physics and Astronomy, University of Hawaii, Honolulu, HI 96822, USA*
^{v}*Institut für Kernphysik, Forschungszentrum Jülich, 52425 Jülich, Germany*
^{w}*RWTH Aachen University, 52062 Aachen, Germany*
^{x}*Kepler Center for Astro and Particle Physics, Universität Tübingen, 72076 Tübingen, Germany*
^{y}*Department of Physics, University of Houston, Houston, TX 77204, USA*
^{z}*Institute of Physics, Sachivalaya Marg, Sainik School Post, Bhubaneswar 751005, India*
^{aa}*Homi Bhabha National Institute, Training School Complex, Anushakti Nagar, Mumbai 400085, India*

Abstract

The beginning of the Borexino experiment data taking dates back to 2007 May 15th. During almost 10 years of analysis we published results at the forefront of the measurements of the solar neutrino and geo-neutrino fluxes, and we set unprecedented limits on rare processes. A big improvement in the precision measurement of the solar neutrino was achieved recently and reported in our most representative article, published on Nature on 2018.

In this short report we will review the most recent results and we will briefly describe the last challenge of our detector: a strategy for improving the detector sensitivity to CNO solar neutrino interaction rate. The unprecedented conditions of background stability achieved after almost four year of thermal insulation campaign is making this project quite promising.

Introduction

Solar neutrinos provide key pieces of information for either accurate solar physics modelling and neutrino oscillation understanding. The Borexino experiment is presently the only detector able to measure the solar neutrino interaction rate with a threshold of $\gtrsim$ 150 keV and to reconstruct the energy spectrum of the events.

In this report we focus on the major accomplishments of the experiment over one year elapsed from the last update, in which we outlined the overall goals set by the Collaboration for the next couple of years of data taking. Within that general framework centered on the CNO quest, we progressed towards further thermal stabilization of the detector, one of the key prerequisites for the CNO goal.

Tightly coupled to this effort, we have improved our quantitative understanding of the thermal condition of the detector, specifically the scintillator, through the improvement of the accurate simulation, which models the evolutions of the temperatures in different zone of the experiment, and comparing the results with the output of the temperature probes.

Another important new hardware activity is the precision cleaning of the plants, with the aim to condition and prepare them for the possible final purification (through water extraction) of the scintillator as ultimate push for the lower background ever in Borexino. We remind that the ^{210}Bi would be the most important species to remove with an additional purification, given its crucial

role of major obstacle for the CNO detection. The use of the water in the CTF Water Tank to profit of its reduced, long decayed ^{210}Po content, is also described.

On the front of the analysis results and related published papers. We will give an exhaustive list of the on-going studies and publications.

Last, we complete this work with an illustration of the activities that the Collaboration is planning for the next two years, with a time line that will be adjusted to take into account the evolution of the overall experimental scenario.

1. The Borexino Detector

Borexino is located in the Hall C of Laboratori Nazionali Gran Sasso. The detector is made of concentric layers of increasing radiopurity (see for details e.g. [7]). According to the scheme sketched in Fig. 1, the innermost core consists of 300 tons of liquid scintillator (PC plus 1.5 g/l of PPO) contained in a 125 μm of ultrapure nylon vessel of radius 4.25 m. A stainless steel sphere (SSS) filled up with $\sim$ 1000 of buffer liquid (PC plus DMP quencher) is instrumented with more than 2000 PMTs for detecting the scintillation light. Finally, the SSS is immersed in a 2000 ton water Cherenkov detector, equipped with 200 PMTs. The position of events is reconstructed with an accuracy of $\sim$ 10 cm and the energy resolution scales approximately as $\sigma(E)/E = 5\%/\sqrt{(E/[MeV])}$. This sensitivity has been achieved after an accurate calibration campaign [8] carried out in 2010. In addition the detector features a satisfactory pulse shape discrimination for α/β particles and even a challenging β^+/β^- separation, see as a review [7].

The intrinsic radiopurity of the scintillator reached unprecedented levels after an intense purification campaign carried out in between 2010 and 2011. The two stages, namely before and after the purification campaign, are referred as Phase-I and Phase-II. Tab. 1 shows the record background levels in the two Borexino phases.

Contaminant	Phase-I	Phase-II
^{14}C/^{14}C		2.7×10^{-18} [g/g]
^{238}U		$< 9.7 \times 10^{-19}$ [g/g] (95% CL)
^{232}Th		$< 1.2 \times 10^{-18}$ [g/g](95% CL)
^{210}Po	$\sim$2000 [cpd/100t]	$\sim$50 [cpd/100t] (2016)
^{210}Bi	$\sim$45 [cpd/100t]	$\sim$20 [cpd/100t] (2016)
^{85}Kr	$\sim$30 [cpd/100t]	< 5 [cpd/100t] (95% CL)

Table 1: Borexino contaminant rates before and after the purification campaign.

Thanks to the very low background condition o Phase-II , we performed a complete study of the *pp-chain*. We measured the neutrinoelectron elastic-scattering rates for neutrinos produced by four reactions of the chain: the initial *pp* fusion, the electron-capture decay of ^{7}Be 7, the three-body *pep* fusion, here measured with the highest precision so far achieved, and the ^{8}B beta decay, measured with the lowest energy threshold. We also set a limit on the neutrino flux produced by *hep* reaction. These measurements provide a direct determination of the relative intensity of the two primary terminations of the pp chain (pp-I and pp-II) and an indication that the temperature profile in the Sun is more compatible with solar models that assume high surface metallicity. We also determine the survival probability of solar electron neutrinos at different energies, thus probing
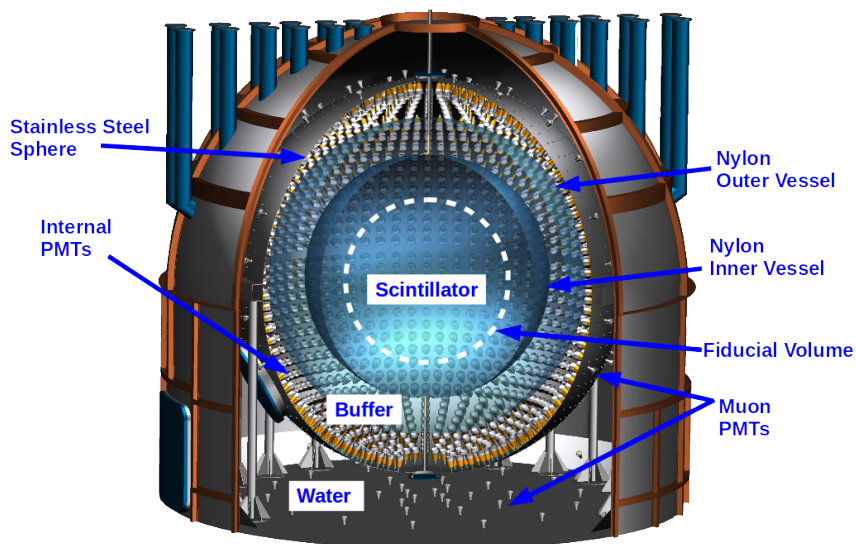
Figure 1: Schematic view of Borexino detector (Picture based on the original drawing, courtesy of A. Brigatti and P. Lombardi).

simultaneously and with high precision the neutrino flavour-conversion paradigm, both in vacuum and in matter-dominated regimes. All of these results are summarized in table Tab. 1

Species	Rate [cpd/100t]	Flux [cm^{-2} s^{-1}]
pp	$134 \pm 10^{+6}_{-10}$	$6.1 \pm 0.6 \times 10^{10}$
^{7}Be	$48.3 \pm 1.1^{+0.4}_{-0.7}$	$4.99 \pm 0.13 \times 10^9$
pep (HZ)	$2.43 \pm 0.36^{+0.15}_{-0.22}$	$1.27 \pm 0.21 \times 10^8$
^{8}B(> 3 MeV)	$0.223 \pm 0.013 \pm 0.004$	$5.7 \pm 0.4 \pm 0.1 \times 10^6$
CNO	< 8.1 (95% CL)	$< 7.9 \times 10^8$ (95% CL)
hep	< 0.002 (90% CL)	$< 2.2 \times 10^5$ (90% CL)

Table 2: Solar neutrino interaction rates and fluxes measured by the Borexino experiment. Rates are normalized on a mass of 100 tons.

2. Analyses in Progress and Forthcoming Papers

After the publication of the latest solar neutrino result concerning the measurement of all components of the pp-chain solar neutrinos (pp, ^{7}Be, pep, ^{8}B) in October 2018 in Nature [1], the submission of the 2 more technical papers [2, 3] to Phys. Rev. D, dealing with the detailed description of the analysis in the lower and in the higher energy window, respectively, is imminent.

A study of the cosmic muon signal, concerning namely the seasonal variation of the muon rate and its correlation with atmospheric temperature variations, extraction of the effective temperature

coefficient α_T correlated with the kaon-to-pion production ratio in the atmosphere, observation of the long-term $\sim$3000 days modulation of the muon flux, as well as observation of the seasonal variation of the cosmogenic neutron production, has been published in the Journal of Cosmology and Astroparticle Physics [4].

The latest Borexino result on geo-neutrinos, published in 2015, had 26% precision on the measured geo-neutrino flux. A new updated analysis, with the improved antineutrino selection in the enlarged fiducial volume is nearly finalized. Further improvements concerning the muon veto, that will lead to the reduction of the dead time, are being finalized. A comprehensive discussion concerning the geological interpretation of the new result is also ongoing. The new release, with the expected precision of about 20% is planned to be presented at TAUP conference in September 2019 in Japan and at Neutrino Geoscience conference in October 2019 in Prague.

Borexino excellent radio-purity enables to set the world best limits on MeV antineutrinos from unknown sources. The latest publication is from 2011 and an updated one is about to be finalized. Significant effort has been put in the estimation of the background due to atmospheric neutrinos. The first Borexino limit on the Diffuse-Supernovae-Background neutrinos as well as on the fluence of MeV neutrinos correlated with solar flares will be also part of the new release.

The precise understanding of Borexino data energy spectrum allows us to set limits on non-standard neutrino interactions, in particular those which could modify the $\nu_e e^-$ and $\nu_e \tau^-$ couplings. The analysis has been performed assuming the solar neutrino fluxes from the Standard Solar Model both in the high and in the low metallicity hypothesis. No indications for new physics were found at the level of sensitivity of the detector and constraints on the parameters describing the NSI's are placed. This analysis is described in [5], which is currently under review from the collaboration. Soon after the end of the revision process it will be submitted to JHEP.

In addition, the combined solar analysis of the Phase I and II data, justified by the data convergence, is ongoing and feature a promising improvement either of the limit on the effective neutrino magnetic moment and of the precision of the solar neutrino fluxes.

Finally, Borexino continues to participate in the SNEWS and the GWNU groups. The latter inter-collaboration community works on the multi-messenger astronomical analysis, namely the joint search for gravitational wave and low energy neutrino signals from core-collapse supernovae. It's possible that these two groups will unite within some kind of the "SNEWS 2.0" association this or next year. Moving in this direction we are updating the Borexino SNEWS module in order to increase the sensitivity, prepare low threshold alarms for the low-latency GWNU analysis and provide information about the significance of an alert. The updates will be presented at the SNEWS 2.0 workshop in June 2019 in Sudbury, Canada and at the Lomonosov conference on Elementary Particle Physics in August 2019 in Moscow. It's worth noting that the GWNU MoU has been renewed in March 2019.

3. Thermal Stabilization of the the Detector

3.1. Temperatures Evolution

The Borexino detector thermal stability is constantly monitored by several sensors installed in both the detectors, environmental and utilities positions.

Thermistors installed on the detector itself respect a north-south symmetry and are installed radially from the detector center.

Fi.g **??** show the temperature trends of sensors installed on the Stainless-Steel Sphere, approximately at 0.5 m inside the Sphere, in the Outer Buffer. The overall temperature trend shows a
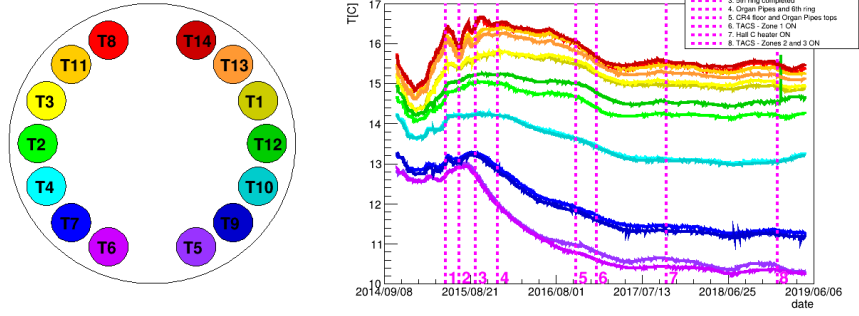
Figure 2: Re-entrant Buffer temperature probes.

drastic regime change, before and after the beginning thermal insulation program (middle 2015). Unless this action stabilized the temperatures inside the detector, a residual seasonal effect of order 0.1 K is still present. A further improvement can be achieved with the active control temperature systems. Many tests are ongoing, even if the final strategy is not finalized yet, being the thermo-dynamic system (Detector plus Hall C) so complex that a lot of simulations and studies are still needed.

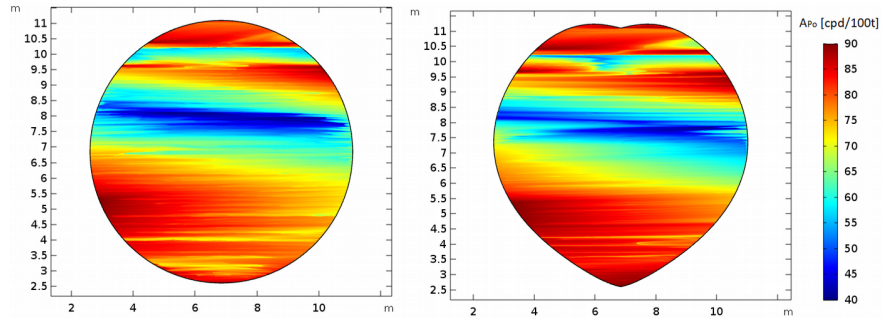### 3.2. Thermal simulation modeling

Figure 3: Calculated Po activity in the period Feb2017 by means of the transport model for the sphere geometry (left) and the real IV heart shape (right).

The simulation of the Borexino scintillator behavior during 2017 and 2018 through a CFD numerical model is required in order to investigate the temporal evolution of the detector, the thermal variations related to external environmental conditions and their relative influence on the internal fluid dynamics during the analyzed periods. This is of great importance for the basic scientific goals of the experiment: since Borexino is under critical time pressure, it is needed to further stabilize the innermost fluid-dynamics, which is directly correlated to the control of the ^{210}Bi background that covers the CNO solar neutrinos. The CFD simulations should provide guidance and perhaps predictive capabilities to understand underlying phenomena and inform decisions on the evolution of the detector thermal field, and thereby its physics results.

This work has been realized in collaboration with Politecnico di Milano. The collaboration, regarding sharing and availability of computational resources (Cluster of the Politecnico di Milano),
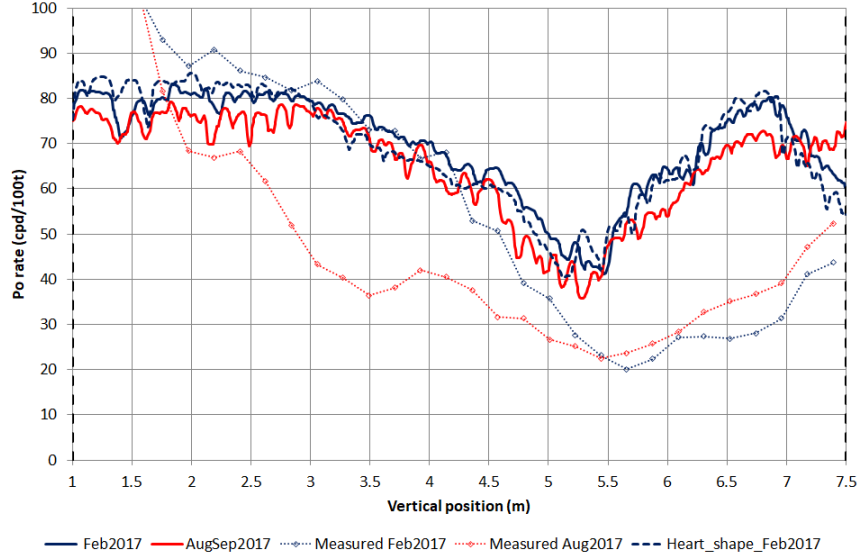
Figure 4: Calculated vs. measured Po rate along the IV vertical position during Feb2017 and AugSep2017 periods.

Figure 5: Calculated vs. measured Po rate along the IV vertical position during Apr2018 and Oct2018 periods.

implementation of numerical solutions and analysis of numerical results, has permitted to reach the results presented here.

In order to investigate the ^{210}Po *migration* inside the inner vessel a simplified transport model has been developed.

The stationary solution is given in Fig. 3, where also the solution considering the real IV geometry has been included. The comparison with the measured ^{210}Po rate is reported in Fig. 4 and Fig. 5.

Results clearly indicates that the temperature induced convective currents produces a region of

lower ^{210}Po concentration in agreement with experimental findings. The differences between the perfect sphere and the real IV shape are very small, suggesting that the temperature plays the most significant role in the convection behavior rather than the geometry. Nevertheless, the calculated concentration presents several discrepancies compared with the measured data. In particular, the ^{210}Po concentration is underestimated at the very bottom of the IV, whereas it is overestimated at the top part as well as in correspondence of the minimum. In addition, the seasonal variations are not well reproduced by the calculations, showing only some minor differences.

The results are very promising showing that the calculated minimum concentration corresponds to the measured one. From a quantitative point of view, the discrepancies are significant and are likely due to the uncertainties on the temperature boundary conditions. In order to improve the current status, a better temperature profile should be reconstructed based on the available experimental data. Moreover, a 3D CFD model is required to improve the current understanding of the convective currents inside Borexino.

4. ^{210}Bi -^{210}Po Link and CNO Strategy

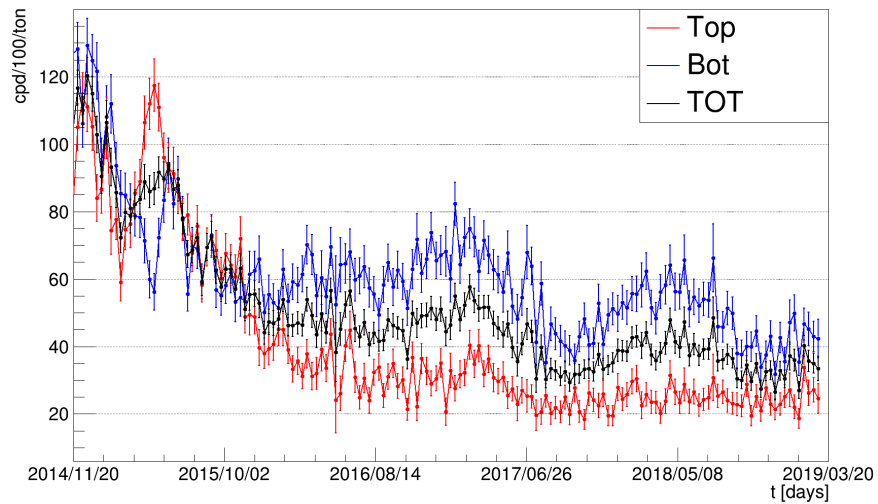*4.1. Update of the ^{210}Po Evolution*

Figure 6: ^{210}Po inside the Standard ^{210}Po Fiducial Volume ($r < 2.5$ m and $|z| < 1.5$ m). The plot show the global ^{210}Po rate (black) and top (red) and bottom (blue) separately.

The ^{210}Po events are selected through a high efficiency $\alpha - \beta$ pulse shape discriminator based on a neural network, trained on a large sample of ^{214}Bi-Po fast coincidences. The ^{210}Po rate is studied in different volumes and correlated in time with the major operations performed on the detector.

Figure 6 shows the ^{210}Po rate in the so-called Standard ^{210}Po Fiducial Volume ($r < 2.5$ m and $|z| < 1.5$ m). Figure 7 shows the ^{210}Po rate in 59 cubes (with 1.5 m edge) inside a sphere of radius 3 m, conveniently arranged from the bottom (0) to the top (58) along the vertical direction.

The most important operations and events, of fundamental importance for the understanding of thermal stabilization process in relationship with the ^{210}Po evolution in the detector are listed here:
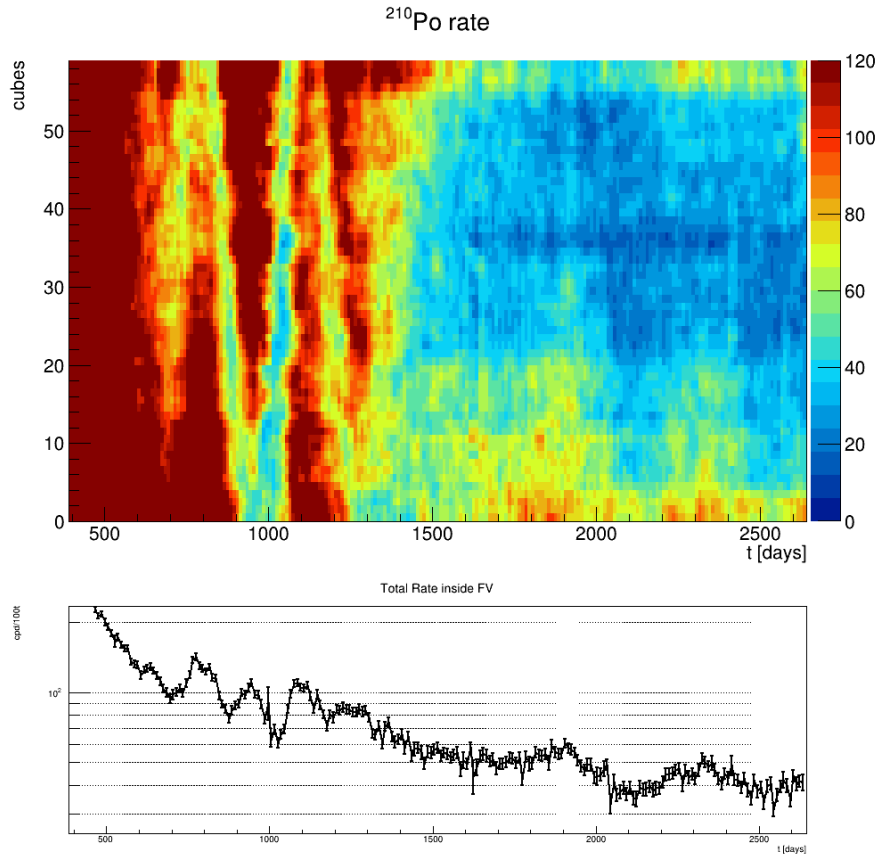
8

Figure 7: ^{210}Po rate in 59 cubes (of side 1.5 m) inside a sphere of radius 3 m, conveniently arranged from the bottom (0) to the top (58). The black graphic below shows the total rate in a larger volume, ($r < 3$ m and $|z| < 1.67$ m), often referred as Standard ^{7}Be Fiducial Volume.

- **14 May, 2015:** Start of the insulation. This date defines the phases before and after the insulation campaign.

- **07 Jul, 2015:** Turn off of the Water Loop system. This operation enhances the cooling of the detector bottom.

- **11 Sep, 2015:** Completion of the 5th ring insulation. The detector is almost covered.

- **09 Dec, 2015:** Completion of the Organ Pipes and the 6th ring insulation. The external parts of the detector are insulated.

- **20 Oct, 2016:** Insulation of the clean room "CR4" floor. Besides the basis, the detector is completely insulated.

- **10 Jan, 2017:** First test of the Temperature Active Control System.

- **01 Oct, 2017:** The heater of the Hall C is turned on. This operation seems to improve the ^{210}Po uniformity even if it will be not completely sufficient for contrasting the winter temperature lowering.

9

- **25 Feb, 2018:** A serious power failure happens underground, making all control system shut down. The detector had been turned off for three days.

- **19 Apr, 2018:** The Radon Abatement System turn off produces a lowering of the Hall C temperature by more than one Celsius degrees. For technical reasons this system is still down.

- **30 May, 2018:** Interruption of the Hall C active control for a technical failure. The system was resumed on July 9th.

- **8 Jan, 2019:** Start-up of the upgraded active control system

Experimental observations of the evolution of the ^{210}Po in the Nylon Vessel indicate a transition between the phases before and after the insulation campaign. Nevertheless a residual migration of the contaminants, associated to a long time scale of order of a few years, especially at the bottom, is due to residual convective motions, even if a global improvement of the detector radio-purity is clearly visible, especially in connection with the most thermally stable periods. Such optimal conditions have been interrupted by accidental factors, external and unpredictable, as the the shut down of the Radon Abatement System that caused a sudden drop of the Hall C temperature by more than one Celsius degree. Finally, a residual "seasonal" component cannot be ruled out, even if is difficult to establish the real strength of such an effect, due to the overlapping other operations and accidents.
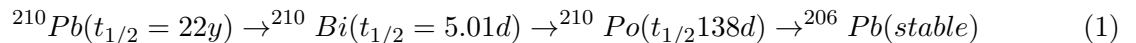
Those facts inspired us to realize the further improvement of the active temperature control describe above. In particular this systems aims to definitely decouple the Borexino Water Tank from rest of the experimental Hall C.

Nevertheless we still highlight that surprisingly, even in presence of residual migrations of the ^{210}Po , resulting in the average rate oscillations visible in Fig. 6 and a clean core in the innermost part of the detector (see Fig. 7 have been keeping the minimum rate, and in the very last period this rate is of the same order of the rate determined for the ^{210}Bi from the spectral fit. We expect that this core would allow us a reliable and statistically consistent measurement of the ^{210}Po supported term, directly linked to the ^{210}Bi rate. Once the ^{210}Bi homogeneity is proved, this measurement will be sufficient to be applied on a wider exposure.

4.2. Recent Progress toward a Measurement of CNO Neutrinos

For the past five years, Borexino has been working on the possibility to measure CNO neutrinos. One of the main obstacles to this measurement is background due to ^{210}Bi which has a half-life of 5 d and a beta spectrum with end-point energy of 1.16 MeV, which largely overlaps with the energy spectrum of recoil electrons produced by CNO neutrinos. Since the overlapping spectra are difficult to separate by measuring the energy spectrum, we are forced to find another method to measure ^{210}Bi independently.

The strategy we have been following is based on a suggestion [6] to take advantage of the decay chain of

$$^{210}Pb(t_{1/2} = 22y) \rightarrow^{210} Bi(t_{1/2} = 5.01d) \rightarrow^{210} Po(t_{1/2}138d) \rightarrow^{206} Pb(stable) \tag{1}$$

This is the final sequence of decays following the decay of ^{222}Rn, which is part of the ^{238}U decay chain. The source of the ^{210}Bi background in the detector comes from the long-lived decay ^{210}Pb in the scintillator, which likely came as a minor contaminant of purified ground water.

It was suggested [6] that ^{210}Bi rate could be independently measured by measuring the rate alpha particles emitted by ^{210}Po (using alpha/beta pulse shape discrimination), provided that the full decay sequence from ^{210}Pb to ^{206}Pb is in secular equilibrium. However, it was soon realized that surface radioactivity of ^{210}Pb on the nylon vessel that contains the scintillator was a source of ^{210}Po that could be carried by slow convection currents into the fiducial volume because of its long half-life, whereas ^{210}Bi on the vessel surface with its short half life would not move far enough to reach the fiducial volume before it decayed. Contamination of the scintillator in the fiducial volume due to radioactivity on the vessel surface would break secular equilibrium and block a measurement of ^{210}Bi .

However, if we can slow convection currents sufficiently to prevent ^{210}Po from reaching the fiducial volume, we can restore secular equilibrium. In addition, if ^{210}Pb is uniformly distributed in the fiducial volume, we only need to obtain secular equilibrium to measure ^{210}Po in a limited region of the fiducial volume.

To minimize convection currents, a few years ago we started by adding thermal insulation to the outside surface of the Borexino water tank. This made a significant change in the detector temperature stability. We then added heaters under the insulation to provide active temperature control on the surface of the Borexino water tank. The last stage of active temperature control was completed at the end of 2018 and was started up in early January 2019. The result of this work are preliminary, but very positive.

With these new more stable conditions, we observe from a very recent analysis of the data, the following:

1. The beta events in the spectrum are most likely uniformly distributed in the FV and constant in time within the energy band that contains significant contribution of CNO neutrinos, indicating the ^{210}Pb is uniformly distributed after the insulation (2016).

2. A limited region of the FV has a low and stable ^{210}Po decay rate which may be sufficient for determining the ^{210}Bi rate in the FV, and then the CNO rate.

The analysis is recent, still preliminary, and is on-going. However, it is possible that we are very close to achieving the requirements for observing CNO neutrinos that we set for ourselves a few years ago. We will send a report to LNGS Scientific Committee as soon as possible.

5. Cleaning of the plants

For cleaning operations, as new strategy, has been defined crucial the use of water contained in the CTF tank. This water taken from this Tank will pass through the Water Plant to have High Purity Water and then distilled by the upgraded structured packing column placed in USA Skids.

The water, so distilled, will be stored in the D1 tank (placed in Storage Area) and then used for the Cleaning of the plants. This means the milestone for the Cleaning are the Cleaning of D1 tank and water plant improvements. At present, D1 tank cleaning is ongoing, meanwhile the emptied EPN and EPS vessel have been already cleaned.

5.1. Water Plant Improvements

The aim of water plant improvements is to have the chance to purify both the common raw-water and the one taken from the CTF water tank. This could be significant for the next cleaning

activities in view of a future purification campaign involving the Borexino scintillator. The reason for the use of the CTF water is the lower content of Polonium organic compounds present in it if compared with common raw-water (water coming from Gran Sasso rock). This feature should guarantee a higher reduction of the ^{210}Po content after the water distillation performed with the new distillation column. Such a kind of water could be the key to reduce the content of ^{210}Po inside the Borexino scintillator after its purification.

On one side, the modifications on the plant consist in the installation of new pipes and valves in order to make the Water Plant able to process both raw water and water coming from the CTF tank. Handling just some ball valves it will be possible to choice which water to use as feed for the Water Plant. On the other side, further modifications of the system consist in the installation of some simple flexible hose (with ball valves) in order to avoid the draining of the waste water (as a waste of the water purification process) and reintegrate it inside the CTF tank. Considering the implementations just described above, well be able to take the water from the CTF water tank (from the bottom), purify it, and reintegrate the total amount of waste water (around 60% of the extracted water) inside the CTF water tank (from the top). This will reduce the impact on the DarkSide-50 water veto deriving from the reduction of its level. We estimated that in this way we will be able to produce 120 cubic meters of purified water extracting 120 cubic meters.

5.2. Schedule

The process above described is planned to start after the cleaning of the D1 Storage Tank, scheduled to be accomplished within the March 15th 2019. The overall time duration needed for the water purification process is 34 working days. This means that the CTF water level will be reduced until the half of May 2019.

6. Outline of the General Experimental Strategy Over the Next Months

At the time of writing, the collaboration is carefully deliberating the scientific schedule of the experiment until the currently foreseen end-date of Borexino operations in late 2020. The guiding motive is to optimize the sensitivity for a final CNO measurement of Borexino, which crucially depends on the knowledge of background levels and detector response. In fact, there is a number of tasks to perform to bring Borexino to a successful conclusion, that have to be carefully weighed against the limited time line:

- **Detector stabilization:** After the successful implementation of two further active temperature control zones, we expect a further reduction of convective motion within the scintillator target. This will be useful to increase the integrated exposure of data taken in the stable low Po-210 zone in the northern hemisphere of the vessel but can hopefully lead as well to an extension of this low-background region if permitted by improved stability conditions. Both measures will lead to a reduction in the uncertainty of residual Po-210 and thus of Bi-210 background level that will be crucial for CNO analysis.

- **Detector calibration:** Of equal importance for the analysis is a final calibration of the detector response. Almost ten years have passed since the first and only calibration campaign in 2009. Detector parameters have changed considerably over this time frame, most notably but not only due to the loss of several hundred PMTs over the last years. A per-cent level discrepancy of data to Monte Carlo simulations present since 2016 is yet to be understood.

Thus, new calibration data is essential to exploit the most recent ultra-low background data set from 2016 to 2019 for solar neutrino analysis.

- **Scintillator purification:** Borexino's sensitivity to the CNO neutrinos would profit from a significant reduction in Bi-210 background levels. Based on the experience from the past purification campaign 2011/12 and subsequent tests, the collaboration has developed a strategy that promises a further reduction of the Bi-210 background rate to a level comparable or lower than the CNO signal. The revised strategy will be employed before the end of Borexino to demonstrate the potential of the improved purification setup and to allow for an even more sensitive search for CNO neutrinos in case Borexino's operation time could be prolonged.

While the three steps should be necessarily conducted in the above order, there is still some flexibility concerning the exact time line. Depending on the further development of detector stabilization and thus the potential benefit for the CNO analysis that can be hoped for by accumulating more exposure, data taking in the current detector configuration may proceed for another 6 to 12 months. This period will provide sufficient time for the final preparations required for calibrations and purification. Subsequently, each of the two operations will take about 2-3 months to accomplish. In this scenario, purification will be followed by a short period of data taking before before the stop of the activity.

7. Conclusions

The main message conveyed in this report is that the Collaboration, in line with the general plan discussed at length six months ago, is working very hard to continue to deliver important physics results, with the CNO as focus.

On the technical side, we have pushed successfully for even better thermal stabilization and understanding, and for maintaining a very reliable data taking, with high duty cycle. Moreover, with the perspective of a final purification cycle, a strong effort has been undertaken to clean and condition the plants so to have them ready for the water extraction. As collateral action, the quality of the water has been ameliorated, setting up also the use of the water in the CTF tank to profit of its negligible Polonium content.

Also the analysis is marking important progress, first in understanding the background behavior in the inner core of the detector, precondition for any CNO attempt, and also in pushing for other significant releases, like those just done with the recent publications and those planned for the near future (Non Standard interactions limit and improved Geoneutrino data).

In summary, the Collaboration is fully committed to squeeze the most from the present and future data taking, and to deliver high quality, rich and diverse, physics results, the CNO being the most sought, but not unique, achievement.

References

[1] M. Agostini et al. (Borexino Collaboration), *Comprehensive measurement of pp-chain solar neutrinos with Borexino*, Nature 562 (2018) 496.

[2] M. Agostini et al. (Borexino Collaboration), *First Simultaneous Precision Spectroscopy of pp, ^{7}Be, and pep Solar Neutrinos with Borexino Phase-II*, arXiv:1707.09279.

[3] M. Agostini et al. (Borexino Collaboration), *Improved measurement of ^8B solar neutrinos with 1.5 kt y of Borexino exposure*, arXiv:1709.00756.

[4] M. Agostini et al. (Borexino Collaboration), *Modulations of the Cosmic Muon Signal in Ten Years of Borexino Data*, arXiv:1808.04207, JCAP 02 (2019) 046.

[5] M. Agostini et al. (Borexino Collaboration), *Constraints on Non Standard Neutrino Interactions from Borexino Phase -II".*

[6] F. L. Villante, A. Ianni, F. Lombardi, G. Pagliaroli and F. Vissani, Phys. Lett. B **701** (2011) 336 doi:10.1016/j.physletb.2011.05.068 [arXiv:1104.1335 [hep-ph]].

[7] . G. Bellini *et al.* [Borexino Collaboration], Phys. Rev. D 89, 112007 (2014)

[8] H. Back *et al.* [Borexino Collaboration], JINST 7 P10018 (2012)

[9] G. Bellini *et al.* [Borexino Collaboration], Phys. Rev. Lett. 107, 141302 (2011)

[10] G. Bellini *et al.* [Borexino Collaboration], Phys. Lett. B 707, 22 (2012)

[11] G. Bellini *et al.* [Borexino Collaboration], Phys. Rev. D82:033006 (2010)

[12] G. Bellini *et al.* [Borexino Collaboration], Phys. Rev. Lett. 108, 051302 (2012)

[13] G. Bellini *et al.* [Borexino Collaboration], Nature, 512:383-386, (2014)

[14] M. Agostini *et al.* [Borexino Collaboration], Phys. Rev. D 92, 031101 (2015)

[15] M. Agostini *et al.* [Borexino Collaboration], Phys. Rev. Lett. **115** (2015) 231802 [arXiv:1509.01223 [hep-ex]].

[16] M. Agostini *et al.* [Borexino Collaboration], arXiv:1704.02291 [physics.ins-det].

[17] M. Agostini *et al.* [BOREXINO Collaboration], arXiv:1701.07970 [hep-ex].

[18] M. Agostini *et al.* [BOREXINO Collaboration], Astropart. Phys. **86** (2017) 11 doi:10.1016/j.astropartphys.2016.10.004 [arXiv:1607.05649 [astro-ph.HE]].

COBRA

The COBRA collaboration

Lucas Bodenstein-Dresler[a], Yingjie Chu[b], Daniel Gehre[b], Claus Gößling[a], Arne Heimbold[b], Christian Herrmann[a], Rastislav Hodak[c], Joel Kostensalo[d], Kevin Kröninger[a], Julia Küttler[b], Christian Nitsch[a], Thomas Quante[a], Ekaterina Rukhadze[c], Ivan Stekl[c], Jouni Suhonen[d], Jan Tebrügge[a], Robert Temminghoff[a], Juliane Volkmer[b], Stefan Zatschler[b], Kai Zuber[b,*]

[a] TU Dortmund, Chair of Experimental Physics IV, Germany
[b] TU Dresden, Institute of Nuclear and Particle Physics, Germany
[c] CTU Prague, Institute of Experimental and Applied Physics, Czech Republic
[d] University of Jyvaskyla, Department of Physics, Finland
(* Spokesperson)

Abstract

The aim of the COBRA experiment (an abbreviation for **C**admium Zinc Telluride **0** neutrino double **B**eta **R**esearch **A**pparatus) is to investigate neutrinoless double beta ($0\nu\beta\beta$) decays using CdZnTe semiconductor detectors.

Since 2013 the COBRA demonstrator setup has been in operation at the LNGS with the goal to investigate the experimental issues of operating CdZnTe detectors in low background mode and to explore this technique's prospects. It is built from 64 monolithic CdZnTe detector crystals with a size of $1 \times 1 \times 1\,\mathrm{cm}^3$ each, arranged in an array of $4 \times 4 \times 4$ crystals. Based on the knowledge gained from the work with this demonstrator and after extensive preparation, the experiment has been upgraded to COBRA XDEM (short for e**X**tended **DEM**onstrator) in 2018. Nine additional, larger CdZnTe crystals with a volume of $6\,\mathrm{cm}^3$ each are now under operation, almost doubling the active volume of the experiment and expected to show significantly reduced background levels.

The process of this upgrade, analysis results from the demonstrator done in the course of 2018 and first results from the operation of COBRA XDEM will be presented in this report.

1 Activities at the LNGS

1.1 The COBRA demonstrator

In 2001 the construction of a $0\nu\beta\beta$ detector made from CdZnTe was proposed. This room temperature semiconductor material shows low levels of radioactivity and a good energy resolution as it is essential for the decays' investigation. Additionally, CdZnTe features several different $\beta\beta$ decays (compare Table 1) and hence offers the possibility to perform a wide range of examinations: The most promising $0\nu\beta^-\beta^-$ emitter contained in the material is ^{116}Cd, due to its high Q-value of 2814 keV, which exceeds the energy of the most high-energetic prominent γ line originating from natural decay chains. But also the investigation of decays towards excited states, the examination of various $\beta^+\beta^+$ decay modes and the analysis of the g_A-dependent spectral shape of the β^- decay of ^{113}Cd are possible.

Table 1: List of β and $\beta\beta$ decay candidates contained in CdZnTe with their corresponding decay modes, natural abundances [1] and Q-values [2].

Isotope	Decay mode	Nat. ab.	Q-value [keV]
^{113}Cd	β^- (fourfold forbidden)	12.23%	322.6
^{123}Te	EC (twofold forbidden)	0.91%	53.7
^{64}Zn	$\beta^+/EC, EC/EC$	49.17%	1094.7
^{70}Zn	$\beta^-\beta^-$	0.61%	997.1
^{106}Cd	$\beta^+\beta^+, \beta^+/EC, EC/EC$	1.25%	2775.4
^{108}Cd	EC/EC	0.89%	271.8
^{114}Cd	$\beta^-\beta^-$	28.73%	542.5
^{116}Cd	$\beta^-\beta^-$	7.50%	2813.4
^{120}Te	$\beta^+/EC, EC/EC$	0.10%	1730.4
^{128}Te	$\beta^-\beta^-$	31.69%	866.5
^{130}Te	$\beta^-\beta^-$	33.80%	2527.5

Since 2013 the COBRA demonstrator setup has been under operation – with the aim to explore the prospects and experimental challenges of CdZnTe as detector material at low background conditions. It is constructed as a $4 \times 4 \times 4$ array of 64 CdZnTe crystals. Each of the crystals measures $1 \times 1 \times 1 \times$ cm^3, has a mass of approximately 6 g and is equipped with an especially designed read-out electrode, the so-called coplanar grid. This read-out technique is necessary because of the material's poor hole mobility – the coplanar grid provides a signal only dependent on the electrons created as part of electron-hole-pairs in particle interactions.

In order to achieve the low background essential for the investigations, the setup is shielded by multiple layers of shielding materials (compare Figure 1). The array of CdZnTe crystals is surrounded by layers of Copper and Lead and placed inside of a box constantly flushed with evaporated dry Nitrogen, preventing Radon from entering the setup. Together with the first stage of the read-out chain – the custom-made preamplifiers – this box is placed inside of a Faraday cage made from carefully connected welded metal plates, protecting the signals from electromagnetic interferences (EMI). A box made from borated Polyethylene acts as the outmost shielding layer, mainly against neutrons.

While the detector and the described passive shielding are placed inside of a clean-room like
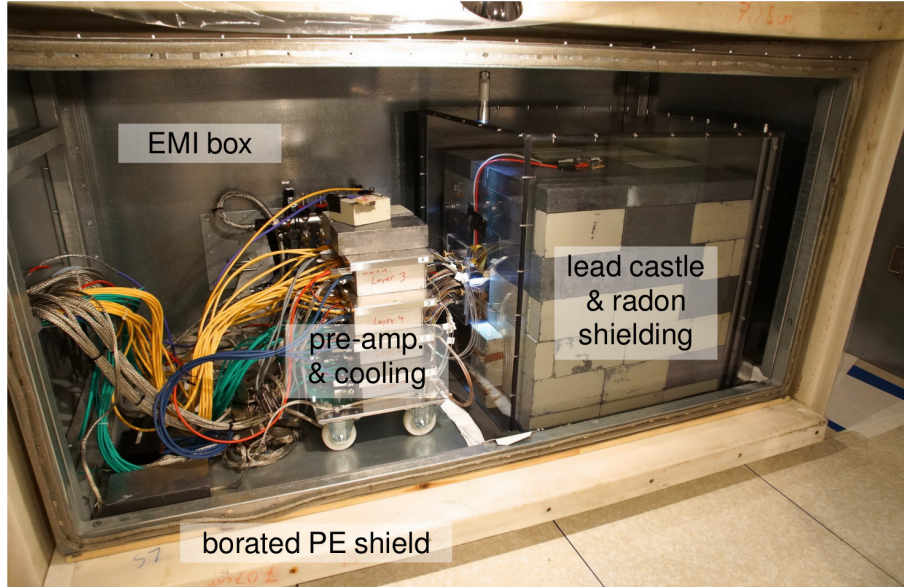
Figure 1: Overview of the experimental setup of the COBRA demonstrator. Highlighted are the different shielding layers as well as the first stage of the read-out chain – the preamplifiers. The detector crystals themselves are housed inside a Copper nest surrounded by the Lead castle and an air-tight box constantly flushed with Nitrogen.

area on the first floor of the experiment's housing at the LNGS, the heat-producing main electronics and data-acquisition can be found on the second floor of this building. A more detailed description of the COBRA demonstrator setup can be found in the references [3] and [4].

1.2   Upgrade to COBRA XDEM

Since the construction of the COBRA demonstrator, the CdZnTe crystal growth techniques have been improved. Larger crystals are available now. A augmented detector crystal volume promises a higher detection efficiency. Additionally, it was found, that the main background for the COBRA demonstrator stems from contaminations on its crystals' surfaces. Larger crystals have a smaller surface compared to their volume and thus are expected to improve the signal-to-background ratio significantly.

This is why the collaboration's main goal for 2018 was the expansion of the COBRA experiment by nine CdZnTe detector crystals with $2 \times 2 \times 1.5 \, \text{cm}^3$ in size, resulting in the COBRA extended demonstrator (COBRA XDEM). This nearly doubles the detector's sensitive mass.

The new detectors have been tested extensively beforehand and their exact structure has been chosen carefully (see for example [5]). Figure 2 shows different detector designs investigated concerning their prospects for a use in the COBRA experiment. One potential problem with large CdZnTe crystals is, that due to the more difficult growth process they could have a slightly lower crystal quality than the smaller crystals. Additionally, a large coplanar grid suffers from leakage currents. To compensate for this, it was decided to equip the large crystals with an adapted version of a coplanar grid: the quad coplanar grid. It is built from four single grid sectors, which are rotated against each other and provide the possibility of reading out signals from different parts of a detector crystal separately, making it possible to compensate for a changing performance over the larger volume.

The XDEM detector crystals are larger than their predecessors, reducing the influence of surface
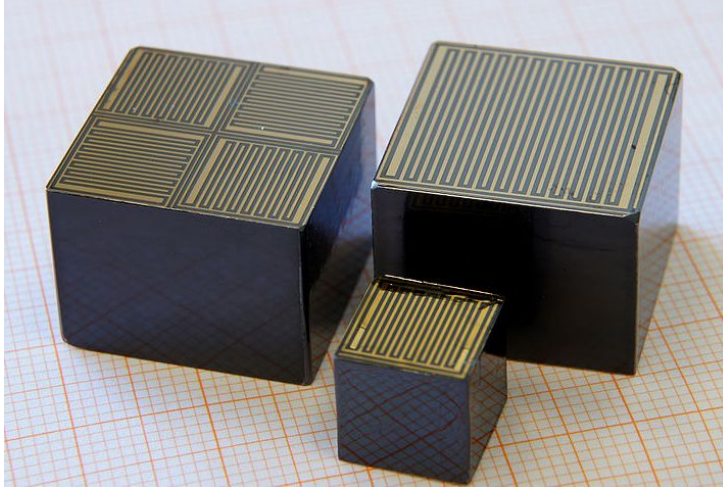
Figure 2: Picture of CdZnTe crystals investigated by the COBRA collaboration. The $1\,cm^3$ version in the front is used in the 4×4×4 array of the COBRA demonstrator. The larger $6\,cm^3$ crystals are prototypes that were studied in detail over the last two years. It was found that the up-scaled single coplanar grid version (right) is facing problems with leakage currents limiting the achievable resolution. To overcome this problem, the anode side was segmented into four individual sectors (left), called quad coplanar grid, offering additional veto capabilities.

contaminations. Compared to the crystals of the demonstrator they were handled with special care already by the manufacturers, shipped under an airtight environment and constantly stored in a Nitrogen atmosphere during their testing. Especially selected highly radio-pure materials have been used for the detectors' contacting. And the so-called guard-ring electrode, with which the detectors are equipped additionally to their quad coplanar grid, has been shown to be able to reduce surface-related background from α decays by more than three orders of magnitude [6]. For those reasons the XDEM detectors are expected to show a significantly reduced background index compared to the demonstrator setup.

In the course of about 70 man-days of work during three shifts carried out at the LNGS in 2018, the experiment's upgrade to COBRA XDEM was achieved.
The first shift took place in March. Within two weeks a complete first setup of COBRA XDEM was installed. In order to add the additional detector crystals to the experiment, the entire passive shielding first had to be deconstructed carefully and under great effort. A Copper housing with a layer of the nine new large XDEM crystals, carefully contacted beforehand, was added on top of the demonstrator crystals' copper housing (compare Figure 3, for more details see [7]). Also a Teflon tube, leading from outside of the passive shield to the layer of XDEM crystals and providing the possibility of placing a calibration source next to the detectors without opening the whole setup, was installed.
Not only the XDEM detectors themselves but also the according read-out electronics had to be installed. Three new preamplifier boxes were added to the ones for the demonstrator inside the neutron shield. Due to the amounts of additional electronics required for the extended version of the experiment, it was also necessary to set up an additional electronic rack, located next to the old one on the upper floor of the experiment's hut. It provides space for a new NIM crate – containing the linear amplifiers for the additional detectors, a new VME crate, which houses the according FADCs (fast analogue to digital converters), and a new UPS (uninterruptible power supply) to provide the power for the additional crates.
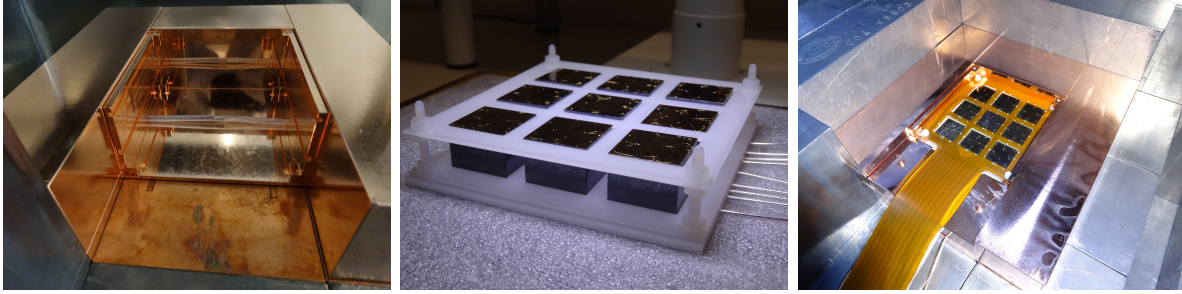
Figure 3: Impressions of the upgrade to COBRA XDEM. Left: new Copper housing made from electro-polished Copper and calibration routing. Middle: final XDEM detector layer consisting of a Poly-oxymethylen holder and nine $6\,cm^3$ quad coplanar grid detectors. Right: installed XDEM detector layer within the Copper nest on top of the COBRA demonstrator array.

Unfortunately some problems occurred during the initial installation. Both the NIM and the VME crate – which had already been under extensive use for other purposes – broke independently after a few days of operation. For the NIM crate a spare part could be found but the same was not possible for the VME crate. As a makeshift one of the VME crates originally housing the demonstrator FADCs was used instead, so that the new XDEM detectors were operational but the demonstrator detectors could not be read out anymore. Additionally, on some channels of the high-voltage board in one of the new preamplifier boxes sparkovers occurred, making it impossible to operate some of the detectors at their normal voltages. Also some of the new detector channels could not be read out at all, because of an error in the connection between the detectors and the preamplifiers.

Still, despite those unforeseeable problems, it was managed to install all the hardware for CO-BRA XDEM, start data taking with the new detectors and thereby achieve the experiment's biggest expansions since the completion of the demonstrator in 2013.

During a second shift in July it was aimed to rectify the defects, which had occurred during the XDEM installation. A new VME crate was installed, providing room for the demonstrator's FADCs and thus making it possible to operate the demonstrator again. Now for the first time both the old demonstrator as well as the new XDEM detectors were operational at the same time. Unfortunately, though, a new problem arose: The spare NIM crate installed for the XDEM detectors during the previous shift broke. It was managed to redistribute some of the electronics stored in the three NIM crates used for the demonstrator, making room for the the linear amplifiers of XDEM again. However, this was only another makeshift solution. It was later discovered, that this XDEM NIM crate crammed like this was not consistently able to provide enough power for the linear amplifiers. As a result the contained linear amplifiers were not able to process signals in the high-energy region roughly above $2\,MeV$ correctly, leading to falsely reconstructed energies.

Additionally, it was discovered, that with the entire electronics needed for the complete XDEM running, the temperature near the electronic racks rose up to $35\,°C$. The FADCs are only certified for up to $40\,°C$. Thus in the following the temperature was monitored with increased attention and one started to search for cooling solutions.

Additionally, the connection boards between the XDEM detectors and the preamplifiers, previously flawed, were changed – making it now possible to read out all of the XDEM channels. A separate high-voltage board was installed, reducing the sparkover problems. Besides that a power supply for the detector's cooling system as well as a new UPS were added to the setup,

so that now the complete COBRA electronics can be supplied with power by those devices and hence are able to be remote controlled.

The last shift of 2018 was performed in the end of October. Once more it was worked heavily on the data acquisition electronics of the experiment. Another NIM crate was added to the setup, so that enough power for all the linear amplifiers could be provided, also when processing signals in the high-energy region. Moreover one of the demonstrator VME crates, broken shortly before the shift, was exchanged. Furthermore, an external clock, providing synchronized time information to all the FADCs, was installed. This was an important step which will make it easier to analyze multi-detector coincidences in the future.

In an attempt to reduce the temperatures in the vicinity of the experiment's main electronics – at that time rising up to $53\,^{\circ}\mathrm{C}$ – the spacing between the devices was optimized in order to improve air flow around each of the electronic units. This reduced the temperature in the setup just slightly. However, during the shift contact with LNGS officials was established regarding the installation of a new cooling and air ventilation system for the part of the COBRA hut, where the electronics are located. We are delighted to say, that the cooling system was installed by the LNGS in December of 2018, causing a tremendous decrease of the temperatures in the COBRA hut and ensuring the stable operation of the experiment's electronics since then.

As a result of all this work of the collaboration at the LNGS in 2018 – despite quite an amount of broken electronics – the complete COBRA XDEM is now under stable operation, with the new detectors strongly increasing the detector's mass, the expectation of lower background ratios and the new detectors' changed anode design providing the possibility of new analysis methods.

2 Data taking and analysis

The data taken at the beginning of 2018 was dedicated to a measurement of the spectral shape of the ^{113}Cd β decay (see section 2.1), which had already been started in 2017. The use of only the very best of the demonstrator's detector crystals, operated with lowered thresholds, was to ensure an optimal quality of the data.

After the XDEM installation shift in March the demonstrator was not operational anymore, because of missing read-out electronics. In exchange, the new XDEM crystals provided first data, however, still with some problems and the data of only 15 of the $4 \times 9 = 36$ crystal sectors utilizable. The situation could be resolved during the shift in July. The demonstrator started to take data again with 59 of its 64 detector crystals and has been under operation since. The thresholds still are set to higher values than it has been the case during the dedicated ^{113}Cd run, but are searched to be reduced progressively to optimal values again. Also of the XDEM detectors 28 sectors have been under stable operation since the shift, providing the possibility of making first analyses of the new data's quality and potential.

2.1 Spectral shape analysis of ^{113}Cd

It is theorized, that the effective weak axial-vector coupling strength $g_{\mathrm{A}}^{\mathrm{eff}}$ inside nuclei deviates considerably from its free value $g_{\mathrm{A}}^{\mathrm{free}} = 1.276$ [8]. Such a changed value of $g_{\mathrm{A}}^{\mathrm{eff}}$ in turn would have a considerable influence on the predictions made for $0\nu\beta\beta$ half-lives, hence on the prospects of current and future $0\nu\beta\beta$ experiments.

Recent calculations suggest, that the spectral shape of the ^{113}Cd β^- decay – fourfold forbidden

and non-unique – is strongly dependent on $g_\mathrm{A}^\mathrm{eff}$ and thus can be used to investigate the proposed quenching effects. It is not clear, however, to what degree the result of such an analysis can be transferred to other nuclei and other decay modes, as the $0\nu\beta\beta$ decay for example, but such a measurement can still serve as a very important step towards understanding a possible quenching of g_A in general.

More than 98 % of the events measured by the COBRA detector stem from this β decay of ^{113}Cd as a natural component of the detector material. While those events usually act as a background in the search for $0\nu\beta\beta$ decays, this provides also the possibility to gain a high quality spectrum of this interesting decay. Therefore it was decided to conduct a dedicated ^{113}Cd data taking run, with all the detector characteristics optimized and adjusted to the measurement of this concrete decay. A major part of this was to reduce the detector thresholds as far as possible in order to be able to measure the spectrum also at low energies. The optimal threshold for each detector crystal was found by lowering the threshold progressively while monitoring the crystal's trigger rate. The thresholds then were controlled weekly and adjusted in order to account for possible changes in those rates. The resulting average threshold for all detector crystals during the time of data taking lay at 83 keV. In order to be able to lower the detector thresholds this far, the detector also was cooled more heavily than before, reducing the occurrence of thermal noise.
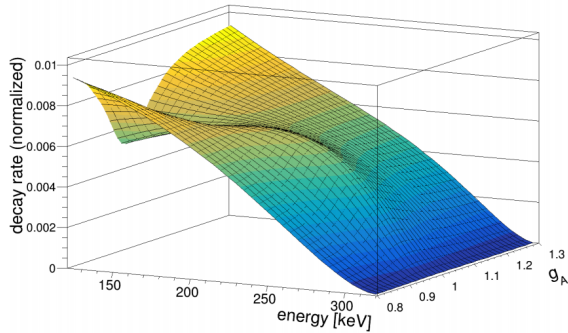
Additionally to the use of low thresholds only the detector crystals with a comparatively good performance were used. All the crystals showing unstable trigger rates during the calibration, hinting to noise problems, were switched off. The same was done for all the crystals where it was not possible to lower the thresholds sufficiently. While those detector crystals would not have provided quality information of the spectrum anyways, they might have worsened the performance of the other crystals by cross-talk effects. Hence, switching them off ensured a more stable operation of the rest of the crystals.

This dedicated measurement was performed under the settings described, from July 2017 to February 2018. One was able to obtain 45 independent spectra of the decay – one for each detector crystal in operation – with an exposure of 1.10 kgd per crystal. This corresponds to a total isotopic exposure of 2.89 kgd.
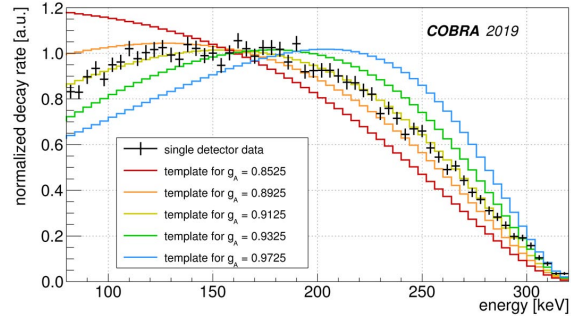

Investigations of the spectrum of the ^{113}Cd β decay had been performed before – under the use of CdWO$_4$ scintillator crystals [9, 10]. The COBRA detector however provides a much better energy resolution than those scintillator crystals and the long run time of the dedicated ^{113}Cd measurement makes it the most data ever gathered on the decay. Additionally, the main objective of all the previous investigations has always been the determination of the decay's half-life or Q-value. In [10] the spectral shape was investigated more closely and also compared to theoretical predictions, but the theory templates used are simplified strongly, approximating the transition as threefold forbidden and unique.

The COBRA collaboration however has detailed theoretically calculated spectra not featuring this simplification at its disposal. Three sets of spectra, calculated under the use of different nuclear models – the interacting shell model (ISM), the microscopic quasiparticle phonon model (MQPM) and the microscopic interacting boson fermion model (IBFM-2) – are available, with each set containing spectra for different values of $g_\mathrm{A}^\mathrm{eff}$ between 0.8 and 1.3 in steps of 0.01. In order to have access to a theoretical spectrum not only for the provided values of $g_\mathrm{A}^\mathrm{eff}$, but for arbitrary ones, so-called splines are used to interpolate the region in between the calculated spectra. Furthermore, the spectra are adapted to make them comparable to the real data: they are folded with functions accounting for the detectors' finite energy resolution, the energy-dependent signal efficiency and the constant change of the detector thresholds. The resulting dependency is unique to each single crystal since the energy threshold and the energy resolution both differ
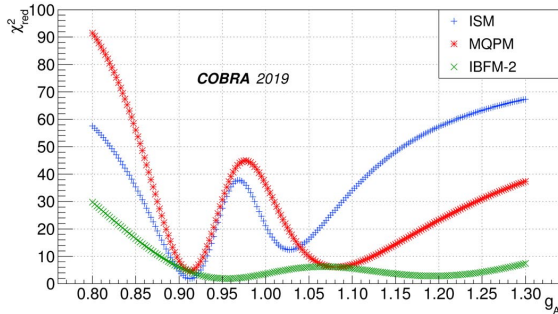
between the crystals. An example for the so obtained spectral shape in dependence of g_A^{eff} for the ISM is shown in Figure 4 a.
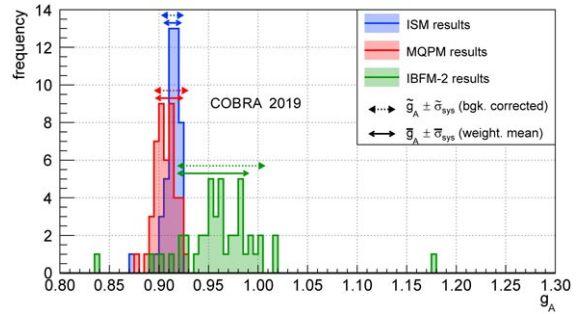

(a) ISM-calculated spectrum in dependency of g_A^{eff}, evaluated for an example detector crystal.

(b) Comparison between the ISM-calculated spectra for five different interpolated values of g_A^{eff} and the according data from an example detector crystal.

(c) χ^2 distribution for the comparison between the template spectra of the different nuclear models and the data of an example detector crystal.

(d) Distribution of the resulting best match g_A values for the three nuclear models ISM, MQPM and IBFM-2 and all the different detector crystals.

Figure 4: Different steps in the spectral shape analysis for the ^{113}Cd β decay with the goal of determining the value of g_A^{eff} involved in the decay mechanism. The figures b, c, and d are taken from a pre-print version of a paper describing the analysis [18].

With the theoretical templates prepared like this, one is able to compare the measured spectrum of each detector crystal to the set of theoretical ones. For each of the nuclear models it can be searched for the g_A^{eff} providing the best agreement between theory and data (compare Figure 4 b). Which of the values for g_A^{eff} causes the highest agreement is evaluated via a χ^2 test (compare Figure 4 c). The result is the distribution shown in Figure 4 d: The spectra measured with the different detector crystals favor slightly different values of g_A^{eff}, also depending on which nuclear model is used. The resulting averages for the g_A^{eff} values agreeing best with the data lie at 0.914 ± 0.008 for ISM, 0.910 ± 0.013 for MQPM and 0.955 ± 0.035 for IBFM-2. This is a significant deviation from the free value $g_A^{\text{free}} = 1.276$.

It can be concluded, that the data supports the idea of a quenched g_A, independently of the concrete nuclear model used. More detailed descriptions of COBRA's investigations of the spectral shape of ^{113}Cd can be found in [11] and [12]. A paper with the current status of the analysis will be published soon.

2.2 Investigation of double beta decays

2.2.1 New cuts towards a stronger background reduction

One of the main objectives of the COBRA experiment is to observe and investigate the $2\nu\beta^-\beta^-$ decay of ^{116}Cd. However, the detector's background is still too dominant for this endeavor to succeed. This is why in [13] new cuts for the experiment's background reduction were investigated.

The rate of the $2\nu\beta^-\beta^-$ decay in the detector is expected to stay constant during the complete run time of the experiment. Increased count-rates measured in single detector crystals or also the whole experiment thus are a hint for an increased background. To discard data with such comparatively high count rates – enriched in background – can help to improve the overall signal-to-background ratio. Figure 5 gives an overview of the different detector crystals' count rates over time.
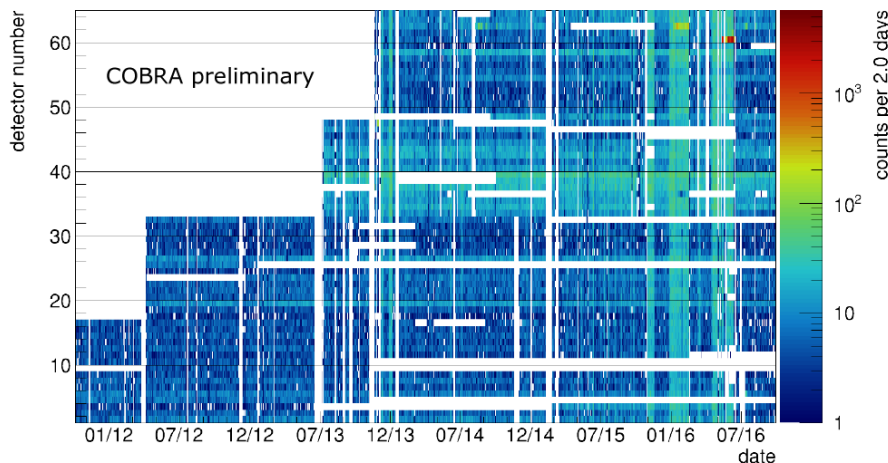

Figure 5: Count rate for all 64 detectors of the COBRA demonstrator between end of 2011 and fall 2016 for events in the energy region $350\,\mathrm{keV} \leq E \leq 2800\,\mathrm{keV}$. The big white area on the left shows the layer-wise extension of the setup [13].

There can be different reasons for increased count rates. From time to time single crystals show high rates of unphysical events, stemming from signal disturbances at some point of the data acquisition. Also some of the detector crystals – mainly the Layer 3 crystals – in general show higher count rates than the others. This is suspected to be caused by contaminations on the specific detector surfaces. During the installation of Layer 3 there were some works at the experiment's hut ongoing which might have produced such. Additionally, there are some time periods in which all the crystals see increased event rates. Those coincide with the times in which the Nitrogen flushing of the detector failed and Radon diffused into the crystals' environment. By discarding all this background-enriched data, one is able to reduce the background in the region ($350\,\mathrm{keV} \leq E \leq 2800\,\mathrm{keV}$) of interest by a factor of 2.8 (compare Figure 6).

Already in the past cuts on events close to the detector crystals' surface have been used, because those events are likely caused by α decays of contaminations on the crystal surfaces. One of those cuts is the so-called z- or interaction depth cut, discarding the events close to the anode or cathode of each crystal. With the anode lying at $z = 0$ and the cathode at $z = 1$ up to now all the events with $z < 0.2$ or $z > 0.97$ have been discarded. It was found, however, that also
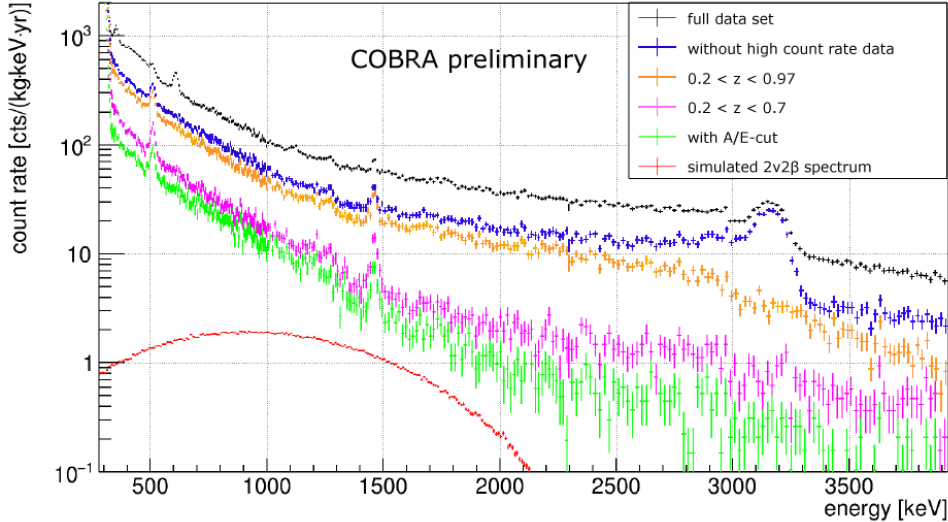
23

Figure 6: Effect of the different cuts applied to the COBRA data in order to improve the signal-to-background ratio. The cuts are executed after each other so that the background gets reduced further and further with each cut. As a comparison the simulated $2\nu\beta\beta$ spectrum of ^{116}Cd for the case that all cuts shown are applied is depicted. Due to the high signal efficiency of the cuts their influence on the simulated spectrum is only marginal, however.

the data with events occurring in $0.7 < z < 0.97$ are characterized by comparatively high count rates, which seem to be caused by contaminations on the Delrin holder the crystals are placed in. Hence, a stricter z-cut, also discarding the events with $z > 0.7$, is beneficial (compare Figure 6).

Another cut on the detector's surface used in the past is the lateral-surface-event-cut (LSE-cut), exploiting that the crystals' potentials are slightly distorted in the region of the detector surface, which has an influence on the signal pulses originating there and hence makes events from those lateral surfaces recognizable. It was used together with a multi-site-event-cut (MSE-cut), which uses pulse shape analysis to recognize and discard events with multiple particle interactions inside one detector crystal, hence reducing the γ background. Those cuts are not flawless, however. One drawback is, that the data discarded by the two cuts can overlap, making it difficult to calculate the cut efficiencies. That is why a new cut, which combines the rejection of both LSEs and MSEs, was investigated. The so-called A/E-cut uses the ratio between the maximum current occurring during the charge collection at the anode and the energy calculated for an event as a parameter to access whether the event should be discarded or not. This parameter is comparatively small for MSEs as well as LSEs. With the help of ^{228}Th calibration data, where peaks are available, which nearly purely contain multi-site events and single-site events respectively, the optimal A/E-cut value was searched for.

In terms of resulting signal-to-background ratio, this newly developed cut can compete with the old combination of LSE- and MSE-cuts. At the same time the A/E-cut shows an improved signal efficiency and and can be optimized much more easily with calibration data. The spectrum of the data set obtained after applying data partitioning, the new strict z-cut as well as the A/E-cut is depicted in Figure 6.

With all cuts applied, the background is still too high in order for the $2\nu\beta\beta$ decay to be observable. However, the A/E-cut still offers more potential. Especially the recognition of LSEs will be optimized further.

A further step towards background reduction made this year was the reactivation of the COBRA time synchronization tool. With the synchronized data – with a global time information for all the detector crystals – one is able to investigate coincidence events. $2\nu\beta^-\beta^-$ events usually leave a signature in only one detector crystal, while background γ radiation can hit multiple detectors. Hence, the exclusion of multi-crystal hits will improve the signal-to-background ratio further. Also a Bismuth-Polonium-tagging might be an option.

2.2.2 Feasibility study for the investigation of EC/β^+ decays

Next to $\beta^-\beta^-$ decays also $\beta^+\beta^+$ decay modes occur in the detector material (compare Table 1). Of those the EC/β^+ might be especially interesting. Compared to the other $\beta^+\beta^+$ decay modes the 2νEC/β^+ decay could be comparatively easy to detect. The 0νEC/β^+ decay on the other hand shows an enhanced sensitivity to the involvement of right-handed currents in neutrinoless double beta decays [14] and hence can be used to investigate the physics behind those processes. In 2018 a feasibility study for the investigation of ^{106}Cd EC/β^+ decays with COBRA was executed (for more details see [15]). The characteristic signatures produced in the detector by the decays were simulated and analyzed. Based on this, cuts with the goal of reducing the background but keeping the EC/β^+ events were developed. They were tested using simulations of the signal decays, assuming their predicted half-lives of about 10^{28} yr for the 0νEC/β^+ decay of ^{116}Cd and 10^{23} yr for the 2νEC/β^+ decay [16]. Those half-lives are so large, that no EC/β^+ decay is expected to have occurred during data taking up to now. Therefore the data set was used as a representative of the background.

The best cuts found show good signal efficiencies and background rejection (compare Table 2). The COBRA detector's composition of multiple single crystals is highly useful in the recognition of EC/β^+ decays. In contrast to most background events EC/β^+ decays often cause energy depositions in multiple crystals instead of only one. Additionally, if the different particles released in an EC/β^+ decay deposit their energies in different detector crystals, as it is often the case, highly characteristic signatures – hardly ever mimicked by background decays – are seen.

Table 2: Overview of the characteristics of the best cuts found for the investigation of EC/β^+ decays of ^{116}Cd with COBRA.

signal decay	signal efficiency	background efficiency	resulting signal-to-background ratio
2νEC/β^+	15.1 %	$7 \cdot 10^{-4}$ %	10^{-7}
0νEC/β^+	8.5 %	$7 \cdot 10^{-8}$ %	10^{-5}

Despite the ability of theoretically recognizing the EC/β^+ decays in the detector, neither the observation of 2νEC/β^+ decays nor the improvement of the current limit on the half-life of the 0νEC/β^+ are feasible at the time, however. The amount of data gathered to date is not sufficient and especially for the 2νEC/β^+ analysis also the background level had to be reduced further.

One potential future project, however, could be the use of CdZnTe detector crystals enriched in ^{106}Cd. Such an experiment could use the same granular design as the current COBRA experiment and at the same time gather data on the decay much faster.

2.3 First data from the XDEM detectors

First of all an extensive calibration, using three different calibration sources, was performed for the XDEM detector. The sources cover the energy region between 121 keV and 2615 keV. Figure 7 shows the result of the calibration – a comparison between the true measured energy, known from the characteristics of the source, and the energy reconstructed from the detector signal. Except for the lowest energetic line, from ^{152}Eu, all deviations between those two values stay below 0.3 %. They originate from the fit uncertainties of the individual peaks seen in the data.
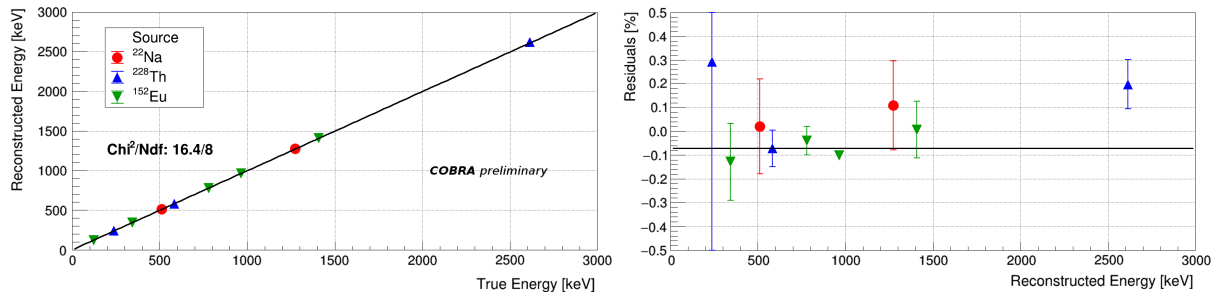

Figure 7: Results for the first calibration of the complete XDEM setup. With the three different radioactive sources a good linearity over a wide energy range could be shown. The small deviations between reconstructed energy and true energy value result from the peak fit uncertainties.

The deviations are much smaller than the detector crystals' energy resolution. The average relative FWHM of the demonstrator crystals, extrapolated to the Q-value of ^{116}Cd, lies at 1.40 %. Despite the new XDEM crystals being six times larger than those old crystals, the design goal for the XDEM had been set to an improved relative FWHM of 1.3 %. This aim has been surpassed distinctly with a value of 1.07 ± 0.34 %. If a z-cut is applied, this improves further to 0.97 %.

Additionally, the γs released by the ^{228}Th calibration source can be used to study the possibility of vetoing against γ-related background by excluding events with multiple sectors of the same crystal hit simultaneously. Indeed such an anti-coincidence analysis shows potential. The coincident events in the ^{228}Th calibration show many notable features caused by γs interacting in multiple sectors of one detector crystal. Those characteristic signatures can be used to exclude γ events from the data.

The first physics run of XDEM was started in November 2018. The data taken until January of 2019 – resulting in an exposure of 17 kgd – was used to perform a first preliminary analysis of the detector's data.

Due to the new anode design of the XDEM crystals compared to the demonstrator ones, the signal evaluation and the data cleaning cuts used with the demonstrator cannot simply be transferred to the XDEM data. This is why, for this preliminary analysis only a z-cut is applied to the XDEM data. Since the reconstruction of the interaction depth for XDEM, is more complicated than before, a comparatively strong cut of $0.2 < z < 0.9$ (compare standard for demonstrator: $0.2 < z < 0.97$) was chosen. Like this it is still assured, that all background events stemming from the detector crystals' anode are removed.

The resulting spectrum, compared to the one of the demonstrator crystals, is shown in Figure 8. One observes, that the XDEM data shows a significantly reduced rate of background events compared to the demonstrator. In fact in the region around 2814 keV, the Q-value of the $0\nu\beta\beta$ decay of ^{116}Cd, only two events remain. This results in a background index of
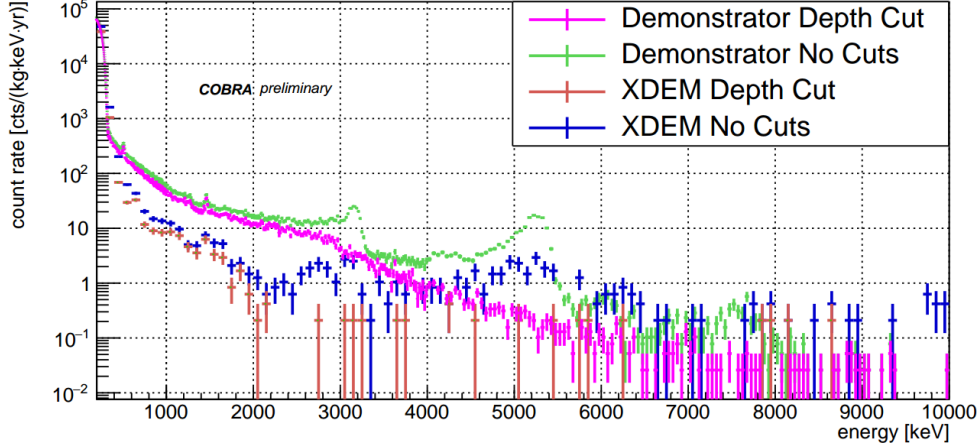
Figure 8: Spectra for the demonstrator and the XDEM setup with and without interaction depth cut respectively. Compared to the demonstrator's spectrum the XDEM count rate is reduced significantly, especially around the Q-value of ^{116}Cd at 2814 keV. It should be noted, that the exposures of the two setups differ strongly from each other (XDEM: 17 kgd, demonstrator: 234 kgd).

$(7 \pm 5) \cdot 10^{-2}$ cts/keV/kg/yr. At lower energies the count rate is also significantly reduced, resulting in a much more beneficial situation to analyze the $2\nu\beta\beta$ decay of ^{116}Cd and additional double beta decay modes.

Concerning features in the background spectrum, there are some characteristics already known from the demonstrator, but also some so far unidentified components. One notable new feature is visible below 3 MeV. It is separated distinctly from the signature of the known α decay of ^{190}Pt with a Q-value of 3.2 MeV. Platinum is part of the electrode for some of the detectors. Further notable features are a γ line at 1460 keV from ^{40}K, present in several parts surrounding the detectors, and another one at 662 keV presumably from ^{137}Cs, which may be attributed to contaminations in the detector holders. This assumption needs further investigation through Monte Carlo simulations. The 511 keV line, which is rather prominent in the demonstrator data, cannot be seen in the XDEM spectrum.

3   Steps towards a background model

In 2018 many measures towards the development of a background model have been taken. Potential background sources for XDEM have been explored by measuring the radio-purity of the materials surrounding the detector crystals. For example a 50 kg sample of the Copper used as a the inner shield as well as in the detector holder has been measured at the Modane underground laboratory. The Uranium and Thorium content of various materials used in the vicinity of the detector crystals has been investigated with the Inductively Coupled Plasma-Mass Spectrometer at LNGS.

Based on the newly gained knowledge on activities of different nuclides in the materials used, Monte Carlo simulations studying the effects of those impurities as well as of external background have been executed (for more details see [17]). All background sources investigated so far stay below 10^{-3} cts/keV/kg/yr after the analysis cuts are applied. Further measurements of potential background sources will be executed and more simulations will be done in order to obtain a complete model of the overall expected background in the near future.

In order to approximate the background for the spectral shape analysis of ^{113}Cd (compare section 2.1), a first simplified background model for the demonstrator has been developed (compare Figure 9). It comprises contributions of the ^{222}Rn decay chain in the gas surrounding the detector, intrinsic contaminations with nuclides from the ^{232}Th and ^{238}U decay chains and contributions of ^{40}K which can be found in various materials surrounding the detector.
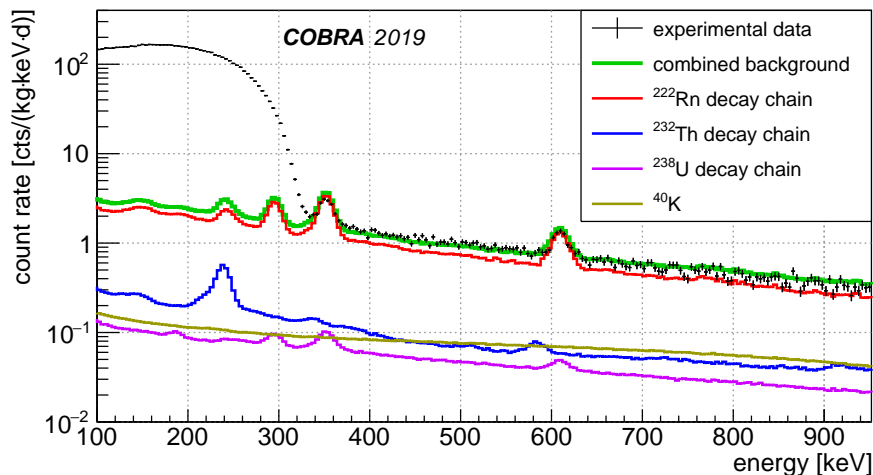

Figure 9: Data of the dedicated ^{113}Cd run compared to a first simplified background model. Considered are the ^{222}Rn, ^{232}Th and ^{238}U decay chains as well as ^{40}K with different origins of the primary decays.

4 Outlook

The new XDEM detectors offer the potential of physics analyses, especially the search for the $2\nu\beta\beta$ decay of ^{116}Cd, with a strongly reduced background level compared to before. The newly developed data cleaning cuts improve the situation further. An observation of the $2\nu\beta\beta$ decay of ^{116}Cd requires to adapt the A/E approach to the XDEM data as well as a further preparation of its event reconstruction and analysis.

Additionally, it will be continued to intensely work on the development of a background model for the complete detector. For the next shift scheduled to May 2019 it is planned to rectify the problems of the currently 8 of 36 XDEM detector crystal sectors, so that one will be able to use the complete power of XDEM in the further search for interesting physics.

References

[1] M. Berglund and M. Wiesner, *Isotopic compositions of the elements 2009 (IUPAC Technical Report)*, Pure and Applied Chemistry 83 (2011)

[2] M. Wang et al., *The AME2012 atomic mass evaluation*, CPC(HEP & NP), Vol.36, No.12 (2012)

[3] J. Ebert et al., *The COBRA demonstrator at the LNGS underground laboratory*, NIM A (2016), 10.1016/j.nima.2015.10.079, arXiv:1507.08177

[4] D. Gehre, *Investigations on CdZnTe-Semiconductor-Detectors for the Search of the Neutrinoless Double Beta Decay*, PhD thesis, TU Dresden (2017)

[5] I. Höfmann, *Effizienzbestimmung von CdZnTe-CPqG-Detektoren für das COBRA-XDEM-Upgrade*, bachelor thesis, TU Dortmund (2018)

[6] M. Fritts et al., *Analytical model for event reconstruction in coplanar grid CdZnTe detectors*, NIM A 708 (2013), 10.1016/j.nima.2013.01.004, arXiv:1211.6604

[7] L. Bodenstein-Dresler, *Preparation for the C0BRA XDEM phase including design of mechanical parts, tests of electronics and measurement of $\beta-$ suppression*, master thesis, TU Dortmund (2018)

[8] J. Liu et al., *Determination of the Axial-Vector Weak Coupling Constant with Ultracold Neutrons*, Phys. Rev. Lett. 105, 181803 (2010)

[9] F. Danevich et al., *Beta decay of ^{113}Cd*, Phys. Atom. Nucl. 59, 1–5 (1996)

[10] P. Belli et al., *Investigation of β decay of ^{113}Cd*, Phys. Rev. C 76, 064603 (2007)

[11] L. Bodenstein-Dresler et al., *Quenching of g_A deduced from the β-spectrum shape of ^{113}Cd measured with the COBRA experiment*, arXiv:1806.02254v1 (2018)

[12] A. Heimbold, *Spectral shape analysis of the fourfold forbidden beta decay of Cd-113 with the COBRA experiment*, master thesis, TU Dresden (2018)

[13] J. Küttler, *Investigation of the $2\nu2\beta$-spectrum of ^{116}Cd with the COBRA experiment*, master thesis, TU Dresden (2019)

[14] M. Hirsch et al., *Nuclear structure calculation of $\beta^+\beta^+$, β^+/EC and EC/EC decay matrix elements*, Z. Phys. A 347, 151-160 (1994)

[15] J. Volkmer, *Prospects of the investigation of $EC/beta^+$ decays with the C0BRA experiment*, master thesis, TU Dresden (2018)

[16] V. Tretyak and Y. Zdesenko, *Tables of double beta decay data*, Atomic data and nuclear data tables 61, 43-90 (1995)

[17] C. Herrmann, *Monte-Carlo Based Studies of Potential Background in the XDEM-phase of the C0BRA Experiment*, master thesis, TU Dortmund (2018)

[18] L. Bodenstein-Dresler et al., *Quenching of g_A deduced from the β-spectrum shape of ^{113}Cd measured with the COBRA experiment* , arXiv:1806.02254v1 [nucl-ex] (2018)

COSINUS *

G. Angloher[a], P. Carniti[b,c], N. Di Marco[d], S. Fichtinger[e],
M. Friedl[e], A. Fuss[e,f], C. Gotti[b,c], M. Mancuso[a], L. Pagnanini[b,c],
G. Pessina[b], F. Petricca[a], S. Pirro[d], F. Pröbst[a], F. Reindl[e,f],
K. Schäffner[d,g], J. Schieck[e,f], C. Schwertner[e,f], M. Stahlberg[e,f],
V. Zema [†] [d,g,i] and Y. Zhu[h]

[a]Max-Planck-Institut für Physik, 80805 München - Germany
[b]INFN - Sezione di Milano Bicocca, 20126 Milano - Italy
[c]Dipartimento di Fisica, Università di Milano-Bicocca, 20126
Milano - Italy
[d]INFN - Laboratori Nazionali del Gran Sasso, 67010 Assergi - Italy
[e]Institut für Hochenergiephysik der Österreichischen Akademie der
Wissenschaften, 1050 Wien - Austria
[f]Atominstitut, Technische Universität Wien, 1020 Wien - Austria
[g]Gran Sasso Science Institute, 67100 L'Aquila - Italy
[h]SICCAS - Shanghai Institute of Ceramics, Shanghai, P.R.China
200050
[j]Chalmers University of Technology, SE-412 96 Göteborg, Sweden

---

COSINUS is a NaI-based cryogenic calorimeter operated at mK temperature. The goal of COSINUS is to cross-check the results of the DAMA/LIBRA experiment, that has been detecting since more than 20 years a signal compatible with the expectations for the dark matter (DM) galactic halo. The use of the same target material as DAMA as planned in COSINUS is crucial to get new insights on the puzzling dark matter experimental panorama. The experimental panorama is in fact characterised by null-results of most of the other direct DM searches which exclude dark matter interpretation of the DAMA results when the most common theoretical dark matter scenarios are considered. In this report the activities of COSINUS done during 2018 are described.

Contents

1 The COSINUS project

COSINUS (Cryogenic Observatory for SIgnatures seen in Next-generation Underground Searches) consists in the development of a cryogenic calorimeter based on radio-pure NaI crystals operated at $O(10\text{mK})$ temperature. The initial R&D phase has been funded by the National Scientific Committee 5 (CSN5) of INFN, for three years of prototype development, from 2016 to 2018 [1]; one year prolongation to 2019 was approved. Starting in 2019, a Max Planck Research Group Grant has been assigned, with the duration of 5 years, for the realisation of COSINUS from an R&D project to an experiment.

Other NaI-based experiments share the COSINUS urgency of confirming/rejecting the DAMA results for testing the annual modulation signal. In terms of detection principle COSINE-100 [2], ANAIS-112 [3], SABRE [4], PICO-LON [5] and DAMA/LIBRA [6], are single channel experiments: any event, both electron and nuclear recoils, manifests as scintillation light and the discrimination of the signal from background relies on the time dependence of the count rate over the year. COSINUS aims at a dual channel detector, which collects both the light and the heat produced by a particle interaction in the crystal. The discrimination of e^-/γ events from nuclear recoils is possible thanks to the expected different light yield, which can provide a powerful test of the nature of the DAMA signal.

2 Experimental concept

The COSINUS prototype design consists of a small cubic NaI crystal, resting on a thin disc of a harder material (*e.g.* CdWO$_4$) named carrier, of about 4cm in diameter and $\sim 1-2$mm of thickness, which hosts the Transition Edge Sensor (TES), the temperature

sensor. The carrier is necessary to exclude the hygroscopic NaI from the TES fabrication process, which would harm the NaI crystal. Epoxy resin or silicone oil make an interface between the cubic NaI crystal and the carrier. The crystal is enclosed in a silicon beaker of about $4 - 5$cm of diameter and height and about 600μm of wall-thickness, also instrumented with a TES, working as an absorber for the scintillation light. The interactions of a particle inside the NaI volume produce both heat, which is dissipated by phonon propagation, that is by vibrations of the crystal lattice, and scintillation light. The NaI crystal, interfaced to the carrier and the TES, is the phonon detector. The silicon beaker, instrumented with a second TES, constitutes the light detector. While silicon serves as absorber for the scintillation light, the beaker shape is chosen to achieve a good light collection efficiency. Furthermore the carrier and the light absorber are designed to optimise the active surrounding coverage, which works as background veto for α-induced-surface events. For this purpose the carrier disc diameter exceeds the crystal dimensions and fits the silicon beaker diameter.
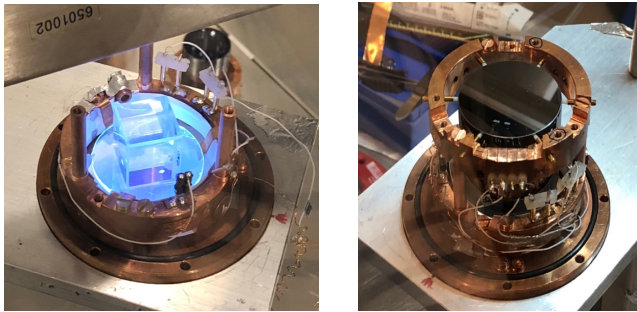

Figure 1: Example of COSINUS module. Right: NaI(Tl) crystal. Left: silicon beaker equipped with the TES and embedded in the copper housing.

The detection of both heat and light is the basis of particle discrimination provided by cryogenic scintillating calorimeters, since, unlike room temperature scintillators, they can measure the phonon signal, which makes the largest part of the detected signal ($\simeq 90\%$). The energy directly converted in phonons allows to reconstruct the incoming particle energy, because it is almost independent of the particle type. The amount of emitted light is instead a function of the particle nature, because of the phenomenon of light quenching. The ratio between the light energy and the phonon energy, called Light Yield (LY), allows the discrimination between e^-/γ events and nuclear recoil events and, to some extent, even between recoils off Na and I.

The Transition Edge Sensor (TES) is a superconducting thermometer. It is a thin metal film of metal, operated within its superconducting and normal conducting phase transition. Small variations in temperature ($\mathcal{O}(\mu K)$) induced by the interaction particles cause a steep increase of the TES resistance ($\mathcal{O}(m\Omega)$), which is registered by SQUID

(Superconducting Quantum Interference Device) amplifiers.

3 Prototype development: Status

From 2016 to 2018 COSINUS has run several different prototypes. In table 1 the main steps are listed. The first prototype measurement represents the first time a NaI crystal was successfully operated as cryogenic detector. The linearity between the light and the phonon energy was experimentally proven. The peculiar behaviour of the pulse shape was encountered for the first time [7]. The second prototype was the first realisation of the COSINUS light detector design, with the silicon beaker-shaped absorber, which showed a performance well beyond the expectations, since the goal was $\simeq 4\%$ [8]. From the 4th prototype on, several NaI crystals have been produced by SICCAS, whose collaboration with COSINUS has been formally established. The new batch of NaI/NaI(Tl) crystals from SICCAS are currently employed in the COSINUS tests for detector development.

Table 1: Chronology of the main COSINUS prototype developments. LD: Light Detector. PD: Phonon Detector. The column 'Interface' specifies the material used for the NaI/carrier interface, where the carrier is the crystal carrying the TES (SO = Silicone Oil, ER = Epoxy Resin). Wafer SOS stands for Silicon-On-Sapphire, initially used as light absorber. The column LC for percentage of absolute light yield, calibrated with the help of an ^{55}Fe source shining onto the Si beaker. NaI(Tl) crystal was measured only in Meier-Leibnitz Laboratorium (MLL).

Prototype	LD	PD	Interface	LC	PD Threshold
1st (2016)	wafer SOS	NaI	SO	$\simeq 3.7\%$	10 keV
2nd (2016/17)	Si beaker	NaI	ER	$\simeq 13\%$	8.3 keV
3rd (2017)	"	"	SO	"	6.5 keV
$4^{st}- 10^{st}$ (2017/18)	"	NaI/NaI(Tl)	"	"	$5-6$ keV

3.1 Results of the crystal program

The crystal production is a key step of the prototype development. The experts I. Dafinei from INFN, Roma 1 and Yong Zhu from the SICCAS company are fully involved in the crystal production campaign. In 2018 SICCAS produced NaI crystals from Astrograde-powder: COSINUS purchased 12 kg of powder and two 3-inch crystals have been successfully grown.
During 2018, the goal of producing high radio-purity crystals was achieved: COSINUS crystals potassium concentration is 5-9 ppb at crystals' nose and 22-35 ppb at crystals' tail. COSINUS crystal radio-purity, for what concerns the concentration of potassium, which is considered the most important because its decay emission is a source of background in the region of interest of DAMA, has reached and overcame the one of DAMA.

3.2 New TES concept

COSINUS detector-prototype design consists of a NaI crystal interfaced to a non hygro-scopic crystal which works as carrier for the TES. The TES is glued to the carrier on the opposite face with respect the interface between the NaI and the carrier. Phonons produced in the NaI crystal need to propagate through different boundaries (NaI, interface, carrier) before reaching the TES. A configuration with inverted order of boundaries, with the TES directly interfaced to the NaI, could result in a higher transmission of phonons and in a reduction of energy threshold. The measurement testing this new design was done in September 2018, but a bad performance of the TES did not allow to make conclusions. The TES deposition failed, the film had tiny holes as confirmed after the cryogenic test. The further testing is foreseen in next future.
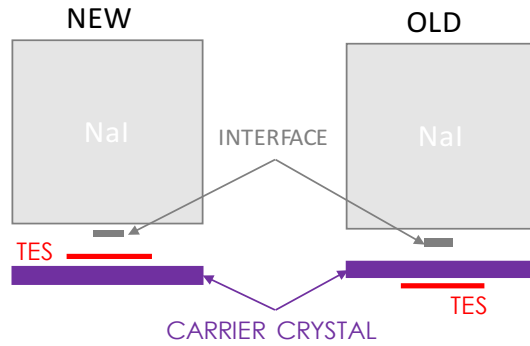

Figure 2: Scheme of a possible new TES concept.

4 Quenching factors measurement

The evidence that different class of particles interacting in the crystal volume produce different amount of scintillation light is empirically described by the Birk's law [9]. According to the Birk's law, heavier projectiles produce less scintillation light and the factor of suppression is commonly called Quenching Factor (QF). Knowledge of quenching factors is extremely important for particle discrimination because it allows the reconstruction of the deposited energy and the identification of the e^-/γ band and the nuclear recoil band.

QF measurement can be performed via calibration with neutron sources as well as via calibration with a mono-energetic source of neutrons at accelerator facilities. A systematic study to establish the optimal concentration of thallium to be used as NaI dopant is being performed at the Meier-Leibnitz Laboratorium (MLL), where a Tandem-van-de-Graaf accelerator produces and accelerates ^{11}B ions on a cell of pressurised hydrogen, provide a mono-energetic beam of 11 MeV neutrons. COSINUS already ran two measurements at the MLL, one on a NaI(pure) crystal in April 2018, and one on a NaI(Tl) crystal, in November 2018. Interpretation of results is challenging.

4.1 Tl-concentration: a systematic study

To understand if the level of thallium dopant can influence the quenching factor, a systematic study of the performances of NaI crystals with different thallium (Tl) concentrations has been planned. Crystals with different amount of Tl-dopant (200ppm, 500 ppm, 1000 ppm, 1500 ppm) will be operated both as cryogenic detectors, at mK-temperature, at the Max Planck Institute using AmBe neutron source and as scintillation detector at room temperature, at the Triangle University Nuclear Laboratory (TUNL) scattering facility, USA, using a neutron beam as calibration source.

4.2 Recoil source measurement

An additional setup which has been realised to measure the quenching factors[1] consisted in the implantation of a radium source on a slice of TeO_2 crystal. The TeO_2 crystal was equipped with a NTD. The TeO_2 was then mounted inside the silicon beaker. With a half life of 3.66 days, ^{224}Ra decays into ^{220}Rn, which further alpha-decays into ^{216}Pb, ^{212}Pb, ^{212}Bi, ^{212}Po. Since the alpha decay is a back-to-back process, the expectation is to observe alphas at about 5 MeV in TeO_2 and a coincident nuclear recoil of 90 keV in NaI.

The implantation and the mounting of the setup were successfully realised. The TeO_2 crystal could not be operated. Checking the TeO_2 crystal after the measurement showed that the NTD sensor came of (bad gluing). This triple-coincidence measurement needs to be redone.
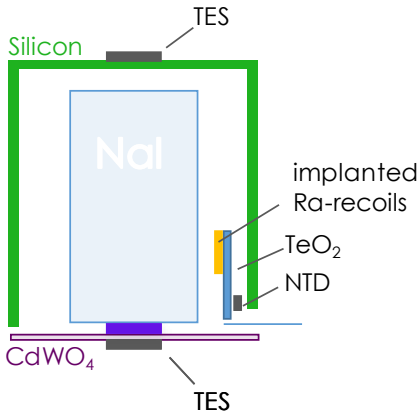

Figure 3: Scheme of the setup for the triple-coincidence measurement.

---

[1]In this case the recoiling nucleus is a heavy daughter of the radium decay chain, not sodium or iodine.

5 Background budget evaluation and shielding concept

COSINUS is planning to build the facility which will host the detectors. A core part of the structure is the shielding. The conclusions on the shielding concept obtained by studying the various source of background via simulations are explained in the following sections.

5.1 Background for direct dark matter experiments

The search for rare events requires a careful background budget evaluation in order to minimise events that could mimic or interfere with signal detection. Both environmental radioactivity and intrinsic contamination of materials used for detectors, shielding and infrastructure, have to be taken into account.

It is worth to note that neutrons interacting inside the crystals can easily mimic a dark matter nuclear recoil and thus have to be considered the most dangerous type of background. Neutrons, in underground sites, are produced in reactions initiated both by natural radioactivity and cosmic rays. Radiogenic neutrons originate from spontaneous fission and (α, n) interactions from natural radioactive contaminants (^{238}U and ^{232}Th) present in the rock, water and concrete as well as in the materials used in the experimental setup. Cosmogenic neutrons are produced either in muon-induced spallation or negative muon capture processes, or by secondary particles generated in muon-induced cascades, in the rock and in the surrounding materials, through photon or hadron-induced spallation or disintegration reactions [10]. In the former case, the neutron energy is in the fast range (up to ~10 MeV), while in the latter extends up to few GeV.

Ambient γ flux originates from long-lived natural radioisotopes ^{40}K, ^{238}U and ^{232}Th present in the rock. Moreover, cosmic muons can induce bremsstrahlung both in the rock and in high-Z materials used as passive shielding. The dual channel read-out of the COSINUS approach ensures a good discrimination capability against β/γ-particles. Nevertheless, gamma radioactivity has to be properly taken into account especially in the very low energy region where the discrimination power is weaker.

Finally, special attention has to be dedicated to cosmogenic activation of materials employed and radon contamination inside the experimental apparatus and during manufacturing of detectors and shielding.

The reduction of the external background radiation relies on the use of an appropriate shielding. The classical approach ([6][11]) is based on the use of a layer of a low mass number material (usually polyethylene, PE) as moderator against the ambient neutron flux, followed by a layer of a high-Z material (usually lead) to absorb the ambient gamma flux. A further layer of copper is then needed to cope with the gamma radiation due to the ^{210}Pb isotope contained in the lead. Nevertheless, in high-Z materials as Pb, nuclear capture of negative cosmic muons results in further emission of neutrons. Such a background can be suppressed by using a muon veto system, usually made of plastic scintillator panels. Radiogenic neutrons produced in the shielding itself can be moderated adding a further layer of polyethylene near the detector volume. A

different approach based on the use of an ultra-pure water volume instrumented with photomultiplier tubes (PMTs), as e.g. in the XENON1t design [12], would satisfy both, the requirement to have a passive shield against ambient radioactivity and the need for an active veto against muon-induced events. Ultra-pure water has a better radio-purity than polyethylene and, as will be presented in next sections, allows to globally reduce the amount of passive shielding materials employed, thus minimising the background in the experiment.

Following the latter approach, we evaluated five different shielding configurations as listed in table 2. For each material and design configuration we computed the radiogenic neutron and gamma fluxes due to the intrinsic radioactivity, using material screening essay found in literature. The intrinsic neutron and gamma yields are then used as a benchmark and compared to the attenuation of the environmental fluxes offered by the various options in order to optimise the thickness of the different shielding layers and to choose the preferred design configuration.

In [13] the detailed MonteCarlo simulations performed are presented together with the results obtained.

Option	Tank (stainless) [cm]	Water radius [cm]	Dry-well (stainless) [cm]	Pb [cm]	Cu [cm]	PE [cm]	Cryostat (Cu) [cm]	Top shield Pb+Cu+PE [cm]
1	1.5	150	0.4	10	15	10	0.8	10+15+10
2	1.5	200	0.4	0	15	10	0.8	0+40+10
3	1.5	200	0.4	0	15	0	0.8	0+40+0
4	1.5	300	0.4	0	8	0	0.8	0+30+0
5	1.5	300	0.4	0	0	0	0.8	0+40+0

Table 2: The five different options for our shielding configuration, featuring different thicknesses of water, Pb, Cu and PE.

5.2 Results on the shielding configuration

The detailed simulations performed and illustrated in [13] lead us to conclude that, at present, Option 4 of table 2 would be the best compromise minimising both the total amount of expected background and costs. Solely looking at the numbers presented in [13], one could even consider the rather exotic solution without any inner shielding (Option 5) as the best one. A minimum of 3 m of water could be able to reduce the ambient gamma flux efficiently enough without placing any further shielding material inside the dry-well, at the same time minimising the sources of radiogenic and cosmogenic neutron production. A more refined analysis will be performed once the final design of the cryostat and of the NaI target is fixed.

5.3 Results on the Cherenkov veto design

An optical simulation was performed in order to study the possible configuration and the performance of the water Cherenkov veto. The results is that an efficient muon veto system can be obtained using $\sim$18 - 28 PMTs and defining a 5-fold PMT coincidence with a trigger on the single photoelectron within a time window of a few 100 ns. The final configuration will be defined on the basis of the background rate study in order to optimise both tagging efficiency and dead-time.

Summary

COSINUS prototype development fully reached the goal for the light detector functioning and for the high radio-purity level The crystal radio-purity level is even higher than DAMA crystals. The phonon detector threshold of 1 keV has not yet been achieved and the quenching factor measurement is still an open question, whose answer is one of the main focus of the future activities. The optimal concentration of thallium is under investigation and a systematic study of the detector performance both at room temperature and at milli-kelvin temperature is planned. MonteCarlo simulations were performed as first model for the shielding configuration and of the Cherenkov veto design of the COSINUS experimental setup. A official proposal to the scientific committee and the LNGS director was made to host COSINUS at LNGS underground site.

References

[1] G. Angloher *et al.*, Eur. Phys. J. C **76**, no. 8, 441 (2016) doi:10.1140/epjc/s10052-016-4278-3 [arXiv:1603.02214 [physics.ins-det]].

[2] G. Adhikari *et al.*, Eur. Phys. J. C **78**, no. 2, 107 (2018) doi:10.1140/epjc/s10052-018-5590-x [arXiv:1710.05299 [physics.ins-det]].

[3] J. Amaré *et al.*, J. Phys. Conf. Ser. **718**, no. 4, 042052 (2016) doi:10.1088/1742-6596/718/4/042052 [arXiv:1512.04239 [astro-ph.IM]].

[4] C. Tomei [SABRE Collaboration], Nucl. Instrum. Meth. A **845**, 418 (2017). doi:10.1016/j.nima.2016.06.007

[5] K. I. Fushimi *et al.*, JPS Conf. Proc. **11**, 020003 (2016) doi:10.7566/JPSCP.11.020003 [arXiv:1605.04999 [astro-ph.IM]].

[6] R. Bernabei *et al.* [DAMA Collaboration], Nucl. Instrum. Meth. A **592**, 297 (2008) doi:10.1016/j.nima.2008.04.082 [arXiv:0804.2738 [astro-ph]].

[7] G. Angloher *et al.* [COSINUS Collaboration], JINST **12**, no. 11, P11007 (2017) doi:10.1088/1748-0221/12/11/P11007 [arXiv:1705.11028 [physics.ins-det]].

[8] K. Schäffner *et al.*, J. Low. Temp. Phys. **193**, no. 5-6, 1174 (2018). doi:10.1007/s10909-018-1967-3

[9] J. B. Birks, International series of Monographs on Electronics and Instrumentation, v. 27 Macmillan, New York

[10] V. A. Kudryavtsev, L. Pandola and V. Tomasello, Eur. Phys. J. A **36**, 171 (2008) doi:10.1140/epja/i2007-10539-6 [arXiv:0802.3566 [astro-ph]].

[11] G. Angloher *et al.*, Eur. Phys. J. C **72**, 1971 (2012) doi:10.1140/epjc/s10052-012-1971-8 [arXiv:1109.0702 [astro-ph.CO]].

[12] E. Aprile *et al.* [XENON1T Collaboration], JINST **9**, P11006 (2014) doi:10.1088/1748-0221/9/11/P11006 [arXiv:1406.2374 [astro-ph.IM]].

[13] G. Angloher *et al.* [COSINUS Collaboration], "COSINUS Conceptual design report", (2019).

CUORE

C. Alduino,[1] K. Alfonso,[2] F. T. Avignone III,[1] O. Azzolini,[3] M. Balata,[4] G. Bari,[5]

F. Bellini,[6,7] G. Benato,[8] A. Bersani,[9] M. Biassoni,[10] F. Bragazzi,[9] A. Branca,[11,12]

C. Brofferio,[13,10] C. Bucci,[4] C. Bulfon,[7] A. Caminata,[9] A. Campani,[14,9] L. Canonica,[15,4]

X. G. Cao,[16] S. Capelli,[13,10] M. Capodiferro,[7] L. Cappelli,[8,17,4] L. Cardani,[7] M. Cariello,[9]

P. Carniti,[13,10] N. Casali,[7] L. Cassina,[13,10] R. Cereseto,[9] G. Ceruti,[10] A. Chiarini,[5]

D. Chiesa,[13,10] N. Chott,[1] M. Clemenza,[13,10] S. Copello,[14,9] C. Cosmelli,[6,7] O. Cremonesi,[10,*]

R. J. Creswick,[1] J. S. Cushman,[18] A. D'Addabbo,[4] D. D'Aguanno,[4,19] I. Dafinei,[7] C. J. Davis,[18]

F. Del Corso,[5] S. Dell'Oro,[20] M. M. Deninno,[5] S. Di Domizio,[14,9] M. L. Di Vacri,[4,21]

V. Dompè,[4,22] A. Drobizhev,[8,17] G. Erme,[4,19] D. Q. Fang,[16] M. Faverzani,[13,10] E. Ferri,[13,10]

F. Ferroni,[6,7] S. Finelli,[5] E. Fiorini,[10,13] M. A. Franceschi,[23] S. J. Freedman,[17,8,†]

B. K. Fujikawa,[17] R. Gaigher,[10] A. Giachero,[13,10] L. Gironi,[13,10] A. Giuliani,[24] L. Gladstone,[15]

P. Gorla,[4] C. Gotti,[13,10] C. Guandalini,[5] M. Guerzoni,[5] M. Guetti,[4] T. D. Gutierrez,[25]

K. Han,[26] K. M. Heeger,[18] R. Hennings-Yeomans,[8,17] H. Z. Huang,[2] M. Iannone,[7] L. Ioannucci,[4]

J. Johnston,[15] G. Keppel,[3] Yu. G. Kolomensky,[8,17] A. Leder,[15] C. Ligi,[23] K. E. Lim,[18]

Y. G. Ma,[16] L. Marini,[14,9] M. Martinez,[6,7,27] R. H. Maruyama,[18] R. Mazza,[10] Y. Mei,[17]

N. Moggi,[28,5] S. Morganti,[7] S. S. Nagorny,[4,22] T. Napolitano,[23] M. Nastasi,[13,10] S. Nisi,[4]

C. Nones,[29] E. B. Norman,[30,31] V. Novati,[24] A. Nucciotti,[13,10] I. Nutini,[4,22] T. O'Donnell,[20]

D. Orlandi,[4] J. L. Ouellet,[15] C. E. Pagliarone,[4,19] M. Pallavicini,[14,9] V. Palmieri,[3]

L. Pattavina,[4] M. Pavan,[13,10] R. Pedrotta,[11] A. Pelosi,[7] M. Perego,[10] G. Pessina,[10] C. Pira,[3]

S. Pirro,[4] S. Pozzi,[13,10] E. Previtali,[10] A. Puiu,[13,10] F. Reindl,[7] C. Rosenfeld,[1] C. Rossi,[9]

C. Rusconi,[1,4] M. Sakai,[2] S. Sangiorgio,[30] D. Santone,[4,21] B. Schmidt,[17] N. D. Scielzo,[30]

V. Singh,[8] M. Sisti,[13,10] D. Speller,[18] F. Stivanello,[3] L. Taffarello,[11] L. Tatananni,[4]

F. Terranova,[13,10] M. Tessaro,[11] C. Tomei,[7] M. Vignati,[7] S. L. Wagaarachchi,[8,17] J. Wallig,[32]

B. S. Wang,[30,31] H. W. Wang,[16] B. Welliver,[17] J. Wilson,[1] K. Wilson,[1] L. A. Winslow,[15]

T. Wise,[18,33] L. Zanotti,[13,10] C. Zarra,[4] G. Q. Zhang,[16] S. Zimmermann,[32] and S. Zucchelli[28,5]

[1]*Department of Physics and Astronomy, University of South Carolina, Columbia, SC 29208, USA*

[2]*Department of Physics and Astronomy, University of California, Los Angeles, CA 90095, USA*

[3]*INFN – Laboratori Nazionali di Legnaro, Legnaro (Padova) I-35020, Italy*

[4]*INFN – Laboratori Nazionali del Gran Sasso, Assergi (L'Aquila) I-67100, Italy*

[5]*INFN – Sezione di Bologna, Bologna I-40127, Italy*

[6] *Dipartimento di Fisica, Sapienza Università di Roma, Roma I-00185, Italy*

[7] *INFN – Sezione di Roma, Roma I-00185, Italy*

[8] *Department of Physics, University of California, Berkeley, CA 94720, USA*

[9] *INFN – Sezione di Genova, Genova I-16146, Italy*

[10] *INFN – Sezione di Milano Bicocca, Milano I-20126, Italy*

[11] *INFN – Sezione di Padova, Padova I-35131, Italy*

[12] *Dipartimento di Fisica e Astronomia, Università di Padova, I-35131 Padova, Italy*

[13] *Dipartimento di Fisica, Università di Milano-Bicocca, Milano I-20126, Italy*

[14] *Dipartimento di Fisica, Università di Genova, Genova I-16146, Italy*

[15] *Massachusetts Institute of Technology, Cambridge, MA 02139, USA*

[16] *Shanghai Institute of Applied Physics, Chinese Academy of Sciences, Shanghai 201800, China*

[17] *Nuclear Science Division, Lawrence Berkeley National Laboratory, Berkeley, CA 94720, USA*

[18] *Wright Laboratory, Department of Physics,*
Yale University, New Haven, CT 06520, USA

[19] *Dipartimento di Ingegneria Civile e Meccanica,*
Università degli Studi di Cassino e del Lazio Meridionale, Cassino I-03043, Italy

[20] *Center for Neutrino Physics, Virginia Polytechnic Institute*
and State University, Blacksburg, Virginia 24061, USA

[21] *Dipartimento di Scienze Fisiche e Chimiche,*
Università dell'Aquila, L'Aquila I-67100, Italy

[22] *INFN – Gran Sasso Science Institute, L'Aquila I-67100, Italy*

[23] *INFN – Laboratori Nazionali di Frascati, Frascati (Roma) I-00044, Italy*

[24] *CSNSM, Univ. Paris-Sud, CNRS/IN2P3,*
Université Paris-Saclay, 91405 Orsay, France

[25] *Physics Department, California Polytechnic State University, San Luis Obispo, CA 93407, USA*

[26] *INPAC and School of Physics and Astronomy,*
Shanghai Jiao Tong University; Shanghai Laboratory for
Particle Physics and Cosmology, Shanghai 200240, China

[27] *Laboratorio de Fisica Nuclear y Astroparticulas,*
Universidad de Zaragoza, Zaragoza 50009, Spain

[28] *Dipartimento di Fisica e Astronomia, Alma Mater*
Studiorum – Università di Bologna, Bologna I-40127, Italy

[29] *Service de Physique des Particules, CEA / Saclay, 91191 Gif-sur-Yvette, France*

[30] *Lawrence Livermore National Laboratory, Livermore, CA 94550, USA*

[31] *Department of Nuclear Engineering, University of California, Berkeley, CA 94720, USA*

[32] *Engineering Division, Lawrence Berkeley National Laboratory, Berkeley, CA 94720, USA*

[33] *Department of Physics, University of Wisconsin, Madison, WI 53706, USA*

Cryogenic Underground Observatory for Rare Events (CUORE) is an experiment which aims to achieve a half-life sensitivity of 10^{26} years for neutrinoless double beta decay ($0\nu\beta\beta$) in ^{130}Te using cryogenic bolometry. $0\nu\beta\beta$ decay is one of the most sensitive probes for physics beyond the Standard Model, providing unique information on the nature of neutrinos.
The detector consists of a close-packed array of TeO$_2$ crystals containing $\sim$206 kg of ^{130}Te in total, operated at $\sim$10 mK inside a large, dedicated cryostat.

In this report we summarize the activities of the collaboration at the Laboratori Nazionali del Gran Sasso (LNGS) during 2018. The first period of the year was dedicated to a maintenance of the internal calibration system, followed by a period of data collection. The data taking was suspended for few months during Fall 2018 due to problems of the cryogenic system and retrieved by the end of the year.

---

* spokeperson

† Deceased

I. SCIENTIFIC GOAL

The Cryogenic Underground Observatory for rare events (CUORE) is an experiment searching for the neutrinoless double beta decay of ^{130}Te.

Neutrinoless double beta decay ($0\nu\beta\beta$) is a rare nuclear process not predicted by the Standard Model in which a pair of neutrons inside a nucleus transforms into a pair of protons, with the emission of two electrons: $(A, Z) \rightarrow (A, Z+2)+2e^-$. This transition clearly violates the conservation of the number of leptons. The observation of $0\nu\beta\beta$ would thus demonstrate that the lepton number is not a symmetry of nature. At the same time, $0\nu\beta\beta$ provides a key tool to study neutrinos by probing whether their nature is that of Majorana particles and providing us with important information on the neutrino absolute mass scale and ordering. The huge impact on Particle Physics has motivated and continues to motivate a strong experimental effort to search for $0\nu\beta\beta$.

A. Search for neutrinoless double beta decay

The experimental search for $0\nu\beta\beta$ is based on the detection and precise measurement of the sum of the kinetic energies of the two emitted electrons or positrons. In fact, since the energy of the recoiling nucleus is negligible, the sum of the two leptons' kinetic energies must be equal to the Q-value of the transition, $Q_{\beta\beta}$, and it should appear in the sum energy spectrum as a monochromatic peak.

The experimental parameter extracted from the data is the half-life of the decay of the isotope under study, $t_{1/2}^{0\nu}$, and the sensitivity of a $0\nu\beta\beta$ experiment is usually defined as the minimum half-life compatible with the background fluctuations n_B at a given confidence level:

$$t_{1/2}^{0\nu} = \ln 2 \; \varepsilon \; \frac{1}{n_\sigma} \; \frac{x \, \eta \, N_A}{\mathcal{M}_A} \; \sqrt{\frac{M \, T}{B \, \Delta}} \tag{1}$$

where M is the detector mass, B is the background level per unit mass, energy, and time in the region of interest (ROI) around $Q_{\beta\beta}$, Δ is the FWHM energy resolution (used conventionally as the region over which to integrate B), x is the stoichiometric multiplicity of the element containing the $\beta\beta$ candidate, η is the $\beta\beta$ candidate isotopic abundance, N_A is the Avogadro number, $\mathcal{M}_A$ is the compound molecular mass and n_σ is the number of sigmas corresponding to the requested C.L..

In case the decay is not observed, a lower limit $t_{1/2}^{0\nu}$ can be set on the process half-life, corresponding to an upper bound on the Effective Majorana mass, $m_{\beta\beta}$, the parameter that carries the

information on the neutrino masses, whose measurement is the main goal of the $0\nu\beta\beta$ searches. The relation between the half-life and the effective neutrino mass can be expressed as:

$$\left[t_{1/2}^{0\nu}\right]^{-1} = \frac{m_{\beta\beta}^2}{m_{\rm e}^2}\, G_{0\nu}\, g_{\rm A}^4\, |\mathcal{M}_{0\nu}|^2 \tag{2}$$

where $G_{0\nu}$ is the Phase Space Factor (PSF), $\mathcal{M}_{0\nu}$ is the Nuclear Matrix Element (NME), $g_{\rm A}$ is the axial coupling constant and $m_{\rm e}$ is the electron mass, conventionally taken as a reference. Both $G_{0\nu}$ and $\mathcal{M}_{0\nu}$ cannot be measured but only calculated. They require a deep knowledge of the involved nuclear physics and, while $G_{0\nu}$ can be evaluated with high precision, the uncertainty in the calculation of $\mathcal{M}_{0\nu}$ is still one of the most serious limits to the determination of $m_{\beta\beta}$.

Actually, an experimental limit on $t_{1/2}^{0\nu}$ translates into a range of values for $m_{\beta\beta}$ due to the theoretical uncertainties, mostly coming from the nuclear physics associated to the parameters of Eq. (2).

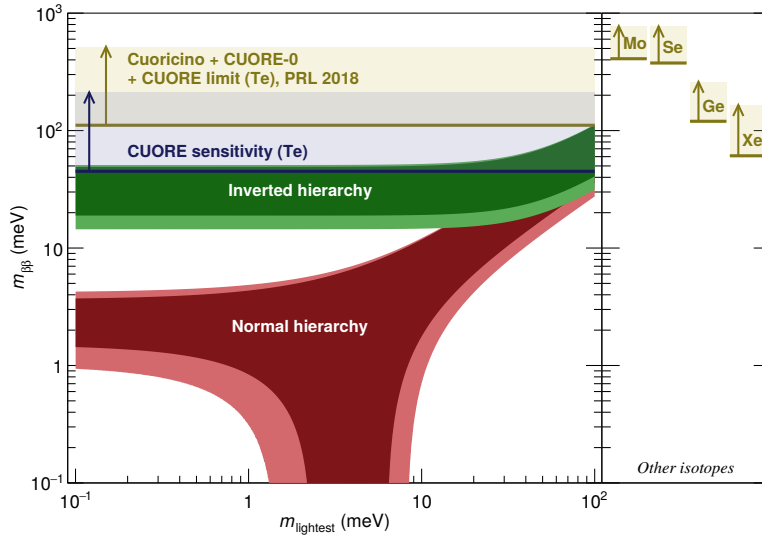### B.   CUORE sensitivity on $0\nu\beta\beta$

FIG. 1: Constraints on $m_{\beta\beta}$ vs $m_{\rm lightest}$ from CUORE: the first data release and the final projected sensitivity. The bound is compared with the similar ones on other studied isotopes.

The initial result on the search for $0\nu\beta\beta$ from CUORE was released at the end of 2017. We found no evidence for $0\nu\beta\beta$ of ^{130}Te. Including the systematic uncertainties, we could place a lower limit on the decay half-life of $1.3 \cdot 10^{25}$ yr at 90% C. L.. Combining this result with those of two earlier experiments, Cuoricino and CUORE-0, we obtained the most stringent limit to date on this decay, i.e. $1.5 \cdot 10^{25}$ yr at 90% C. L..

We converted the combined half-life limit to an upper limit on the effective Majorana neutrino mass, $m_{\beta\beta}$, in the framework of models that assume $0\nu\beta\beta$ to mediated by light Majorana neutrino exchange. We found $m_{\beta\beta} < (110 - 520)\,\mathrm{meV}$, where the range reflects the uncertainties coming from the nuclear physics. In Fig. 1, the bound from CUORE is compared to the "official" bounds coming from some of the most studied isotopes using the representation $m_{\beta\beta}\ vs\ m_{\mathrm{lightest}}$, the latter parameter being the mass of the lightest neutrino, in the two (mutually exclusive) scenarios of Normal and Inverted Hierarchy (NH and IH) of the neutrino mass spectrum. It can be seen that the constraint from ^{130}Te, i.e. the current CUORE limit is comparable with that from ^{76}Ge, while the projected CUORE sensitiviy is expected to reach (or pass) the most stringent present limit, coming from ^{136}Xe, approaching the Inverted Hierarchy region.

CUORE will collect data for a total of five years of live-time. The predicted final sensitivity is $9.0 \cdot 10^{25}\,\mathrm{yr}$ at $90\%\,\mathrm{C.\,L.}$.

C.   Other studies with CUORE

Although $0\nu\beta\beta$ of ^{130}Te is the main objective of TeO_2 bolometers, a number of other processes is open to experimental investigation. The excellent energy resolution and the anticipated low background rates allow competitive sensitivities for many of them. The accessible processes include alternative modes of double beta decay as well as more exotic processes predicted by some extensions of the SM.

Indeed, natural tellurium includes $\beta\beta$-active isotopes other than ^{130}Te, namely ^{120}Te and ^{128}Te, and the $\beta\beta$ transitions to excited states can provide unique information on the $0\nu\beta\beta$ mechanism. On the other hand, the precise measurement of the $2\nu\beta\beta$ half-lives is crucial to test the constraints of the $\beta\beta$ nuclear matrix elements.

Among the exotic processes, the experimental investigation of the validity limits of fundamental principles such as the charge conservation or the CPT/Lorentz invariance deserve particular attention since most of our theoretical construction is based on them. Likewise, the search for Dark Matter candidates (which, by the way, began with the first $\beta\beta$ experiments), is still a subject on which TeO_2 bolometers can provide competitive results.
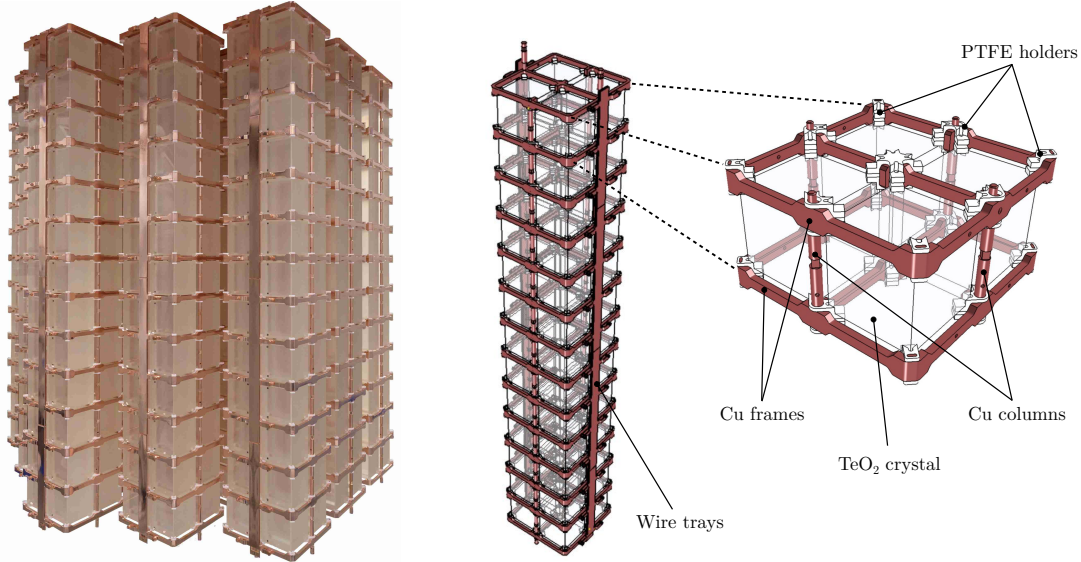
FIG. 2: (Right) The completed 19-tower CUORE detector. (Left) Rendering of an individual tower with a detail of a single floor.

II. CUORE DETECTOR OVERVIEW

The CUORE detector consists of 988 ultra-radiopure TeO_2 bolometers arranged into 19 towers. Each crystal serves both as source and detector of $0\nu\beta\beta$ decay in ^{130}Te. An individual CUORE tower consists of 52 crystals held inside a copper structure by Teflon (PTFE) brackets in an arrangement of 13 four-crystal floors. A picture of the assembled CUORE detector is shown in Fig. (2), together with a detailed view of an individual tower and floor.

In order to operate as a bolometer, a neutron transmutation doped (NTD) germanium thermistor and a joule heater are glued to one face of each crystal. The thermistors measure the μK-scale temperature fluctuations due to particle interactions with the crystal/absorber. The heaters deliver a fixed (and extremely precise) amount of energy to generate a pulse as similar as possible to the signal corresponding to a physical event, thus allowing to correct the detector response to the same energy deposition. These sensors are directly wire-bonded to readout ribbons held by copper trays, in turn fixed to the tower structure. All the copper components directly facing the crystals have been cleaned according to a strict protocol specifically designed and developed at the Legnaro National Laboratory (LNL). Furthermore, in order to minimize the recontamination of the components during the subsequent handling, all the towers were assembled in dedicated airtight N_2 flushed glove boxes.
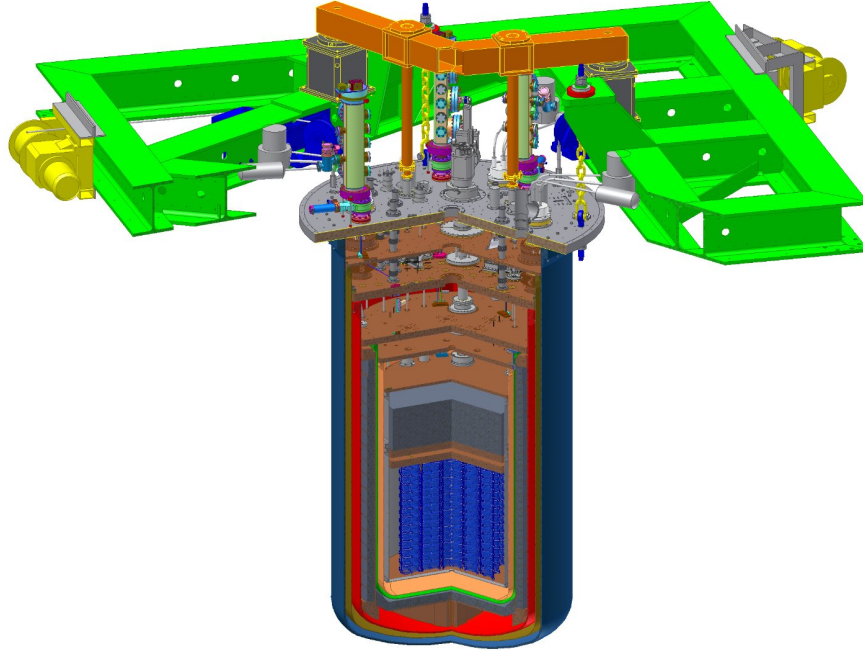
FIG. 3: Rendering of the CUORE cryostat.

The CUORE detector cannot operate in a standard dilution refrigerator. Therefore, a custom cryogenic system had to be designed and commissioned in order to guarantee the optimal operation of the experiment for a live-time of years, satisfying a set of very stringent experimental requirements in terms of high cooling power, low noise environment and low radioactivity content.

The adopted solution consisted in a large custom cryogen-free cryostat cooled by 5 Pulse Tube refrigerators (PTs) and by a high-power ^{3}He/^{4}He Dilution Unit (DU). The CUORE cryostat comprises six nested vessels, the innermost of which encloses the experimental volume (Fig. 3). To avoid radioactive background, only a few construction materials were acceptable and about 7 tonnes of lead was utilized for shielding and had to be cooled below 4 K. The different stages are maintained at temperatures of about 300 K, 40 K, 4 K, 800 mK (Still), 60 mK (HEX) and 10 mK (MC). The 300 K and the 4 K vessels are vacuum-tight and enclose the Outer Vacuum Chamber (OVC) and the Inner Vacuum Chamber (IVC), respectively. The IVC contains the detector shielding lead. The lead shields include the Top Lead and the Internal Lateral and bottom Shield, the latter being made of ancient Roman lead. The Tower Support Plate holding the detector is attached to a dedicated suspension system in order to reduce the amount of vibrations and it is placed right below the Top Lead. The 4 K and the 40 K vessels are externally covered with a multilayer aluminized superinsulation in order to limit the thermal radiation coming from higher temperature vessels. The IVC cool down to $\sim 50\,K$ is driven by the Fast Cooling System, which injects cold He gas

inside its volume for a faster and more efficient cooling process. The whole cryostat is protected from the external radioactivity by the External Lateral and bottom Shield, a 18 cm polyethylene + 2 cm H_3BO_3 + 25 cm lead shield on the side and 25 cm lead + 20 cm borated polyethylene shield on the bottom. In order to calibrate the detector while in operation, a dedicated system had been integrated in the cryostat, allowing for the insertion and extraction of the sources without perturbing the cryogenic environment.

III.   REPLACEMENT OF THE DCS GATE VALVES

At the beginning of 2018, we warmed up the cryostat in order to perform the replacement of the four gate valves of the CUORE internal calibration system (IDCS). This activity resulted to be necessary since air intake from the system had been observed during the various calibrations in 2017.

The PTs were turned off on January 11, 2018. After collecting the mixture from the DU, we began to inject clean He exchange gas inside the IVC. We stabilized the 4 K stage at about 100 K by turning on and off the PTs. The temperatures of the inner stages were thus ranging in the tens of K (the coldest part was the Top Lead, due to the large thermal inertia).

In order to gain access to the gate valve area we moved the IDCS motion boxes placed on top of the gate valves, by means of a dedicated lifting system. This consisted in a small manual crane that could be anchored to the electronics Y-beam support placed over the cryostat. This system allowed to keep the motion boxes suspended during the valve replacement without interfering with the operation and, at the same time, without the need of moving away and reinstalling the motion boxes themselves, which would have proved to be an uneasy task.

The actual valve replacement was a quick operation, which would have been straightforward in normal conditions. However, the low temperature of the system and the presence of the CUORE detector inside the cryostat required additional care, in order to avoid any risk of recontamination, especially by Rn. To this extent, in order to operate in 'safe' conditions for the detector, we kept the IVC at about 70 mbar of (He) overpressure and we continuously injected new He gas during the replacement. In the short intervals in which the IVC was open to the external world, we were thus able to avoid any air return inside the cryostat. In particular, we first removed the old valve and temporarily sealed the IDCS port with a blank flange. Then, after making sure that the IVC was still maintaining the needed overpressure (otherwise we had to wait for insertion of additional gas), we removed the flange and installed the new valve. In all the cases, we never went below

50 mbar of overpressure.

Before the installation, each new valve was tested and leak-checked. We also constantly monitored the cryogenic system conditions to ensure the success of the each individual replacement. We thus performed one replacement per day and, including all the preparation work, the complete replacement of the valves took about two weeks.
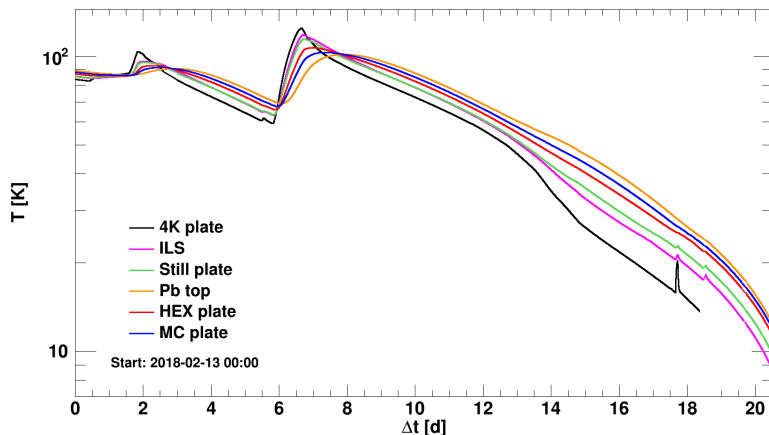
IV.   CUORE NEW COOLDOWN

FIG. 4: Time evolution of the different thermal stage temperatures during the winter 2018 cooldown (CUORE Run 6). The cooldown starts from about 90 K, after the completion of the IDCS valve replacement. The initial temperature rises are due to problems with the pumping system. In about 20 days, all the stages are at about 10 K. It will take another 10 days of pumping before starting the circulation with the DU.

The new cooldown (Run 6, following the sequence of cooldowns performed during the cryostat commissioning) started by mid February 2018 (Fig. 4). The temperatures of the 4 K and inner stages were about 90 K. In the end, we reached the planned detector working temperature (11.8 mK based on the results of the optimization campaign performed in the late 2017) by mid March 2018.

V.   DETECTOR CALIBRATION SYSTEMS

A.   Internal detector calibration system

CUORE was originally designed to implement and use an internal detector calibration system (IDCS) based on low activity sources deployed inside the detector region. This system was designed to guarantee uniform illumination of all the detectors and a proper calibration in the whole energy range of interest.

The IDCS represents a very advanced low-temperature technology, capable of deploying radioactive sources through the CUORE shielding to place them close to the detectors. This requires moving the sources from room temperature into the 10 mK environment without disrupting the cryostat vacuum or the subkelvin operating temperatures of the detector. Key features of this system include a series of counteractions to minimize any increase in temperature of the cryostat during the deployment and the construction from pure and clean materials in order to maintain the radio-pure environment of the detector. The IDCS consists of 6 inner strings between the detectors towers and 6 outer strings surrounding the detector array outside the 50 mK vessel. A detailed description of the IDCS system is reported in NIM (Nucl. Instrum. Methods A **844**, 32-44 (2017)).

Using the IDCS, we were able to successfully calibrate the detectors during both the 2017 data taking and the first science run of 2018 after the substitution of the gate valves. However, due to a small vacuum leak, we started experiencing problems in the deployment related to the presence of frozen air in the guide tubes. Despite the substitution of the gate valves at the end of the opening calibration of July 2018 science run (DS4), one of the IDCS strings from the inner part of the detector got stuck in the guide tube above the 4 K plate. The issue was caused by the accumulation of frozen air in the strings guide tube which created an obstruction. Monte Carlo simulations have determined and the measured event rates and spectra confirmed that the presence of a calibration string just above the 4 K represents a negligible background in the region of interest, thanks to the top lead shield and to multiple cryostat plates.

As a result, in the following calibrations the deployment of the strings was troublesome and some of the strings could not be fully deployed. The calibration of the detectors and a smooth data taking was nevertheless possible during summer 2018. An unsuccessful attempt to extract the source was carried out in September 2018, exploiting the warm-up of the system during another cryostat maintenance.

B. External detector calibration system

Given the complexity of the IDCS and the evident interference with the cryogenic system operation, the risks of continuing IDCS calibrations were analyzed. In the case of a new failure, warming-up and opening the CUORE cryostat would have implied a stop of the data taking of the order of six months/one year. To mitigate such a risk the collaboration decided to design and install an External Detector Calibration System (EDCS) as a back-up device and as a complement to the original calibration system.

EDCS consists of 8 PVC guide tubes for string-like sources deployed inside the external lead and polyethylene shields, but outside the cryostat Outer Vacuum Chamber (OVC). The pipes are equally spaced around the OVC and aligned with the corners of the octagonal external shield for better clearance (see Fig. 5). The tops of the PVC pipes are positioned at locations around the perimeter of the $300\,K$ plate and are equipped with thermoformed funnels for guiding the string. A set of 8 winches are anchored to the ceiling of the Faraday Room, aligned with the pipe openings and remotely controlled in order to minimize the access in proximity of the cryostat. The strings can be clipped to the winch cables with quick-release carabiners that require no tools. The strings can also be inserted or removed manually without major contraindications.
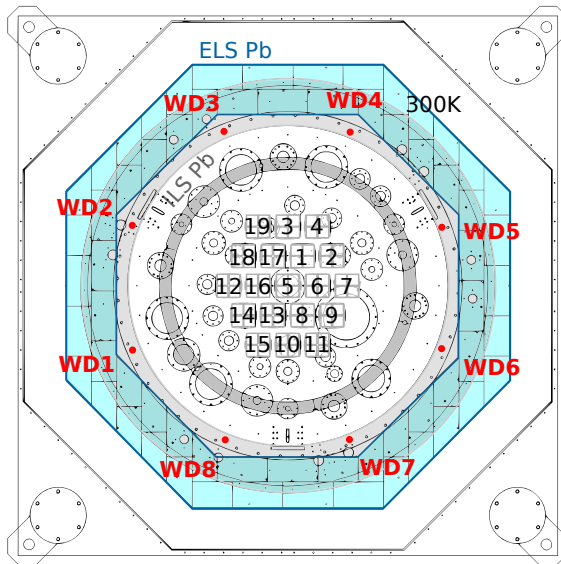

FIG. 5: Schematic of the CUORE external calibration system and position of the strings.

This back-up system can provide an almost uniform luminosity but is limited to energy lines larger than 500 keV. On the other hand it is technically simple and robust, easily accessible and

can be deployed and retract quickly, without waiting for the strings to thermalize. Furthermore, the use of the EDCS allows for a rapid source replacement in case a non-standard calibration like ^{56}Co or ^{60}Co is needed. The installation and technical testing of the EDCS was carried out in February of 2018, in parallel with the IDCS valve replacement, taking advantage of the data taking interruption. The first calibration tests were carried out using strings consisting of standard thoriated tungsten welding rods of 2.5 cm length, and strung together with a flexible mesh nylon sheath. In November 2018 new calibration sources (including also ^{60}Co) were produced.

The total string length and activity were based on a careful simulation of the EDCS, aiming to guarantee the most uniform illumination possible considering that the outer towers are more exposed than the inner ones to the EDCS sources. A total activity 70 kBq was eventually chosen.

The main challenge of the EDCS is to provide a uniform illumination to all the channels and a uniform sample of the full energy range. While the first challenge can be overcome by adjusting the activity of the strings and can result as a side effect of the pile-up cuts, the second one represent an insurmountable difficulty. In fact the Roman lead shield blocks the low energy lines, allowing only higher energy gammas to reach the detector. Moreover the towers act as self-shielding for the inner towers and absorb the residual low energy gammas. Most of the sources that can be chosen for the calibration strings are indeed single line sources which means that they provide only one point for the calibration fit.

As mentioned above, a second set of sources was prepared in November 2018 to overtake the single calibration point problem and provide 2 additional calibration lines. The new calibration device was created by irradiating with neutrons 80 Al-Co wires 1 mm in diameter and $\sim$1.5 cm long. The irradiation process activates the Co and produces ^{60}Co which has 2 main gamma lines at 1173 keV and 1332 keV, in the center of our energy range. These sources have been alternated in the strings with thoriated tungsten welding rods which provide the line from ^{232}Th. The number of calibration capsules in the string has been chosen thanks to MC simulations in order to provide a total activity of 42.5 kBq for the ^{232}Th sources and a total activity of 39.7 kBq for the ^{60}Co sources. The criteria to choose this values are the uniformity of the illumination, balance between the two sources (peaks intensity) and the quantisation of the capsules themselves.

In order to get a direct comparison with IDCS results, the EDCS was first operated with strings of ^{232}Th for the closing calibration of DS3 (opening calibration of DS4) together with part of the strings of the IDCS. The closing calibration of DS4 and the opening calibration of DS5 were also carried out using only the EDCS ^{232}Th strings. The closing calibration of DS5 was the first with both ^{232}Th and ^{60}Co. The use of the different methods in calibration made the data analysis of

these datasets slightly more complex, but did not degrade the performance of the detector.

VI. CRYOGENIC SYSTEM

The CUORE cryogenic system is the most crucial subsystem of the experiment since the bolometers must operate at temperatures of about ~ 10 mK.

Similarly the temperature stability is as important as the overall temperature of the thermal bath. In fact the heat capacity is proportional to the third power of the temperature, therefore a temperature variation introduces a change in the thermal gain, thus in the amplitude of the signals. Even if we have methods to compensate for these variations, it is important for a stable data taking to maintain a constant operational temperature, which in our case has been be fixed to 15 mK in the initial runs and eventually to 11.8 mK.

Therefore the CUORE detector is placed in a large custom cryogen-free cryostat. The cooling power is supplied by 4 Pulse Tube Cryocoolers (PT) down to about 4 K while a high-power ^{3}He/^{4}He Dilution Unit (DU) provides the cooling power to reach base temperature. The fifth PT is kept as a backup. The CUORE cryostat comprises six nested vessels arranged in two vacuum-tight volumes. The innermost vacuum-tight volume is the Inner Vacuum Chamber (IVC), delimited by the 4 K vessel and enclosing the experimental volume, the 10 mK stage (MC), the 50 mK stage (HEX), the 600 mK stage (Still) and the inner detector lead shield. Its total volume is 3.4 m^3, kept at a pressure lower than 10^{-8} mbar. The second vacuum-tight volume is the Outer Vacuum Chamber (OVC). This OVC is on one side in contact with the IVC and on the other side it reaches the outer world with the 300 K vessel. Its volume is 5.9 m^3 and a pressure lower than 10^{-6} mbar. Any variation in pressure of the two vacuum-tight volumes, any change in the cooling power supply, any strong vibration could compromise the stability of the detector temperature, thus of the data taking.

After the cooldown in February 2018 the cryogenic system behaved as expected until September 2018, when the ongoing science run was interrupted due to a sudden rise in temperature. This was eventually ascribed to the presence of an abnormal quantity of helium in the OVC which caused a thermal short between the room temperature vessel and 4 K stage.

While the impact of this leak could be mitigated by regular pumping of the OVC, it was important to identify the source of the leak so that the appropriate actions could be planned. Therefore, by the end of September we started investigating the source of the leak and warmed up the system to about 4 K. Two possible candidates for the helium leak were immediately identified:

the PTs and the DU. Indeed, both of them cross the OVC volume and are the only elements of the system carrying helium.

The PTs were soon ruled out since by varying the helium pressure inside each one of the PTs, no evidence of correlation with the OVC pressure or helium leak rate was found. One of the condensing lines of the DU was instead found to be responsible of the leak. Indeed, the CUORE cryostat has two condensing lines (denoted as line 6 and 7, of which only one is usually used at a time) and the tests performed on the DU highlighted that the condensing line then in use, line 7, was leaking, while the other one was undamaged. The problem of the gas in the OVC was thus solved simply by switching the condensing line used by the DU.

The tests on the DU performed during this period, also revealed a deterioration of a known clog in the condensing lines. Such clogs, due to frozen air, can be easily cured by warming the system just above $\sim 80\,\mathrm{K}$, to let ice in the lines evaporate, while pumping the evacuated lines. This issue did not seem to prevent the correct operation of the system and was postponed to the first months of 2019, when a major maintenance of the cryogenic system had been planned. The system, even if not in perfect conditions, was therefore considered able to stand a new cooldown and science run. Accordingly, starting by mid October, we proceeded with the cooldown from $4\,\mathrm{K}$ to base temperature.

Overall the cooldown took longer than usual but, despite the clogging in the DU condensing line, we reached base temperature by mid November and, following our standard detector setup operations (PT phase optimization, detector threshold scans etc), we started science data taking at the end of November, with a detector calibration using the external calibration system.

Unexpectedly, we had to terminate the science run at the end of December due a drop of the circulation flux induced by a failure of the primary circulation pump. The maintenance plan was however ready and therefore we immediately started its execution.

VII. ONLINE MONITORING

CUORE Online/Offline Run Control (CORC), developed by the University of California, Berkeley (UCB) and Lawrence Berkeley National Labs (LBNL) groups, and Slow Monitoring (SM) developed by the Massachusetts Institute of Technology (MIT) group consist of high-level user interfaces for monitoring the detector health and cryostat performance in a flexible, real-time fashion. This is accomplished via a Python based web server (Pyramid) on the back-end and a responsive JavaScript front-end package (AngularJS). A MongoDB database stores required data for various

detector parameters (e.g., baseline, event type) and cryostat performance parameters (e.g., temperatures, pressures, seismic data). In the year 2018 various code enhancements were made to some of the underlying SM code and large scale upgrades to the underlying JavaScript were made to facilitate an eventual upgrade to a more modern Angular system. Additionally a complete re-write of the bad interval synchronization script was performed which yielded significantly more reliable behavior.

In the SM part of CORC/SM, long-needed fixes to plot displays were implemented which allow for improved performance when querying large amounts of data or handling multiple parameters being displayed simultaneously. Originally SM code on the back-end had a hard-coded binning algorithm that would reduce data to only 2048 points for display regardless of the amount of data queried. This was altered and lazy loading and server-side binning enhancements now allow for more seamless switches in temporal resolution. Users can start off with a broad view of a particular parameter and zoom in in time and obtain a refreshed set of data that will provide fine-scale time resolution. Additional code changes to the SM back-end restructured the MongoDB query to use an aggregation pipeline to allow for faster querying of only the desired data from documents. This resulted in a notable speed up in SM queries by roughly 25 %. Additional SM improvements include allowing for the display of horizontal bars to denote a parameter's acceptable, warning, and error ranges (these can be adjusted by users with the appropriate roles), the addition of the PID temperature stabilization data as a display option, and improvements to the CRON scripts that periodically run to add data.

On the CORC side of CORC/SM, various upgrades were also handled. An improved set of option handling now allows the default ranges for colormaps assigned to display parameters to reflect more realistic values given the nature of the distributions. Quantities like rates or baseline RMS are bounded by 0 at a lower end so the prior mean $\pm 3\sigma$ approach was invalid. Quantities such as these now use a median $\pm 2.5\times$ IQR (inter-quartile range) for their computation with a floor of 0 in case the median - 2.5 $\times$ IQR value is negative. This has allowed a more direct comparison of bad channels for these parameters without risk of important variations being washed out due to poor colormap assigned values.

A large upgrade to the CORC system was to implement so-called offline quantity support. These are values and parameters that are computed after preprocessing of the data such as optimum filter (OF) related quantities or stabilization parameters. This is accomplished via updates to the modMongo software module. Due to the large amount of new data being sent a batched query update is used which is by and large only compatible with more modern Mongo CXX drivers. These

drivers are themselves only compatible with c++14 features, which are not generally supported by CUORE as yet and so a special branch of the Diana processing software was fully tested which supports compilation with these updated c++ versions. A special tag will allow the user to see if a particular run has been processed offline with modMongo and if not the instructions for doing so are simple. Until a run is tagged as having been offline processed the parameters that are added remain un-selectable to the user so empty charts cannot be accidentally created. Once added the user is able to examine these offline parameters much the same as the default online quantities.

Another large upgrade was to correct an unreliable bad interval synchronization between the ones created in CORC and the Postgres database used by the analysis and data production software. Previously tables were not locked and so some bad intervals may not have been present when requested by analysis software. This was caused primarily by a brute-force update of the entire table. Now specialized classes for PSQL rows and Mongo dictionary objects exist as helpers and using Python modules for iteration and grouping allowed for direct comparison in software of all records. These are sorted into 4 categories (insert, update, delete, do-nothing) based on the operation that has to be performed. During the update stage if the proposed update would cause a duplicate PSQL key to exist it is simply not performed and folded into the do-nothing list. The insertion operation takes place last and after one last sort check to verify entries being inserted are unique. A hard limit of 10000 rows to change is currently in place to act as an alert against changing all rows (though this can be met by creating 11 whole-detector flags in under 2 minutes).

Two additional small additions were the creation of the ability to handle microphone channels in CORC, and an ability to check if an alarm is actually live before the alarm program attempts to call.

Work has also started at the end of 2018 to do a complete overhaul of the alarm subsystem and to extract it from SM into it's own independent service, allowing for cleaner code and a more easy extension into other alarm types (such as an alarm to check if data has become stale due to a population error or other log file update error). This work is also seeing a major upgrade in the ECMAScript (aka JavaScript) language and code style being used from plain vanilla ECMAScript to ECMAScript2015 (or ES6). This introduces a lot more modern functionality into the language including default values for function arguments, destructuring assignments and a compact function declaration system. Additionally the use of a dedicated ESLinter (via a .eslintrc file) allows for the enforcement of a cross-application style to be used so that code in all parts of CORC/SM can be followed by all developers. These changes will allow for an easier upgrade to modern AngularJS versions and eventually to Angular in the future.

VIII.   COMPUTING INFRASTRUCTURE

We make use of six computing clusters for data analysis and Monte Carlo simulations. The Unified LNGS IT Environment (U-LITE) at LNGS is the primary computing resource for CUORE on-line data processing. U-LITE has 32 CPUs (64 cores) with 237 terabytes (TB) of usable hard disk drive (HDD) storage space, formatted with a RAID-6, and 9.3 TB of fast solid-state drive (SSD) cache dedicated to CUORE. An additional 400 cores are available when not used by other experiments. CNAF is the main resource for complete data re-processing, while CNAF itself, PDSF, Cori, Savio and Omega are secondary computing clusters available for Monte Carlo simulations, user analyses, code development, and other tests. Also, the High Performance Storage System (HPSS) located at NERSC, along with the CNAF clusters, serve as backup storage for the official CUORE data. CNAF, located in Bologna, Italy, has up to 1500 cores available to CUORE and 170 TB of dedicated storage. PSDF, which is part of the National Energy Research Scientific Computing Center (NERSC) located in Berkeley, California, USA, has up to 1536 cores available to CUORE and 80 TB of dedicated storage. The PDSF cluster was retired in April 2019. Cori, also part of NERSC, is new a Cray XC40 supercomputer that uses that same storage as PDSF. We have fully migrated the CUORE analysis and simulation environment from PDSF to Cori. Savio is a 8040-core cluster of the University of California Berkeley, Berkeley, California, USA. So far CUORE has used Savio for running MC simulations, as well as for the studies of CUORE sensitivity to $0\nu\beta\beta$ decay. The Omega cluster, which has 640 cores with minimal permanent storage, is located at the Yale University in New Haven, Connecticut, USA. CUORE uses the Omega cluster exclusively for Monte Carlo simulations. The CUORE Data Acquisition System (DAQ) collects about 50 GB of raw data per day. The data are automatically copied from storage in the underground labs to the U-LITE computing center in the above ground labs at LNGS. From there, the collaboration begins the data analysis process. From the above ground labs the data are copied to 2 backup sites: one at the CNAF computing center in Italy and the second at NERSC HPSS in the USA.

We employ the open source relational database PostgreSQL to store and retrieve structured objects used by the data acquisition system and analysis, and the document-oriented database MongoDB to manage the diagnostics from the data analysis and the slow control. The master PostgreSQL database is located in the main surface building at LNGS and is copied, with native replication, to slave databases in the underground CUORE lab, to CNAF, and to the LBNL in Berkeley, California. The rare event where communication to the master database is lost triggers a failover and the database located in the CUORE lab becomes the master to prevent interruptions

to data taking. The master MongoDB is also located in the main surface building at LNGS and is natively replicated on slave databases located in the underground CUORE lab and at LBNL with a similar failover system.

We use the version control system `Git` to manage the source code for CUORE data acquisition and analysis, simulations, control systems, as well as drafts for journal articles and reports. We host the CUORE `Git` repository on an Enterprise `GitHub` server located at the MIT that includes issue tracking and online software documentation. We have also built a website that includes both public and collaborator specific information on CUORE. The collaborator specific information includes automatically generated Doxygen software documentation, author list generators, and shift management.

IX. DATA ANALYSIS

In this section we will present an overview of the data taking in 2018 and the main analysis and reconstruction software topics addressed in 2018, apart for the study of $0\nu\beta\beta$ decay. The studies reported here will impact future analysis and the overall detector performance.

A. Data taking in 2018

The data collection is organized in runs of about one day of duration. In turn, the runs are grouped into datasets, each started and ended with a calibration and containing about one month of physics data (the data collected for the $0\nu\beta\beta$ decay and other rare event search analysis).

At the end of 2017 a temperature scan was performed around the detector operating temperature of (15.0 ± 0.1) mK used in the previous data taking period. The scan demonstrated that better performance in terms of energy resolution and detector stability can be achieved by choosing a lower operating temperature. A temperature of (11.8 ± 0.1) mK was chosen for the 2018 data taking, in order to maximize the signal to noise ratio. Given the experience of 2017, for every triggered signal, we continued to save event windows of 10 seconds.

As for the previous science runs, a period dedicated to the detector setup preceded the physics data taking: in this period of about two weeks we set the front-end electronics parameters, checked the NTD resistances for every channel, tuned the pulse tubes phase differences in order to minimize the pulse tubes induced noise on the detector, setup the derivative and optimum trigger thresholds and evaluated the trigger efficiency at low energy, hence the energy threshold of all the channels.

The detector setup is repeated every time there is a long stop of the data taking because of maintenance of the cryogenics or calibration systems. The science run of 2018 has been divided in three datasets, starting from May to December 2018: the first dataset is called DS3 and lasted 50 days (from May 19th to July 9th 2018), the second one is DS4 and lasted 40 days (from July 18th to August 27th 2018) and the third one is dataset DS5 which lasted only 12 days (from December 7th to December 26th 2018, including the final calibration). Between DS4 and DS5 the CUORE data taking had to stop due to the issues reported in Sec. VI. Each one of the datasets was bracketed by an initial and final calibration. Since DS3 and DS4 where back to back, the final calibration of the former corresponds to the initial calibration of the latter.
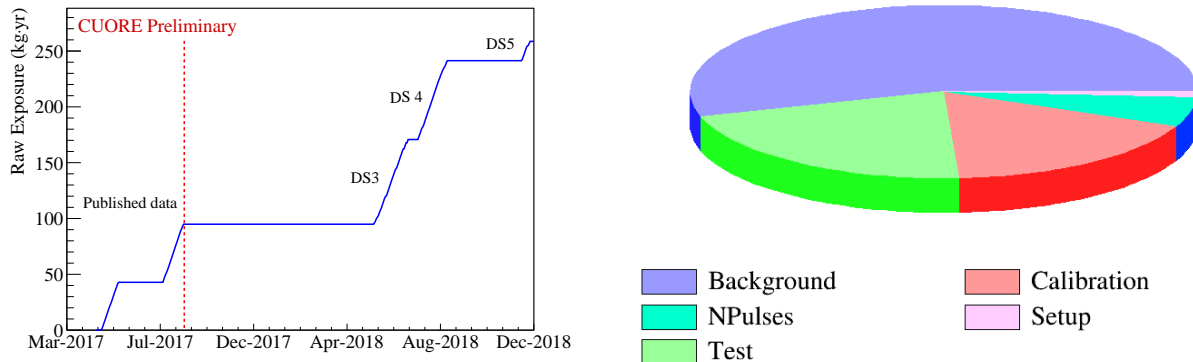

FIG. 6: *Left:* cumulative exposure of all the active channels from the beginning of the data taking in 2017 up to the end of 2018. The data on the left of the red dashed line has already been published in Phys. Rev. Lett. 120, 132501 (2018). Note that for all the datasets the number of active channels was 984. However, during the analysis a fraction of these had to be removed for different reasons: some of the channels were too noisy, others failed during one or more analysis steps, others did not collect a sufficient number events during the calibration and so on. In this case the channel selection is not included in the cumulative exposure since the selection is analysis dependent. *Right:* detector livetime breakdown for run type. Background indicates physics runs for $0\nu\beta\beta$ decay analysis or other rare event searches, NPulser indicates the run type used for the evaluation of the energy thresholds for both derivative and optimum trigger, Setup indicates the runs used for the NTD resistance evaluation and most of the Test runs are actually dedicated to the pulse tube induced noise minimization.

The CUORE cumulative exposure up to the end of 2018 is reported on Figure 6 left, while on the right the breakdown of the different contributions to the runs acquired in 2018 (including

test runs and maintenance or detector setup) is shown. The total exposure accumulated in 2018 (167.20 kg·yr) is almost twice than the previous year (94.87 kg·yr). The reported values correspond to the 'Raw Exposure', and do not include any data selection cut.

Given the upgrades to the cryogenic system and the significant simplification resulting from the adoption of the external calibration system (CUORE-0 style), a smooth data taking is anticipated for 2019.

In order to achieve a prompt result production, a strong effort has been devoted during 2018 to pursue a stable software tag (and a corresponding set of data production procedures) for the complete reconstruction of the events. The resulting data production workflow is demanding both from the point of view of the operator and of the computing resources. The full data production of the first available CUORE datasets (four since the initial cooldown) was performed during fall 2018 on the CNAF cluster, exploiting the large parallel computing power of the infrastructure and at the same time identifying and trying to fix the weak points, in view of the ever growing needs related to the fast accumulation of data to be processed.

A significant effort was directed also to strengthen the on-line processing, developing a stable and reliable procedure for the analysis of the acquired data with the goal of providing a one-day time scale feedback on the data quality and detector operation stability. The workflow of this online data production has been maintained as simple as possible in order to allow an almost automated procedure requiring only a small (if any) intervention from the analysis shifter. It includes the evaluation of the event energy, few basic quality cuts, but no coincidence or pulse shape-based selection. The channels that fail the energy reconstruction with this procedure are momentarily discarded. This procedure is performed on the ULITE computing infrastructure at LNGS, and was refined and tested during the summer 2018 data taking.

Besides the improvements of the analysis chain outlined above, we are also started implementing new algorithms to improve the overall performance of the event reconstruction software, and develop and test the corresponding workflow. Many new algorithms are being considered. Some of them are focused on the improvement of the energy resolution (noise de-correlation, Optimum Trigger, notch filtering), some other on the event selection (faster coincidence algorithm, improved channel synchronisation, pile-up rejection).

B. Calibrating with EDCS

The first two datasets of 2018 (DS3 and DS4) were calibrated using only the internal DCS. A joint calibration including also the external DCS was carried out for the final calibration of DS4. The successful operation of the external calibration system represented an important benchmark for CUORE since it guaranteed an intrinsically simple system with essentially no interference with the CUORE cryogenics. Since DS5, the detector is calibrated purely with the EDCS.

The opening calibration of DS5 was performed with the ^{232}Th sources which provide only 2 visible calibration lines: 511 and 2615 keV. For the closing calibration, we made use of the newly produced ^{232}Th/^{60}Co combined sources, adding two more lines at 1173 and 1332 keV. The DS5 opening and closing calibration spectra are compared in Figure 7. The two additional lines due to ^{60}Co are evident. As anticipated by the simulations, the detector illumination is reasonably uniform (after the base cuts) and the CUORE detectors can be calibrated with approximately 4 days calibrations at the beginning and the end of the dataset. The required time is comparable to the one expected for the calibration with the IDCS. Also the performance of the detector in terms of energy resolution is comparable with the two calibration systems.

C. Lowering the energy thresholds with the Optimum Trigger

In order to achieve trigger thresholds closer to the RMS of the detector noise, the Optimum Trigger (OT) algorithm has been adapted from the original CUORE-0 implementation. The algorithm identifies a signal when the amplitude of the waveform processed with the optimum filter exceeds a configurable threshold. The threshold is determined by the baseline resolution of each channel, making the configuration of the trigger easy to manage for the 1000 channels of the CUORE detector. The OT is demanding from the computational point of view, since in CUORE the sampling frequency and number of channels have been increased by factors of 8 and 19 repectively, with respect to CUORE-0. In order to reduce the computational charge, data are down-sampled, after the application of an anti-aliasing digital low-pass filter (recursive time-domain Chebyshev).

Test runs in which the OT has been operated in parallel to the usual derivative trigger have been successfully performed (August 2018) in order to prove that the OT can be used directly on the on-line acquisition chain. A configurable dead-time has been introduced in the algorithm in order to guarantee the robustness and stability of the trigger algorithm during the online data-taking.

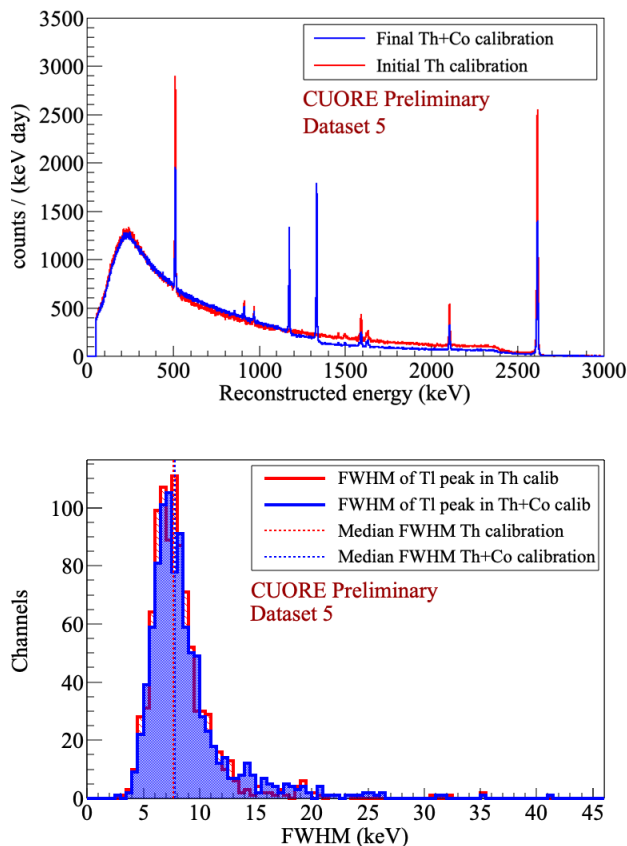Apart from the on-line implementation, OT can be applied also offline on the continuous

FIG. 7: *Left:* comparison of initial and final calibration for the science run of November-December 2018: the former calibration was performed using the EDCS with the ^{232}Th sources only while the latter included also a set of 60Co strings in order to increase the number of calibration lines. *Right:* FWHM distribution of the 2615 ^{208}Tl line for channels calibrated with the external calibration system.

recorded stream of data. Off-line retriggering is not computationally demanding and can be applied at any moment. It is the presently applied choice. Indeed, whatever is the reason why we want to retrigger a dataset, whether it is to cure problems found during the data processing, to improve the energy thresholds or to apply a trigger for a specific analysis, this can be done in less than a day.

The OT energy trigger thresholds have been determined in test runs where heater signals with predefined multiple amplitudes had been artificially injected. The heater signal amplitudes were selected to span a range of values matched with the threshold efficiency curves. For each detector channel, the efficiency at the considered amplitude is measured as the ratio between the number

of signals flagged by the OT algorithm over the number of injected signals. Results show that the OT thresholds improve (decrease) by 60-90% with respect to the derivative trigger thresholds (see Figure 8) ranging between ∼20 and 100 keV.
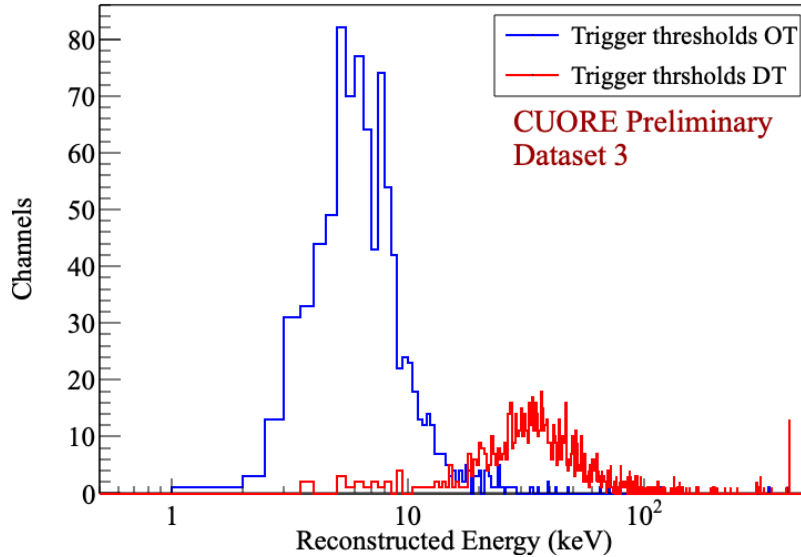

FIG. 8: Comparison between the distribution of the detector energy thresholds with the OT (blue) and the DT (red) algorithms.

D.   Noise Filtering and decorrelation

As part of the campaign to improve the detector resolution, a new multi-channel Decorrelating Optimum Filter (DOF) has been introduced. Some, if not most, of the noise in CUORE detectors comes from common sources. The concept is therefore to exploit the noise correlations between channels to improve the signal to noise ratio.

The traditional Optimum Filter (OF) uses, for each channel, an average noise power spectrum and a reference signal response to filter the bolometer signals. In order to take into account the correlations between channels, the DOF adds also channel-channel average noise covariance matrices and simultaneous noise traces. This approach uses information on transient noise from other channels and thus is expected to perform better than OF. Tests carried out on initial datasets have been using only the 15 most correlated channels for filtering and create separate noise covariance matrices for each tower instead of the full detector. These limits are due to the computing complexity of

inverting thousands of matrices and the need to process additional neighboring signal traces. This offers a good compromise between filter performance and computing efficiency. Especially for what concerns science runs, DOF shows an improvement of about 10-20% in noise baseline resolution in most channels and around 10% better resolutions of stabilization pulser events (before calibration). In calibration runs, however, the DOF performance is comparable to that of OF. In this case, the higher event rate results in fewer pure noise traces coincident in the selected correlated channels, hence lowering the performance. Yet we can witness an overall percent level increase in resolution after calculating final energy on the background data, and expect to improve on this performance by optimizing filter parameters and channel selection.
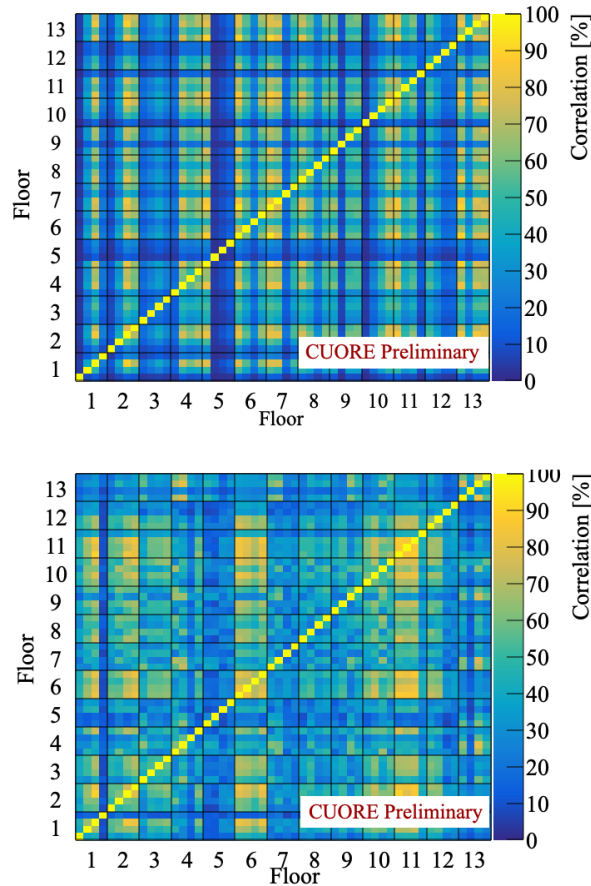

FIG. 9: Sample noise covariance matrices. *Left:* noise average between 1-2Hz. *Right:* noise average around $50\,\mathrm{Hz}$ for run 301145, tower 1.

E. Background model

The CUORE background model aims to reconstruct the dominant radioactive background sources that produce the observed spectra, using a technique largely based on the one developed for CUORE-0. We select a set of contaminants that, based on the construction material assay or identified through specific lines appearing the observed spectra, are likely to be present in the cryostat. The selected contaminants either come from the main natural decay chains (^{232}Th, ^{238}U), ^{40}K or cosmogenic activation of materials (e.g. ^{60}Co and ^{54}Mn). They are spread across the whole experimental setup.

We simulated first the spectra of all the likely background sources, both induced by cosmogenic muons and from contaminations of the crystals or nearby materials (bulk and surface separately), using a dedicated software based on the GEANT4 package. Then the outputs are grouped in characteristic sub-spectra which convey the most relevant information. The first spectrum gather the events due to single crystal energy depositions, denoted as multiplicity 1 (M1) events: here we can find about 90% of the events from two-neutrino double-beta decay ($2\nu\beta\beta$ decay) as well as events from any other environmental, bulk or surface contamination. The second event selection includes only double sited events, also called multiplicity 2 (M2), where the energy of the interaction is shared between two bolometers: given the low event rate, the events in this category are almost free from random coincidences and are purely due to physics processes such as γ Compton scattering from one crystal or α-decays occurring on the surface of the crystals. A third spectrum is made out of the sum of the two energies of the coincident events in the M2 spectrum and for this reason is denoted as M2-sum. Finally we split the M1 spectrum in inner and outer layers, respectively denominated M1L0 and M1L1, depending on the location of the involved crystals within the detector: the outer towers are indeed closer to the cryostat materials and to the outer world and therefore are more likely to see contamination due to environmental radioactivity; the inner towers, on the other hand, are expected to be self shielded from the outer towers and thus to less susceptible of contributions from the cryostat materials.

We perform a combined fit of the simulated contamination sources on these four spectra using the JAGS Bayesian analysis toolkit. The fit has a total of 60 free parameters corresponding to the contamination levels of each background component that we aim to reconstruct and also of the ^{130}Te $2\nu\beta\beta$ decay. This allows us to estimate the location and activity of the main contaminations in our cryostat, as well as to measure the half-life $2\nu\beta\beta$ decay in ^{130}Te. The two neutrino double beta decay, $2\nu\beta\beta$ decay, of ^{130}Te accounts for most of the observed spectrum in the multiplicity

1 data in the 1 to 2 MeV region and its activity can therefore be estimated with a high degree of precision.

So far the fit to reproduce the background model was run on the first two datasets, giving promising preliminary results but also underlining the need to increase the statistics in order to obtain an accurate reconstruction of the background.

X. MAJOR RESULTS OBTAINED IN 2018

The year 2018 saw the publication of the first CUORE results for $0\nu\beta\beta$ decay in Phys. Rev. Lett. 120, 132501. The analysis presented in this first paper was performed in 2017 and based on the first 2 datasets acquired by the experiment, for a total exposure of 86.3 kg·yr. With only few months of data CUORE was able to set a limit on the $0\nu\beta\beta$ decay half-life of ^{130}Te of $T^{0\nu}_{1/2} > 1.3 \times 10^{25}$ yr. This result exceeds the expectation for the half-life sensitivity due to a $\sim 2\sigma$-downward fluctuation in the background at the Q-value of $0\nu\beta\beta$ decay of ^{130}Te.

Using the same statistics of 86.3 kg·yr, the CUORE Collaboration was committed in understanding every aspect of the energy spectrum, from the radioactive background to the intrinsic irreducible contribution coming from the 2 neutrino double beta decay $(2\nu\beta\beta)$ of ^{130}Te.

As outlined in sec. IX E We first study the effect on the observed spectra of each contamination by means of a highly detailed GEANT4-based simulation. Then, exploiting the granularity of the CUORE detector, we split the observed data into the spectra corresponding to different multiplicities and/or detector layers. Figure 10 shows two of these spectra.

The simultaneous fit to the four background spectra (M1L0, M1L1, M2 and M2-sum) is able to reproduce most of the observed distinctive features, as shown in Figure 11 (left) that reports the fit results for one of the spectral components (M1L0). However some of the α and γ peaks are poorly reconstructed and this is an indication of a deficit in the modeling of some of the background components. A fit improvement, and a great help in disentangling the origin of the contamination, is expected from the increase of the statistics. Indeed, all the data acquired in 2018 are currently being reprocessed. The cumulative exposure for 2017-2018 is then larger than 200 kg·yr. We expect a significant improvement both of the overall background model and of the $0\nu\beta\beta$ decay region of interest (ROI) in particular.

An important result of the background model is that the estimate of the $2\nu\beta\beta$ decay half-life is practically insensitive to the details of the features observed in the spectra at higher energies. Therefore, despite the uncertainty in the reconstruction of some of these features, the estimate of
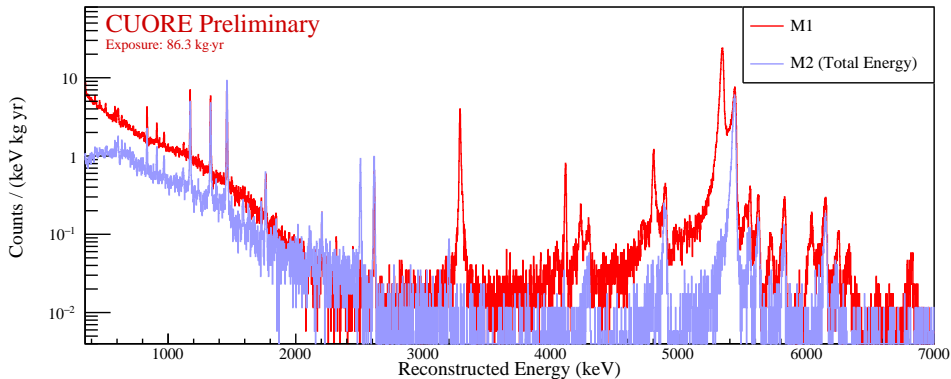
FIG. 10: The plot shows the background spectra for the first two datasets acquired with CUORE, for a total exposure of 86.3 kg·yr. In red is reported the multiplicity 1 (M1) spectrum, while in blue is plotted the M2-sum spectrum of multiplicity 2 events, representing the total energy deposited in the two bolometers.

the $2\nu\beta\beta$ decay half-life is robust and we get a very precise value already with the 2017 exposure (86.3 kg·yr): $T_{1/2} = (7.9 \pm 0.1(\text{stat.}) \pm 0.2 \text{ (syst.)}) \times 10^{20}$ yr. We estimate the systematic uncertainty on this value by repeating the fit in different conditions, changing the energy threshold, the geometrical splitting of the spectra or by fitting only fractions of the exposure. The final result is compatible with the previous result from CUORE-0 ($T_{1/2} = (8.2 \pm 0.2 \text{ (stat.)} \pm 0.6 \text{ (syst.)}) \times 10^{20}$ yr) and shows a significant reduction both in statistical and systematic uncertainty, thanks to the reduced background and improved analysis techniques. This result has been presented at the Neutrino 2018 conference. An update including all the available exposure is ongoing.

XI. LIST OF PUBLICATIONS

A. Papers

[1] A. Caminata *et al.* (CUORE Collaboration), "Results from the Cuore Experiment", Universe 5, no.1, 10, (2019);

[2] C. Alduino *et al.* (CUORE Collaboration), "First Results from CUORE: A Search for Lepton Number Violation via $0\nu\beta\beta$ Decay of ^{130}Te", Phys. Rev. Lett. 120, 132501 (2018) (arXiv:1710.07988).

This Letter has been highlighted by the editors as an Editors' Suggestion and was covered in
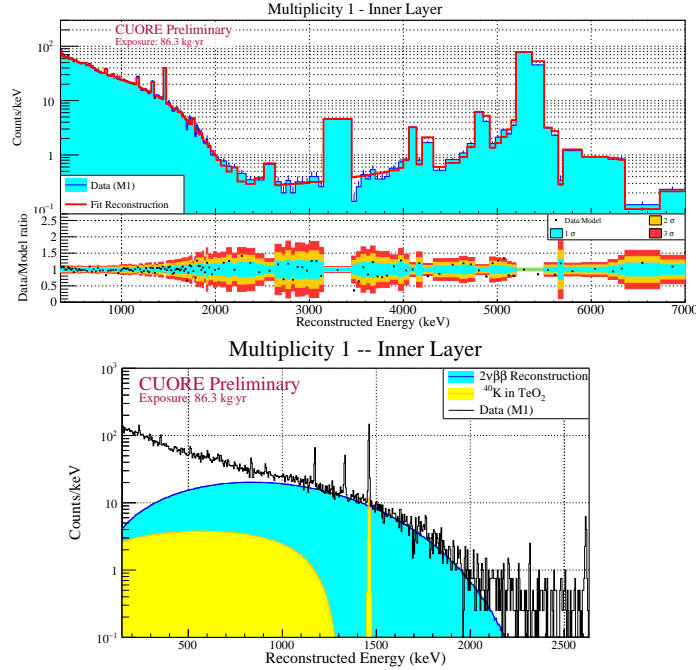
FIG. 11: *Left:* measured M1L0 spectrum (blue) and its reconstruction (red) from the fit result. A variable size binning is adopted in order to contain each dominant peak into a single bin thus avoiding the dependence on the details of line shape. The plot also shows the ratio of the data to the reconstructed model with 1σ, 2σ and 3σ error bars. Overall we are able to perform a faithfully reconstruction of the continuum, with only a moderate disagreement in the normalization of a few lines. *Right:* measured M1L0 spectrum (black) with a reconstruction of the $2\nu\beta\beta$ decay background component (blue). The plot also shows the greatest source of uncertainty for the estimate of the $2\nu\beta\beta$ decay half-life in ^{130}Te, which is the ^{40}K background component in TeO$_2$ crystals (yellow).

Physics along with papers from GERDA and Majorana (https://physics.aps.org/articles/v11/30);

[3] C. Alduino *et al.* (CUORE Collaboration), "Study of rare nuclear processes with CUORE", Int. J. Mod. Phys. A 33, 1843002 (2018) (arXiv:1801.05403);

[4] C. Alduino *et al.* (CUORE Collaboration), "Search for neutrinoless $\beta+$/EC decay of ^{120}Te with CUORE-0", Phys. Rev. C 97, 055502 (2018) (arXiv:1710.07459);

[5] C. Arnaboldi, P. Carniti, L. Cassina, C. Gotti, X. Liu, M. Maino, G. Pessina, C. Rosenfeld, B.X. Zhu, "A front-end electronic system for large arrays of bolometers", JINST 13 P02026 (2018), (arXiv: 1710.06365);

[6] K. Alfonso, P. Carniti, L. Cassina, A. Giachero, C. Gotti, G. Pessina, "A high precision pulse generation and stabilization system for bolometric experiments", JINST 13 P02029 (2018) (arXiv:1710.05565);

[7] G. Benato, D. Biare, C. Bucci, L. Di Paolo, A. Drobizhev, Yu.G. Kolomensky, J. Schreiner, V. Singh, T. Sipla, J.'Wallig, S. Zimmerman, "Radon mitigation during the installation of the CUORE $0\nu\beta\beta$ decay detector", JINST 13 P01010 (2018) (arXiv:1711.07936);

[8] A. D'Addabbo, C. Bucci, L. Canonica, S. Di Domizio, P. Gorla, L. Marini, I. Nutini, C. Rusconi, B. Welliver, "An active noise cancellation technique for the CUORE Pulse Tube Cryocoolers", Cryogenics 93, 56–65, (2018) (arXiv:1712.02753);

[9] A. D'Addabbo *et al.*, "The CUORE Cryostat", J. Low Temp. Phys. 193, no. 5–6, 867–875 (2018) (arXiv:1805.06209);

[10] S. Di Domizio, A. Branca, A. Caminata, L. Canonica, S. Copello, A. Giachero, E. Guardincerri, L. Marini, M. Pallavicini, M. Vignati, "A data acquisition and control system for large mass bolometer arrays", JINST 13 P12003 (2018) (arXiv:1807.11446).

B. Conference Proceedings

[1] D.Q. Adams *et al.* (CUORE Collaboration), "Update on the recent progress of the CUORE experiment", Zenodo research data repository (arXiv:1808.10342). Prepared for the XXVIII International Conference on Neutrino Physics and Astrophysics (Neutrino 2018), 4-9 June, 2018, Heidelberg, Germany;

[2] C. Alduino *et al.* (CUORE Collaboration), "The CUORE and CUORE-0 experiments at LNGS", J. Phys. Conf. Ser. 1056, no.1, 012009 (2018). Prepared for the Conference on Neutrino and Nuclear Physics (CNNP2017), 15-21 October 2017, Catania, Italy;

[3] L. Cassina, *et al.* (CUORE Collaboration), "The CUORE Bolometric Detector for Neutrinoless Double Beta Decay Searches", Springer Proc.Phys. 213, 202-207 (2018). Prepared for the 4th International conference on Technology and Instrumentation in Particle Physics (TIPP2017), 22-26 May, 2017, Beijing, China;

[4] V. Novati *et al.* (CUORE Collaboration), "CUORE: first results and prospects", PoS NuFact2017, 164, (2017). Prepared for the 2017 International Workshop on Neutrinos from

Accelerators (NuFact17), 25-30 September, 2017, Uppsala, Sweden;

[5] S. Copello *et al.* (CUORE Collaboration), "The commissioning of the CUORE experiment: the mini-tower run", PoS NEUTEL2017, 072 (2018). Prepared for the 17th International Workshop on Neutrino Telescopes (Neutel 2017), 13-17 March, 2017, Venice, Italy.

[6] D. Chiesa *et al.* (CUORE Collaboration), "Results from the CUORE experiment", J. Phys. Conf. Ser. 1137, no.1, 012052 (2019). Prepared for 13th International Conference on Beauty, Charm and Hyperons (BEACH2018), 17-23 Jun 2018. Peniche, Portugal.

CUPID-0

CUPID-0 collaboration

1   Introduction

CUPID-0 is the first experiment searching for neutrinoless double beta decay ($0\nu\beta\beta$) using the scintillating bolometers technique. It consists of an array of enriched $Zn^{82}Se$ crystal detectors operated at LNGS since 2017. During the Phase I of data taking, concluded at the end of 2018, the experiment collected an exposure of 9.95 kg·yr. Thanks to simultaneous readout of the heat and light signals, CUPID-0 has the excellent capability to identify (and reject) α particles with respect to β/γ events, obtaining the lowest background ever measured with thermal detectors in the energy region where the signature of ^{82}Se $0\nu\beta\beta$ decay is expected. Thanks to this achievement, CUPID-0 set the most stringent lower limit on the $0\nu\beta\beta$ ^{82}Se half-life, as well as on $0\nu\beta\beta$ of ^{82}Se into the 0_1^+, 2_1^+ and 2_2^+ excited states of ^{82}Kr.

2   CUPID-0 detector

The CUPID-0 detector [1] is a five-tower array of 26 ZnSe scintillating crystals, 24 enriched in ^{82}Se at 95% level and 2 with ^{82}Se natural isotopic abundance. The total amount of ZnSe is 10.5 kg, corresponding to 5.17 kg of ^{82}Se.

The light emitted by the ZnSe crystals together with the thermal signal after particle interaction is measured with 0.170 mm thick, 4.4 cm in diameter Germanium Light Detectors (Ge-LDs) interleaved with the crystals, operated as bolometers themselves. In order to increase the light collec-tion, each ZnSe crystal is surrounded by a 3M VIKUITI^{TM} reflecting foil. P TFE clamps held both ZnSe crystals and Ge-LDs in position in a copper structure, thermally coupled to the mixing chamber of a dilution refrigerator installed in the Hall A of LNGS (the very same that hosted the Cuoricino and CUORE-0 experiments [2, 3]) and operated at ∼10 mK.

Both ZnSe crystals and Ge-LDs are equipped with a Neutron Transmutation Doped (NTD) Ge thermistor [4] to convert the energy deposits in readable voltage signals. In addition, a P-doped Si Joule heater [5], glued to each device, periodically injects a constant energy reference pulse used to measure gain variations induced by temperature fluctuations of the cryogenic apparatus [6, 8].

The front-end electronics comprises an amplification stage, a six-pole anti-aliasing active Bessel filter and an 18 bits ADC board. The complete data-stream is digitized with a frequency of 1 kHz (2 kHz) for ZnSe (Ge-LD) and saved on disk in NTuples based on the ROOT software framework. A software derivative trigger with channel dependent threshold is implemented online. When a trigger fires on a crystal, the waveforms of the corresponding Ge-LDs are also flagged as signals.

3   Data production and selection

The collected data are processed off-line using a C^{++} based analysis framework originally developed by the CUORE-0 collaboration [7]. The specific analysis tools developed for scintillating calorimeters in the framework of CUPID-0 are presented in Ref. [9, 10].

The continuous data stream is converted into acquisition windows of 5 s for ZnSe events (1 s before the trigger and 4 s after it) and 500 ms for Ge-LD events (100 ms before the trigger and 400 ms after it). The sampling before the trigger provides the baseline temperature of the detector, while the remaining one is used to determine the pulse amplitude and shape.

We use the optimum filter technique [11, 12] to estimate pulse height and pulse shape parameters. We build the signal waveform template averaging the physical events with energy between 1800 and 2700 keV and compute the noise power spectrum on randomly chosen waveforms that do not contain triggered pulses. Then the filtered data are corrected for gain instabilities.

The corrected amplitude is converted into energy by fitting a parabolic function with zero intercept to the energy of the most intense peaks produced by a ^{232}Th source periodically positioned close to the cryostat external shield [1]. We use the 2615 keV line from the ^{208}Tl line as a proxy for the detector response function for the $0\nu\beta\beta$ event. However we exploit also other sources to fully characterize the energy region of $0\nu\beta\beta$.

To study the energy dependency of the shape parameters in the region of interest, we use an Am:Be neutron source, emitting a broad distribution of γ rays up to several MeV. This calibration was made every time

73

we modified the working parameters of the detectors, in order to evaluate and correct possible changes in the shape-dependency on the energy. Furthermore, we validated the ^{232}Th energy calibration with a ^{56}Co source, producing γ peaks well above the ^{82}Se Q-value. The heat released by α and β/γ of the same energy is slightly different because of the different energy spent in the light channel. To re-calibrate the α events, we identify the most intense α peaks produced by ^{238}U and ^{232}Th internal contaminations, and convert the amplitude to energy using a parabolic function.

Data acquired between two calibrations are grouped in a DataSet and processed together through the analysis chain. We compute time coincidences between detectors within a ± 20 ms window, optimized by studying the time distribution of physical coincident events collected during calibrations. Time coincident events are organized in a multiplet structure, which includes information about the triggered crystals and the total energy released in the detector.

The energy region chosen for the analysis of the background is a 400 keV interval centered around the ^{82}Se Q$_{\beta\beta}$-value (2800–3200 keV). At higher energies, indeed, we expect the background to decrease, as the contributions from ^{214}Bi and ^{208}Tl (the dominant background sources) drop above 3200 keV. Therefore, further enlarging the analysis window would result in a lower background. The lowest bound of the interval was chosen to have a symmetric region around Q$_{\beta\beta}$ and, at the same time, to avoid contributions from the 2615 keV photon or from the tail of the 2ν double beta decay.

In order to maximize our sensitivity to physics events, we implement a series of event selection cuts on the Zn^{82}Se thermal pulses [9]. First of all, periods of detector instability because of cryostat or electronics malfunctioning are excluded on a crystal-by-crystal basis (reducing the exposure by less than 1%) We require only one pulse in a triggered window and the waveform to be consistent with the signal template. A time veto around each event (4 s before and 4 s after) is applied to re-move piled up events. We exploit heater pulses to calculate the trigger efficiency (i.e. the probability that an event is detected and reconstructed at the right energy) and the pile-up cut efficiency [7]. We select particle events by requiring a non-zero light signal simultaneously recorded by Ge-LDs.

We then exploit the information of the Ge-LDs. We estimate the Ge-LD signal amplitude at a fixed time delay with respect to the Zn^{82}Se signal as described in Ref. [18]. Typical rise and decay times are 4 and 8 ms respectively. Since the time development of the light pulses generated by α particle interaction is different with respect to the ones produced by β/γ interactions, we use a shape parameter computed on the filtered light pulse

Event selection	Background Index [counts/(keV kg year)]	Efficiency [%]
Heat	$(3.6\pm0.5)\times10^{-2}$	$95\pm2\%$
Heat + α rejection	$(1.5\pm0.3)\times10^{-2}$	$95\pm2\%$
Heat + veto with ^{212}Bi	$5.1^{+2.4}_{-2.0}\times10^{-3}$	$94.5\pm2\%$
Heat + veto with all α's	$3.6^{+1.9}_{-1.4}\times10^{-3}$	$93\pm2\%$
Total signal efficiency	$3.6^{+1.9}_{-1.4}\times10^{-3}$	$75\pm2\%$

Figure 1: Summary of the BI (counts/keV·kg·y) and signal efficiency averaged on the DataSets exposure, measured in the region 2800 - 3200 keV with a ZnSe exposure of 3.44 kg·y (1.34×10^{25} emitters·y). Uncertainties are reported at 68% C.L.. First row: events that pass the cuts on the heat channel. Second row: the events are further selected requiring that the shape parameter of the light is consistent with interactions of electrons (α rejection). Third row: we added a time-veto of 3 half-lives after the detection of an α particle with energy compatible with the Q-value of ^{212}Bi. Fourth row: we added a time-veto of 3 half-lives after the detection of an α particle with energy larger than 2 MeV. Last row: we report the total efficiency, including the data selection efficiency computed as in fourth row, the trigger efficiency, and the electrons containment efficiency of 81.0 ± 0.2.

as defined in Ref. [19] to reject α particles.

Finally, we implement delayed coincidences to suppress the background induced by the internal ^{208}Tl $\beta/\beta+\gamma$ decay from the ^{232}Th chain. The ^{212}Bi α decays to ^{208}Tl (Q_α=6207 keV), which, in turn, decays to the stable isotope ^{208}Pb with Q =5001 keV and a half-life $\tau_{1/2}$=3.01 min. We veto any event succeeding a primary ^{212}Bi α event in a window corresponding to three times the half-life. If the contamination is close to the surface and the α escapes the crystal, only part of the energy of the parent decay is collected. To identify such events we require the pulse shape of the primary event to be consistent with the reference α shape and the energy to be in the range (2.0 - 6.5) MeV.

Fig. 1 shows the Background Indexes (BIs) resulting after the application of each selection criteria to the first part of data collected in the Phase I of data taking, corresponding to an exposure of 3.44 kg·y (1.34×10^{25} emitters·y).

It clearly appears that the heat-light readout provides a powerful tool for the rejection of α particles and allows us to suppress the background in the region of interest down to $(3.6^{+1.9}_{-1.4}) \times 10^{-3}$ counts/(keV·kg·yr), an unprecedented level for this technique.

4 First Result on the Neutrinoless Double Beta Decay of ^{82}Se to the ground state of ^{82}Kr

If ^{82}Se decays to the ground state of ^{82}Kr, the two emitted electrons share the entire $Q_{\beta\beta}$-value of the transition. We determine the probability of a $0\nu\beta\beta$ to be fully contained in a single crystal from GEANT4 simulation to be $(81.0\pm0.2)\%$. This probability, together with the one that the $0\nu\beta\beta$ signal is triggered and its energy properly reconstructed, concurs in the computation of the signal efficiency, which is $(99.44\pm0.01)\%$. We estimate the selection efficiency from a simultaneous fit on both the spectra of accepted and rejected events in the 1115 keV ^{65}Zn peak in the sample not used for the optimization [2]. We sum all channels due to the limited statistics and derive a selection efficiency of $(93\pm2)\%$.

We cross-check the selection efficiency as a function of the energy selecting double-hit events; these are very likely a sample of true particle events since spurious coincidences are negligible. The ratio of events before and after applying the selection criteria is compatible with the efficiency computed on the peak of ^{65}Zn in a range up to 2.6 MeV. The total signal efficiency is, therefore, $(75\pm2)\%$.

We estimate the number of $0\nu\beta\beta$ candidates and the BI from a simultaneous unbinned extended maximum likelihood (UEML) fit in the analysis window. For each DataSet the fit comprises the bi-Gaussian line shape for the $0\nu\beta\beta$ signal, with primary peak position fixed at $Q_{\beta\beta}$, and a flat background component. The efficiency and the energy resolution are DataSet dependent. The decay rate $\Gamma_{0\nu}$ and the BI are treated as free parameters common to all the detectors and DataSets. In a 1.83 kg·yr ^{82}Se (3.44 kg·yr Zn^{82}Se) exposure we find no signal evidence and a BI= $(3.6^{+1.9}_{-1.4}) \times 10^{-3}$ counts/(keV·kg·yr), consistent with the five observed events in the 400 keV analysis window (see Fig. 2). We estimate the systematics due to the uncertainty on the absolute energy scale, the detector response function, the efficiency and the exposure. For each influence parameter we weight the likelihood with a Gaussian probability density function with the mean and width fixed to the best estimated values and uncertainties respectively. We then integrate the likelihood via numerical integration. We set a 90% C.I. Bayesian upper limit on $\Gamma_{0\nu}$ using a uniform prior in the physical region of $\Gamma_{0\nu}$ and marginalizing over the BI nuisance parameter: $\Gamma_{0\nu} < 0.285 \times 10^{-24}$ yr^{-1}.

This corresponds to a lower limit on the half-life of $T_{1/2}(0\nu) > 2.4 \times 10^{24}$ yr (90% C.I.). We evaluate the median 90% C.I. lower limit sensitivity from
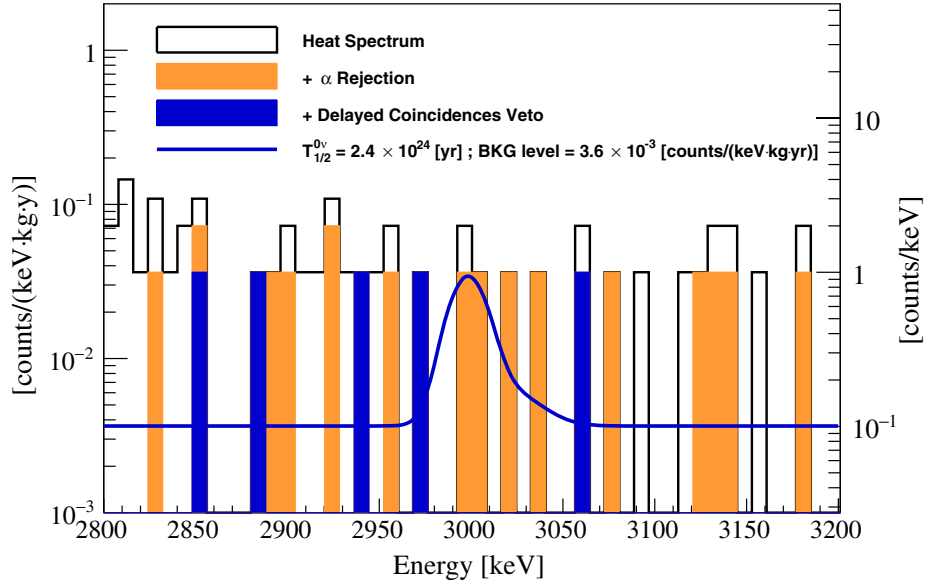
Figure 2: The energy spectrum in the analysis window. The open histogram is the spectrum obtained with the selection on Zn82Se thermal pulses. The filled orange histogram includes the α rejection through the Ge-LD pulse shape. The filled blue histogram is the final spectrum after the delayed-coincidences veto is applied. The blue line is the fitted spectrum together with a hypothetical signal corresponding to the 90% credible interval (C.I.) limit of $T_{1/2}(0\nu) = 2.4 \times 10^{24}$ yr. The bin width is 8 keV.
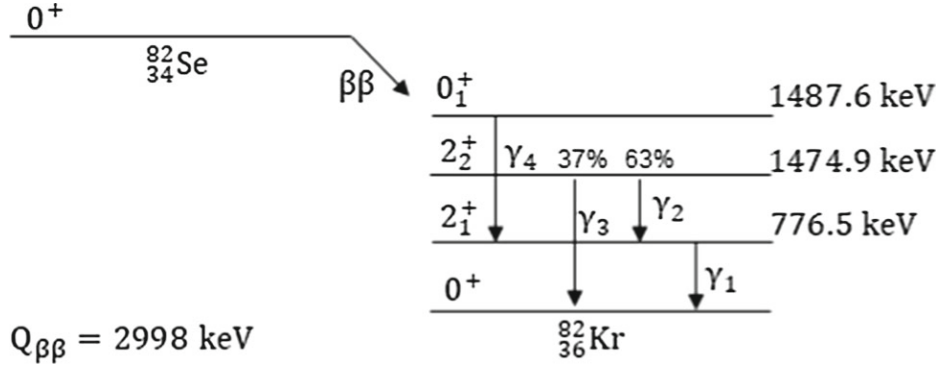
Figure 3: Decay scheme of ^{82}Se to ^{82}Kr.

toy MC experiments to be: $T_{1/2}(0\nu) > 2.3 \times 10^{24}$ yr.

With the considered exposure, the probability to obtain a limit greater than the one we report in this paper is 44%. The CUPID-0 result surpasses by almost 1 order of magnitude the previous limit of $T_{1/2}(0\nu) > 3.6 \times 10^{23}$ yr [13] obtained by NEMO with a larger ^{82}Se exposure ($\sim$3.5 kg·yr).

In the light Majorana neutrino exchange model for the $0\nu\beta\beta$ decay, the effective neutrino mass $m_{\beta\beta}$ is related to $T_{1/2}(0\nu)$ by:

$$[T_{1/2}(0\nu)]^{-1} = \mathcal{G}_{0\nu}|\mathcal{M}_{0\nu}|^2 g_a^4 \left(\frac{m_{\beta\beta}}{m_e}\right)^2 \tag{1}$$

where $\mathcal{G}_{0\nu}$ and $\mathcal{M}_{0\nu}$ are the phase space factor of the decay and the dimensionless nuclear matrix element (NME). Using $\mathcal{G}_{0\nu}$ from Refs.[20, 21], the NME from Refs. [22, 23, 24, 25, 26, 27] and an axial coupling constant g_a=1.269 we find an upper limit on $m_{\beta\beta} < (376 - 770)$ meV. Despite the small CUPID-0 scale, the achieved $m_{\beta\beta}$ approaches the range of the most sensitive experiments in the field [28, 29, 30, 31, 32, 33, 34].

5 Search for the neutrinoless double beta decay of ^{82}Se into the excited states of ^{82}Kr

Double beta decay of ^{82}Se can also proceed thorough the 0_1^+, 2_1^+, and 2_2^+ excited levels of its daughter nucleus, ^{82}Kr, as shown in Fig. 3.

These decays were studied in the past using a high purity Germanium detector operated underground at LNGS with an exposure of 3.64×10^{24}

emitters×yr [14]. Stringent limits on the decay widths were set, of the order of 10^{-23} yr^{-1}. However, the sensitivity of such measurements was limited by the poor detector efficiency (ranging from 0.3 to 3.2%, depending on the chosen signature) and by the background level of 9.6±0.5 c/keV/yr, ascribed to multi-Compton interactions in the detector. In contrast to the measurements made with γ spectroscopy, in CUPID-0 we can distinguish also the decay mode (i.e. with or without the two neutrinos).

Differently from the decay of ^{82}Se to the ground state of ^{82}Kr, in which the Q$_{\beta\beta}$ of the transition is shared only between the two emitted electrons, if the decay occurs to an excited level of ^{82}Kr, the energy of the decay is split between the electrons and the γ rays emitted during the de-excitation of ^{82}Kr.

While the containment efficiency of the two electrons does not vary significantly, the probability that a coincident γ ray with energy ranging from 698 keV (γ_2) to 1475 keV (γ_3) releases its full energy in the crystal is very low, leading to an important decrease of the detection efficiency. The γ rays produced in the de-excitation, indeed, can be fully absorbed in the crystal, or escape the crystal and be absorbed in an other one, or escape the crystal and scatter in another crystal, or completely escape detection. Depending on the scenario, we expect different signatures. In addition, more decay schemes can result in the same signature, further complicating the analysis. The redundancy of states, as well as the different detection efficiency of the processes, imposes a down-selection of the decay schemes.

First, we exclude from the analysis the events in which a single crystal triggers, such as those in which the γ rays escape detection. This choice is motivated by the high background produced mainly by the two-neutrino double beta decay of ^{82}Se. Then, we restrict the analysis to events in which only two ZnSe crystals trigger, thus rejecting interactions in three or more crystals. The criteria excludes events involving electrons and two γs interacting in three different crystals. This choice is motivated by the very low efficiency of these signatures. Finally, we discard the remaining signatures with efficiency lower than 0.01% that would not give a substantial contribution to the analysis. The signatures chosen for the analysis presented in this paper and their detection efficiencies are summarized in Fig. 4.

The number of decays N$_i$ corresponding to the ith signature can be written as a function of the exposure (2.24×10^{25} emitters·yr), the detection efficiency ϵi (see 4), the data selection efficiency η and the width of the corresponding decay channel (Γ).

Each signature can be modeled with a function describing the detector response to a monochromatic energy deposit (Σ) and a flat background

	Signature	E_{main} [keV]	E_{coinc} [keV]	ϵ [%]	
1	$\beta\beta_1 \mid \gamma_1$	2220.5	776.5	1.817±0.009	A
2	$\beta\beta_2 \mid \gamma_1$	1522.1	776.5	0.604±0.004	B
3	$\beta\beta_2 \mid \gamma_2$	1522.1	698.4	0.664±0.004	C
4	$\beta\beta_2 \mid \gamma_3$	1522.1	1474.9	0.919±0.007	D
5	$\beta\beta_2 \mid \gamma_1 + \gamma_2$	1522.1	1474.9	0.0141±0.0004	D
6	$\beta\beta_2 + \gamma_1 \mid \gamma_2$	2298.6	698.4	0.201±0.002	E
7	$\beta\beta_2 + \gamma_2 \mid \gamma_1$	2220.5	776.5	0.211±0.002	A
8	$\beta\beta_3 \mid \gamma_2$	1509.4	776.5	0.606±0.006	B
9	$\beta\beta_3 \mid \gamma_4$	1509.4	711.1	0.660±0.006	F
10	$\beta\beta_3 + \gamma_1 \mid \gamma_4$	2285.9	711.1	0.196±0.003	G
11	$\beta\beta_3 + \gamma_4 \mid \gamma_1$	2220.5	776.5	0.200±0.003	A

Figure 4: Signatures of the ^{82}Se decays to the excited states of ^{82}Kr, grouped according to the decay level: $\beta\beta$ is the energy carried away by electrons in the decay to the 2+1 state ($\beta\beta_1$), to the 2+2 state ($\beta\beta_2$), or to the 0+1 state ($\beta\beta_3$); γ_i are the γ rays emitted in the de-excitation to the ground state (Fig. 3); the vertical bar separates the particles releasing their full energy (E_{main}) in the first crystal, and the particles releasing their full energy (E_coinc) in the second crystal. The detection efficiency ε is determined by a Monte Carlo simulation. Different decay schemes resulting in the same signature (for example, 1, 7, 11) are labelled with the same letter in the last column; the letter B indicates two states with a slightly different energy $\beta\beta$, that were grouped given the resolution of the detector.

component (ρ_{flat}). In the case of signatures B, C, D and F, a gaussian component is added to represent the background from the ^{40}K line. The simultaneous fit of the models to the data allows to extract the values of $\Gamma_{0_1^+}$, $\Gamma_{2_1^+}$ and $\Gamma_{2_2^+}$.

The 90% credible intervals Bayesian upper limit are set using a uniform prior on the values of $\Gamma_{0_1^+}$, $\Gamma_{2_1^+}$ and $\Gamma_{2_2^+}$ and marginalizing over the flat and peaking background parameters, obtaining the most stringent limits on the widths of these processes:

- $\Gamma(^{82}Se \rightarrow^{82} Kr_{0_1^+}) < 8.55 \times 10^{-24}$ yr^{-1};

- $\Gamma(^{82}Se \to^{82} Kr_{2_1^+}) < 6.25 \times 10^{-24}$ yr^{-1};

- $\Gamma(^{82}Se \to^{82} Kr_{2_{+_2}}) < 8.25 \times 10^{-24}$ yr^{-1}.

6 Background Model of the CUPID-0 experiment

The experimental spectra obtained from the CUPID-0 detector has been deep analyzed non only in the $0\nu\beta\beta$ region of interest but also in wide energy ranges, from a few hundred keV to $\sim$10 MeV in order to identify the sources of the CUPID-0 background.

Based on the results from previous experiments [35, 36, 37], the sources of background expected in CUPID-0 are:

- The $2\nu\beta\beta$ decay of ^{82}Se;

- Contaminations of the experimental setup (including the detector itself, the cryostat and the shielding) due to ubiquitous natural radioisotopes of ^{232}Th, ^{238}U and ^{235}U decay chains, and ^{40}K;

- Isotopes produced by cosmogenic activation of detector materials, such as ^{60}Co and ^{54}Mn in copper and ^{65}Zn in ZnSe;

- Cosmic muons, environmental γ-rays and neutrons.

For a better disentanglement of background sources, we exploit the discrimination of α versus β/γ events and the detector modular design, that allows tagging events that produce simultaneous energy depositions in different ZnSe crystals. We then build the following energy spectra:

- $M_{1\beta/\gamma}$ is the energy spectrum of β/γ events that triggered only one bolometer (multiplicity-1 events); this spectrum includes also α events with E<2 MeV that, however, provide a minor contribution;

- $M_{1\alpha}$ is the energy spectrum of multiplicity-1 events produced by α particle interactions;

- M_2 is the energy spectrum of events that simultaneously triggered two bolometers (multiplicity-2 events), built with the energies detected in each crystal;

- Σ_2 is the energy spectrum associated to multiplicity-2 events that contains, for each couple of time coincident events, the total energy released in both crystals.

Events with higher order multiplicity are used to evaluate the contribution of muons, that generate electromagnetic showers triggering several bolometers at the same time.

For each spectra, we identified the signatures of background sources, that were then simulated with a Monte Carlo toolkit, called Arby, based on the GEANT4 toolkit [38] in order to identify the sources location.

The cryostat components where the background sources are generated are the following:

- the Cryostat External Shields (*CryoExt*) include the Inner Vacuum Chamber (IVC), the super-insulation layers, the Outer Vacuum Chamber (OVC), and the main bath, whose spectra are degenerate;

- the Cryostat Internal Shields (*CryoInt*) group the 600 mK and the 50 mK shields, that are made of the same copper;

- the Internal Lead Shield (*IntPb*) is inserted between the IVC and the 600 mK shield and is made of low back-ground ancient Roman lead.

The CUPID-0 detector itself, reconstructed with high detail in MC simulations, is made of three main components where the background sources are generated:

- The *Holder* is the supporting structure for the detectors;

- The *Crystals* are ZnSe cylinders with heights and positions mirroring the real experimental setup;

- The *Reflectors* are the foils laterally surrounding the crystals. This component is also used to account for the minor contribution from light detectors, from the amount (<15 cm^2/crystal) of copper surface directly facing the edges of ZnSe crystals, and from the others small parts close to the crystals (PTFE spacers, NTDs, and wires), whose spectra are degenerate with those of reflecting foils.

The background model is constructed by selecting a representative list of sources, the so-called reference model, whose spectra are combined in a Bayesian fit to the experimental data. Information about contaminant activities available from independent measurements or analyses are included through apposite prior distributions. From the fit we identify the contribution of the various background sources to the ROI$_{bkg}$ counting rate and we perform an analysis of the corresponding systematic uncertainties. In Fig.
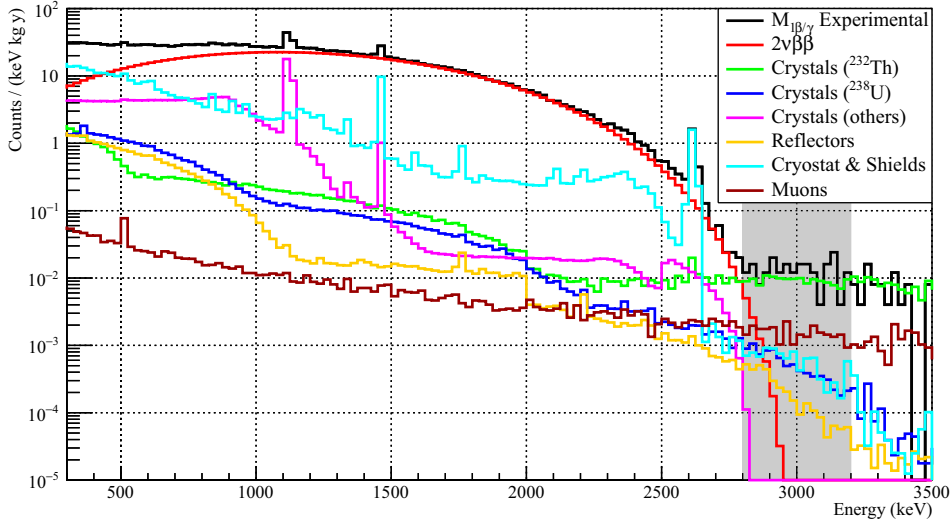
Figure 5: Background sources contributing to the $M_{1\beta/\gamma}$ reconstruction, grouped by source and component. The shaded area corresponds to the 400 keV energy range from 2.8 to 3.2 MeV (ROI_{bkg}) chosen to analyze the background in the region of interest around the ^{82}Se $0\nu\beta\beta$ $Q_{\beta\beta}$. In this plot, the time veto for the rejection of ^{208}Tl events is not applied, thus the ROI_{bkg} is dominated by the β/γ events from ^{232}Th chain contaminations located in *Crystals*.

5, the reconstructed $M_{1\beta/\gamma}$ spectra of different groups of sources, and their contribution to the ROI_{bkg} counting rate, is shown.

Excluding the $2\nu\beta\beta$ decay contribution (which is negligible at the Q-value of ^{82}Se $\beta\beta$ decay), we obtain that $\sim$44% of background rate in the ROI_{bkg} is produced by cosmic muon showers, while the remaining fraction is due to radioactive decays in *Crystals* ($\sim$33%), in *Reflectors* and Holder ($\sim$6%), and in Cryostat and Shields ($\sim$17%).

7 Perspectives

The first goal of the CUPID-0 collaboration for 2019 is to update all the limits on the $0\nu\beta\beta$ ^{82}Se half-life, as well as on $0\nu\beta\beta$ of ^{82}Se in to the excited states of ^{82}Kr exploiting the full statistics collected in the Phase I of data taking.

Moreover, based on the results from the background model, an upgrade

of the CUPID-0 detector has been scheduled at the beginning of 2019 in order to reduce the background level in the ROI and to further improve the comprehension of background sources. The plans for CUPID-0 Phase II include the installation of a muon veto in the external experimental setup. Moreover, the reflecting foil surrounding the crystals will be removed, to get more information about surface contaminations of the crystals. Finally, the addition of an ultra-pure copper vessel at 10 mK, acting as thermal and radioactive shield, will further reduce the counting rate due to contaminations of cryostat and outer shielding. The CUPID-0 results on α-background rejection are a founding pillar of the next-generation CUPID experiment [12, 13], based on scintillating calorimeters.

Acknowledgments

Publications in 2018

O. Azzolini et al., Eur. Phys. J. C (2018) 78: 428
O. Azzolini et al., Phys. Rev. Lett. 120, 232502 (2018) – Editors' suggestion
O. Azzolini, et al., Eur. Phys. J. C (2018) 78: 734
O. Azzolini, et al. Eur. Phys. J. C (2018) 78: 888
O. Azzolini, et al., Nucl. Instrum. Meth. A 61638 (2018)

F. Bellini, et al., Universe 2019, 5(1), 2

References

[1] O. Azzolini, et al., Eur. Phys. J. C 78(5), 428 (2018).

[2] E. Andreotti, et al., Astropart. Phys.34, 822 (2011).

[3] K. Alfonso, et al., Phys. Rev. Lett. 115(10), 102502(2015).

[4] E.E. Haller, Infrared Physics & Technology 35, 127(1994).

[5] E. Andreotti et al., Nucl. Instr. Meth. A664, 161 (2012).

[6] A. Alessandrello et al., Nucl. Instr. Meth. A412, 454(1998).

[7] C. Alduino, et al., Phys. Rev. C 93(4), 045503 (2016).

[8] K. Alfonso et al., JINST13, P02029 (2018).

[9] O. Azzolini, et al., Eur. Phys. J.C 78(9), 734 (2018).

[10] O. Azzolini, et al., Eur. Phys. J.C 78(11), 888 (2018).

[11] E. Gatti, P.F. Manfredi, Riv. Nuovo Cimento9, 1 (1986)23.

[12] V. Radeka, N. Karlovac, Nucl. Instrum. Meth.52, 86(1967)

[13] A.S.Barabash and V.B. Brudanin (NEMO), Phys. Atom. Nucl.74, 312 (2011).

[14] J.W. Beeman, et al., Eur. Phys. J.C 75(12), 591 (2015).

[15] C. Alduino, et al., JINST11(07), P07009 (2016).

[16] CUPID Interest group, arXiv: 1504.03599 (2015).

[17] CUPID Interest group, arXiv: 1504.03612 (2015).

[18] G. Piperno, S. Pirro, and M. Vignati, JINST 6, P10005(2011).

[19] D.R. Artusa et al., Eur. Phys. J. C76, 364 (2016).

[20] J. Kotila and F. Iachello, Phys. Rev. C85, 034316 (2012).

[21] S. Stoica and M. Mirea, Phys. Rev. C88, 037303 (2013).

[22] J. Engel and J. Menéndez, Rept. Prog. Phys.80, 046301(2017).

[23] J. M. Yao, L.S. Song, K. Hagino, P. Ring, and J. Meng, Phys. Rev. C 91, 024316 (2015).

[24] J. Menéndez, A. Poves, E. Caurier, and F. Nowacki, Nucl. Phys. A818, 139 (2009).

[25] F. Simkovic, V. Rodin, A. Faessler, and P. Vogel, Phys. Rev. C 87, 045501 (2013).

[26] T.R. Rodriguez and G. Martinez-Pinedo, Phys. Rev. Lett. 105, 252503 (2010).

[27] A. Meroni, S.T. Petcov, and F. Simkovic, JHEP02, 025 (2013), arXiv:1212.1331.

[28] J.B. Albert et al. (EXO-200), Nature510, 229 (2014).

[29] J.B. Albert et al. (EXO), Phys. Rev. Lett.120, 072701(2018).

[30] A. Gando et al. (KamLAND-Zen), Phys. Rev. Lett. 117, 082503 (2016), [Addendum: Phys. Rev. Lett. 117, no. 10, 109903(2016)].

[31] C.E. Aalseth et al. (Majorana), Phys. Rev. Lett. 120, 132502 (2018).

[32] C. Alduino et al. (CUORE), Phys. Rev. Lett.120, 132501 (2018).

[33] M. Agostini et al. (GERDA), Nature 544, 47 (2017).

[34] M. Agostini et al. (GERDA), Phys. Rev. Lett. 120, 132503 (2018).

[35] C. Alduino et al., Eur. Phys. J. C 77(1), 13 (2017).

[36] C. Alduino et al., Eur. Phys. J. C 77(8), 543 (2017).

[37] R. Arnold et al., Eur. Phys. J. C 78(10), 821 (2018).

[38] S. Agostinelli et al., Nucl. Instrum. Methods A506, 250 (2003).

DAMA

Collaboration:

P. Belli[a], R. Bernabei[a,@], A. Bussolotti[a,*], R. Cerulli[a], A. Di Marco[a], V. Merlo[a], F. Montecchia[a,f], S. Ghorui[a,g], F. Cappella[b], A. d'Angelo[b], A. Incicchitti[b], A. Mattei[b,*], V. Caracciolo[c], C.J. Dai[d], H.L. He[d], X.H. Ma[d], X.D. Sheng[d], Z.P. Ye[d,h]

and in some detector developments, by-product results and small scale experiments:

A. Addazi[i], A.S. Barabash[j], R.S. Boiko[e], V.B. Brudanin[k], D.M. Chernyak[e], F.A. Danevich[e], D.V. Kasperovych[e], R.V. Kobychev[e], V.V. Kobychev[e], S.I. Konovalov[j], B.N. Kropivyansky[e], M. Laubenstein[c], A. Marcianò[i], S.S Nagorny[l], S. Nisi[c], D.V. Poda[e,m], O.G. Polischuk[e], O.E. Safonova[n], V.N. Shlegel[o], N.V. Sokur[e], V.I. Tretyak[e], V.I. Umatov[j], Ya.V. Vasiliev[o], M.M. Zarytskyy[e]

[a]Dip. di Fisica, Univ. Roma "Tor Vergata" and INFN Tor Vergata, 00133 Roma, Italy.
[b]Dip. di Fisica, Univ. Roma "La Sapienza" and INFN-Roma, 00185 Roma, Italy.
[c]Laboratorio Nazionale del Gran Sasso, INFN, 67010 Assergi (Aq), Italy.
[d]IHEP, Chinese Academy of Sciences, P.O. Box 918/3, Beijing 100049, China.
[e]Institute for Nuclear Research, 03028, Kiev, Ukraine.
[f]Dip. di Ing. Civile e Ing. Informatica, Univ. Roma "Tor Vergata", 00133 Rome, Italy.
[g]Indian Institute of Technology Ropar, Ropar, India.
[h]Dep. of Physics, Jinggangshan University 343009, Jiangxi, China.
[i]Dep. of Physics & Center for Field Theory and Particle Physics,
Fudan University, 200433 Shanghai, China.
[j]National Research Centre "Kurchatov Institute," Institute of Theoretical and Experimental
Physics, 117218 Moscow, Russia.
[k]Joint Institute for Nuclear Research, 141980 Dubna, Russia.
[l]Physics Dep., Queen's University, Kingston, Canada.
[m]CSNSM, Univ. Paris-Sud, CNRS/IN2P3, Université Paris-Saclay, 91405 Orsay, France.
[n]Sobolev Inst. of Geology and Mineralogy, Russian Academy of Sciences, Novosibirsk, Russia.
[o]Nikolaev Institute of Inorganic Chemistry, 630090 Novosibirsk, Russia.

[@] Spokesperson; [*] technical staff

Abstract

DAMA is an observatory for rare processes located deep underground at the Gran Sasso National Laboratory of the I.N.F.N. (LNGS); low background scintillators are developed and exploited. During 2018 the main activities have been performed with: i) the DAMA/LIBRA–phase2 set-up (second phase of the second generation DAMA/LIBRA set-up with sensitive mass $\simeq$ 250 kg highly radiopure NaI(Tl), upgraded in 2008, 2010 and at the end of 2012); ii) the DAMA/R&D set-up (a facility to perform relatively small scale experiments, mainly investigating double beta decay modes in various isotopes); iii) the DAMA/Ge set-up (mainly dedicated to sample measurements and to specific measurements on rare processes); some activities are also performed with the Ge-Multi, GeCris and Broad Energy Germanium detectors of the STELLA facility; iv) the DAMA/CRYS set-up (a small set-up for prototype tests, detectors' qualification and small scale experiments); v) the DAMA/LXe set-up (sensitive mass $\simeq$ 6.5 kg liquid Kr-free Xenon enriched either in ^{129}Xe or in ^{136}Xe); it has been put out of operation in 2018 as planned since time.

The main DAMA activities during 2018 are summarized in the following.

1 DAMA/LIBRA

DAMA/LIBRA (Large sodium Iodide Bulk for Rare processes) is a unique apparatus for its sensitive mass, target material, intrinsic radio-purity, methodological approach and all the controls performed on the experimental parameters both for DAMA/LIBRA–phase1 configuration [1, 2, 3, 4, 5, 6, 7, 8, 9, 10, 11, 12, 13, 14, 15, 16, 17] and DAMA/LIBRA–phase2 (see in Refs. [6, 8] and in the 2018 publication list). It is the successor of DAMA/NaI [18, 19, 20, 21, 22, 23, 24, 25, 26, 27, 28, 29, 30], with a larger exposed mass, higher duty cycle and increased sensitivity. The main goal of DAMA/LIBRA is the investigation of the Dark Matter (DM) particles in the galactic halo by exploiting the DM model independent annual modulation signature [31, 32] with increasing sensitivities. This signature is due to the Earth's revolution around the Sun which is moving in the Galaxy. Thus, a larger flux of DM particles crossing the Earth is expected around $\simeq$ 2 June, while a smaller one is expected around $\simeq$ 2 December, depending on the composition of Earth orbital velocity and the Sun velocity with respect to the Galaxy. This signature for DM is a powerful tool because of many requirements have to be simultaneously satisfied: i) the rate must contain a component modulated according to a cosine function, ii) with one year period, and iii) a phase peaked roughly around $\simeq$ 2 June (3); iv) this modulation should be present only in a well-defined low energy range, where DM particle induced events can be present; v) it applies only to those events in which just one detector of many actually "fires" (*single-hit* events), since the DM particle multi-interaction probability is negligible; vi) in the region of maximal sensitivity the modulation amplitude must be $\simeq$ 7% for usually adopted halo distributions, but it can be larger (even up to $\simeq$ 30%) for some cases, such as e.g. those of Refs. [33, 34, 35, 36, 37]. Therefore, many DM candidates, interaction types and scenarios can be explored. Only systematic effects or side reactions accounting for the measured modulation amplitude and satisfying all the peculiarities of the signature could mimic it, but none is available (see Refs. [1, 2, 3, 4, 7, 8, 12, 21, 22, 23, 13] and in the 2018 publication list).

The granularity of the apparatus (25 detectors in a matrix 5×5) is an important feature to study DM and for background identification since DM particles can just contribute to events where only one of the 25 detectors fires (*single-hit* events) and not to those where more than one detector fire in coincidence (*multiple-hit* events). The apparatus – in both configurations – has also the unique feature (as well as the former DAMA/NaI) that gamma calibrations are regularly performed down to the software energy threshold in the same conditions as the production runs, without any contact with the environment and without switching-off the electronics. After the phase1, at present the DAMA/LIBRA–phase2, installed at the end of 2010, is continuously

running. The high light yield and other response features have allowed working in a safe and reliable way down to 1 keV, profiting of new photomultipliers (PMTs) with higher quantum efficiency [6] and of new preamplifiers and of improvements on the electronics and DAQ. The first year was dedicated to the commissioning of the experiment.

Among the scientific goals of this running set-up we briefly mention: i) the investigation with high sensitivity of the DM particle component in the galactic halo by the model independent approach known as DM annual modulation signature, with highly precise determination of the modulation parameters (which carry crucial information); ii) the corollary investigations on the nature of the candidate and on the many possible astrophysical, nuclear and particle physics scenarios; iii) the investigations on other possible model dependent and/or model independent approaches to study DM particles, second order effects and some exotic scenarios; iv) the improvement on the sensitivity to explore rare processes other than DM as performed by the former DAMA/NaI and DAMA/LIBRA–phase1 set-ups (see e.g. Refs. [9, 10, 11, 30]).

This requires dedicated work for reliable collection and analysis of large exposures to reach more competitive sensitivities. As regards the DM features, see e.g. the Sect. 6 of Ref. [23] and the Appendix of Ref. [2]. In particular, the latter shows how the decreasing of the software energy threshold can offer the possibility to disentangle among some of the many possible DM scenarios.

During 2018 the first model independent results, obtained by the DAMA/LIBRA–phase2 experiment investigating the model independent DM annual modulation signature, have been released and published (see in 2018 publication list). The data have been collected over 6 full annual cycles corresponding to a total exposure of 1.13 ton $\times$ yr, deep underground at the Gran Sasso Laboratory, as summarised in the next subsection. The data taking is continuing and various kinds of analyses have been progressed.

1.1 First model independent results from DAMA/LIBRA–phase2 and perspectives

The DAMA/LIBRA apparatus and all the related features and procedures of *phase1* are fully described e.g. in Ref. [1, 2, 3, 4, 8]. In particular, the residual internal contaminations have been discussed in Ref. [1]. At the end of 2010 the upgrade of DAMA/LIBRA towards the *phase2* started. All the PMTs were replaced by a second generation PMTs Hamamatsu R6233MOD, with higher quantum efficiency (Q.E.) and with lower background with respect to those used in *phase1*; they were produced after a dedicated R&D, tests and selections [6, 38]. The new PMTs have Q.E. in the range 33-39% at 420 nm, wavelength of NaI(Tl) emission, and in the range 36-44% at peak. The commissioning of the experiment was successfully performed in 2011, allowing the achievement of the software energy threshold at 1 keV, and the improvement of some detector's features such as energy resolution and acceptance efficiency near software energy threshold. The adopted procedure for noise rejection near software energy threshold has been discussed in Ref. [6]; in particular, the procedure has been the same along all the data taking, throughout the months and the annual cycles. The overall efficiency for *single-hit* events as a function of the energy is also reported in Ref. [6].

In *phase2* a range from 6 to 10 photoelectrons/keV is obtained for the light response of the 25 detectors. Calibrations with X-rays/γ sources are periodically performed down to the keV energy region in the same running condition (see Ref. [1] and in 2018 publication list). In addition, double coincidences accumulated over long periods (from internal X-rays produced by ^{40}K, present at ppt levels in the crystals) give a 3.2 keV calibration point proximal to the software energy threshold. The data acquisition system (DAQ) acquires both *single-hit* events

(where just one of the detectors fires) and *multiple-hit* events (where more than one detector fires) up to the MeV region, despite the optimization is performed for the lowest energy.

The details of the new DAMA/LIBRA–phase2 data are reported in Table 1. The first annual cycle was dedicated to the commissioning and to the optimizations towards the achievement of the 1 keV software energy threshold [6]. Thus, the considered annual cycles of DAMA/LIBRA–phase2 are six (exposure of 1.13 ton×yr). The cumulative exposure, including the former DAMA/NaI and DAMA/LIBRA–phase1 (where the software energy threshold was 2 keV) is 2.46 ton×yr.

Table 1: Details about the annual cycles of DAMA/LIBRA–phase2. The mean value of the squared cosine is $\alpha = \langle cos^2 \omega(t - t_0) \rangle$ and the mean value of the cosine is $\beta = \langle cos\omega(t - t_0) \rangle$ (the averages are taken over the live time of the data taking and $t_0 = 152.5$ day, i.e. June 2nd); thus, the variance of the cosine, $(\alpha - \beta^2)$, is $\simeq 0.5$ for a detector being operational evenly throughout the year.

DAMA/LIBRA–phase2 annual cycle	Period	Mass (kg)	Exposure (kg×day)	$(\alpha - \beta^2)$
1	Dec. 23, 2010 – Sept. 9, 2011	commissioning of *phase2*		
2	Nov. 2, 2011 – Sept. 11, 2012	242.5	62917	0.519
3	Oct. 8, 2012 – Sept. 2, 2013	242.5	60586	0.534
4	Sept. 8, 2013 – Sept. 1, 2014	242.5	73792	0.479
5	Sept. 1, 2014 – Sept. 9, 2015	242.5	71180	0.486
6	Sept. 10, 2015 – Aug. 24, 2016	242.5	67527	0.522
7	Sept. 7, 2016 – Sept. 25, 2017	242.5	75135	0.480
DAMA/LIBRA–phase2	Nov. 2, 2011 – Sept. 25, 2017	411137 $\simeq$ 1.13 ton×yr		0.502
DAMA/NaI + DAMA/LIBRA–phase1 + DAMA/LIBRA–phase2:		2.46 ton×yr		

The total number of events collected for the energy calibrations during DAMA/LIBRA–phase2 is about 1.3×10^8, while about 3.4×10^6 events/keV have been collected for the evaluation of the acceptance window efficiency for noise rejection near the software energy threshold [1, 6]. The duty cycle of the experiment is rather high (see Table 1), ranging between 76% and 85%; it is mainly affected by the routine calibrations and, in particular, by the data collection for the acceptance windows efficiency. The same procedures already adopted for the DAMA/LIBRA–phase1 [1, 2, 3, 4, 8] have been exploited in the analysis of DAMA/LIBRA–phase2; the main ones are reported in the following.

The former DAMA/LIBRA–phase1 and the new DAMA/LIBRA–phase2 residual rates of the *single-hit* scintillation events are reported in Figure 1 from 2 keV, the software energy threshold of DAMA/LIBRA–phase1, up to 6 keV. The residual rates are calculated from the measured rate of the *single-hit* events after subtracting the unmodulated part, as described in Refs. [2, 3, 4, 8, 22, 23]. The null modulation hypothesis is rejected at very high C.L. by χ^2 test: $\chi^2/d.o.f. = 199.3/102$, corresponding to P-value = 2.9×10^{-8}.

The residual rates versus time for 1 keV energy threshold are reported in the papers of the 2018 publication list. The *single-hit* residual rates shown in Figure 1 and those of DAMA/NaI have been fitted with the function: $A \cos\omega(t - t_0)$, considering a period $T = \frac{2\pi}{\omega} = 1$ yr and a phase $t_0 = 152.5$ day (June 2nd) as expected by the DM annual modulation signature. The $\chi^2/d.o.f.$ is equal to 113.8/138 and a modulation amplitude in the 2–6 keV interval in the NaI(Tl): $A = (0.0102 \pm 0.0008)$ cpd/kg/keV, is obtained (see the 2018 publication list).

Keeping the period and the phase free in the fit, the achieved C.L. for the full exposure (2.46 ton × yr) is 12.9 σ; the modulation amplitude of the *single-hit* scintillation events is: (0.0103 ± 0.0008) cpd/kg/keV, the measured phase is (145 ± 5) days and the measured period is
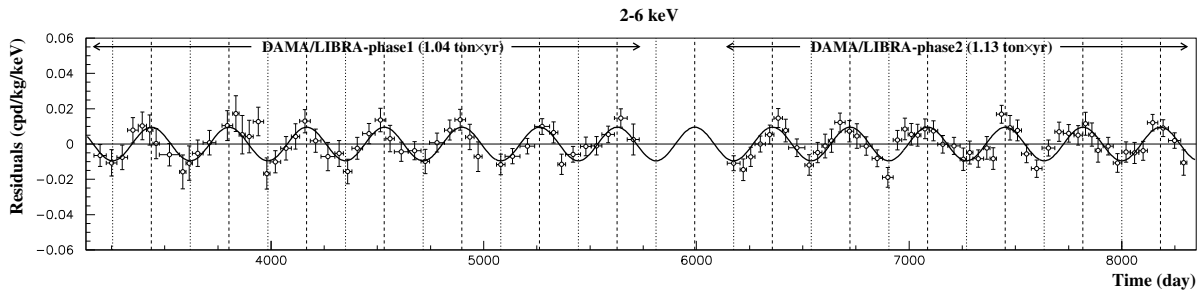
2-6 keV

Figure 1: Residual rate for *single-hit* scintillations measured by DAMA/LIBRA–phase1 and DAMA/LIBRA–phase2 in the (2–6) keV energy interval. The superimposed curve is the cosinusoidal functional forms $A\cos\omega(t-t_0)$ with a period $T = \frac{2\pi}{\omega} = 1$ yr, a phase $t_0 = 152.5$ day (June 2nd) and modulation amplitude, A, equal to the central value obtained by best fit on the data points of DAMA/LIBRA–phase1 and DAMA/LIBRA–phase2.

(0.999 ± 0.001) yr, all these values are well in agreement with those expected for DM particles.

Thus, the DAMA/LIBRA–phase2 data confirm the evidence of a signal that meets all the peculiarities of the model independent DM annual modulation signature. No systematics or side reactions have been found or suggested by anyone able to mimic the exploited DM signature (i.e. to account for the whole measured modulation amplitude and to simultaneously satisfy all the requirements of the signature).

No background modulation has been observed in the energy regions above 6 keV. For example, the measured rate integrated above 90 keV, R_{90}, as a function of the time has been analysed (see Refs. [4, 8] and in the 2018 publication list); similar results are obtained in other energy regions. This analysis holds for whatever kind of background; moreover, as mentioned, there is no background process able to satisfy all the peculiarities of the annual modulation signature and to account for the measured modulation amplitude (see e.g. also Refs. [1, 2, 3, 4, 7, 8, 13, 12] and the 2108 publication list).

A further notable investigation on DAMA/LIBRA–phase2 data was done – as already performed on the two last annual cycles of DAMA/NaI and on the whole DAMA/LIBRA–phase1 [2, 3, 4, 8, 23] – by applying to the *multiple-hit* residual rate[1] the same hardware and software procedures, used to acquire and to analyse the *single-hit* ones. Since the probability that a DM particle interacts in more than one detector is negligible, a DM signal is expected only in the *single-hit* residual rate. Therefore, by comparing *single-hit* and *multiple-hit* results is equivalent to compare the cases of DM particles beam-on and beam-off. In this way a further test is possible on the background behaviour in the same energy range in which the positive effect is observed.

Figure 2 shows the residual rates of the *single-hit* scintillation events of DAMA/LIBRA–phase2, as collected in a single cycle, and the residual rates of the *multiple-hit* events, in the (1–6) keV energy range. A clear modulation, satisfying all the peculiarities of the DM annual modulation signature, is present in the *single-hit* events, while the fitted modulation amplitude for the *multiple-hit* residual rate is well compatible with zero: (0.0004 ± 0.0004) cpd/kg/keV. So, again evidence of annual modulation with the proper peculiarities of the exploited signature is present in the *single-hit* residuals (events class to which the DM particle induced events belong),

---

[1]An event is considered multiple if a deposition of energy occurs in coincidence in more than one detector of the set-up. In DAMA/LIBRA the multiplicity can, in principle, range from 2 to 25. A multiple event in a given energy interval, say (1–6) keV, is given by an energy deposition between 1 and 6 keV in one detector and other deposition(s) in other detector(s).
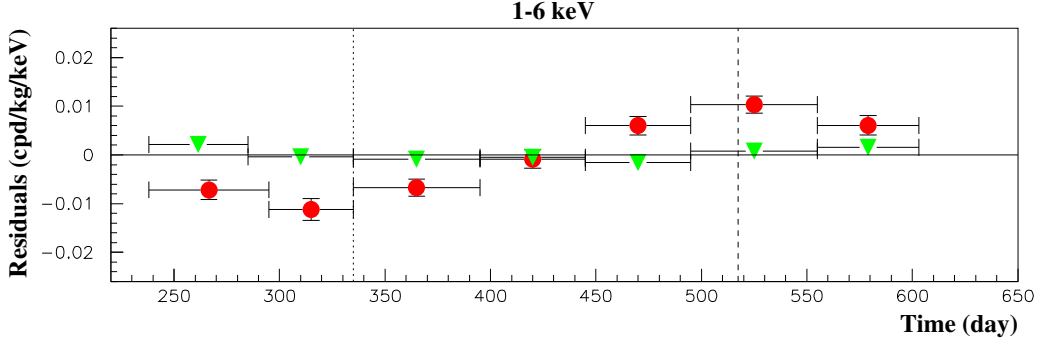
1-6 keV

Figure 2: Experimental residual rates of DAMA/LIBRA–phase2 *single-hit* events (circles), class of events to which DM events belong, and for *multiple-hit* events (filled triangles), class of events to which DM events do not belong. For each class of events the data were considered as collected in a single annual cycle; in both cases the same hardware and software procedures have been applied. The time scale is the same as the previous DAMA papers for consistency. The experimental points present the errors as vertical bars and the widths of the associated time bins as horizontal bars.

while it is absent in the *multiple-hit* residual rate (event class to which only background events belong). Similar results were also obtained for the two last annual cycles of DAMA/NaI [23] and for DAMA/LIBRA–phase1 [2, 3, 4, 8]. The two classes of events were analysed through the same hardware and software procedures; this offers an additional strong support for the presence of a DM particle component in the galactic halo.

In conclusion, no background that can mimic the exploited DM signature, simultaneously accounting for the measured modulation amplitude and satisfying all the peculiarities of the signature, has been found or suggested by anyone throughout some decades thus far (see e.g. in Refs. [1, 2, 3, 4, 8, 7, 13] and in the 2018 publication list).

The *single-hit* residuals were also investigated by Fourier analysis. The analysis procedure is detailed in the papers reported in the 2018 publication list. An evident peak corresponding to a period of 1 year is present in the low energy region; only aliasing peaks are instead present in the (6–14) keV energy region. No structures were observed at different frequencies.

The annual modulation measured at low energy can also be highlighted by studying as a function of energy the modulation amplitude, S_m, obtained by maximum likelihood method fixing $T = 1$ yr and $t_0 = 152.5$ day. The modulation amplitudes for the whole data sets: DAMA/NaI, DAMA/LIBRA–phase1 and DAMA/LIBRA–phase2 (total exposure 2.46 ton×yr) are plotted in Figure 3; the data below 2 keV refer only to the DAMA/LIBRA–phase2 exposure (1.13 ton×yr). As already done for the other data releases [2, 3, 4, 8, 16], the observed annual modulation effect has been verified to be well distributed in all the 25 detectors. In particular, the modulation amplitudes S_m integrated in the range (2–6) keV for each of the 25 detectors for the DAMA/LIBRA–phase1 and DAMA/LIBRA–phase2 periods were calculated. They have random fluctuations around the weighted averaged value, confirmed by the $\chi^2/d.o.f.$ equal to 23.9/24. Other approaches are described in the papers in the 2018 publication list. Thus, the hypothesis that the signal is well distributed over all the 25 detectors is accepted.

In addition, the modulation amplitudes were calculated for DAMA/LIBRA–phase2 separately for the nine inner detectors and the sixteen external ones, as already done for the other data sets [2, 3, 4, 8]. The obtained values are fully in agreement; in particular, it has been verified by χ^2 test that the two sets of modulation amplitudes, as a function of the energy, belong to
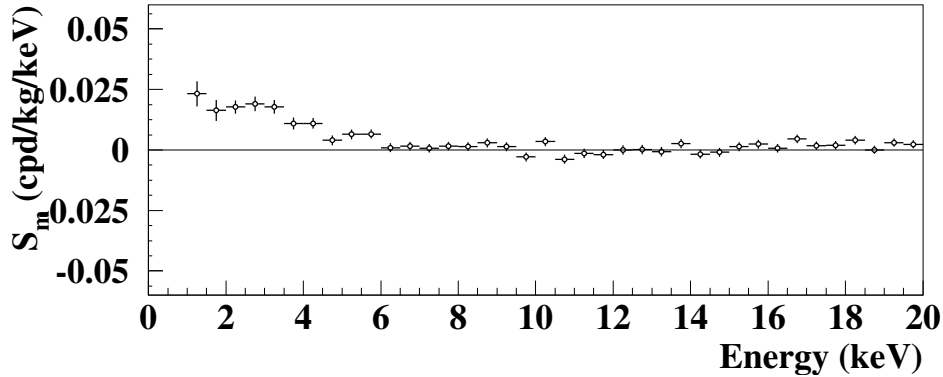
Figure 3: Modulation amplitudes, S_m, for the whole data sets: DAMA/NaI, DAMA/LIBRA–phase1 and DAMA/LIBRA–phase2 (total exposure 2.46 ton×yr) above 2 keV; below 2 keV only the DAMA/LIBRA–phase2 exposure (1.13 ton × yr) is available and used. A modulation is evident in the lowest energy interval, and only S_m's compatible with zero are present just above. In particular, the S_m have random fluctuations around zero in (6–20) keV energy region with χ^2 equal to 42.6 for 28 *d.o.f.* (upper tail probability of 4%); see papers in the 2018 publication list for comments.

same distribution, obtaining e.g.: $\chi^2/d.o.f. = 2.5/6$ and $40.8/38$ for the energy intervals (1–4) and (1–20) keV, respectively ($\Delta E = 0.5$ keV). Thus, the annual modulation effect is well shared between inner and outer detectors.

The hypothesis that the modulation amplitudes singularly calculated for each annual cycle of DAMA/LIBRA–phase1 and DAMA/LIBRA–phase2 are compatible and normally fluctuating around their mean values has been tested by χ^2 and *run test*. It confirms the hypothesis that the data collected in all the annual cycles with DAMA/LIBRA–phase1 and phase2 are statistically compatible and can be analysed together.

Finally, if the assumption of the phase $t_0 = 152.5$ day is released in the procedure to evaluate the modulation amplitudes, the signal can be written as:

$$
\begin{aligned}
S_{ik} &= S_{0,k} + S_{m,k} \cos \omega(t_i - t_0) + Z_{m,k} \sin \omega(t_i - t_0) \\
&= S_{0,k} + Y_{m,k} \cos \omega(t_i - t^*).
\end{aligned}
\tag{1}
$$

For DM one should expect: i) $Z_{m,k} \sim 0$ (because of the orthogonality between the cosine and the sine functions); ii) $S_{m,k} \simeq Y_{m,k}$; iii) $t^* \simeq t_0 = 152.5$ day. In fact, these conditions hold for most of the dark halo models, even if slight differences are expected for possible contributions from non-thermalized DM components (see e.g. Ref. [36, 37, 25, 39, 40, 41]).

The allowed 2σ contours in the plane (S_m, Z_m) and the allowed 2σ contours in the plane (Y_m, t^*), obtained by maximum likelihood method, further show a modulation amplitude significantly different from zero in the lower energy ranges and the phase agrees with the expectation for DM induced signals. For details see the papers in the 2018 publication list.

Finally, the Z_m can also be worked out by the same procedure under the hypothesis that S_m is zero in eq. (1). They are expected to be zero. The χ^2 test applied to the data supports such hypothesis; in fact, in the (1–20) keV energy region the $\chi^2/d.o.f.$ is equal to $44.5/38$ corresponding to a P-value = 22%.

No modulation has been found in any possible source of systematics or side reactions; therefore, cautious upper limits on possible contributions to the DAMA/LIBRA measured modulation

amplitude have been obtained (see Refs. [2, 3, 4, 21, 22, 23, 7, 13] and in the 2018 publication list) They do not account for the measured modulation amplitudes, and also are not able to simultaneously satisfy all the many requirements of the signature; similar analyses were also performed for the DAMA/NaI data [22, 23].

The long-standing annual-modulation evidence observed by the DAMA experiments is model-independent, i.e. without any a-priori assumption of theoretical interpretations about the identity of the DM particle and its interactions. It can be related to a variety of interaction mechanisms of DM particles with the detector materials and is compatible with a wide set of scenarios regarding the nature of the DM candidate and related astrophysical, nuclear and particle physics (see e.g. Refs. [22, 23, 24, 25, 26, 27, 28, 29, 2, 8, 16, 15, 17] and references therein). Additional literature is available on the topics (see e.g. in Ref. [8]) and many possibilities are open.

In conclusion, the data of the new DAMA/LIBRA–phase2 further confirm a peculiar annual modulation of the *single-hit* scintillation events in the (1–6) keV energy region which satisfies all the many requirements of the DM exploited signature.

As required by the investigated DM annual modulation signature: 1) the *single-hit* events show a clear cosine-like modulation as expected for the DM signal; 2) the measured period is equal to (0.999 ± 0.001) yr well compatible with the 1 yr period as expected for the DM signal; 3) the measured phase (145 ± 5) days is compatible with the roughly $\simeq 152.5$ days expected for the DM signal; 4) the modulation is present only in the (1–6) keV low energy range and not in other higher energy regions, consistently with expectation for the DM signal; 5) the modulation is present only in the *single-hit* events, while it is absent in the *multiple-hit* ones as expected for the DM signal; 6) the measured modulation amplitude of the *single-hit* scintillation events in the (2–6) keV energy range (where data are available also by DAMA/NaI and DAMA/LIBRA–phase1) is: (0.0103 ± 0.0008) cpd/kg/keV (12.9 σ C.L.). No systematic or side processes able to mimic the signature, i.e. able to simultaneously satisfy all the many peculiarities of the signature and to account for the whole measured modulation amplitude, has been found or suggested by anyone throughout some decades thus far. Thus, on the basis of the exploited signature, the model independent DAMA results give evidence at 12.9 σ C.L. (over 20 independent annual cycles and in various experimental configurations) for the presence of DM particles in the galactic halo.

The long-standing annual-modulation evidence observed by DAMA is model-independent and it can be compatible with a wide set of DM scenarios. Preliminary results recently reported by other experiments using NaI(Tl) detectors have e.g. not enough sensitivity to be comparable with the annual modulation evidence reported by DAMA. They require e.g. longer data taking and further developments. Both the negative results and all the possible positive hints, achieved so-far in the field, can be compatible with the DAMA results in many scenarios, considering also the existing experimental and theoretical uncertainties.

Finally, we stress that to efficiently disentangle among at least some of the many possible candidates and scenarios an increase of exposure in the new lowest energy bin and the lowering of the energy threshold below 1 keV are important. Thus, during 2018 DAMA/LIBRA–phase2 has continued its data taking. Moreover, related R&D's towards the so-called phase3 have been funded and are in progress. In particular, new PMTs with high quantum efficiency have been especially developed by HAMAMATSU: R11065-20MOD, which satisfy all the needed requirements, and a new voltage divider allocating the preamplifier on the same basis has been designed and already tested.

2 DAMA/LXe

In 2018 – as planned since years – the set-up has been decommissioned, and moved to Tor Vergata DAMA laboratory where it has been reassembled for other purposes. The DAMA/CRYS set-up, which is presently located in an extremely small area (about 6 m^2), is planned to be moved to the inner ground floor of that barrack as soon as a new floor will be completed. This will allow us to suitably install and operate the already built cryogenic system for DAMA/CRYS and use some components of the set-up previously available there.

3 DAMA/R&D

The DAMA/R&D installation is a general-purpose low background set-up used for measurements on low background prototypes and on relatively small-scale experiments [42, 43, 44, 45, 46, 47, 48, 49, 50, 51, 52, 53, 54, 55] and 2018 publication list. The measurements mainly investigate 2β decay modes in various isotopes; both the active and the passive source techniques have been exploited as well as the coincidence technique. Particular attention is dedicated to the isotopes allowing the investigation of the $2\beta^+$ processes and, in particular, to resonant 2ϵ or $\epsilon\beta^+$ decay channels. The investigation of neutrino-less $2\beta^+$, 2ϵ and $\epsilon\beta^+$ processes can refine the understanding of the contribution of right-handed currents to neutrino-less 2β decay; therefore developments of experimental technique to search for $2\beta^+$, 2ϵ and $\epsilon\beta^+$ processes are strongly required considering also that in the $2\beta^+$ investigations a gap of several orders of magnitude between theoretical expectations and experimental results is the usual situation and the better achieved sensitivities do not exceed the level of $T_{1/2} \approx 10^{21}$ yr. Even more important motivation to search for double electron capture appears from a possibility of a resonant process thanks to energy degeneracy between initial and final state of the parent and daughter nuclei. Such a resonant process could occur if the energy of transition minus the energies of two bounded electrons on K or/and L atomic shells of daughter nucleus is near to the energy of an excited level of the daughter isotope. Therefore, investigations on various kinds of new scintillators and preliminary works for the future measurements are also in progress within the DAMA activities.

Some of the main results during 2018 are listed in the following.

- **Investigations of 2β decay of ^{116}Cd with ^{116}CdWO$_4$ crystal scintillators: final results of AURORA and prospects**

  The double-beta decay of ^{116}Cd has been investigated with the help of radiopure enriched ^{116}CdWO$_4$ crystal scintillators (mass of 1.162 kg) at the Gran Sasso underground laboratory. The half-life of ^{116}Cd relatively to the $2\nu2\beta$ decay to the ground state of ^{116}Sn was measured with the highest up-to-date accuracy as $T_{1/2} = (2.63^{+0.11}_{-0.12}) \times 10^{19}$ yr. Figure 4 shows a comparison of the ^{116}Cd $2\nu2\beta$ half-life obtained in the Aurora experiment with other experiments.

  A new improved limit on the $0\nu2\beta$ decay of ^{116}Cd to the ground state of ^{116}Sn was set as $T_{1/2} \geq 2.2 \times 10^{23}$ yr at 90% C.L., which is the most stringent known restriction for this isotope. It corresponds to the effective Majorana neutrino mass limit in the range $\langle m_\nu \rangle \leq (1.0 - 1.7)$ eV, depending on the nuclear matrix elements used in the estimations. Figure 5 shows the results with the $\gamma(\beta)$ events accumulated over 35324 h.

  In the paper on Phys. Rev. D given in the 2018 publication list a lower exposure was reported; there all the details of the data taking and of the data analyses are outlined.
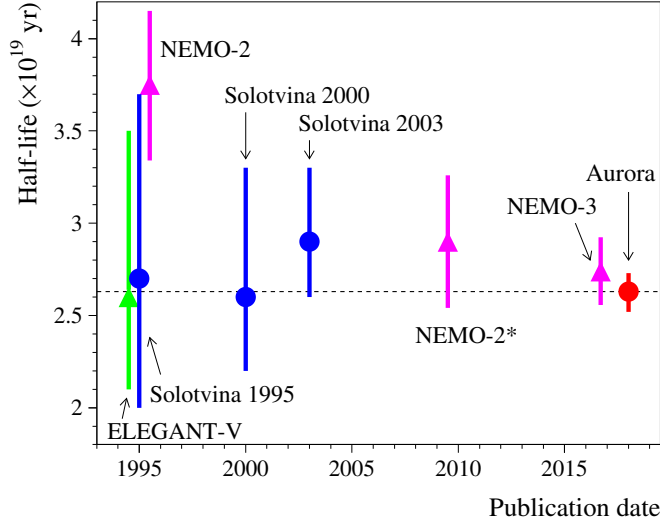
Figure 4: Comparison of the ^{116}Cd $2\nu2\beta$ half-life obtained in the Aurora experiment with other experiments: ELEGANT V [56], Solotvina (three stages of the experiment published in 1995, 2000 and 2003) [57, 58, 59], NEMO-2 [60], and NEMO-3 [61]. A re-estimation of the NEMO-2 experiment (NEMO-2*) [62] is shown too.

Furthermore, new improved half-life limits for the $0\nu2\beta$ decay with majoron(s) emission, Lorentz-violating $2\nu2\beta$ decay and 2β transitions to excited states of ^{116}Sn were set at the level of $T_{1/2} \geq 10^{20} - 10^{22}$ yr. New limits for the hypothetical lepton-number violating parameters (right-handed currents admixtures in weak interaction, the effective majoron-neutrino coupling constants, R-parity violating parameter, Lorentz-violating parameter, heavy neutrino mass) were set.

• **Developments for the production of more radio-pure ^{116}CdWO$_4$**

The investigation on the production of more radio-pure ^{116}CdWO$_4$ detectors with improved performances for a new stage of the research is in progress exploiting various possible solutions.

• **Towards the investigation of 2β decay of ^{116}Cd to excited levels of ^{116}Sn**

Efforts are continuing towards an experiment to search for 2β decay of ^{116}Cd to excited levels of ^{116}Sn (first of all to the 1st 0^+ 1757 keV excited level) by using the highly radiopure enriched ^{116}CdWO$_4$ crystal scintillator with mass 133 g obtained by re-crystallization [53]. The ^{116}CdWO$_4$ scintillation detector is planned to operate in coincidence with external gamma counters. HPGe detectors, scintillation detectors with CdWO$_4$ crystals or some other effective radio-pure detectors can be used to detect gamma quanta expected in the transition (463 keV and 1294 keV). The experiment can also profit of the higher-energy-resolution Ge-Multi ultra-low background HPGe gamma spectrometer. In the period of interest the work has been progressed.

• **Studies of the first forbidden ^{113m}Cd beta decay**

The studies of the first forbidden ^{113m}Cd beta decay have been continued and a paper will be finalized. A 3rd measurement of the ^{113m}Cd beta-spectrum by the ^{106}CdWO$_4$ crystal scintillator, which is contaminated by this isotope, is foreseen in summer 2019 to determine the half-life of ^{113m}Cd precisely.
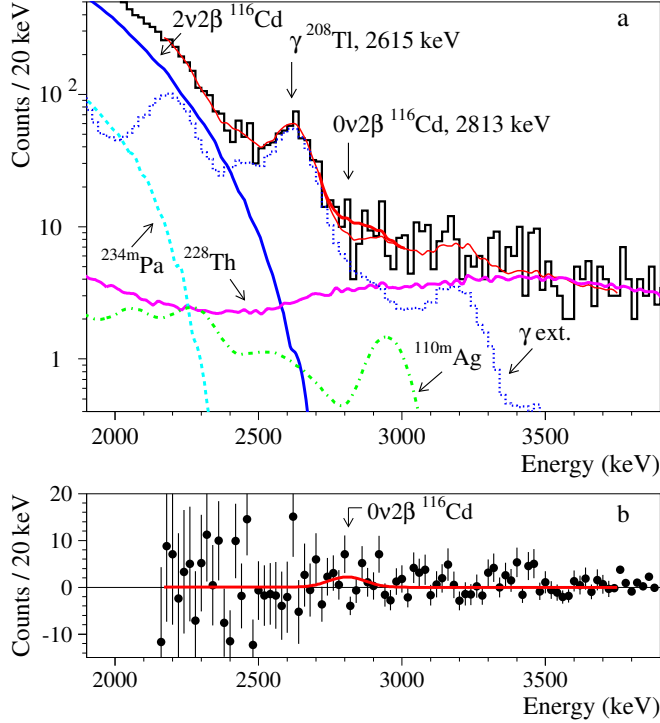
Figure 5: Part of the energy spectrum of $\gamma(\beta)$ events accumulated over 35324 h with the $^{116}CdWO_4$ detectors together with the background model: the $2\nu2\beta$ decay of ^{116}Cd, the internal contamination of the $^{116}CdWO_4$ crystals by ^{110m}Ag, ^{228}Th and ^{234m}Pa, and the contribution from external γ quanta ("γ ext."). The peak of the $0\nu2\beta$ decay of ^{116}Cd excluded at 90% C.L. is shown too (a). The difference between the experimental energy spectrum and the Monte Carlo background model (points with error bars) together with the excluded peak of the $0\nu2\beta$ decay of ^{116}Cd (solid line) is shown in (b).

- **Developments of ultra-radio-pure scintillators**

  The investigation to develop ultra-radio-pure scintillators for rare events searches is continuing, and radioactive elements segregation in crystals is progressed.

- **New development of radiopure $ZnWO_4$ crystal scintillators**

  A new development of radiopure $ZnWO_4$ crystal scintillators has been finalized. The residual radioactive contaminations of zinc tungstate crystal scintillators, produced by low-thermal-gradient Czochralski technique in various conditions, has been measured in the DAMA/R&D low background setup. In particular, the total alpha activity has been measured in the detectors realized with different processes and the activity of internal ^{228}Th contamination has been estimated. A paper is under completion.

- **R&D of radio-pure $Gd_2SiO_5(Ce)$ crystal scintillators, GSO(Ce)**

  An R&D of radio-pure $Gd_2SiO_5(Ce)$ crystal scintillators, GSO(Ce), is continuing; such detector(s) can be used to search for 2β decay of ^{152}Gd and ^{160}Gd. The ^{152}Gd is interesting due to the possibility of resonant double electron capture, while ^{160}Gd is a double beta active nucleus with one of the highest natural isotopic abundance. However, lanthanides are typically contaminated by thorium and uranium since bastnasites (minerals used to

produce lanthanides) are contaminated at $\simeq 1\%$ level by uranium and thorium. Measurements aiming at their purification and test of radioactive contamination, especially of actinium, lutetium and lanthanum, are planned since other radioactive impurities can be removed by using the already developed methods of purification. The measurements in HPGe detector have been carried out and a paper will be finalized most probably in 2019. The next step will be a deep purification of the sample with lower activity of ^{138}La, ^{176}Lu and ^{234m}Pa by liquid-liquid extraction method.

- **R&D for production of SrI$_2$(Eu) scintillators**

  SrI$_2$(Eu) scintillators look promising detectors to search for 2β decay of Sr (see Ref. [49]). In addition, SrI$_2$(Eu) scintillators show a rather high scintillation efficiency (light yield of $\simeq 90000$ photons/MeV was reported in Ref. [63]) that makes the material promising for various searches. Further development of purification methods for europium oxide (that is expected to be the most contaminated raw material for crystal growth) is under study before the crystal scintillators can be grown.

- **Other activities**

  Among the other activities in preparation we mention that at the end of the present measurements, new measurements are foreseen in DAMA/R&D; developments on new enriched CdWO$_4$ scintillators depleted in ^{113}Cd, on highly radio-pure BaWO$_4$, etc. The R&D of low background barium containing crystal scintillators to investigate double beta processes in ^{130}Ba and ^{132}Ba is continuing profiting of new scintillator detectors.

In conclusion, DAMA/R&D is a general-purpose set-up and can assure future possibility of producing many kinds of low background measurements in an efficient way at well reduced cost.

4   DAMA/CRYS

DAMA/CRYS is a small test set-up mainly dedicated to tests on the performances of new scintillation detectors and to small-scale experiments. As mentioned above, in order to operate it more suitably and to install the already built cryogenic part, it is planned to be moved in the inner part of the ground floor level of DAMA/LXe that has been dismounted in the period of interest here.

Main activities in 2018:

- **The experiment to search for 2β decay of ^{106}Cd**

  The experiment to search for 2β decay of ^{106}Cd with a ^{106}CdWO$_4$ crystal scintillator (enriched in ^{106}Cd to 66%) in coincidence with two large CdWO$_4$ detectors in closed geometry continues its data taking. The possible double beta decay processes and the background components have been simulated by a Monte Carlo procedure, the data analysis is in progress. The sensitivity of the experiment is approaching the theoretical predictions for the two-neutrino electron capture with positron emission in ^{106}Cd: $T_{1/2} > 4 \times 10^{21}$ yr (the best previous limit was $T_{1/2} > 1.1 \times 10^{21}$ yr, the theoretical predictions are in the region of half-lives $10^{20} - 10^{22}$ yr).

- **The two parts of the cryogenic system**

  The two parts of the cryogenic system to be installed in DAMA/CRYS (to allow also measurements of the responses of various new/improved scintillators as a function of the

temperature) are ready to be installed in the set-up as soon as it will be moved in the new site since the DAMA/CRYS set-up is presently located in an extremely small area (about 6 m^2). It is planned to be moved to the inner ground floor of the dismounted DAMA/LXe barrack with the aim to suitably install and operate that cryogenic system, and to use some components of the set-up previously available there. The DAMA/LXe barrack at ground floor was fully emptied in order to allow the preparation of the renewed floor (we remind that the first floor of the DAMA/LXe site hosts materials and a working place underground which is strictly necessary to maintain). Unfortunately, there was some delay in setting the order for this floor restoration and the works have been delayed and this has caused delay in the installation and use of the cryogenic system, ready since time.

- **R&D of higher quality ^{arch}PbWO$_4$**

  The R&D of higher quality ^{arch}PbWO$_4$ light guide by double crystallization from highly purified archaeological lead is continuing with the aim to improve the present ^{106}CdWO$_4$ detector energy resolution, and to use in the experiment in preparation to search for double beta decay of 116Cd to excited levels of 116Sn (see Sec. 3)

- **Perspectives**

  Preparations of other future measurements are in progress.

DAMA/CRYS is a general-purpose set-up and can also assure us in future the possibility to produce many kinds of low background measurements in an efficient way at well reduced cost.

5 DAMA/Ge and LNGS STELLA facility

In addition to samples measurements, the following activities have been carried out in 2018. Recent published results can be found in Ref. [64, 65, 66, 67, 68] and in the 2018 publication list.

- **The experiment to search for 2β decay of ^{150}Nd to the excited levels of ^{150}Sm**

  The experiment to search for 2β decay of ^{150}Nd to the excited levels of ^{150}Sm by using deeply purified 2.381 kg neodymium oxide (Nd$_2$O$_3$) samples, installed in the GeMulti ultra-low background HPGe gamma spectrometer, was in progress. A paper describing preliminary results was published. The measurements are in progress to increase the statistics and to improve the half-life value accuracy. Other double beta decay processes with emission of gamma quanta (double beta decay of ^{148}Nd to excited level of ^{148}Sm and double beta decay of ^{150}Nd to higher excited levels of ^{150}Sm) will be analysed too. In the preliminary published results the double beta decay of ^{150}Nd to the first excited 0$^+$ level of ^{150}Sm (E$_{exc}$ = 740.5 keV) was investigated with the help of ultra-low-background setup with four HP Ge detectors (225 cm^3 volume each one) of the STELLA facility. The sample of Nd$_2$O$_3$ was used as a source of γ quanta expected in the decays. Gamma quanta with energies 334.0 keV and 406.5 keV emitted after the deexcitation of the 0$_1^+$ 740.5 keV excited level of ^{150}Sm are observed in the coincidence spectra accumulated over 16375 h. The half-life relatively to the two neutrino double beta decay ^{150}Nd $\rightarrow$ ^{150}Sm (0$_1^+$) is measured as $T_{1/2} = [4.7^{+4.1}_{-1.9}(stat) \pm 0.5(syst)] \times 10^{19}$ yr, in agreement with the results of the previous experiments. Figure 6 shows the coincidence energy spectra accumulated over 16375 h by the GeMulti set-up with the Nd$_2$O$_3$ sample, when the energy in one detector

is fixed in the energy interval where γ quanta from the decay ^{150}Nd $\to$ ^{150}Sm(0_1^+, 740.5 keV): 334.0 keV $\pm 1.4\times$ FWHM (top), 406.5 keV $\pm$ 1.4 $\times$ FWHM (middle), are expected.
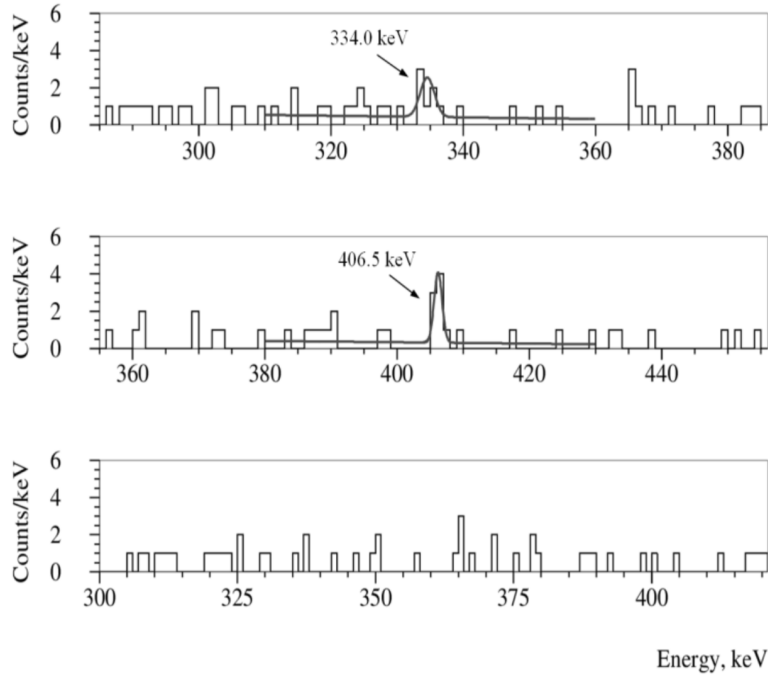

Figure 6: The coincidence energy spectra accumulated over 16375 h by the GeMulti set-up with the 2.381 kg Nd$_2$O$_3$ sample, when the energy in one detector is fixed in the energy interval where γ quanta from the decay ^{150}Nd $\to$ ^{150}Sm(0_1^+, 740.5 keV): 406.5 keV $\pm 1.4\times$ FWHM (*top*), 334.0 keV $\pm 1.4\times$ FWHM (*middle*), are expected. The *bottom* spectrum demonstrates the random coincidence background in the energy range of interest when the energy of the events in one of the detectors was taken as 375 keV $\pm 1.4\times$ FWHM (no γ quanta with this energy are expected neither in the 2β decay of ^{150}Nd nor in the decays of nuclides that are radioactive contamination of the Nd$_2$O$_3$ sample or of the set-up).

Details on the data taking and all the adopted analysis procedures are given in the preliminary paper quoted in the 2018 publication list.

- **Search for rare α and 2β decay of osmium isotopes**

  The experiment to search for α decay of ^{184}Os and ^{186}Os to the first excited levels of daughter nuclei, and for 2β decay of ^{184}Os and ^{192}Os is in progress. A first paper is in preparation. In fact, 118 g of ultra-pure osmium was installed on the BEGe detector of the STELLA facility deep underground at LNGS. A preliminary indication of a peak at 100.1 keV with an excess of 32^{+22}_{-17} counts is present which can be ascribed to ^{186}Os $\to$ ^{182}W* (100.1 keV). Thus, the data taking is in progress to confirm or disprove this result.

  A next stage of the experiment is in progress with the osmium sample placed directly inside the cryostat of the BEGe detector of the STELLA facility at LNGS to improve the detection efficiency and the experimental sensitivity.

- **First searches for 2β decay of Er, Sm, Yb isotopes**

  Low background measurements aiming at a first search for 2ϵ and $\epsilon\beta^+$ decay of ^{162}Er,

^{168}Yb, and search for $2\beta^-$ decay of ^{170}Er,^{154}Sm, ^{176}Yb to the excited levels of daughter nuclei, have been prepared/carried out with highly purified ytterbium, erbium and samarium oxide samples. Near resonant neutrino-less double electron capture is possible in ^{162}Er and ^{168}Yb, which makes these nuclei especially interesting. Preliminary results have been published and presented at conferences; in particular, a first search for 2ϵ and $\epsilon\beta^+$ decay of ^{162}Er and new limit on $2\beta^-$ decay of ^{170}Er to the first excited level of ^{170}Yb were published, while a first paper on results obtained with Yb sample is finalizing.

In particular, the first search for double electron capture and electron capture with positron emission of ^{162}Er to the ground state and to several excited levels of ^{162}Dy was realized with 326 g of highly purified erbium oxide. The sample was measured over 1934 h by the ultra-low background HPGe γ spectrometer GeCris (465 cm^3) at the STELLA facility of the LNGS. No effect was observed, the half-life limits were estimated at the level of lim $T_{1/2} \simeq 10^{15} - 10^{18}$ yr. A possible resonant $0\nu KL_1$ capture in ^{162}Er to the 2^+ 1782.7 keV excited state of ^{162}Dy is restricted as $T_{1/2} \geq 5.0 \times 10^{17}$ yr at 90% C.L. A new improved half-life limit $T_{1/2} \geq 4.1 \times 10^{17}$ yr was set on the $2\beta^-$ decay of ^{170}Er to the 2^+ 84.3 keV first excited state of ^{170}Yb.

In Table 2 the radioactive contaminations of the erbium oxide sample before and after the applied purification are shown.

Table 2: Radioactive contamination of the erbium oxide sample before and after the purification, measured with the help of an ultra-low background HP Ge γ spectrometer. The upper limits are presented at 90% C.L., the uncertainties are given at $\approx$ 68% C.L.

Chain	Nuclide	Activity (mBq/kg)	
		Before purification	After purification
	^{40}K	≤ 27	≤ 1.7
	^{137}Cs	≤ 2.1	1.4 ± 0.3
	^{176}Lu	6 ± 1	4.2 ± 0.4
^{232}Th	^{228}Ra	≤ 7.2	≤ 1.0
	^{228}Th	5 ± 2	≤ 1.1
^{235}U	^{235}U	≤ 12	≤ 1.6
^{238}U	^{226}Ra	6 ± 2	1.1 ± 0.4
	^{234}Th	≤ 1800	≤ 91
	^{234m}Pa	≤ 74	≤ 16

The details on the data taking, data analyses and results are given in the published paper quoted in the 2018 publication list.

- **R&D of methods to purify rare earths**

The R&D of methods to purify samarium, ytterbium, erbium, europium and gadolinium oxides has been progressing. Investigations on deep purification of the samples, at hands, are continuing.

- **Measurements with a BaWO$_4$**

A Barium Tungstate single crystal (BaWO$_4$) has been produced by using the low thermal gradient Czochralski technique. Its light emission and radioactive contaminants have been

investigated. The result of these studies, with the aim to use crystal scintillators to investigate double beta decay of ^{130}Ba and ^{132}Ba isotopes with the *source = detector* approach, indicates the forward way to try to overcome the limits and to profit of the potentiality of this single crystal. A paper has been published. A BaWO$_4$ crystal scintillator was measured with the ultra-low background HPGe gamma-ray spectrometer GEMPI3 of the STELLA facility at LNGS. The characteristics of the detector have been studied and a related paper published.

Improvements and preparations of other future measurements are in progress.

6   Other activities

- **Precise measurement of the half-life of ^{212}Po**

  A precise measurement of the half-life of ^{212}Po (one of the daughter nuclides in radioactive chain of ^{232}Th) was realized at sea level with the help of a liquid scintillator based on toluene doped by complex of thorium and trioctylphosphine oxide with concentration of Th $\simeq 0.1$ mass %. A fast PMT and high frequency oscilloscope were used to acquire the scintillation signals waveforms. The algorithms were developed to find pairs of ^{212}Bi β decays and subsequent ^{212}Po α decays, to calculate time differences between the events in the pair, and to build ^{212}Bi β decay and ^{212}Po α decay energy spectra. A preliminary result giving ^{212}Po half-life equal to $T_{1/2} = (294.8 \pm 1.9)$ ns has been published. The final paper is in preparation looking for a reduction of the statistical and systematic uncertainties. It is expected that the most accurate value of the ^{212}Po half-life will be obtained.

- **Further measurements of the anisotropy of ZnWO$_4$ to nuclear recoils at low energy**

  A new dedicated set-up has been developed and installed at ENEA-Casaccia in a new experimental site to better quantify the anisotropy of the ZnWO$_4$ crystal scintillators in the light output and in the pulse shape at keV range for heavy particles (p, α, nuclear recoils), depending on their direction with respect to the crystal axes. A neutron beam by neutron gun is used. New data have been collected at various angles. Further measurements are already scheduled.

- **Testing noncommutative spacetimes and violations of the Pauli Exclusion Principle with underground experiments**

  A paper has been published (see the 2018 publication list). Limits that arise from different tests of the Pauli Exclusion Principle have been deployed: i) to provide theories of quantum gravity with experimental guidance; ii) to distinguish, among the plethora of possible models, the ones that are already ruled out by current data; iii) to direct future attempts to be in accordance with experimental constraints. Firstly the experimental bounds on nuclear processes forbidden by the Pauli Exclusion Principle, which have been derived by several experimental collaborations making use of various detector materials, have been reviewed. Distinct features of the experimental devices entail sensitivities on the constraints hitherto achieved that may differ from one another by several orders of magnitude. It has been shown that with choices of these limits, well-known examples of flat noncommutative space-time instantiations of quantum gravity can be heavily constrained, and eventually ruled out. We devote particular attention to the analysis of the κ-Minkowski and θ-Minkowski noncommutative spacetimes. These are deeply connected

102

to some scenarios in string theory, loop quantum gravity, and noncommutative geometry. We emphasize that the severe constraints on these quantum spacetimes, although they cannot rule out theories of top-down quantum gravity to which they are connected in various ways, provide a powerful limitation for those models. Focus on this will be necessary in the future. Details are in the paper in the 2018 publication list.

7   Conclusions

During 2018 DAMA/LIBRA has continued to take data in the phase2 configuration and the model independent results from the data collected during six full annual cycles has been published.

During 2018 DAMA/LIBRA–phase2 data taking has been continued.

Some new electronic cards are in development and in test; they will allow the simplification of the electronic chain.

Studies on corollary model dependent analyses in some of the many scenarios possible for DM particles are in progress to point out the implications of the new data; moreover, studies on other DM features, second order effects, and several other rare processes are in progress with the aim to reach very high sensitivity also thanks to the progressive increasing of the exposure.

The developments towards DAMA/LIBRA–phase3, based on the already funded R&Ds, have been definitively progressed in order to lower the software energy threshold below 1 keV with the aim e.g. to disentangle among several of the many possible physical scenarios.

Results on several 2β decay processes and developments on new highly radio-pure scintillators for the search of rare processes have been published and are under further developments. In particular, the final results of the Aurora measurement have been published as well as first results on double beta processes in Erbium isotopes and in ^{150}Nd. Various other results have been published as well.

During 2018, more than 20 presentations at Conferences and Workshops (many of them by invitation) have been performed.

Finally, in 2018 all the operative DAMA set-ups have regularly been in data taking and various kinds of measurements have been in progress and planned for the future.

8   List of Publications during 2018

1. A. Di Marco, A.S. Barabash, P. Belli, R. Bernabei, R.S. Boiko, V.B. Brudanin, F. Cappella, V. Caracciolo, R. Cerulli, D.M. Chernyak, F.A. Danevich, A. Incicchitti, D.V. Kasperovych, V.V. Kobychev, S.I. Konovalov, M. Laubenstein, V. Merlo, F. Montecchia, O.G. Polischuk, D.V. Poda, V.N. Shlegel, V.I. Tretyak, V.I. Umatov, Y.V. Vasiliev, M.M. Zarytskyy, "Recent Developments and Results on Double Beta Decays with Crystal Scintillators and HPGe Spectrometry", Universe 4(12) (2018) 147.

2. P. Belli, R. Bernabei, R.S. Boiko, F.A. Danevich, A. Di Marco, A. Incicchitti, D.V. Kasperovych, F. Cappella, V. Caracciolo, V.V. Kobychev, O.G. Polischuk, N.V. Sokur, V.I. Tretyak, R. Cerulli, "Half-life measurements of ^{212}Po with Thorium-loaded liquid scintillator", Nucl. Phys. and Atomic Energy 19 (2018) 220-226.

3. A.S. Barabash, P. Belli, R. Bernabei, F. Cappella, V. Caracciolo, R. Cerulli, D.M. Chernyak, F.A. Danevich, S. d'Angelo, A. Incicchitti, D.V. Kasperovych, V.V. Kobychev, S.I. Konovalov, M. Laubenstein, D.V. Poda, O.G. Polischuk, V.N. Shlegel, V.I. Tretyak, V.I. Umatov, Ya.V. Vasiliev, "Final results of the Aurora experiment to study 2β decay of ^{116}Cd with enriched ^{116}CdWO$_4$ crystal scintillators", Phys. Rev. D 98 (2018) 092007.

4. R. Bernabei, P. Belli, A. Bussolotti, F. Cappella, V. Caracciolo, R. Cerulli, C.J. Dai, A. d'Angelo, A. Di Marco, H.L. He, A. Incicchitti, X.H. Ma, A. Mattei, V. Merlo, F. Montecchia, X.D. Sheng, Z.P. Ye, "First model independent results from DAMA/LIBRA–phase2", Nucl. Phys. and Atomic Energy 19 (2018) 307-325.

5. R. Bernabei, P. Belli, A. Bussolotti, F. Cappella, V. Caracciolo, R. Cerulli, C.J. Dai, A. d'Angelo, A. Di Marco, H.L. He, A. Incicchitti, X.H. Ma, A. Mattei, V. Merlo, F. Montecchia, X.D. Sheng, Z.P. Ye, "First model independent results from DAMA/LIBRA–phase2", Universe 4 (2018) 116.

6. A.S. Barabash, P. Belli, R. Bernabei, R.S. Boiko, F. Cappella, V. Caracciolo, R. Cerulli, F.A. Danevich, A. Di Marco, A. Incicchitti, D.V. Kasperovych, R.V. Kobychev, V.V. Kobychev, S.I. Konovalov, M. Laubenstein, D.V. Poda, O.G. Polischuk, V.I. Tretyak, V.I. Umatov, "Double beta decay of ^{150}Nd to the first excited 0^+ level of ^{150}Sm: preliminary results", Nucl. Phys. and Atomic Energy 19 (2018) 95-102.

7. R. Bernabei, P. Belli, A. Bussolotti, R. Cerulli, A. Di Marco, V. Merlo, F. Montecchia, F. Cappella, A. d'Angelo, A. Incicchitti, A. Mattei, V. Caracciolo, C.J. Dai, H.L. He, X.H. Ma, X.D. Sheng, Z.P. Ye, "New Model independent Results From the First Six Full Annual Cycles of DAMA/LIBRA–phase2", Bled Workshops in Physics vol. 19, no. 2 (2018) 27-57.

8. R. Bernabei, P. Belli, A. Bussolotti, F. Cappella, V. Caracciolo, R. Cerulli, C.J. Dai, A. d'Angelo, A. Di Marco, H.L. He, A. Incicchitti, X.H. Ma, A. Mattei, V. Merlo, F. Montecchia, X.D. Sheng, Z.P. Ye, "First results from DAMA/LIBRA–phase2", Nuclear and Particle Physics Proceedings 303-305 (2018) 74-79

9. A. Addazi, P. Belli, R. Bernabei, A. Marcianò, "Testing Noncommutative Spacetimes and Violations of the Pauli Exclusion Principle through underground experiments", Chinese Physics C 42 (2018) 094001.

10. P. Belli, R. Bernabei, R.S. Boiko, F. Cappella, V. Caracciolo, R. Cerulli, F. Danevich, A. Incicchitti, B.N. Kropivyansky, M. Laubenstein, S. Nisi, D.V. Poda, O.G. Polischuk, V.I. Tretyak, "First search for 2ϵ, $\epsilon\beta^+$ decay of ^{162}Er and new limit on 2β decay of ^{170}Er to the first excited level of ^{170}Yb", J. Phys. G: Nucl. Part. Phys. 45 (2018) 095101.

11. R. Bernabei, P. Belli, F. Cappella, V. Caracciolo, R. Cerulli, C.J. Dai, A. d'Angelo, A. Di Marco, H.L. He, A. Incicchitti, H.H. Kuang, X.H. Ma, F. Montecchia, X.D. Sheng, R.G. Wang, Z.P. Ye, "DAMA/LIBRA Results and Perspectives", EPJ Web of Conf. 182 (2018) 02027.

12. A.S. Barabash, P. Belli, R. Bernabei, R.S. Boiko, V.B. Brudanin, F. Cappella, V. Caracciolo, R. Cerulli, D.M. Chernyak, C.J. Dai, F.A. Danevich, A. d'Angelo, A. Di Marco, H.L. He, A. Incicchitti, D.V. Kasperovych, V.V. Kobychev, S.I. Konovalov, H.H. Kuang, X.H. Ma, V. Merlo, F. Montecchia, D.V. Poda, O.G. Polischuk, X.D. Sheng, V.N. Shlegel, V.I. Tretyak, V.I. Umatov, R.G. Wang, Z.P. Ye and M.M. Zarytskyy, "Search for rare processes with DAMA experimental set-ups", EPJ Web of Conf. 182 (2018) 02026.

13. F. Cappella, V. Caracciolo, R. Cerulli, A. Di Marco, M. Laubenstein, S.S. Nagorny, V.N. Shlegel, O.E. Safonova, "Limits and Performances of a $BaWO_4$ Single Crystal", Nucl. Inst. and Methods A 901 (2018) 150-155.

14. R. Bernabei, F. Cappella, "Investigation of rare nuclear decays with the DAMA set-ups", Int. J. Mod. Phys. A 33 (2018) 1843005.

15. A. Incicchitti, Guest Editor's Preface, Special Issue: "Results and Developments in the Investigation of Rare Nuclear Decays and Processes", Int. J. of Mod. Phys. A 33, N. 09 (2018) 1802002.

16. R. Bernabei, P. Belli, F. Cappella, V. Caracciolo, R. Cerulli, A. d'Angelo, A. Di Marco, A. Incicchitti, V. Merlo, F. Montecchia, C.J. Dai, H.L. He, H.H. Kuang, X.H. Ma, X.D. Sheng, R.G. Wang, Z.P. Ye, "DAMA/LIBRA results and perspectives", J. Phys.: Conf. Ser. 1056 (2018) 012005.

17. R. Bernabei, P. Belli, A. Di Marco, V. Merlo, F. Montecchia, F. Cappella, A. d'Angelo, A. Incicchitti, V. Caracciolo, R. Cerulli, C.J. Dai, H.L. He, H.H. Kuang, X.H. Ma, X.D. Sheng, R.G. Wang, Z.P. Ye, "Dark Matter Particles in the Galactic Halo", in the volume of Proceed. "New Trends in High-Energy Physics": Proceedings of the Conference (Budva, Becici, Montenegro, 2-8 October 2016), ISBN 978-5-9530-0486-2, Dubna: JINR, 2018, pages 41-50.

References

[1] R. Bernabei et al., Nucl. Instr. and Meth. A 592 (2008) 297.

[2] R. Bernabei et al., Eur. Phys. J. C 56 (2008) 333.

[3] R. Bernabei et al., Eur. Phys. J. C 67 (2010) 39.

[4] R. Bernabei et al., Eur. Phys. J. C 73 (2013) 2648.

[5] P. Belli et al., Phys. Rev. D 84 (2011) 055014.

[6] R. Bernabei et al., J. of Instr. 7 (2012) P03009.

[7] R. Bernabei et al., Eur. Phys. J. C 72 (2012) 2064.

[8] R. Bernabei et al., Int. J. of Mod. Phys. A 28 (2013) 1330022 (73 pages).

[9] R. Bernabei et al., Eur. Phys. J. C 62 (2009) 327.

[10] R. Bernabei et al., Eur. Phys. J. C 72 (2012) 1920.

[11] R. Bernabei et al., Eur. Phys. J. A 49 (2013) 64.

[12] R. Bernabei et al., Eur. Phys. J. C 74 (2014) 2827.

[13] R. Bernabei et al., Eur. Phys. J. C 74 (2014) 3196.

[14] R. Bernabei, et al., Eur. Phys. J. C 75 (2015) 239.

[15] A. Addazi, et al., Eur. Phys. J. C 75 (2015) 400.

[16] DAMA coll., issue dedicated to DAMA, Int. J. Mod. Phys. A 31 (2016).

[17] R. Cerulli et al., Eur. Phys. J. C 77 (2017) 83.

[18] P. Belli, R. Bernabei, C. Bacci, A. Incicchitti, R. Marcovaldi, D. Prosperi, DAMA proposal to INFN Scientific Committee II, April 24th 1990.

[19] R. Bernabei et al., Phys. Lett. B 389 (1996) 757; R. Bernabei et al., Phys. Lett. B 424 (1998) 195; R. Bernabei et al., Phys. Lett. B 450 (1999) 448; P. Belli et al., Phys. Rev. D 61 (2000) 023512; R. Bernabei et al., Phys. Lett. B 480 (2000) 23; R. Bernabei et al., Phys. Lett. B 509 (2001) 197; R. Bernabei et al., Eur. Phys. J. C 23 (2002) 61; P. Belli et al., Phys. Rev. D 66 (2002) 043503.

[20] R. Bernabei et al., Il Nuovo Cim. A 112 (1999) 545.

[21] R. Bernabei et al., Eur. Phys. J. C18 (2000) 283.

[22] R. Bernabei el al., La Rivista del Nuovo Cimento 26 n.1 (2003) 1-73.

[23] R. Bernabei et al., Int. J. Mod. Phys. D 13 (2004) 2127.

[24] R. Bernabei et al., Int. J. Mod. Phys. A 21 (2006) 1445.

[25] R. Bernabei et al., Eur. Phys. J. C 47 (2006) 263.

[26] R. Bernabei et al., Int. J. Mod. Phys. A 22 (2007) 3155.

[27] R. Bernabei et al., Eur. Phys. J. C 53 (2008) 205.

[28] R. Bernabei et al., Phys. Rev. D 77 (2008) 023506.

[29] R. Bernabei et al., Mod. Phys. Lett. A 23 (2008) 2125.

[30] R. Bernabei et al., Phys. Lett. B408 (1997) 439; P. Belli et al., Phys. Lett. B460 (1999) 236; R. Bernabei et al., Phys. Rev. Lett. 83 (1999) 4918; P. Belli et al., Phys. Rev. C60 (1999) 065501; R. Bernabei et al., Il Nuovo Cimento A112 (1999) 1541; R. Bernabei et al., Phys. Lett. B 515 (2001) 6; F. Cappella et al., Eur. Phys. J.-direct C14 (2002) 1; R. Bernabei et al., Eur. Phys. J. A 23 (2005) 7; R. Bernabei et al., Eur. Phys. J. A 24 (2005) 51; R. Bernabei et al., Astrop. Phys. 4 (1995) 45.

[31] K.A. Drukier et al., Phys. Rev. D 33 (1986) 3495.

[32] K. Freese et al., Phys. Rev. D 37 (1988) 3388.

[33] D. Smith, N. Weiner, Phys. Rev. D 64 (2001) 043502.

[34] D. Tucker-Smith, N. Weiner, Phys. Rev. D 72 (2005) 063509.

[35] D.P. Finkbeiner et al., Phys. Rev. D 80 (2009) 115008.

[36] K. Freese et al., Phys. Rev. D 71 (2005) 043516.

[37] K. Freese et al., Phys. Rev. Lett. 92 (2004) 111301.

[38] R. Bernabei, A. Incicchitti, Int. J. Mod. Phys. A 32 (2017) 1743007.

[39] P. Gondolo et al., New Astron. Rev. 49 (2005) 193-197.

[40] G. Gelmini, P. Gondolo, Phys. Rev. D 64 (2001) 023504.

[41] F.S. Ling, P. Sikivie, S. Wick, Phys. Rev. D 70 (2004) 123503.

[42] R. Bernabei et al., Astropart. Phys. 7 (1997) 73; R. Bernabei et al., Il Nuovo Cim. A 110 (1997) 189; P. Belli et al., Astropart. Phys. 10 (1999) 115; P. Belli et al., Nucl. Phys. B 563 (1999) 97; R. Bernabei et al., Nucl. Phys. A 705 (2002) 29; P. Belli et al., Nucl. Instr. and Meth. A 498 (2003) 352; R. Cerulli et al., Nucl. Instr. and Meth. A 525 (2004) 535; R. Bernabei et al., Nucl. Instr. and Meth. A 555 (2005) 270; R. Bernabei et al., Ukr. J. Phys. 51 (2006) 1037; P. Belli et al., Nucl. Phys. A 789 (2007) 15; P. Belli et al., Phys. Rev. C 76 (2007) 064603; P. Belli et al., Eur. Phys. J. A 36 (2008) 167; P. Belli et al., J. Phys. G 38 (2011) 015103; D. Poda et al., Radiation Measurements 56 (2013) 66.

[43] P. Belli et al., Nucl. Instr. and Meth. A 615 (2010) 301.

[44] P. Belli et al., Nucl. Phys. A 826 (2009) 256; P. Belli et al., Phys. Lett. B 658 (2008) 193.

[45] P. Belli et al., Nucl. Instr. and Meth. A 626-627 (2011) 31.

[46] P. Belli et al., J. Phys. G: Nucl. Part. Phys. 38 (2011) 115107.

[47] A.S. Barabash et al., JINST. 6 (2011) P08011.

[48] P. Belli et al., Phys. Rev. C 85 (2012) 044610.

[49] P. Belli et al., Nucl. Instr. and Meth. A 670 (2012) 10.

[50] F. Cappella et al., Eur. Phys. J. C 73 (2013) 2276.

[51] P. Belli et al., Eur. Phys. J. A 50 (2014) 134.

[52] P. Belli et al., Phys. Scripta 90 (2015) 085301.

[53] A.S. Barabash et al., Nucl. Instr. and Meth. A 833 (2016) 77.

[54] P. Belli et al., Phys. Rev. C 93 (2016) 045502.

[55] R. Cerulli, Int. J. Mod. Phys. A 32 (2017) 1743009.

[56] H. Ejiri et al., J. Phys. Soc. Japan 64 (1995) 339.

[57] F.A. Danevich et al., Phys. Lett. B 344 (1995) 72.

[58] F.A. Danevich et al., Phys. Rev. C 62 (2000) 045501.

[59] F.A. Danevich et al., Phys. Rev. C 68 (2003) 035501.

[60] R. Arnold et al., Z. Phys. C 72 (1996) 239.

[61] R. Arnold et al., Phys. Rev. D 95 (2017) 012007.

[62] A.S. Barabash, Phys. Rev. C 81 (2010) 035501.

[63] N.J. Cherepy et al., Applied Physics Letters 92 (2008) 083508.

[64] P. Belli et al., Nucl. Instr. and Meth. A 572 (2007) 734; P. Belli et al., Nucl. Phys. A 806 (2008) 388; P. Belli et al., Nucl. Phys. A 824 (2009) 101; O.P. Barinova et al., Nucl. Instr. and Meth. A 607 (2009) 573; P. Belli et al., Eur. Phys. J. A 42 (2009) 171; P. Belli et al., Nucl. Phys. A 846 (2010) 143; P. Belli et al., Nucl. Phys. At. Energy 11 (2010) 362; P. Belli et al., Nucl. Phys. A 859 (2011) 126; P. Belli et al., Phys. Rev. C 83 (2011) 034603; P. Belli et al., Eur. Phys. J. A 47 (2011) 91; P. Belli et al., Phys. Lett. B 711 (2012) 41; P. Belli et al., Nucl. Instr. and Meth. A 704 (2013) 40; P. Belli et al., Phys. Rev. C 87 (2013) 034607; S. Das et al., Nucl. Instr. and Meth. A 797 (2015) 130.

[65] P. Belli et al., Eur. Phys. J. A 49 (2013) 24.

[66] P. Belli et al., Nucl. Phys. A 930 (2014) 195.

[67] O.G. Polischuk et al., AIP Conf. Proc. 1549 (2013) 124.

[68] P. Belli et al., Eur. Phys. J. A 53 (2017) 172.

DarkSide

Liquid Argon Search for Dark Matter

(The DarkSide Collaboration),
(Spokesperson: Cristiano Galbiati)

Abstract

The DarkSide-50 (DS-50) S2-only nuclear-recoil search for low-mass WIMP dark matter remains the world's most sensitive limit for WIMP masses in the range $1.8\,\mathrm{GeV}/c^2$ to $6.0\,\mathrm{GeV}/c^2$. The DarkSide collaboration has made many large strides during the last year. The DarkSide-20k (DS-20k) detector has undergone a significant redesign during the last year. DS-20k consists now of two detectors: the inner detector and the veto detector, both hosted in a ProtoDUNE-like cryostat. The decision to abandon an organic liquid scintillator veto and to host DS-20k within a ProtoDUNE-like cryostat was originally motivated by the need of minimizing the environmental impact on underground LNGS operations, but carries significant performance advantages. The DarkSide Photo-Electronic group successfully built the first Photo-Detector Module (PDM) made by 24 SiPMs. After the electrical and mechanical tests of the first PDM at $77\,\mathrm{K}$ the group moved forward to complete the next milestone of the construction and test of the first Motherboard (MB) composed of 25 PDMs arranged.

1 DarkSide-50 Results and Status

The DarkSide-50 (DS-50) S2-only nuclear-recoil search for low-mass WIMP dark matter is now published in Physical Review Letters [Agnes et al.(2018a)] and was chosen as an "Editors Suggestion." It remains the world's most sensitive limit for WIMP masses in the range $1.8\,\mathrm{GeV}/c^2$ to $6.0\,\mathrm{GeV}/c^2$. The low-mass dark matter-electron recoil paper has also been published in Physical Review Letters [Agnes et al.(2018b)]. It remains the most sensitive limit for the range of dark matter masses from $30\,\mathrm{MeV}/c^2$ to $50\,\mathrm{MeV}/c^2$ when scattering from electrons via a "heavy mediator." The high-mass WIMP search using the blind analysis of 532.4 live-days of data has been published in Physical Review D [Agnes et al.(2018c)]. It was surpassed as the most sensitive WIMP limit in argon for masses above $70\,\mathrm{GeV}/c^2$ in February of 2019 by DEAP-3600 [Ajaj et al.(2019)].

DS-50 operations continue, but funds for maintenance of the experiment, which has been in continuous operation for five years, are limited. The experiment suffered some damage to auxiliary systems during the February 2018 blackout of LNGS and is operating using borrowed spares. The blackout also resulted in what appears to be (chemical) contamination of the circulating argon. The nature of the contamination is not yet understood. However, a campaign of increased recirculation speed is underway to try to mitigate this, and improvements have been noted. DS-50 operations continue, primarily to diagnose problems that occurred during the February 2018 blackout. The experiment is functional, but the data quality is marginal due to the contamination. While the impact of this contamination has been mitigated with continued purification, the rate of improvement is extremely slow, and, after more than a year, the data are still not of physics quality.
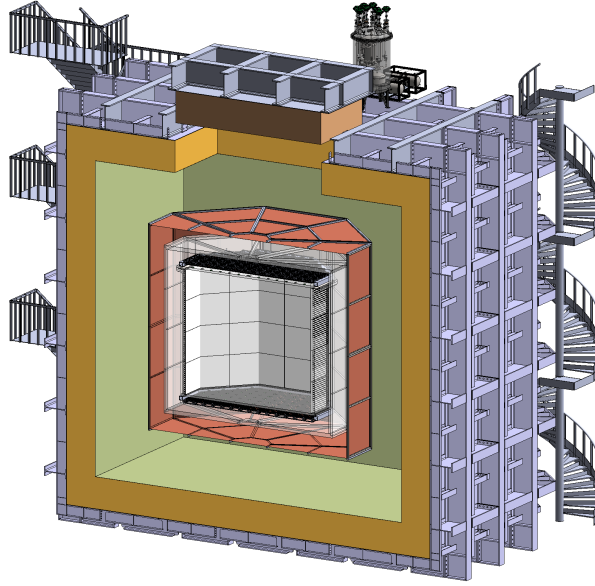
Figure 1: 3D schematic of the DS-20k experiment. The drawing shows the PPMA TPC filled with UAr, surrounded by the VETO detector made of Gd-loaded PMMA shell sandwiched between two AAr active layers (the inner one, named IAB and the outer one, named OAB in the text), all contained in the ProtoDUNE-like cryostat. The OAB is optically separated by the AAr in contact with the cryostat wall.

Currently, the limited resources and manpower available to the project are focused on the commissioning of a system that would allow permanent, safe storage of the full inventory of underground argon (UAr)currently deployed in DS-50.

2   DarkSide-20k Overview

DarkSide-20k (DS-20k) will be located in Hall C at LNGS. It consists of two detectors: the inner detector and the veto detector, both hosted in a ProtoDUNE-like cryostat [Abi et al.(2017), Acciarri et al.(2016)]. The inner detector is a Liquid Argon Time Projection Chamber (LAr TPC) filled with UAr. The veto detector is made of a plastic shell, loaded with Gd, surrounding the inner detector, sandwiched between two active atmospheric argon (AAr) layers. Fig. 1 shows a 3D schematic, with the inner detector placed at the middle position of the veto detector.

The decision to abandon an organic liquid scintillator veto and to host DS-20k within a ProtoDUNE-like cryostat was originally motivated by the need of minimizing the environmental impact on underground LNGS operations, but carries significant performance advantages. Indeed, operating the TPC directly in the ProtoDUNE-like cryostat eliminate the need for a stainless steel (SS) cryostat immediately surrounding the TPC, the leading contribution to the residual background. We are therefore studying a new design for the TPC, in which the fully sealed vessel is built from the same ultra-pure poly(methyl methacrylate) (PMMA) developed for the DEAP-3600 experiment, and filled with UAr. This UAr-filled vessel would be immersed in the bath of liquefied AAr held at the same temperature and pressure. This eliminates the need for a dedicated cryostat as the UAr containment vessel. The outer walls of the TPC will sit approximately 2 m away from inner wall of the much larger ProtoDUNE-like cryostat. This large AAr-filled cryostat will be surrounded by layers of plastic for moderation of cosmogenic and radiogenic neutrons from the rocks surrounding Hall C.

3 The DarkSide-20k Liquid Argon Time Projection Chamber

The conceptual design of DS-20k is finalized: the inner detector is a dual-phase argon time projection chamber (LAr TPC) contained within an ultra-pure acrylic (PMMA) vessel. Thanks to the extensive experience of the DEAP-3600 collaboration with acrylic, an acrylic sealed vessel both reduces the complexity of the TPC assembly, and eliminates the need for some of the most problematic radiogenic neutron contributors that were used in DS-50 (in particular the stainless steel cryostat and PTFE reflector). The target has a total mass of 49.7 t of low-radioactivity argon from an underground source (UAr). The active volume of the TPC is defined by eight vertical reflector panels and the top and bottom windows of the acrylic vessel. The height of the TPC is 350 cm. The body of the acrylic vessel is fused together by 5 cm thick acrylic plates, and then flanged and sealed with the 5 cm thick top and bottom lids. These lids also serve as the anode and cathode plates of the TPC, respectively. 8280 SiPM-based PhotoDetector Modules (PDM) arrays view the argon volume through these windows. The geometrical design of the TPC is determined by the use of SiPM tiles with square and triangular shapes. Based on these two options, an octagon best fits the coverage achievable wth the PDMs while optimizing the fiducial mass.

To maximize the light collection efficiency, Enhanced Specular Reflector (ESR) foils are used as the TPC reflector. They substitute conventional PTFE, which would be the predominant source of neutron and Cherenkov background by its enormous mass required in DS-20k. ESR is a thin layer foil which has reflectivity of up to 98 % for 420 nm light. Work is on-going to study how to hold the ESR foil in place while maintaining its flatness during the operations.

All the TPC surfaces in contact with the active argon volume are coated with wavelength shifter tetraphenylbutadiene (TPB) to convert LAr scintillation light to a wavelength detectable by SiPMs.

Instead of the traditional low background copper field cage shaping rings and Indium-Tin-Oxide (ITO) cathode and anode, DS-20k uses a conductive transparent polymer, poly(3,4-ethylenedioxythiophene) polystyrene sulfonate (also known as PEDOT:PSS and commercialized under the name Clevios^{TM}). Work is on-going to study both the polymer's properties and characteristics at low temperature, and how to coat large surfaces with it.

The conceptual design of DS-20k is being verified with a staged effort. First a small, $\sim$10 kg, prototype DarkSide-ProtoZero (DS-ProtoZero) will be used, and later a $\sim$1 t scale one, DarkSide-Proto (DS-Proto). The small prototype is housed at CERN and uses an existing cryogenics system. Its fabrication and construction is nearly complete and operations at CERN are foreseen during summer of 2019. DS-ProtoZero will test the first 50 PDMs produced by the collaboration and will study the effect of the TPC geometry on the S2 signal generation and detection. The DS-Proto detector will be equipped with 400 PDMs and will be a scaled-down version of the DS-20k LAr TPC, serving as its proof of principle prototype.

4 Cryogenics

The features of the DS-50 cryogenics system are fully implemented into the DS-20k system, not only by simply scaling up the argon volume, but also upgrades based on experience and lessons learned. A major improvement is to increase the circulation speed to the required 1000 std L/min, to initially reach the purity requirement of LAr in a couple of turn-over times of 20 d. Another major improvement is to increase the cooling power needed to accommodate such a large circulation speed. A full-size prototype LAr condenser, the core component in the cryogenics system, has been built and tested at UCLA, and a cooling power of 2.2 kW (latent
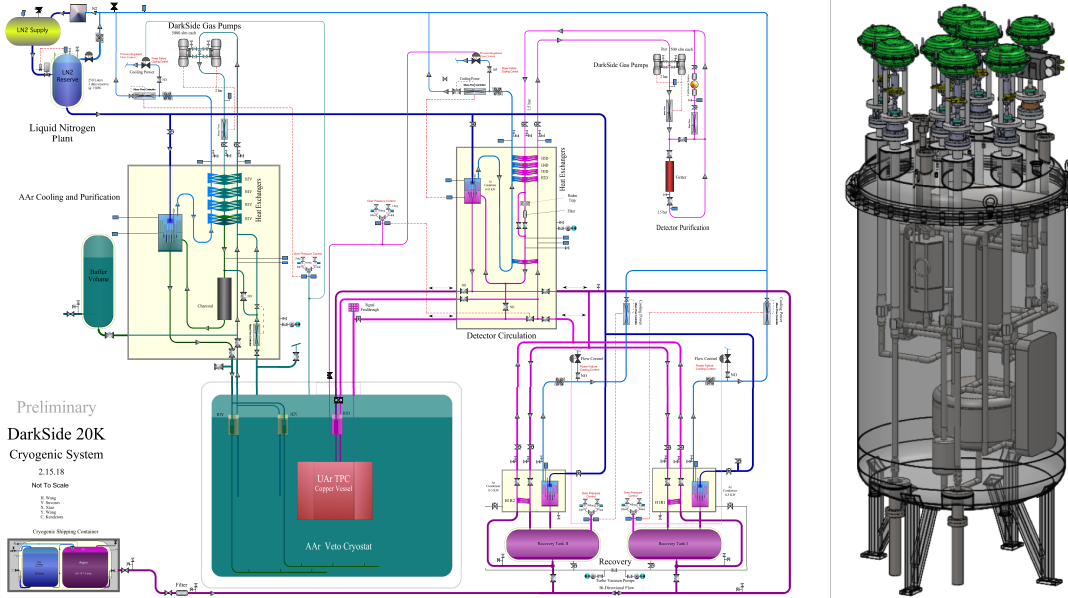
Figure 2: DS-20k full cryogenics P&ID (left), condenser box (right). Features liquid phase or gas phase storage; system automatically act in passive cooling mode during total loss of electric power; high efficiency heat recovery design to minimize operation cost; integrated internal source delivery system; inline radon filtration system, fails safe circulation pump for continuous argon purification; and UAr fill and recovery mode.

heat only) has been achieved, nearly twice that needed for the DS-20k UAr cooling requirement. The main components of the UAr cryogenics system condenser box have already arrived at CERN and are ready for welding and the first test to follow in summer of 2019.

The UAr cryogenics system is made up of several sub-systems (while the AAr system will be similar except at larger scale in volume and power, but with lower requirements on purity): the liquid argon handling system, the liquid nitrogen reserve system, the purification system, the cold box, the gas circulation pump, the recovery and storage system, the integrated heat exchanger system, and heat exchangers close to the TPC. The overall schematic is shown in Fig. 2, including the AAr cryogenics system for the veto detector, which employs the same principle. Two cryogenics systems share the same liquid nitrogen reserve loop, but have separate argon loops of either UAr or AAr. Also shown in the figure is the condenser box integrated with the heat exchangers and inline radon trap.

The integration and tests of the full scale UAr cryogenics system at CERN is ongoing. The first pass FEA engineering has proven the design load is as anticipated and fabrication is officially approved. All condenser box components, large pneumatic cryogenics valves and associated auxiliary components are on site at CERN for integration. The full scale cryogenics test of the DS-20k UAr system will be performed during the summer of 2019.

5 Veto Detector

The veto detector of DS-20k is composed by three separated volumes:

- an inner volume of instrumented liquid AAr (called the Inner argon Buffer, IAB) immediately surrounding the TPC vessel;
- a passive octagonal shell of acrylic (PMMA) loaded with Gd (called the GdA) mounted around the IAB and surrounding the TPC in all directions (lateral, top and bottom with

exceptions due to the service holes);

- an outer instrumented volume of liquid AAr (call the Outer Argon Buffer, OAB) immediately surrounding the GdA.

A copper cage (called the Faraday cage) provides the optical insulation from the rest of the AAr external to OAB and, at the same time, provides the necessary electric isolation from external noise.

We have performed a series of Monte Carlo simulation studies establishing that the required thickness of both the IAB and OAB is 40 cm, with no performance penalty for a thickness increase. The required thickness of the GdA is 10 cm. The mass fraction of Gd in the acrylic should be between 1 to 2 %.

The TPC and GdA are polyhedrons with octagonal cross section. The apothem of the inner face of GdA octagon is 225 cm and the internal height of the GdA is 400 cm. Assuming a density of $1.18 \, \text{g/cm}^3$, the mass of the GdA is 11.7 t. Neutrons are moderated by collisions (mostly with hydrogen) in the acrylic. The presence of Gd ensures the emission of multiple high energy γ-rays after the neutron capture. With a Gd concentration between 1 to 2 % by weight, the capture of neutrons on Gd happens with about 54 % probability and in argon 24 % of the time. The remaining neutrons are caught in hydrogen and copper with 16 % and 8 % probability, respectively. Because the GdA acts as a neutron moderator and capture agent only, there are no strict requirements about its transparency to the scintillation light. γ-rays following the neutron capture interact in the IAB and OAB producing scintillation light that is detected by light sensors mounted on the two opposite faces of the GdA walls and viewing both the IAB and OAB.

The IAB and OAB are segmented into vertical sectors using thin acrylic panels. The segmentation has the purpose of reducing the pile-up event rate due to the decay of ^{39}Ar and to obtain a sufficiently high photoelectron yield. The precise number of sectors is going to be optimized, but for reference we assume to have 5 sectors along each edge of the octagon, both in the IAB and in the OAB volumes.

A sandwich of materials will be made of 3M foil reflector attached to a thin acrylic sheet, and then TPB coated on the face opposite to the one with attached to the 3M foil. Two of such sandwiches will be coupled together and attached to the copper cage and to the external wall of the TPC to make up the sectors. Sectors are not made to be liquid tight and the proper argon flow will be ensured both during filling and recirculation.

The argon light is shifted by the TPB and then detected by SiPM tiles (2000 in the IAB and half as many in the OAB) with the same size as the ones developed for the TPC. Monte Carlo simulations show that the expected light yield is about 2 PE/keV.

The same company that will produce the acrylic panels is available to make small scale laboratory tests to mix a proper Gd compound with the acrylic and then produce the necessary amount for DS-20k. As we do not require the doped plastic to be transparent, several difficulties faced with metal loading of organic materials to make scintillators are mitigated. However the selection of the proper Gd compound requires some R&D work that has already started. Assays of the acrylic produced by this company performed by another collaboration shows that the the U and Th contamination should be acceptable for the veto (at the ppt level). Additional assays will be performed by DS-20k for both the Gd compounds and the final doped acrylic.

6 PhotoElectroncs

On March 2018 the DarkSide Photo-Electronic group successfully built the first Photo-Detector Module (PDM) made by 24 SiPMs arranged in a 4×6 matrix providing a sensitive area of
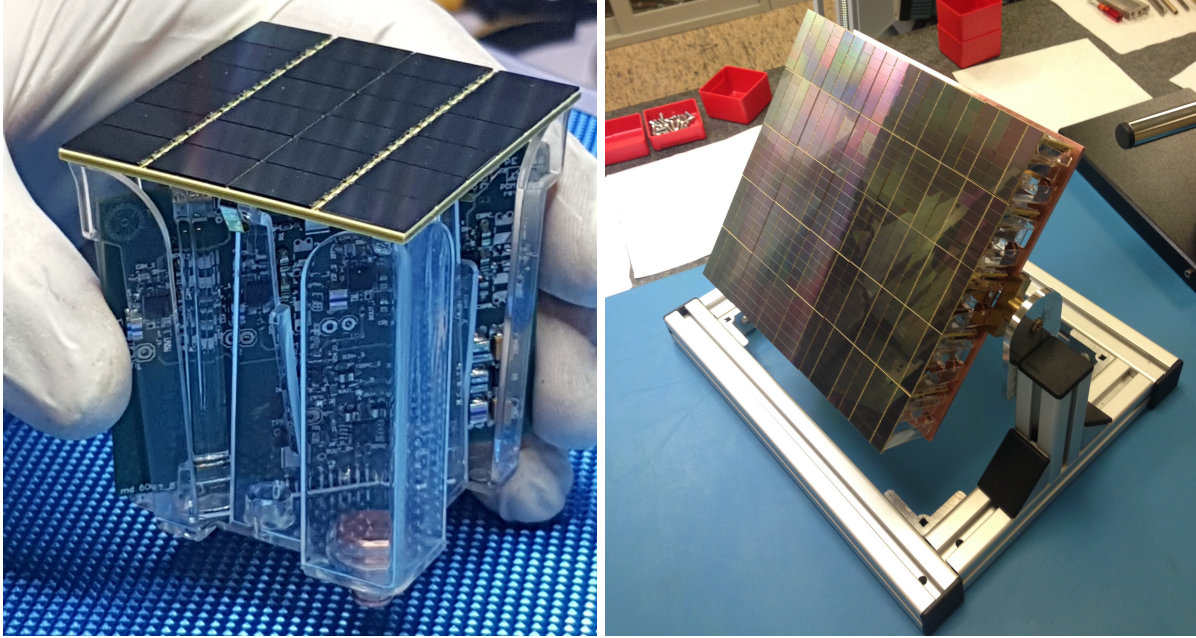
Figure 3: **Left:** The first PDM consisting of 24 SiPMs together with the front-end electronic board. **Right:** The first MB assembled with 25 PDMs.

around $50 \times 50\,\mathrm{mm}^2$ (left panel of Fig. 3). After the electrical and mechanical tests of the first PDM at $77\,\mathrm{K}$ the group moved forward to complete the next milestone of the construction and test of the first Motherboard (MB) composed of 25 PDMs arranged in a 5×5 array (right panel of Fig. 3).

The SiPMs for the first MB were produced by the Fondazione Bruno Kessler (FBK). FBK delivered two batches of SiPMs from two different runs: the first one provided standard doping SiPMs (cell size $25 \times 25\,\mathrm{\mu m}^2$ and quenching resistor $10\,\mathrm{M\Omega}$ at $77\,\mathrm{K}$), the second one triple doping SiPMs (cell size $30 \times 30\,\mathrm{\mu m}^2$ and quenching resistor $5\,\mathrm{M\Omega}$ at $77\,\mathrm{K}$). The SiPMs from the second run are the best candidate for DS-20k since they provide a lower after pulse probability and a wider over-voltage operating range with respect to the devices from the first run.

The runs were characterized by a reasonable yield. About $50\,\%$ of the devices met the requirements on the break down voltage and on quenching resistor (R_q) value at $-40\,^\circ\mathrm{C}$. The measurements on R_q showed good uniformity for most of the wafers, with the exception of the first and of the second wafers (W1,W2) whose SiPMs had a $20\,\%$ larger R_q.

The Photo-Electronic group decided to assemble the very first MB using the single-doping SiPMs from this first run to gain experience on the mounting procedures and to refine the quality control and quality assurance protocol. The good SiPMs selected with the tests at room temperature and at $-40\,^\circ\mathrm{C}$ were mounted on an Arlon 55-NT substrate using conductive cryogenic epoxy to provide the electrical connection to the back of the SiPM while a wire-bonding was used to connect the front side. The Arlon substrate holds 24 SiPMs on the front side. On the back side there are the connectors to the bias voltage and to the front end electronic board (FEB) and a bias network.

A set of 27 tiles have been produced and tested to date. The process required a sizable joint effort of several institutions. The SiPMs were shipped from FBK to the Princeton University, where the tiles were mounted and bonded by personnel from LNGS, Princeton University and TIFPA using a set of multi purpose chucks designed and produced by the Pisa group. The 27 tiles were finally shipped to LNGS using the same multipurpose chucks used during the construction

114

steps as a shelter for the wire bondings and for the SiPMs exposed sensitive surface. Once in LNGS, all the tiles underwent a comprehensive test at room temperature and then in liquid nitrogen. The test includes the measurement of the I-V characteristic curve, the measurement of the noise power spectrum and the measurement of the charge spectra. Just two tiles out of the 27 produced showed any signs of problems. One had two SiPM branches (4 SiPMs total) not working properly and the second showed a noise level higher than average. The overall behavior of the remaining 25 tiles was quite homogeneous. The signal to noise ratio (SNR) consistently exceeded the DS-20k specification (SNR greater than 8).

The FEB substrate is made from the same Arlon 55-NT used for the tile. The electronic components on the FEB were mounted with outsourced equipment, under the supervision of LNGS personnel. The FEBs were fully characterized in LNGS. Power consumption, noise spectral density and frequency response were measured both at room temperature and in LN. After these tests the tiles and the FEBs were finally shipped to Pisa where a full re-characterization at room-temperature was performed following the quality control protocol agreed among the Photo-Electronic group.

Before assembling the first MB, a full mock-up made by an aluminum structure, an MB strip PCB made in FR4 and 25 dummy PDMs was mounted at Bologna. The 25 PDMs were assembled in the Pisa clean room by mating the tile, the FEB, the acrylic components designed in Pisa to hold together the PDM, and the copper components designed in Bologna to hold the PDM on the MB. The copper of the PDMs and of the MB were milled at Bologna, using a pure copper (99.997 %) sold by the Luvata company. The power supply to the FEBs, the bias voltage to the tile and the signal from the PDMs are routed on the back side of the MB on PCB finger strips (FS) connecting the PDMs. The FS made of a thin stack-up (0.5 mm) based on a Pyralux substrate was designed and realized in Bologna.

The mounting of the 25 PDMs on the MB started the third week of September 2018 and was finalized within a few days. Finally the first MB was moved from Pisa to LNGS for the first test in LN. The mechanical structure was working flawlessly. The I-V curves of the 25 PDMs in LN have been measured. One out of the 25 PDMs exhibited an abnormal IV-curve during this test. An optical inspection revealed three broken wire bondings out of 600, likely caused by the violent action of the boiling nitrogen flow on the tile surface.

In summary the construction of the first Motherboard required the production, testing and selection, and to bond more than 600 SiPMs. Although a cryogenic probe and an automatic bonder were not available yet, the collaboration was able to increase the number of successfully built PDMs from 1 to 25 just in 6 months. After the completion of the first MB the collaboration moved forward to produce the second MB equipped with the triple dose SiPMs. At the moment, 30 tiles have been mounted and wire bonded. More than 25 have been successfully tested in liquid nitrogen and 13 PDMs are already mounted on the second MB with full completion expected at the end of June 2019.

The prototype boards of the opto-link system (optical driver and optical receiver board) have been just produced. The optical receiver board (32 channels) was successfully tested, while the optical driver board (25 channels) is currently under test. The next step in the photo-electronics schedule is the production of about 400 PDMs for DS-ProtoThese SiPMs will be produced by the LFoundry company, Avezzano (AQ), Italy, with the first run expected by the end of July 2019. A first engineering run, finalized in September 2018 and tested shortly after, showed the capability of the silicon foundry to implement the FBK technology as the SiPMs from LFoundy showed good performance both at room temperature and in liquid nitrogen.

The production of the 400 PDMs for DS-Proto will be shared among several laboratories. The tiles will be assembled both in Princeton University and LNGS while the PDMs and the

MBs will be produced in three clean rooms hosted by the INFN sections of Pisa, Bologna and Genova.

7   DAQ and readout

The DAQ and trigger system design for DS-20k has been consolidated taking into account the advancement of the design of the Veto detector. The main novel electronic device around which the readout architecture is built, is a new fast ADC developed for advanced digital signal processing, and is close to completion. A few prototypes from the CAEN company in Viareggio, Italy, will be available for testing in summer of 2019, while work in close cooperation between the collaboration and CAEN firmware experts is ongoing to implement the needed DSP algorithms. In parallel, a DAQ system for the first phase of the DS-Proto run is to be deployed in the next weeks at CERN and will be able to acquire data from the first test of the small systems equipped with up to two motherboards and 50 channels.

8   Materials assay

During 2018, the requirements for the amount of radiopurity measurements for DS-20k increased significantly. The intensive campaign has the goal of screening all the materials that will go in the detector, paying special attention to the breaking of the secular equilibrium that has been widely observed in the U-238 decay chain. The breaking of secular equilibrium is monitored performing assays that are sensitive to different section of the decay chain, i.e., ICP-Mass spectrometry, HPGe gamma counting, and alpha counting after Po-210 chemical extraction. The measurement responsibilities will be distributed mainly to LNGS, Lab. Sub. Canfranc, Jagiellonian U. (Krakow) and will utilize the collaboration of other facilities. More than thirty assays have been carried out during last year, most of them devoted to the selection of components for the electronics of the PDMs. The large variety of pieces needed and the large amount of each of them that will be required for DS-20k (around 8300 PDMs), makes this task critical in the short term.

It has been paramount to identify and reject potential sources of background which introduced backgrounds in the order of the Bq/kg, such as:

- Alumino borosilicate for the construction of the SiPMs (both U and Th contamination);
- Specific CCL production process that introduces lead content;
- Different sets of resistors and capacitors (large Po content);
- Arlon polymers for the production of PCBs (large contamination in the middle U chain);
- Solder pastes (large Po content and some contamination throughout the whole U and Th chains).

On the other hand, some materials have already been selected thanks to the assays carried out to date. The ones that have introduced the most significant improvements with respect to the former choices are: PCB substrate, chips (amplifiers), conductive polymer (replacing large amounts of copper and the anode/cathode conducting surfaces), and solder paste. The radioactive budget of the experiment is regularly updated and as of today, the requirement of <0.1 events neutrons in the full $100\,\mathrm{t\,yr}$ exposure is fulfilled.

Special effort was made to have the results of all the assays available for the collaboration, largely through the creation of a database where the location and status of ongoing assays, plus the results of the finished ones can be documented and checked.

Besides the measurements of bulk contamination, a campaign to characterize and select the official cleaning procedures for large surfaces of copper and acrylic has started, and is lead by the INFN-Legnaro group.

The collaboration has the timescale requirements of several large tenders that will be launched in the near future, which will increase the work load of the materials working group as it is foreseen that an increase in the number of assays requested to the facilities will happen.

9 Calibration

While the goals for the calibration of DS-20k have not changed, the actual implementation is being revisited due to changes in the overall design and which the calibration system need to interfaces to. In addition to radioactive sources such as those used in DS-50, the collaboration has been investigating alternative ways of injecting low energy neutrons for low energy nuclear recoil calibration. A recently investigated method that will be used in the DUNE experiment that of the 57 keV neutron scattering resonance in argon, which makes argon nearly transparent to 57 keV neutrons. This feature will allow for the injection of neutrons deep into the Veto while still making their way to the TPC for the nuclear recoil calibration with low energy neutrons. 57 keV neutrons are produced via moderation of 2.45 MeV neutrons from a DD generator. In parallel, plans are being developed for the calibration needs of the DS-20k prototype detectors for x-y positioning, light yield and nuclear recoil calibration.

10 Science and Simulation

The DS-20k Monte Carlo simulation code is in an advanced status. The Geant4-based package (g4ds) is currently completed, and undergoes frequent updates following the changes of the detector design. Recently, we have also implemented a preliminary version of the electronics simulation, which has allowed the development of the event reconstruction code. Data from ReD and other calibration experiments are used to test reconstruction. Simulations are widely employed for different aspects of the experiment (e.g. background budget, optical response, neutron veto optimization) taking advantage of the highly-developed package.

We are very active in the determination of the sensitivity of DS-20k and Argo to Supernova neutrinos exploiting the flavor insensitive coherent scattering channel. Such detection has a unique potential in providing information on total energy emitted by the supernova neutrinos when compared with results from large scale detectors like DUNE, Super-Kamiokande, and JUNO, which are mostly sensitive to electron neutrinos. At the same time, we are still investigating the potential in extending the low-mass WIMP limit with different configurations of the DS-20k prototype and vetoes.

11 Argon Procurement and Purification

A broad strategy has been developed to increase the production of UAr to procure the target required for DarkSide-20k. The Urania project will extract and purify the UAr from the CO_2 wells at the Kinder Morgan Doe Canyon Facility located in Cortez, CO, at a production rate of 250 kg/d. It will be necessary to make a final chemical purification of the UAr before deployment into the LAr TPC (driven by the filtration capacity of the getter purification unit). The Aria project will accomplish this using a cryogenic distillation column called Seruci-I. Additionally, it would be beneficial to further deplete the UAr of ^{39}Ar, giving extended sensitivity

to DarkSide-20k and producing argon with a level of ^{39}Ar that is acceptable to be used in an experiment such as the envisaged DarkSide-LowMass, i.e. to achieve an additional depletion factor between 10 and 100 (on top of the reduction of ^{39}Ar already seen in the UAr).

11.1 Urania

The Urania project will extract at least 60 t of low-radioactivity UAr, providing the required 51.1 t of UAr to fill DarkSide-20k. The Urania project will also lay the groundwork for UAr procurement for future, larger argon-based detectors such as Argo. The goal of the Urania project is to build a plant capable of extracting and purifying UAr at a rate of 250 kg/d, from the same source of UAr that was used for the DarkSide-50 detector.

The Urania feed gas stream is $\sim$95 % CO_2, plus a few percent of N_2, one percent CH_4, 430 ppm of UAr, and traces of higher hydrocarbons. The processing scheme of the UAr extraction plant is optimized for this feed composition in order to achieve an UAr purity of better than 99.9 %. A modular plant consisting of skid-mounted units deployable on concrete platforms is being designed to carry out the processing.

The tender for the construction of the argon extraction plant has been opened and the winner will be selected and contract executed by the end of October, 2019. The plant will be delivered to the Kinder Morgan Doe Canyon Facility by the end of the first quarter of the 2021 calendar year. The current plan is to install and commission the plant during the 2021 calendar year, allowing for extraction of the 60 t of UAr by the middle of the 2022 calendar year, in order to meet the DarkSide-20k schedule. The preparation of the extraction site is being planned now and will be managed by the collaboration with help from the Kinder Morgan CO2 Company and the companies contracted to carry out the major works. A second option for shipping the UAr is now being investigated as an alternative to the baseline option of using cryogenic vessels. It is to ship the UAr in high-pressure gas cylinder placed in trailers which can be hauled by trucks. This option is made possible by special cylinders which allow for the storage of argon at pressures up to 400 bar. With pressures of this magnitude, and cylinders that are able to be the size of large trailers, the number of trailers that would be required for the total DS-20k detector target is something that is manageable, on the order of 10 to 20 depending on the storage pressure. The overall benefit of moving to this option, instead of going with the cryogenic vessel option, is that the gas can be maintained in the cylinders for years without the need of any type of consumable to prevent the loss of the argon. This would basically eliminate the risk of losing any of the UAr during the transport and storage, other than potential loss of the shipment. The Urania project team is now collecting all of the information that is required to make the technical and economic assessment of the two shipping options. Based on the technical risks and the economic impact on the project, the option that is best for the overall project will be chosen.

11.2 Aria

Aria consists of a 350 m tall distillation column, Seruci-I, capable of separating isotopes with cryogenic distillation, a process that exploits the tiny difference in volatility due to the difference in isotopic mass. The design of the plant started in April 2015 with seed funding from the US NSF through PHY-1314507. Aria is to be installed in an underground vertical shaft of 5 m diameter and 350 m depth, located at the Seruci mine campus of CarboSulcis, a mining company owned by the Regione Autonoma della Sardegna (RAS). In February 2015 a proposal was submitted to the Italian INFN and RAS, and the funding for the Seruci-I column was approved on July 24, 2015. Construction of Seruci-I modules started in September 2015 in an Italian company.
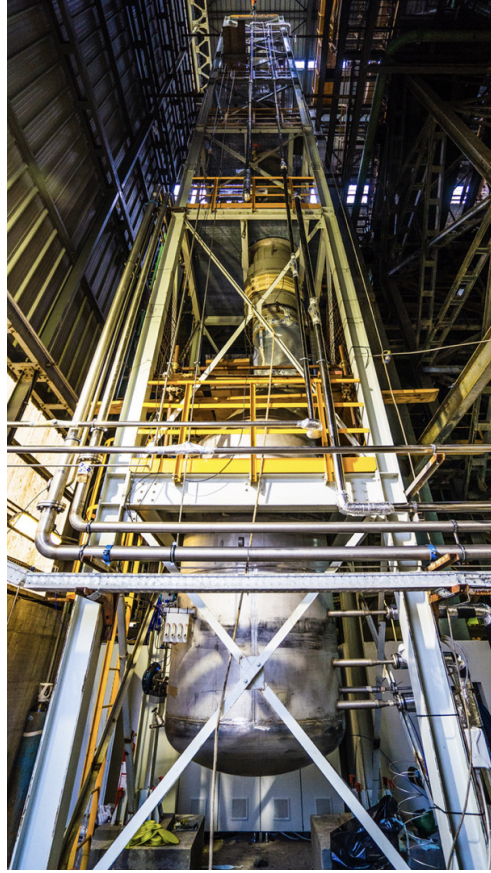
Figure 4: The Seruci-0 cryogenic distillation column, installed in the *Laveria* building of CarboSulcis in Nuraxi Figus, Sardinia, Italy.

Seruci-I will consist of 28 modules of 12 m height, plus a top module (condenser) and a bottom module (reboiler). Calculations indicate that Seruci-I will be able to process UAr at a rate of $O(1\,t/d)$ removing all chemical impurities (including traces of N_2, O_2, and Kr) with a separation power better than 10^3 per pass.

All modules for Seruci-I have already been built and passed a series of quality assurance checks and are now stocked at CarboSulcis. Seruci-0 is a test column that is made with the Seruci-I top and bottom modules and a single central module. The goal of Seruci-0 is to confirm the proper operation of the three main components of the Seruci-I column, as well as to gain experience in operating the column on a smaller scale and to put in place the standard operating procedures. The three modules have been completely installed in an outdoor assembly hall at Nuraxi Figus, Italy, seen in Figure 4. Aria team is currently involved with the commissioning of the single auxiliary devices and with the pressure test for the PED cerfication. After the end of these activities, the commissioning of entire plant will start.

In April, the Aria Project obtained the authorization by SUAPE of Gonnesa for the installation of Seruci-I. In the meantime #2 batches, for a total of 42 platforms (half of the supply) has been delivered to CarboSulcis. Moreover, an accurate check (at millimeter) is currently on going in order to verify the joint of the modules with the plaftorms into the length of the shaft. In July is foreseen the beginning of the installation of the platforms into the shaft.

11.3 DArT

The DArT experiment will re-use the ArDM infrastructure with minimal modifications made and will consists of a radio-pure single-phase LAr detector with about one liter contained inside of its active volume. The DArT detector itself will be placed inside the middle of the ArDM vessel. DArT will be filled with argon to be tested in order to measure the content of ^{39}Ar. The detector will be readout by two cryogenic SiPMs each with a surface area of $1\,cm^2$. The SiPMs and the readout electronics will come from the DS-20k production chain.

The ArDM detector will act as an active veto against internal and external radiation. For this purpose, we are building a dedicated single phase setup with a new set of low-radioactive photo-multipliers (PMT). However, we will also retain the entire present double phase setup for later use, e.g. for measurements of large quantities of depleted argon.

Extensive GEANT4-based simulations were performed using the Monte Carlo simulation package inherited from the DarkSide-50. These simulations show that DArT will achieve a sub-% measurement when operated inside the ArDM detector, for ^{39}Ar concentrations a factor of ten smaller that those of AAr, and in about a week of running. A 2% measurement could be made for ^{39}Ar concentrations as low as two orders of magnitude (statistical uncertainty only) smaller than those in AAr. This setup will also be useful to characterize the performance of Aria, which is expected to suppress the ^{39}Ar content by a factor of 10 per pass.

A very important addition to the setup described above will consist of adding a $6\,t$ lead belt about $140\,cm$ tall around the ArDM vessel, at the mid-height position. This will suppress the impact of external photons that dominate the background budget and allow for the measurement of even larger ^{39}Ar depletion factors, corresponding to that of the UAr. If the depletion levels are those already measured in the past (i.e. of 1400), it will be possible, according to our simulations, to measure them with a 7% uncertainty in about a week of running. Upper limits can be set on depletion factors of order 25 200 (statistical uncertainty only), i.e. UAr with one distillation pass in Aria.

The argon from Urania is expected to be available only after mid-2021. However, it is planned that after the run of DS-50 at LNGS, presumably at the end of 2019, its argon will be measured with DArT to cross-check the original measurement taken with DS-50 and to test the new setup. This DArT experiment is expected to become a useful facility within LSC for the years to come, since it will be needed to measure samples of the extracted argon from Urania over time. An Expression of Interest and a TDR were recently submitted to the LSC Directorate. Detector construction in all collaborating institutions has already started.

12 ReD

The ReD project aims to characterize the light and charge response of a LAr TPC to neutron-induced nuclear recoils, especially at low energy, and to explore for the possible directional dependence suggested by the SCENE experiment. ReD consists in the irradiation of a miniaturized LAr TPC with a neutron beam at the INFN, Laboratori Nazionali del Sud (LNS), Catania. Neutrons are produced via the reaction p(^{7}Li,^{7}Be)n from a primary ^{7}Li beam delivered by the TANDEM accelerator of LNS. A ΔE/E telescope, made by two Si detectors, identifies the charged particles (^{7}Be) which accompany the neutrons emitted towards the TPC. Neutrons scattered from the TPC are detected by using an array of nine 3-in liquid scintillator (LSci) detectors. The entire set-up has been integrated and commissioned in the "80 deg" beamline of LNS, as displayed in Fig. 5.

The core detector of ReD is a small custom-made double phase LAr TPC of $9 \times 9 \times 9$ cm^3.
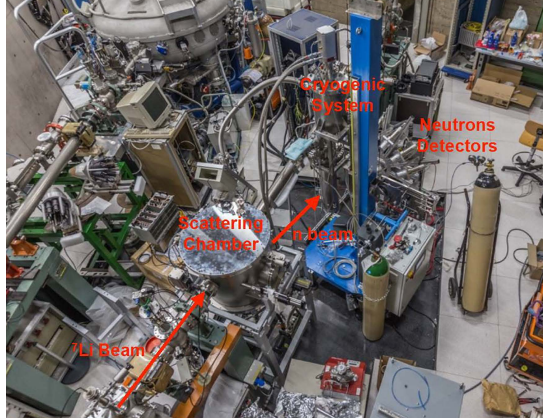
Figure 5: The "80 deg" beam-line at LNS, after the deployment and alignment of ReD. The targets and the Si telescope are hosted inside the vacuum scattering chamber.

The inner part ($5 \times 5 \times 6$ cm^3) is enclosed by vertical acrylic-ESR sandwich reflection panels on the four sides, and by two acrylic windows coated with ITO and then with TPB, on the top (anode) and bottom (cathode). The maximum drift length is 5 cm, delimited by the cathode and by a stainless steel grid located 3 mm below the level of the liquid. A 7 mm-thick gas pocket is formed by means of a diving bell. The ReD TPC uses all the innovative features of the DS-20k design, in particular the optoelectronic readout based on SiPMs developed by FBK and the cryogenic electronics. Two 5×5 cm^2 tiles are available from FBK, each made by 24 rectangular SiPMs. The tile on the top of the LAr TPC has a 24-channel readout, in order to improve the (x,y) sensitivity, while the bottom tile has a 4-channel readout. The individual detectors were first commissioned and tested individually using laser and radioactive sources.

The integration of the three detector systems was performed within two test beams at LNS during 2018. Neutrons were produced by sending a ^{7}Li 28 MeV beam onto a set of CH$_2$ targets having thickness of about 200 μg/cm^2. Events were observed with the proper signature, i.e. a ^{7}Be nucleus detected by the telescope, a nuclear recoil in the LAr TPC and a neutron scattering in the liquid scintillators. The physics measurement with the TANDEM beam will take place during 2019.

13   DarkSide-Proto

The objective of DS-Proto is the construction and operation of a prototype detector of intermediate size ($\sim$1 t), to fully validate the new DS-20k technologies for their integrity in both the mechanical and functional aspects. The prototype will be constructed using the materials before screening, in order to speed up the mechanical validation, and will therefore not necessarily be a physics-results oriented detector. This may evolve over time to include low radioactive components as materials are screened and made available, and eventually all parts could be replaced with radio pure materials to form the basis of another experiment with high-sensitivity to low-mass WIMPs. The prompt execution of DS-Proto is crucial to fulfill the overall schedule of DS-20k.

The program for DS-Proto is expected to span over three different phases (detector designs shown in Fig. 6):

1. Design, construction and assembly at test site of the LAr TPC, with the size available for two motherboards integration;
2. Integration of 50 preproduction PDMs to the LAr TPC; assembly, commissioning, and
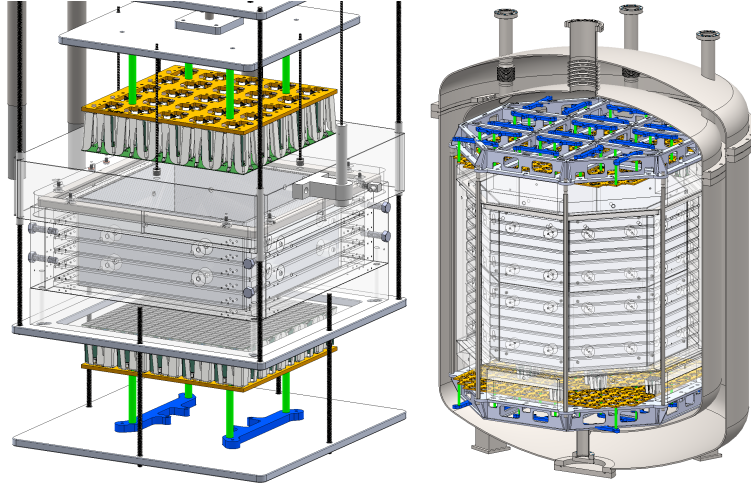
Figure 6: Left: Schematic of the test setup for the phase-I and phase-II as described in the text; Right: Schematic of the full DS-Proto detector, with the cryostat already been built and delivered to CERN.

operation of full read-out and DAQ for 50 PDMs; The xy resolution and S2 gas pocket optimization will be done during this phase.

3. Assembly and commissioning of full system, including 370 first production PDMs; full readout and DAQ operational; evolution towards final configuration.

Construction of DS-Proto is expected at the end of 2019 or early 2020. The first test operation with a reduced number of photosensors is expected by summer 2019, followed by a second operation with a full complement of PDMs by early 2020. Full characterization of the prototype performance and physics runs will be performed after installation at LNGS. The detailed program of the activities to be carried out underground is under study.

14   List of Publications during 2017

1. DarkSide-50 532-day Dark Matter Search with Low-Radioactivity Argon. Physical Review D, 98 (2018): 102006. [arXiv:1802.07198]
2. Low-mass Dark Matter Search with the DarkSide-50 Experiment. Physical Review Letters, 121 (2018): 081307. [arXiv:1802.06994]
3. Constraints on Sub-GeV Dark Matter-Electron Scattering from the DarkSide-50 Experiment. Physical Review Letters, 121 (2018): 111303. [arXiv:1802.06998]
4. Electroluminescence pulse shape and electron diffusion in liquid argon measured in a dual-phase TPC. Nuclear Instruments and Methods A, 904 (2018): 23-34. [arXiv:1802.01427]
5. DarkSide-20k: A 20 Tonne Two-Phase LAr TPC for Direct Dark Matter Detection at LNGS. The European Physical Journal Plus, 133 (2018): 131 [arXiv:1707.08145]

References

[Agnes et al.(2018a)] P. Agnes et al. (The DarkSide Collaboration), Phys. Rev. Lett. **121**, 081307 (2018a).

[Agnes et al.(2018b)] P. Agnes et al. (The DarkSide Collaboration), Phys. Rev. Lett. **121**, 111303 (2018b).

[Agnes et al.(2018c)] P. Agnes et al. (The DarkSide Collaboration), Phys. Rev. D **98**, 102006 (2018c).

[Ajaj et al.(2019)] R. Ajaj et al., arXiv:1902.04048v1 (2019).

[Abi et al.(2017)] B. Abi et al. (The DUNE Collaboration), arXiv:1706.07081v2 (2017).

[Acciarri et al.(2016)] R. Acciarri et al. (The DUNE Collaboration), arXiv:1601.05471v1 (2016).

GERDA

A. Abramov[n], M. Agostini[p], A.M. Bakalyarov[n], M. Balata[a], I. Barabanov[l], L. Baudis[t], C. Bauer[h], E. Bellotti[i,j], S. Belogurov[m,l], A. Bettini[q,r], L. Bezrukov[l], D. Borowicz[f], E. Bossio[p], V. Bothe[h], V. Brudanin[f], R. Brugnera[q,r], A. Caldwell[o], C. Cattadori[j], A. Chernogorov[m], T. Comellato[p], V. D'Andrea[a], E.V. Demidova[m], N. Di Marco[a], A. Domula[e], E. Doroshkevich[l], V. Egorov[f], F. Fischer[o], M. Fomina[f], A. Gangapshev[l,h], A. Garfagnini[q,r], M. Giordano[b], C. Gooch[o], P. Grabmayr[s], V. Gurentsov[l], K. Gusev[f,n,p], C. Hahne[e], J. Hakenmller[h], S. Hemmer[r], R. Hiller[t], W. Hofmann[h], P. Holl[o], M. Hult[g], L.V. Inzhechik[l], L. Ioannucci[a], J. Janicskó Csáthy[p], J. Jochum[s], M. Junker[a], V. Kazalov[l], Y. Kermaidic[h], H. Khushbakht[s], P. Kicsiny[o], T. Kihm[h], K. Kilgus[s], I.V. Kirpichnikov[m], A. Klimenko[h,f], R. Kneißl[o], K.T. Knpfle[h], O. Kochetov[f], V.N. Kornoukhov[m,l], P. Krause[p], V.V. Kuzminov[l], M. Laubenstein[a], A. Lazzaro[p], M. Lindner[h], I. Lippi[r], A. Lubashevskiy[f], B. Lubsandorzhiev[l], G. Lutter[g], C. Macolino[a], S. Maisenbacher[s], B. Majorovits[o], W. Maneschg[h], G. Marissens[g], M. Miloradovic[t], R. Mingazheva[t], M. Misiaszek[d], P. Moseev[l], I. Nemchenok[f], S. Nisi[a], K. Panas[d], L. Pandola[c], K. Pelczar[a], L. Pertoldi[q,r], P. Piseri[k], A. Pullia[k], C. Ransom[t], L. Rauscher[s], M. Reissfelder[h], S. Riboldi[k], N. Rumyantseva[n,f], C. Sada[q,r], E. Sala[o], F. Salamida[b], B. Schneider[e], S. Schnert[p], J. Schreiner[h], O. Schulz[o], M. Schtt[h], A-K. Schtz[s], M. Schwarz[p], B. Schweisshelm[o], B. Schwingenheuer[h], H. Seitz[o], O. Selivanenko[l], E. Shevchik[f], M. Shirchenko[f], H. Simgen[h], A. Smolnikov[h,f], D. Stukov[n], L. Vanhoefer[o], A.A. Vasenko[m], A. Veresnikova[l], K. von Sturm[q,r], V. Wagner[h], T. Wester[e], C. Wiesinger[p], M. Wojcik[d], E. Yanovich[l], I. Zhitnikov[f], S.V. Zhukov[n], D. Zinatulina[f], A. Zschocke[s], A.J. Zsigmond[o], K. Zuber[e], and G. Zuzel[d].

[a]) INFN Laboratori Nazionali del Gran Sasso and Gran Sasso Science Institute, Assergi, Italy

[b]) INFN Laboratori Nazionali del Gran Sasso and Università degli Studi dell'Aquila, L'Aquila, Italy

[c]) INFN Laboratori Nazionali del Sud, Catania, Italy

[d]) Institute of Physics, Jagiellonian University, Cracow, Poland

[e]) Institut für Kern- und Teilchenphysik, Technische Universität Dresden, Dresden, Germany

[f]) Joint Institute for Nuclear Research, Dubna, Russia

[g]) European Commission, JRC-Geel, Geel, Belgium

[h]) Max-Planck-Institut für Kernphysik, Heidelberg, Germany

[i]) Dipartimento di Fisica, Università Milano Bicocca, Milan, Italy

[j]) INFN Milano Bicocca, Milan, Italy

[k]) Dipartimento di Fisica, Università degli Studi di Milano e INFN Milano, Milan, Italy

[l]) Institute for Nuclear Research of the Russian Academy of Sciences, Moscow, Russia

[m]) Institute for Theoretical and Experimental Physics, NRC "Kurchatov Institute", Moscow, Russia

[n]) National Research Centre "Kurchatov Institute", Moscow, Russia

[o]) Max-Planck-Institut für Physik, Munich, Germany

[p]) Physik Department and Excellence Cluster Universe, Technische Universität München, Germany

^{q}) Dipartimento di Fisica e Astronomia dell'Università di Padova, Padua, Italy

^{r}) INFN Padova, Padua, Italy

^{s}) Physikalisches Institut, Eberhard Karls Universität Tübingen, Tübingen, Germany

^{t}) Physik Institut der Universität Zürich, Zurich, Switzerland

Spokesperson: Riccardo Brugnera (*riccardo.brugnera@pd.infn.it*)

Co-Spokesperson: Bernhard Schwingenheuer (*b.schwingenheuer@mpi-hd.mpg.de*)

Technical Coordinator: Konstantin Gusev (*kngusev@gmail.com*)

chair of collaboration board: J. Jochum chair of speakers bureau: B. Majorovits
Analysis coordinator: M. Agostini chair of editorial board: K.-T. Knöpfle
GLIMOS/RAE: M. Balata

URL: `http://www.mpi-hd.mpg.de/GERDA/`

Abstract

The GERDA experiment searches for the lepton number violating neutrinoless double-beta decay of ^{76}Ge operating bare, enriched Ge diodes in liquid argon. The broad energy germanium (BEGe) detectors feature an excellent background discrimination from the analysis of the time profile of the detector signals, while the instrumentation of the cryogenic liquid volume surrounding the germanium detectors acts as an active veto to further suppress the external background. With a total exposure of 82.4 kg·yr , GERDA remains in the background-free regime and a median sensitivity on the half-life of $T_{1/2}^{0\nu}> 1.1 \times 10^{26}$ yr (90% C.L.) is achieved. We observed no signal and derived a lower limit of $T_{1/2}^{0\nu}> 0.9 \times 10^{26}$ yr (90% C.L.). In this paper the basic concept of the GERDA design is summarized, with a special focus on the characteristics and performance of germanium semiconductor detector employed. The data taking and the physics results obtained in Phase II are presented together with the last hardware upgrade performed and the expected performance for the full 100 kg·yr exposure.

1 Introduction

The detection of neutrinoless double beta ($0\nu\beta\beta$) decay, a hypothetical lepton-number-violating nuclear transition, would prove the Majorana nature of neutrinos [1, 2] giving access to the absolute neutrino mass scale and supporting beyond Standard Model theories providing a possible explanation to the dominance of baryonic matter over anti-matter in the Universe [3, 4, 5].

Several experiments around the world, using different approaches and nuclei as ^{76}Ge [6, 7], ^{136}Xe [8, 9] and ^{130}Te [10, 11], are currently searching for $0\nu\beta\beta$. The experimental signature is a peak in the distribution of the energy sum of two electrons at the Q-value of the decay ($Q_{\beta\beta}$). Since only a few signal counts per kg per year are expected, a very strong suppression of all background sources and a high energy resolution are required.

The GERmanium Detector Array (GERDA) experiment [12] searches for $0\nu\beta\beta$ decay of ^{76}Ge by using semiconductor germanium detectors enriched up to $\sim 87\%$ in ^{76}Ge featuring high energy resolution and excellent radio-purity. Given the high density of Ge crystals, acting at the same time as $0\nu\beta\beta$ source and detector, signal events result in a point-like energy deposition at the $Q_{\beta\beta}$-value, thus assuring a very high detection efficiency.
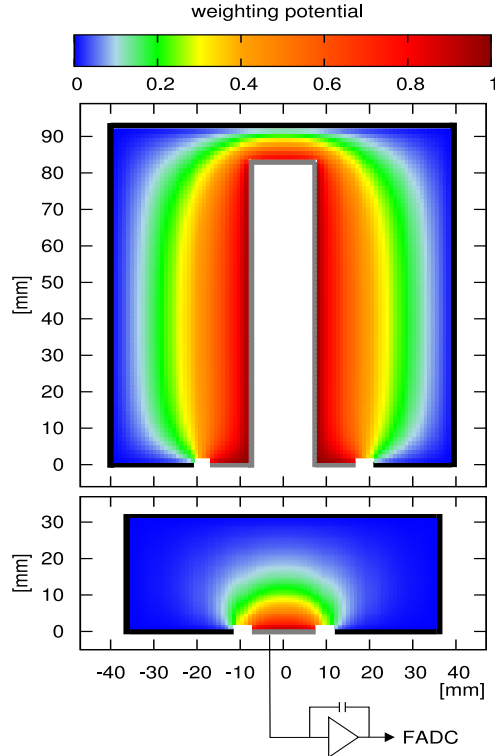
Figure 1: Cross section of a coaxial detector (top) and a BEGe detector (bottom). The p+ electrode is drawn in grey and the n+ electrode in black (thickness not to scale). The electrodes are separated by an insulating groove. Color profiles of the weighting potential are overlayed on the detector drawings. Also sketched for the BEGe is the readout with a charge sensitive amplifier. Figure from [17].

2   Germanium detectors for $0\nu\beta\beta$ decay

Ge crystals employed in the GERDA experiment are p-type semiconductor detector with a cylindrical shape. The n+ electrode, made of diffused lithium with a thickness of 0.5 mm, and the p+ contact of ion-implanted boron and a thickness of the order of 100 μm, are separated by a circular non-conductive grove. The detectors are operated in reverse bias by applying a positive high-voltage (O(kV)) to the n+ electrode, while the p+ is grounded for signal read out. Electron-hole pairs created by charged particles drift in the electric field into opposite directions. The signal read-out is performed using a charge sensitive preamplifier.

Two type of Ge crystals are used in GERDA, differing both in geometry and performance: coaxial detectors, from the former Heidelberg-Moscow [13] and IGEX [14] experiments and broad energy germanium (BEGe) detectors [15, 16] featuring smaller masses, higher energy resolution and better pulse shape discrimination (PSD) capabilities. As shown in Figure 1, due to the different layout of the electrodes, the electric field profile in BEGe detectors strongly differs from that of coaxial ones thus resulting in different pulse characteristics.

The time dependence of the detector current pulse can be used to perform signal-to-background discrimination. While $0\nu\beta\beta$ signal events are expected to deposit energy within a small volume (single-site event, SSE), in background events from photons interacting via multiple Compton scattering, the energy is deposited at several locations in the detector (multi-site events, MSE).
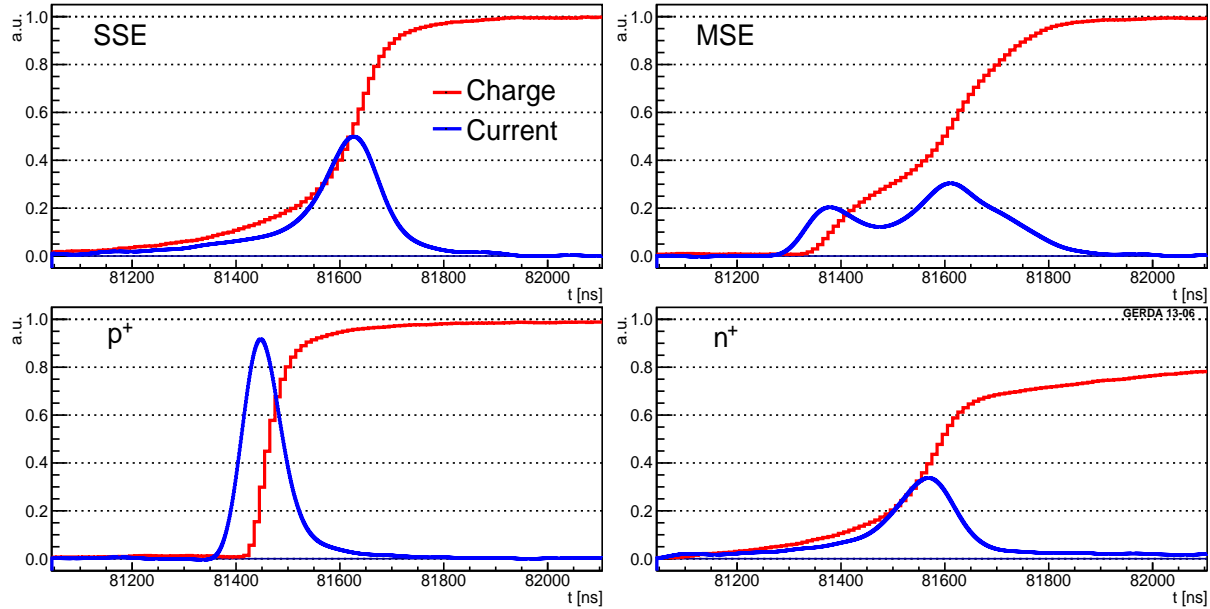
Figure 2: Candidate pulse traces taken from BEGe data for a SSE (top left), MSE (top right), p+ electrode event (bottom left) and n+ surface event (bottom right). Figure from [17].

The pulse shapes will in general be different for the two event classes and can thus be used to improve the sensitivity of the experiment. Moreover energy depositions from α or β-decays near or at the detector surface lead to distinct pulse shapes allowing their identification. Figure 2 shows example traces for a BEGe detector in the case of SSE (top left), MSE (top right) and events on p+ (bottom left) and n+ (bottom right) electrodes, respectively [17].

Based on the trace characteristics, various pulse shape discrimination techniques are applied to both BEGe and coaxial type detectors as described in section 4.

3 The Gerda apparatus

In Phase II of the GERDA experiment, 40 high-purity germanium detectors (HPGe) are employed. 30 enriched BEGe (20 kg) and 7 enriched coaxial (16 kg) detectors, are arranged in 6 strings. The detector array is complemented with a central string instrumented with three coaxial detectors (7.6 kg) made from germanium of natural isotopic composition. HPGes are deployed in liquid argon (LAr), which cools the detectors to their operating temperature of about 90 K while at the same time providing shield against the external radiation (see Figure 3).

The cylindrical volume around the detector strings is instrumented with a curtain of wavelength-shifting fibres read out at both ends with 90 silicon photomultipliers (SiPMs). Sixteen low-background photomultipliers (PMTs) are mounted below and above of the HPGe array.

The 64 m^3 LAr cryostat is made of a stainless steel cylinder with a diameter of 4 m, internally covered with a 6 cm-thick Cu layer. The LAr cryostat is contained in a 590 m^3 water tank (diameter = 10 m, height = 9 m), filled with ultra-pure water and equipped with 66 photomultipliers, thus acting both as Cherenkov veto and additional shield against external radiation.

On the top of the water tank a clean room with a glove box and a lock is used for the assembly of HPGe detectors into strings. The muon veto is complemented by a layer of plastic
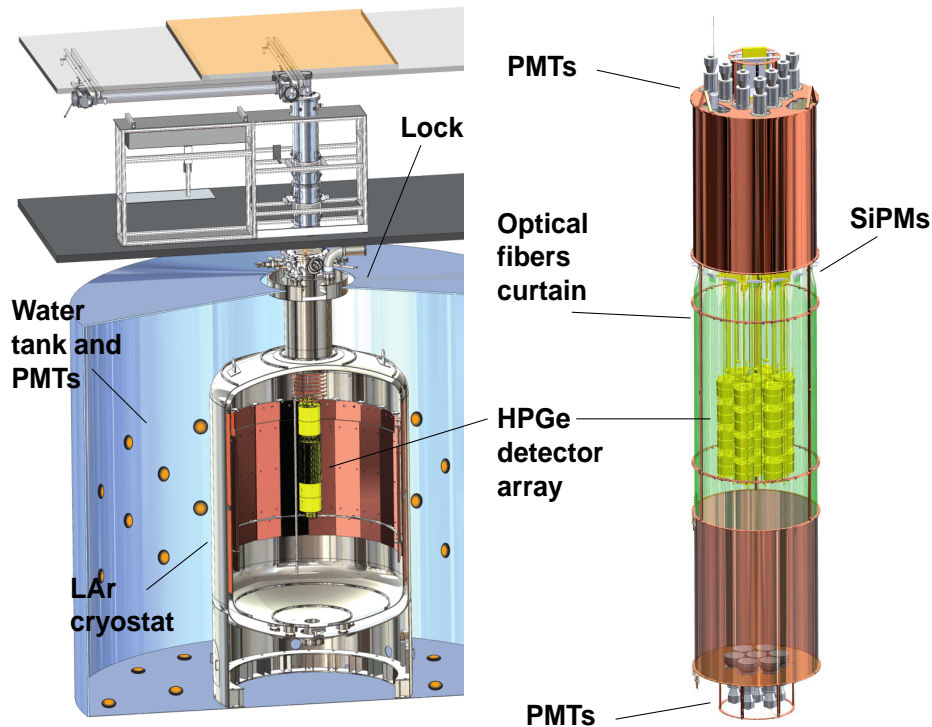
Figure 3: Schematic layout of the GERDA setup. The zoom in the right-hand side of the figure displays the inner part of the setup.

scintillator panels installed above the clean room.

All Ge detectors are connected to low radioactivity charge sensitive amplifiers. The charge signal traces are digitized with a 100 MHz sampling rate and a total window of 160 μs. Data are stored on disk and analyzed offline using the procedure described in [18, 19].

3.1 2018 upgrade

In summer 2018 an upgrade of the setup was carried out. The upgrade campaign has been performed in two stages: 1 month in April-May and 1 week in July 2018. All hardware components have been delivered to LNGS by the middle of April 2018.

3.1.1 First stage of the upgrade campaign

In two days all 40 GERDA detectors have been dismounted from strings and packed in the transportation containers. Within the following two weeks all enriched diodes were disassembled from their holders, mounted back and bonded with new cables exhibiting lower radioactivity made from Kapton. For 12 BEGe detectors the original pair holders have been substituted by single ones such that now all detectors exhibit downwards facing grooves. The ANG1 detector and all natural GTF detectors have been replaced by 5 new inverted coaxial detectors [20]. The old fiber shroud has been exchanged by a new one with improved geometrical coverage. A new central fiber module has been installed to detect scintillation light within the array (see Figure 4 and 5). All readout circuits (CC3) have been modified (by adding JFET protecting diodes,

Figure 4: Bottom view of the GERDA array with the central fiber module and the new fiber curtain.

replacing blocking capacitors with higher voltage rating to allow for a larger drain current of the input JFET), and 3 broken JFETs have been replaced. Test immersion of the assembled array showed that 2 new inverted coaxial detectors had high leakage current. We decided to take them out and to send them back to the producer for repair. GERDA considered the possibility to etch the detectors at LNGS and several attempts with test diodes have been performed on-site in parallel to the upgrade works, however they were unsuccessful. After the second immersion we have found that 2 detectors had shorts to the ground and 3 detectors showed some current, but these 3 diodes had the same problems at the beginning of Phase II. Other detectors were biased up to their operational voltages and all 39 readout channels were working, as well as all SiPMs of the new fiber shroud.

3.1.2 Second stage of the upgrade campaign

Two inverted coaxial detectors which were repaired by the producer have been mounted in their holder, bonded and installed in the central string of the GERDA array. The final string configuration is shown in Figure 6. As before every string is surrounded by nylon mini shroud. Before the final immersion the problem with shorts to ground has been successfully solved without dismounting the detectors from the array, however 3 problematic detectors (two coaxial detectors: ANG5, ANG2, and the inverted coaxial detector IC48B) drove some leakage current and could be used for anti-coincidence only. At the end the whole upgrade operation lasted less than two months. The final results of the upgrade are the following:

- the mass of the enriched detectors has been increased by 10 kg, by adding new enriched inverted coaxial detectors, recovering three BEGe detectors after the repair of their readout channels and taking also into account that the ANG1 detector was not deployed;

- all detector signal and high voltage cables have been replaced by cleaner ones;

- diodes from residual pair holders have been mounted in the single holders such that the grooves of all detectors point downwards to avoid the risk of particulates falling into the groove;
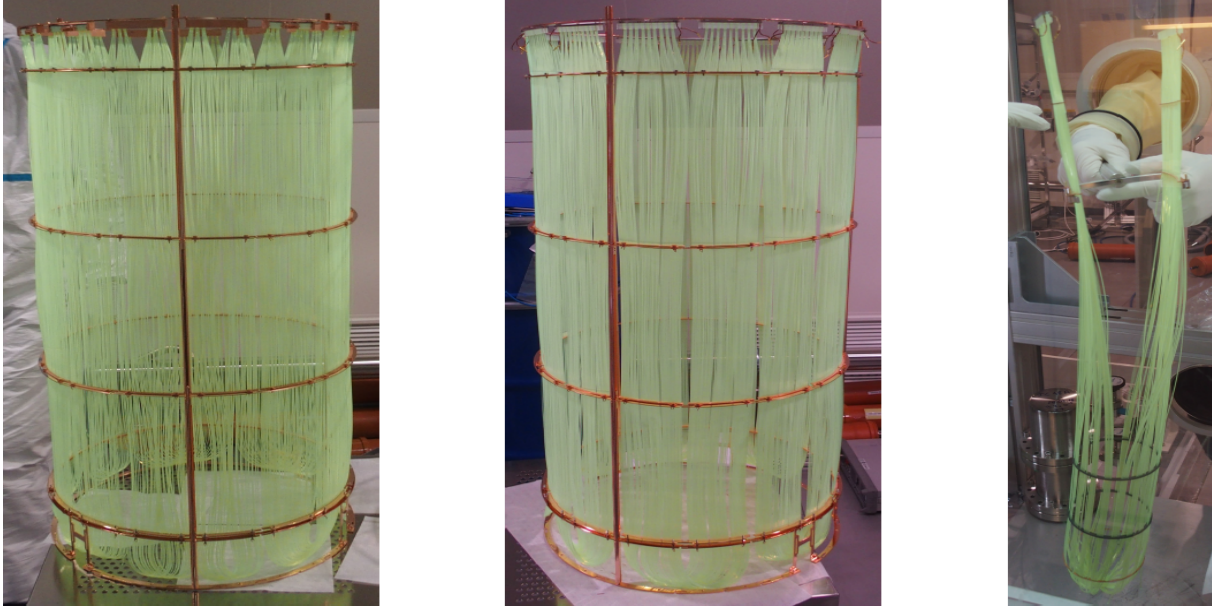
Figure 5: Left and middle: old (810 fiber ends, 90 SiPMs) and new (1215 fiber ends, 135 SiPMs) fiber curtains. Right: central fiber module.

- a new way of cable routing between the detector and the amplifier has reduced the capacitance to neighbouring cables/channels. As a consequence cross talk and noise are reduced for many channels;

- all readout electronic circuits have been modified in order to improve their robustness and noise;

- liquid argon veto system has been improved by replacing the old fiber curtain by a new one with better coverage and adding the central fiber module.

4   Data taking and background suppression

GERDA is taking data since 2011. Data from the first phase of GERDA (Phase I) gave no positive indication of the $0\nu\beta\beta$ decay with an exposure of about 21.6 kg·yr and a background index at the $Q_{\beta\beta}= (2039.061 \pm 0.007)$ keV of 10^{-2} cts/(keV·kg·yr). A lower limit on the half-life of $T_{1/2}^{0\nu} > 2.1 \cdot 10^{25}$ yr (90% C.L.) was set [18]. The second phase (Phase II), is ongoing since December 2015 and initial results were released in June 2016 with 10.8 kg·yr of total exposure and a background index of 10^{-3} cts/(keV·kg·yr) [6]. In June 2017 new data collected up to April 2017 have been fully validated and analyzed for an exposure of 23.2 kg·yr of ^{enr}Ge (18.2 kg·yr from BEGe detectors and 5 kg·yr from coaxial detectors) [21]. With new data release of April 2018 we collected a total exposure for Phase II of 53.9 kg·yr .

After the upgrade performed in summer 2018, the data taking has been restarted and is still on-going.

The deposited energy is reconstructed with an improved digital filter [22] optimized for each detector and each calibration. The energy scale and resolution is determined by taking weekly calibrations with ^{228}Th sources and the stability is continuously monitored by injecting charge
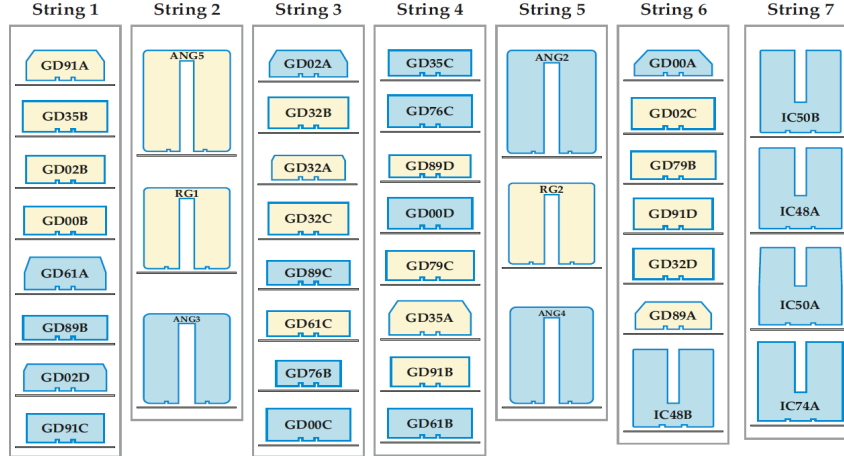
Figure 6: Schematic view of GERDA strings after the upgrade

pulses (test pulses) with a rate of 0.05 Hz and, weekly, by checking the shift of the position of the 2615 keV γ-line between two consecutive calibration. The average resolution at $Q_{\beta\beta}$ evaluated by using the calibrations data, is 3.0(1) keV and 3.6(1) keV full width at half maximum (FWHM) for $^{\mathrm{enr}}$Ge BEGe and coaxial detectors, respectively. A resolution ($\sigma = $ FWHM/2.35) at $Q_{\beta\beta}$ better than 0.1% is therefore achieved.

Unphysical events, originating from electrical discharges or bursts of noise, are rejected by a set of multi-parametric cuts based on the flatness of the baseline, polarity and time structure of the pulse. Physical events at $Q_{\beta\beta}$ are accepted with an efficiency greater than 99.9% while no unphysical event survives the cuts above 1600 keV.

Due to the short range of electrons in germanium ($\sim$1 mm), in 92% of $0\nu\beta\beta$ decays occurring in the active detector volume, the total $0\nu\beta\beta$ energy is detected in that detector. Therefore multiple detector coincidences are discarded as background events. Events are also rejected if a muon trigger occurred within 10 μs before a germanium detector trigger or if any of the LAr light detectors record a signal within 6 μs from the germanium trigger. The application of the muon and LAr veto leads to a signal loss of less than 0.1% and $\sim$ 2%, respectively.

As shown also in section 2, the time profile of the Ge current signal can be used to disentangle $0\nu\beta\beta$ decays (single-site events, SSE) from background events such as γ-rays, which mainly interact via Compton scattering with an average free path of $\sim$1 cm (multi-site events, MSE), or external α/β-rays, which deposit their energy on the detector surface. The geometry of the BEGe detectors allows the application of a simple mono-parametric PSD technique based on the maximum of the detector current pulse A normalized to the total energy E [23, 17, 24]. The cut on A/E allows to reject $>$ 90% of (γ-like) MSEs and basically all α-like surface events, with a $0\nu\beta\beta$ selection efficiency of (87.6 ± 2.5)%.

Due to the shape of the weighting field (see Figure 1), pulses in coaxial detectors show a variety of different shapes and the A/E method is no longer efficient [17]. Therefore, for coaxial detectors two different neural network algorithms (ANN) are applied to discriminate SSEs from MSEs and from α surface events. The selection efficiency for $0\nu\beta\beta$ decays is (71.2 ± 4.3)%.

By applying both the LAr veto and the PSD cut, about 95% of background events are rejected while keeping 69% and 86% $0\nu\beta\beta$ events, for coaxials and BEGes, respectively.

The offline data analysis flow follows a blind approach: events with a reconstructed energy in the interval $Q_{\beta\beta}\pm 25$ keV are only stored on disk and not analyzed. Only when all analysis

procedures and cuts have been finalized, these blinded events are processed.

5 Statistical analysis and results

In summer 2018, data taken from June 2017 and April 2018 were released providing a total exposure for Phase II of 53.9 kg·yr . After the unblinding and the application of all the analysis cuts described in the previous section, only 3 and 4 events in the coaxial and BEGe data sets respectively, remain in the region of interest (ROI) between 1930 and 2190 keV and excluding ± 5 keV wide intervals at the position of know γ-lines (2104 and 2119 keV) and at $Q_{\beta\beta}$. The background in the signal region is the therefore $5.7^{+4.1}_{-2.6}\cdot 10^{-4}$ cts/(keV·kg·yr) for coaxial detectors and $5.6^{+3.4}_{-2.4} \cdot 10^{-4}$ cts/(keV·kg·yr) for BEGes.

Both a frequentist and a Bayesian analysis, based on an unbinned extended likelihood function described in the Methods Section of Ref. [6], is performed considering the whole exposure of 82.4 kg·yr of both Phase I and Phase II. The fit function is a flat distribution for the background and a Gaussian centered at $Q_{\beta\beta}$ with a width according to the resolution for a possible $0\nu\beta\beta$ signal. The signal strength S $= 1/T^{0\nu}_{1/2}$ is calculated for each data set (both for Phase I and Phase II, for coaxial and BEGe detector respectively) according to its exposure and efficiency while the inverse half-life 1/T is a common free parameter. The analysis accounts for the systematic uncertainties of the efficiencies and energy resolutions. The limit on the half-life of $0\nu\beta\beta$ is $T^{0\nu}_{1/2}$ $> 0.9 \cdot 10^{26}$ yr at 90% CL (frequentist) and $T^{0\nu}_{1/2} > 0.8 \cdot 10^{26}$ yr (Bayesian), while the median sensitivity for the 90% CL lower limit of $T^{0\nu}_{1/2}$ is $1.1 \cdot 10^{26}$ yr (frequentist) and $T^{0\nu}_{1/2} > 0.8 \cdot 10^{26}$ yr (Bayesian).

6 Conclusions

The GERDA experiment is currently taking data. The ambitious design goal for the background level of 10^{-3} cts/(keV·kg·yr) was surpassed as well as the goal for half-life sensitivity of 10^{26} yr has already been reached. Nevertheless the data taking will continue to reach a total exposure of 100 kg·yr.

At present, thanks to the powerful pulse shape discrimination of BEGe detectors and to the detection of the argon scintillation light, GERDA has reached the world-best background index (BI) at $Q_{\beta\beta}$ if weighted with the energy resolution of the detectors, thus making GERDA the first "background-free" experiment for the whole design exposure. Moreover an energy resolution better than 0.1% at $Q_{\beta\beta}$ has been achieved for both BEGe and coaxial detectors.

The excellent performance in terms of background index and energy resolution motivates a future extension of the program in a medium term time scale. The LEGEND collaboration aims to build a 200 kg enriched germanium experiment using the GERDA cryostat. Such an experiment would remain background-free up to an exposure of 1000 kg·yr provided the background can be further reduced by a factor 5-10; thus LEGEND-200 [25] would allow to reach a half-life of 10^{27} yr. The 200 kg project is conceived as a first step towards a more ambitious 1-ton experiment that would allow to reach a sensitivity of 10^{28} yr, thus, fully covering the inverted hierarchy region in ten years of data taking.

7 Publications in 2018

- Improved limit on neutrinoless double beta decay of 76Ge from GERDA Phase II, GERDA Collaboration, Phys.Rev.Lett. 120 (2018) no.13, 132503

- GERDA results and the future perspectives for the neutrinoless double beta decay search using 76Ge, GERDA Collaboration, Int.J.Mod.Phys. A33 (2018) no.09, 1843004

- Upgrade for Phase II of the GERDA Experiment, GERDA Collaboration, Eur.Phys.J. C78 (2018) no.5, 388

- Recent results from GERDA Phase II, Christoph Wiesinger for the GERDA Collaboration, Published in PoS NOW2018 (2018) 069

- New Data Release of GERDA Phase II: Search for 0 decay of 76Ge, M. Agostini et al. (GERDA collaboration), Published in KnE Energ.Phys. 3 (2018) 202-209

- Search for 0-decay with GERDA phase II, B. Majorovits for the GERDA Collaboration, Published in AIP Conf.Proc. 1921 (2018) no.1, 060004

References

[1] Schechter J and Valle J W F 1982 *Phys. Rev.* **D25** 2951

[2] Duerr M, Lindner M and Merle A 2011 *JHEP* **06** 091

[3] Davidson S, Nardi E and Nir Y 2008 *Phys. Rept.* **466** 105–177

[4] Mohapatra R N *et al.* 2007 *Rept. Prog. Phys.* **70** 1757–1867

[5] Päs H and Rodejohann W 2015 *New J. Phys.* **17** 115010

[6] Agostini M *et al.* (GERDA) 2017 *Nature* **544** 47

[7] Guiseppe V E *et al.* 2017 *AIP Conf. Proc.* **1894** 020010 (*Preprint* 1708.07562)

[8] Gando A *et al.* (KamLAND-Zen) 2016 *Phys. Rev. Lett.* **117** 082503 [Addendum: Phys. Rev. Lett.117,no.10,109903(2016)] (*Preprint* 1605.02889)

[9] Albert J B *et al.* (EXO) 2018 *Phys. Rev. Lett.* **120** 072701 (*Preprint* 1707.08707)

[10] Alduino C *et al.* (CUORE) 2018 *Phys. Rev. Lett.* **120** 132501 (*Preprint* 1710.07988)

[11] Andringa S *et al.* (SNO+) 2016 *Adv. High Energy Phys.* **2016** 6194250 (*Preprint* 1508.05759)

[12] Ackermann K H *et al.* (GERDA) 2013 *Eur. Phys. J.* **C73** 2330

[13] Klapdor-Kleingrothaus H V, Krivosheina I V, Dietz A and Chkvorets O 2004 *Phys. Lett.* **B586** 198–212

[14] Aalseth C E *et al.* (IGEX) 2002 *Phys. Rev.* **D65** 092007

[15] Agostini M *et al.* (GERDA) 2015 *Eur. Phys. J.* **C75** 39 (*Preprint* 1410.0853)

[16] Agostini M *et al.* (GERDA) 2019 (*Preprint* 1901.06590)

[17] Agostini M *et al.* 2013 *Eur. Phys. J.* **C73** 2583 (*Preprint* 1307.2610)

[18] Agostini M *et al.* (GERDA) 2013 *Phys. Rev. Lett.* **111** 122503

[19] Agostini M, Pandola L and Zavarise P 2012 *J. Phys. Conf. Ser.* **368** 012047

[20] Domula A, Hult M, Kermaidic Y, Marissens G, Schwingenheuer B, Wester T and Zuber K 2018 *Nucl. Instrum. Meth.* **A891** 106–110 (*Preprint* `1711.01433`)

[21] Agostini M *et al.* (GERDA) 2018 *Phys. Rev. Lett.* **120** 132503 (*Preprint* `1803.11100`)

[22] Agostini M *et al.* (GERDA) 2015 *Eur. Phys. J.* **C75** 255

[23] Budjáš D, Barnabé Heider M, Chkvorets O, Khanbekov N and Schönert S 2009 *JINST* **4** P10007

[24] Agostini M, Bellotti E, Brugnera R, Cattadori C M, D'Andragora A, di Vacri A, Garfagnini A, Laubenstein M, Pandola L and Ur C A 2011 *JINST* **6** P04005

[25] Abgrall N *et al.* (LEGEND) 2017 *AIP Conf. Proc.* **1894** 020027 (*Preprint* `1709.01980`)

LUNA
Laboratory for Underground
Nuclear Astrophysics

M. Aliotta[a], D. Bemmerer[b], A. Best[c], A. Boeltzig[d], C. Broggini[e], C. Bruno[a], A. Caciolli[f],
F. Cavanna[g], L. Csedreki[i], T. Chillery[a], G. F. Ciani[d], P. Corvisiero[g], T. Davinson[a],
R. Depalo[f], G. D'Erasmo[i], A. Di Leva[c], L. di Paolo[h], Z. Elekes[j], F. Ferraro[k], E. M. Fiore[i],
A. Formicola[h], Zs. Fülöp[j], G. Gervino[l], A. Guglielmetti[m], C. Gustavino[n], Gy. Gyürky[j],
G. Imbriani[c], M. Lugaro[o], P. Marigo[f], E. Masha[m], V. Mossa[i], M. Junker[h], I. Kochanek[h],
R. Menegazzo[e], F. R. Pantaleo[i], V. Paticchio[i], R. Perrino[p], D. Piatti[f], P. Prati[k],
L. Schiavulli[i], K. Stöckel[b], O. Straniero[q], T. Szücs[j], M. P. Takács[b], A. Valentini[i],
S. Zavatarelli[g]
SPOKESPERSON: P. PRATI

[a]University of Edinburgh, Edinburgh, United Kingdom
[b]Helmholtz-Zentrum Dresden-Rossendorf, Dresden, Germany
[c]Università degli Studi di Napoli "Federico II", and INFN, Napoli, Italy
[d]Gran Sasso Science Institute (GSSI), L'Aquila, Italy
[e]INFN, Padova, Italy
[f]Università degli Studi di Padova and INFN, Padova, Italy
[g]INFN, Genova, Italy
[h]Università degli Studi di Bari and INFN, Bari, Italy
[i]INFN, Laboratori Nazionali del Gran Sasso (LNGS), Assergi (AQ), Italy
[j]Institute for Nuclear Research (MTA ATOMKI), Debrecen, Hungary
[k]Università degli Studi di Genova and INFN, Genova, Italy
[l]Università degli Studi di Torino and INFN, Torino, Italy
[m]Università degli Studi di Milano and INFN, Milano, Italy
[n]INFN, Roma, Italy
[o]Monarch University Budapest, Budapest, Hungary
[p]INFN, Lecce, Italy
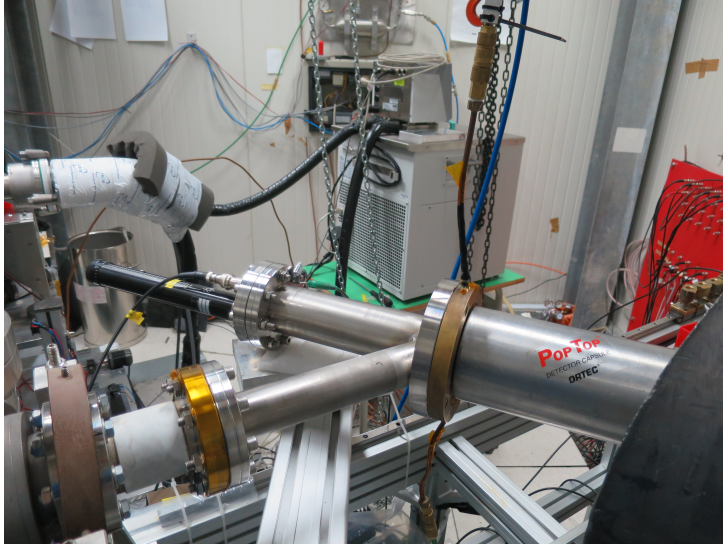[q]Osservatorio Astronomico di Collurania, Teramo, and INFN Napoli, Italy

Figure 1: Photo of the experimental setup for the study of the ^{6}Li(p,γ)^{7}Be reaction.

Abstract

Aim of the LUNA experiment is the direct measurement of the cross section of nuclear reactions relevant for stellar and primordial nucleosynthesis. The year 2018 was dedicated to experiments on the reactions ^{13}C(α,n)^{16}O and ^{22}Ne(α,γ)^{26}Mg boths relevant for the neutron production and the nucleosinthesis beyond iron. Data analysis to extract the cross section at astrophysical energies for the processes ^{2}H(p,γ)^{3}H and ^{6}Li(p,γ)^{7}Be reactions were also carried out. Furthermore, an intense activity has been addressed to design and prepare the first experiments at the fore coming LUNA-MV facility.

1   The ^{6}Li(p,γ)^{7}Be reaction

The ^{6}Li(p,γ)^{7}Be and ^{6}Li(p,α)^{3}He reactions are responsible for lithium depletion in the early stages of stellar evolution and contribute to Bang Nucleosynthesis.

The determination of the ^{6}Li abundance in stars is a powerful tool to understand the early stellar evolution and the structure of stellar convective envelopes. ^{6}Li is produced in small amounts during Big Bang Nucleosynthesis and it is very easily destroyed in stars through proton capture at temperatures higher than 2.5 MK. The cross section of the ^{6}Li(p,γ)^{7}Be reaction is very uncertain at astrophysical energies, since a new resonance-like structure at center of mass energy of 195 keV was discovered in a recent experiment [1]. Such resonance would correspond to a previously unknown excited state with E $\sim$ 5800 keV, J$^\pi$ = (1/2$^+$, 3/2$^+$) and $\Gamma_p \sim$ 50 keV. The existence of such resonance is currently a matter of debate [2], therefore a new direct measurement of the ^{6}Li(p,γ)^{7}Be cross section was performed at LUNA. A proton beam with energy between 80 and 400 keV and intensity of about 200 μA was be delivered to ^{6}Li solid targets of three different types: evaporated lithium oxide, evaporated lithium tungstate and an infinitely thick lithium chloride target. All targets were enriched in ^{6}Li at the 95% level.

A photo of the experimental setup is shown in fig. 1. Gamma rays emitted in the de-excitation of ^{7}Be were detected by an HPGe detector mounted in close geometry at 55° from the beam direction. A silicon detector was mounted at 125° and it was used to detect charged particles from the competing reaction ^{6}Li(p,α)^{3}He.

The data taking has been completed and the analysis has been almost completed.

2 The ^{2}H(p,γ)^{3}He reaction

The first nucleus produced in the Universe is deuterium whose accumulation marks the beginning of the so called Big Bang Nucleosynthesis (BBN). Currently the main source of uncertainty in the primordial deuterium calculations comes from the ^{2}H(p,γ)^{3}He cross section at BBN energies (30-300 keV) [3, 5].

In November and December 2018 an experimental campaign has been concluded using the proton beam produced by LUNA 400 kV accelerator and a gas target setup filled with deuterium. The gamma rays emitted by the ^{2}H(p,γ)^{3}He reaction were detected by an optically segmented 4π Bismuth Germanate (BGO) detector placed around the target chamber [4].

The cross section has been measured in the energy range of interest (30 keV $<$ E $<$ 170 keV) with 30-50 keV steps. A particular effort was devoted to quantify the contribution to the reaction rate due to deuterium implanted on the target walls and subsequent degassing. At each energy two runs were performed: one with deuterium gas inside the scattering chamber and the second with ^{4}He in order to evaluate the beam induced background due to implantation. In Fig. 2, a spectrum at E_p= 100 keV and the beam induced background contribution (bottom plot) is shown.

A very accurate beam current knowledge is mandatory to achieve a precision of the order of a few percent in the measurement of the cross section. The beam current has been measured by a constant-gradient calorimeter characterized by two sides, a hot one heated to 70℃ by thermoresistors and a cold one cooled down to -5℃ by a refrigerating system. The calorimeter has been calibrated evacuating the target chamber and using the calorimeter itself as a Faraday Cup. Thanks to an additional turbomolecular pump connected directly to the chamber, a 10^{-5} mbar vacuum was reached inside the chamber, thus reducing the ionization current due to the residual gas.

The data reduction to extract the astrophysical factor values in the explored energy range is almost concluded.

3 The ^{22}Ne(p,γ)^{23}Na reaction

The ^{22}Ne(p,γ)^{23}Na reaction is part of the hydrogen-burning neon-sodium cycle that is important in stellar scenarios with temperatures from 50-500 MK. Its reaction rate at the relevant temperatures is controlled by a number of resonances and by the direct capture component.

Regarding the study of this nuclear reaction, the year 2018 was devoted to two different analysis questions: First, a re-analysis of the data from the HPGe-based phase that had already been published [6, 7, 8] to take into account beam energy straggling effects, and second, the final analysis and publication of the BGO-based phase data [4, 9].

The re-analysis of the old, HPGe-based data showed that for special cases in nuclear astrophysics experiments, ion beam straggling effects may artificially depress the observed γ-ray yield from narrow resonances. This finding revised the previously published resonance strength data from the HPGe phase upward by 18-19% [10]. Due to its possible application to future experiments, the detailed description of the effect was published as a standalone paper and selected as one of the highlight publications of the year 2018 in Europhysics Letters [11].
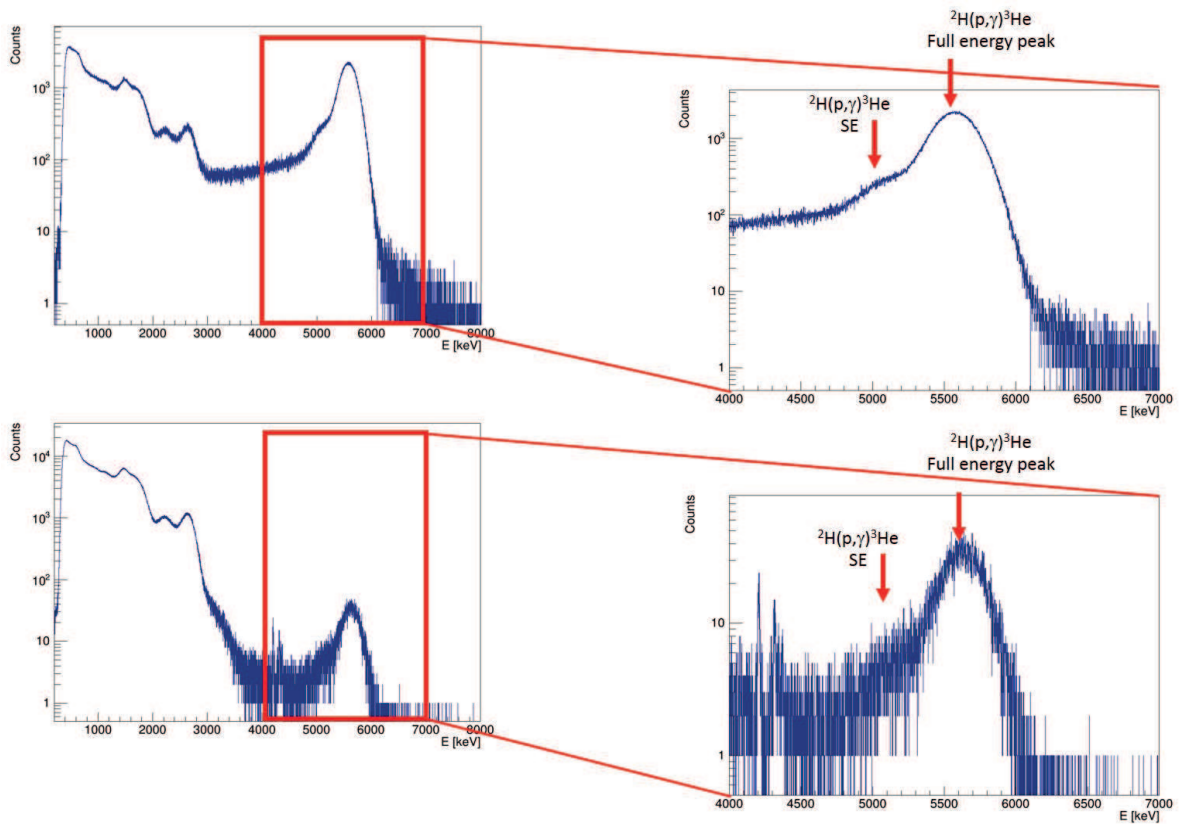
Figure 2: Top panel: ^{2}H(p,γ)^{3}He spectrum at 100 keV beam energy. Bottom panel: beam induced background measured at 100 keV beam energy. In both cases the region of interest for the ^{2}H(p,γ)^{3}He has been highlighted.
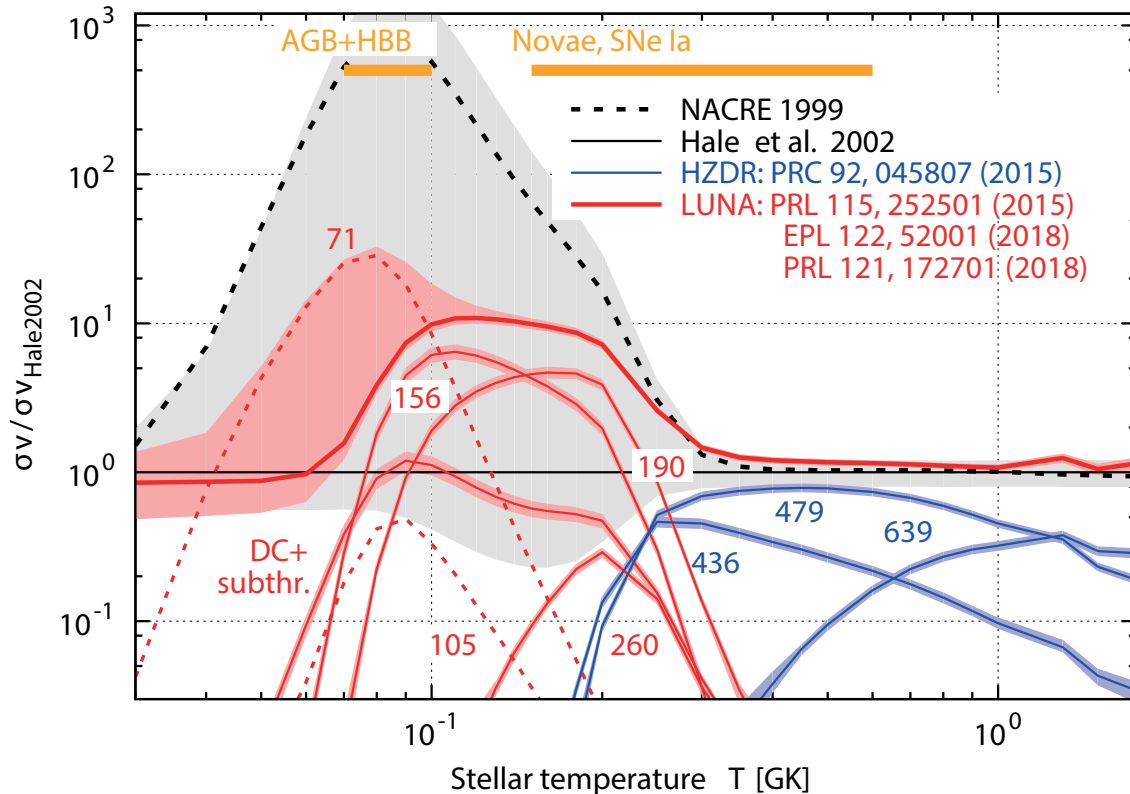
Figure 3: Thermonuclear reaction rate for the $^{22}\mathrm{Ne}(p,\gamma)^{23}\mathrm{Na}$ reaction from evaluations [12, 13] and from experiments: LUNA-HPGe [7, 8, 10, 11], TUNL [14], LUNA-BGO [9]. The rates are shown relative to the frequently used [15, 16, 17] rate by Hale *et al.* [18]. The individual contributions from LUNA-BGO [9] are labeled. For the total rates by Hale *et al.* and from LUNA-BGO [9], as well as the individual contributions from LUNA-BGO [9], shaded error bands have been added. The contribution from the 37 keV resonance dominates at low temperature and has been omitted for clarity.

The new, BGO-based data explored in a first step the limited but not-negligible sensitivity of the LUNA 4π BGO summing detector to γ-decay branching ratios [4]. In a second step, two ultra-low energy resonances at 71 and 105 keV proton beam energy were ruled out for astrophysical purposes, and even a detailed study of the weak non-resonant capture aspect of the reaction was possible. These data were published in Physical Review Letters [9].

With the conclusion of the LUNA efforts of this reaction, $^{22}\mathrm{Ne}(p,\gamma)^{23}\mathrm{Na}$, which used to be the least well known reaction of the cycle, is now the best-studied reaction that can actually serve as reference for efforts elsewhere.

4   Study of the $^{22}\mathrm{Ne}(\alpha,\gamma)^{26}\mathrm{Mg}$ reaction

The $^{22}\mathrm{Ne}(\alpha,\gamma)^{26}\mathrm{Mg}$ reaction competes with the $^{22}\mathrm{Ne}(\alpha,n)^{25}\mathrm{Mg}$ astrophysical s-process neutron source, because both reactions start with the same fuel. $^{22}\mathrm{Ne}(\alpha,\gamma)^{26}\mathrm{Mg}$ is dominated by many resonances that have been studied only to a very limited extent or not at all [19, 20, 21, and references therein], including a number below the neutron production threshold $E_\alpha > 564$ keV.

The study of a possible resonance in $^{22}\mathrm{Ne}(\alpha,\gamma)^{26}\mathrm{Mg}$ at $E_\alpha = 395$ keV was to be continued

in spring 2018 with several weeks of beam time scheduled, but due to unforeseen technical difficulties with the accelerator, no useful new data have been gained. The analysis has instead concentrated on extracting upper limits from the previous run. A new experimental attempt is foreseen for summer 2019.

5   The ^{13}C(α,n)^{16}O reaction

The ^{13}C(α,n)^{16}O (Q=2.215 MeV) reaction is the main neutron source for the astrophysical s and i processes: the temperatures of interest are around 1 and 2 10^8 K, respectively. These temperatures correspond to effective energy ranges of approximately 150 - 240 keV and 285 - 510 keV.

After the successful commissioning of the detector array in late 2017, two beam times have been devoted to the measurement of the ^{13}C(α, n)^{16}O cross section reaction, covering energies between 400 keV and 305 keV, corresponding to 305 - 233 keV in the center of mass energy system. This represents a significant improvement over the state of the art, with an extension of the directly covered energy down by 55 keV, entering the Gamow window of the s process. Figure 4 shows the reaction yield, defined as the number of net counts in the detector per unit of charge as a function of the alpha beam energy. Only statistical uncertainties are shown in the plot A novel technique based on the γ-shape analysis method was developed with the main goal to monitor ^{13}C targets irradiated with an intense alpha beam. This in situ process drastically permitted to drastically reduce the overall uncertainty of the lowest energy data points. In addition, calibration measurements were performed with the reaction ^{51}V(p, n)^{51}Cr (Q=-1.534 MeV) at MTA ATOMKI. This reaction with a neutron threshold of E=1.565 MeV provides near isotropic, monoenergetic neutrons. The reaction product ^{51}Cr is radioactive with a half-life of 27 days, decaying back to ^{51}V through the emission of a characteristic gamma-ray of 320 keV. By comparing the number of detected neutrons to the number of created ^{51}Cr isotopes in a calibrated HPGe counting station at MTA Atomki the absolute detection efficiency of the neutron array has been established.

A final in-beam phase is scheduled for the first months of 2019 as last step before the conclusive data analysis.

6   LUNA MV

The activities to put in operation the new LUNA-MV facility continued along the year under the direct management of LNGS. In particular, the new accelerator room in Hall B has been completed and the control room as well as the preparation of the technological plants made important steps forward. The new accelerator has been completely assembled at the manufacturer site and the in-house acceptance tests will be performed in the year 2019. Several authorization processes are still on the way. On March 23rd, the LUNA-MV project has been the subject of a full review organized by the LNGS Scientific Committee which appointed an evaluation commission composed by T. Noble, L. Patrizii, A. Arcones, D. Santonocito and M. Taiuti. After the review, the commission released a report with a general appreciation and endorsement of the scientific program proposed by the LUNA Collaboration for the first five years of the LUNA-MV life. Furthermore, the commission suggested that the LUNA Collaboration has first rights for the development of the proposed 5-years program. In the meeting of October 2018, the LNGS Scientific Committee, concluded that "The suite of experiments initially proposed by the LUNA Collaboration is considered to be of strong scientific merit and in a relatively mature state of
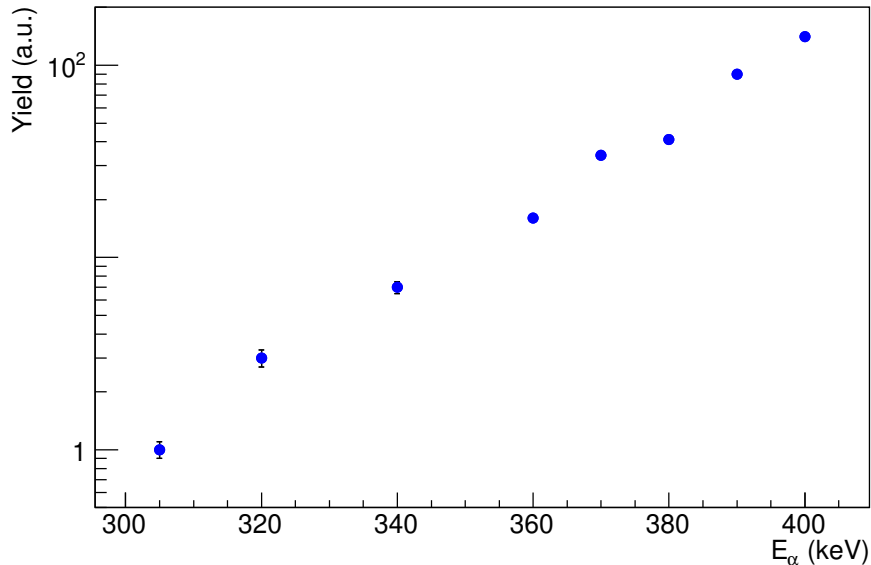
Figure 4: Preliminary $^{13}C(\alpha,n)^{16}O$ reaction yield as a function of alpha beam energy. Only statistical uncertainties are shown in the plot. It is evident the linear energy dependence in a y axis logarithmic scale plot

readiness, and hence will help ensure that the machine is occupied with priority experiments as soon as it is commissioned".

In this frame, the LUNA Collaboration started an intense R&D activity in preparation of the first experiments at LUNA-MV, as reported in the next sub-sections:

6.1 The ^{12}C + ^{12}C reaction

The rate of the ^{12}C+^{12}C reaction, which is the trigger of the carbon burning, is a primary input to predict the behavior of a star at the end of the Helium burning. Stellar models predict that quiescent carbon burning occurs for temperatures ranging between 0.5 and 1 GK, corresponding to center of mass energies between 0.9 and 3.4 MeV. However, the larger the ^{12}C+^{12}C rate, the lower the temperature of the carbon burning. As a consequence, also the duration of the C burning is modified by a variation of the ^{12}C+^{12}C rate [22]. Carbon burning influences the energy generation and nucleosynthesis of massive stars. As a matter of fact, the two main channels of this reaction release protons and α particles in a rather hot environment, thus allowing a complex chain of reactions involving nuclei from C to Si. Some of these reactions, e.g. the ^{13}C(α,n)^{16}O and the ^{22}Ne(α,n)^{25}Mg, may release neutrons and, in turn, activate the s-process which allows the production of about half of the heavy elements. The ^{12}C+^{12}C rate also affects the outcomes of type Ia supernovae at temperatures as low as 0.3 GK (corresponding to 1 MeV) [23]; such objects play a fundamental role in cosmology, allowing the measurements of distances and of the expansion rates of high redshift galaxies.

The ^{12}C+^{12}C reaction, characterized by a Coulomb barrier of about 6.7 MeV, can proceed through different channels corresponding to the emission of a photon, a neutron, a proton, an α particle or even two α particles or a ^{8}Be nucleus. Of these channels, the two more relevant are the emission of protons and α particles. The neutron emission becomes effective only for

center of mass energies larger than 2.6 MeV. The Q-value for proton emission is 2.24 MeV while that for α emission is 4.62 MeV. The proton and alpha channels can be measured either by detecting the charged particles or by revealing the gamma decay of the first excited state to the ground state of the ^{23}Na or ^{20}Ne residual nuclei, respectively. The energy of the two photons are 440 keV for the proton channel and 1634 keV for the alpha channel. Obviously, the gamma measurement cannot take into account the α_0 and p_0 (particles with the full energy which leave the residual nucleus in the ground state) as well as the contributions from high energy states of the residual nuclei which de-excite directly to the ground state. Approximately, the decay of the first excited state to the ground state accounts for 50% of the total cross section. So far, many different experiments attempted to measure the ^{12}C+^{12}C reaction using one of the two above described techniques or both. Direct measurements reached the minimum center of mass energies of 2.1 MeV [24] while only an indirect measurement explored the energy range down to 0.8 MeV [25].

The measurement of the ^{12}C+^{12}C reaction is affected by beam induced as well as natural background issues. The former are primarily due to impurities in the carbon target, since the ^{12}C beam purity achieved so far is extremely high, with contaminations less than one part in 10^{12}. The most prominent background is due to hydrogen and deuterium because of their ease of forming bonds with carbon. These ions are also deposited on the surface of carbon targets from the vacuum rest gas during measurements. The latter derive from naturally occurring sources, primarily ubiquitous natural radioisotopes, and are particularly relevant in the γ-ray spectrum at low beam energies (below 3 MeV): a massive lead shielding is thus required. However, in a laboratory at the Earth's surface, the shielding efficiency cannot be increased by further adding any more shield since the cosmic muons would interact with the added material, creating more background. Of course, this problem is dramatically reduced in the Gran Sasso underground laboratory where the rock overburden reduces the muon component of the cosmic background by a factor of 10^6. Therefore, a deep underground measurement represents a unique possibility to reach the low energy domain of the ^{12}C + ^{12}C reaction.

The ^{12}C+^{12}C reaction can be measured using the intense Carbon beam provided by the LUNA MV accelerator. In the energy range 0.5-3.5 MeV, the expected intensity is 150 μA for the ^{12}C$^+$ beam and 100 μA (corresponding to 50 particle μA) for the ^{12}C^{++} beam. Since the energy in the center of mass system is exactly one-half of the beam energy, the measurement can be performed with the more intense single charge state beam for $E_{cm} \leq 1750$ keV, approximately. For higher energies, only the ^{12}C^{++} beam can play the game. The beam will impinge on a solid ^{12}C target of natural composition with the as low as possible contamination due to hydrogen isotopes. Infintely thick targets (e.g. 1 mm thick) are preferable since they enhance counting rates and are more resistant.

The ^{12}C+^{12}C is the "flagship reaction" of the first 5 year scientific program with the LUNA MV accelerator and a specific working group has been appointed one year ago to define the experimental strategy. In particular, several tasks have been afforded:

- Definition of the energy range in which the reaction can be realistically measured at LUNA MV and calculation of the expected reaction rate, based on literature data and of background expected reduction at LNGS

- Study of ^{12}C target production and characterization, with particular emphasis on the strategy to reduce and quantify residual H and D impurities, which will cause beam induced background.

- Selection of the best detection system (detector and shielding) to be used for gamma and
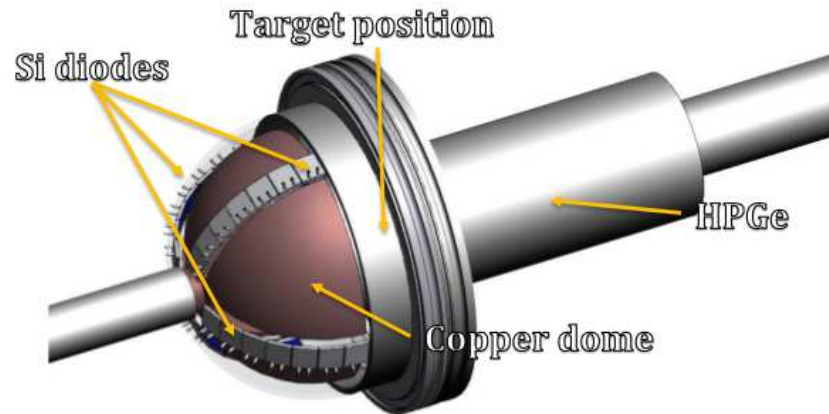
Figure 5: A possible experimental setup for the ^{12}C+^{12}C measurement allowing detection of photons and particles

particles.

Figure 5 shows an example of a possible experimental setup under study. The detection system is composed of an HPGe detector placed at zero degree with respect to the beam and an hemispherical array of silicon pin diode detectors in the backward hemisphere. The two halves of the setup can be used independently to detect the photons (HPGe) and the particles (silicon detectors) or at the same time for a combined measurement. Moreover, the HPGe detector can be heavily shielded as requested. Other solutions are also under evaluation.

6.2   The planned ^{14}N(p,γ)^{15}O experiment at LUNA MV

^{14}N(p,γ)^{15}O is the slowest and thus the most important reaction of the CNO cycle of hydrogen burning [26]. The CNO cycle plays an important role in several astrophysical sites and has therefore its importance in many key question of astrophysics from the solar abundance problem to the age of globular clusters. The knowledge of the ^{14}N(p,γ)^{15}O reaction rate (obtained from the cross section) is needed as it is a crucial a input parameter for various astrophysical models.

Using the 400 kV accelerator, the LUNA collaboration has provided so far the lowest energy data for the ^{14}N(p,γ)^{15}O cross section yielding far-reaching astrophysical consequences [27]. But despite the extensive experimental and theoretical efforts of the recent years, the ^{14}N(p,γ)^{15}O reaction rate is still not known at the required precision and further experiments are clearly necessary.

Armed with the experiences gained at the 400 kV accelerator, the study of the ^{14}N(p,γ)^{15}O reaction is a natural pilot project at the upcoming LUNA MV accelerator. With the new infrastructure, the LUNA 400 energy range can be connected to the higher energy region where contradicting data can be found in the literature and new, precise data are thus needed.

Preparatory works have been started for this projects. The development of solid state nitrogen targets is ongoing and their characterization will be done before the launch of LUNA MV. The design of the experimental setup including the vacuum chamber and detector configuration has also been started. According to the estimations based on the characteristics of the LUNA MV accelerator, the plan of the collaboration is to measure high precision cross sections and angular distribution from the 278 keV resonance up to 3 MeV. With this comprehensive dataset in a wide energy range, the extrapolation to the low, astrophysically relevant energy region can be carried out in a more reliable and accurate way.

References

[1] J. J. He *et al.*, Phys. Lett. B **725** (2013) 287

[2] G. X. Dong *et al.*, J. Phys. G: Nucl. Part. Phys. **44** (2017) 045201

[3] E. Di Valentino *et al.*, Phys. Rev. D **90** (2014) 023543

[4] F. Ferraro et al., Eur. Phys. J A **54** (2018) 44-54

[5] L.E. Marcucci et al., J. Phys. G43, 023002 (2016)

[6] F. Cavanna et al., Eur. Phys. J. A **50**, 179 (2014)

[7] F. Cavanna et al., Phys. Rev. Lett. **115**, 252501 (2015)

[8] R. Depalo et al., Phys. Rev. C **94**, 055804 (2016)

[9] F. Ferraro et al., Phys. Rev. Lett. **121**, 172701 (2018)

[10] F. Cavanna et al., Phys. Rev. Lett. **120**, 239901(E) (2018)

[11] D. Bemmerer et al., Europhys. Lett. **122**, 52001 (2018)

[12] C. Angulo et al., Nucl. Phys. A **656**, 3 (1999)

[13] A.L. Sallaska et al., Astrophys. J. Suppl. Ser. **207**, 18 (2013)

[14] K.J. Kelly et al., Phys. Rev. C **95**, 015806 (2017)

[15] F. Dell'Agli et al., Monthly Notices Royal Astronom. Soc. **475**, 3098 (2018)

[16] P. Ventura et al., Monthly Notices Royal Astronm. Soc. **475**, 2282 (2018)

[17] A.I. Karakas et al., Monthly Notices Royal Astronm. Soc. **477**, 421 (2018)

[18] S.E. Hale et al., Phys. Rev. C **65**, 015801 (2001)

[19] R. Schwengner et al., Phys. Rev. C **79**, 037303 (2009)

[20] R. Longland et al., Phys. Rev. C **85**, 065809 (2012)

[21] P. Adsley et al., Phys. Rev. C **96**, 055802 (2017)

[22] O. Straniero et al., JPhCS 665 (2016) 012008

[23] E. Bravo et al., A&A 535 (2011) 114

[24] T. Spillane et al., Phys. Rev.Lett. 98 (2007) 1225501

[25] A. Tumino et al., Nature 557 (2018) 687

[26] M. Wiescher, Phys. Perspect. **20** (2018) 124

[27] A. Lemut *et al.*, Phys. Lett. B **634** (2006) 483

7 List of Publications

1. *Direct capture cross section , the $E_p = 71, 105$ keV resonances in the ^{22}Ne$(p,\gamma)^{23}$Na reaction*
F. Ferraro, M.P. Takács, D. Piatti, F. Cavanna, R. Depalo, M. Aliotta, D. Bemmerer, A. Best, A. Boeltzig, C. Broggini, C.G. Bruno, A. Caciolli, T. Chillery, G.F. Ciani, P. Corvisiero, T. Davinson, A. Di Leva, Z. Elekes, E.M. Fiore, A. Formicola, Zs. Fülöp, G. Gervino, A. Guglielmetti, C. Gustavino, Gy. Gyürky, G. Imbriani, M. Junker, I. Kochanek, M. Lugaro, P. Marigo, R. Menegazzo, V. Mossa, F.R. Pantaleo, V. Paticchio, R. Perrino, P. Prati, L. Schiavulli, K. Stöckel, O. Straniero, T. Szücs, D. Trezzi, S. Zavatarelli, Physical Review Letters, **120**, 117702, (2018)
doi = 10.1103/PhysRevLett.120.117702

2. *Erratum: Three New Low-Energy Resonances in the ^{22}Ne$(p,\gamma)^{23}$Na Reaction*
F. Cavanna, R. Depalo, M. Aliotta, M. Anders, D. Bemmerer, A. Best, A. Boeltzig, C. Broggini, C. G. Bruno, A. Caciolli, P. Corvisiero, T. Davinson, A. di Leva, Z. Elekes, F. Ferraro, A. Formicola, Zs. Fülöp, G. Gervino, A. Guglielmetti, C. Gustavino, Gy. Gyürky, G. Imbriani, M. Junker, R. Menegazzo, V. Mossa, F. R. Pantaleo, P. Prati, D. A. Scott, E. Somorjai, O. Straniero, F. Strieder, Ts. Szücs, M.P. Takács, D. Trezzi, Physical Review Letters **120**, 239901(E) (2018)
doi = 10.1103/PhysRevLett.120.239901

3. *Improved pulse shape discrimination for high pressure ^3He counters*
   J. Balibrea Correa, G.F. Ciani, R. Buompane, F. Cavanna, L. Csedreki, R. Depalo, F. Ferraro, A. Best, Nuclear Instruments and Methods in Physics Research Section A, **906**, 103-109, (2018)
   doi = 10.1016/j.nima.2018.07.086

4. *Effect of beam energy straggling on resonant yield in thin gas targets: The cases $^{22}Ne(p, \gamma)^{23}Na$ and $^{14}N(p, \gamma)^{15}O$*
   D. Bemmerer, F. Cavanna, R. Depalo, M. Aliotta, M. Anders, A. Boeltzig, C. Broggini, C.G. Bruno, A. Caciolli, T. Chillery, P. Corvisiero, T. Davinson, Z. Elekes, F. Ferraro, A. Formicola, Zs. Fülöp, G. Gervino, A. Guglielmetti, C. Gustavino, Gy. Gyürky, R. Menegazzo, V. Mossa, F.R. Pantaleo, P. Prati, D. A. Scott, K. Stöckel, O. Straniero, T. Szücs, M. P. Takács, D. Trezzi, Europhysics Letters, **122**, 5, 52001 (2018)
   doi=10.1209/0295-5075/122/52001

5. *A high-efficiency gas target setup for underground experiments, , redetermination of the branching ratio of the 189.5 keV $^{22}Ne(p, \gamma)^{23}Na$ resonance*
   F. Ferraro, M. P. Takács, D. Piatti, V. Mossa, M. Aliotta, D. Bemmerer, A. Best, A. Boeltzig, C. Broggini, C.G. Bruno, A. Caciolli, F. Cavanna, T. Chillery, G. F. Ciani, P. Corvisiero, L. Csedreki, T. Davinson, R. Depalo, G. D´Erasmo, A. Di Leva, Z. Elekes, E. M. Fiore, A. Formicola, Zs. Fülöp, G. Gervino, A. Guglielmetti, C. Gustavino, Gy. Gyürky, G. Imbriani, M. Junker, I. Kochanek, M. Lugaro, L. E. Marcucci, P. Marigo, R. Menegazzo, F. R. Pantaleo, V. Paticchio, R. Perrino, P. Prati, L. Schiavulli, K. Stöckel, O. Straniero, T. Szücs, D. Trezzi, S. Zavatarelli, The European Physical Journal A, **54**(3), 44 (2018)
   doi=10.1140/epja/i2018-12476-7

6. *Improved background suppression for radiative capture reactions at LUNA with HPGe and BGO detectors*
   A. Boeltzig, A. Best, G. Imbriani, M. Junker, M. Aliotta, D. Bemmerer, C. Broggini, C. G. Bruno, R. Buompane, A. Caciolli, F. Cavanna, T. Chillery, G. F. Ciani, P. Corvisiero, L. Csedreki, T. Davinson, R. J. DeBoer, R. Depalo, A. Di Leva, Z. Elekes, F. Ferraro, E. M. Fiore, A. Formicola, Zs. Fülöp, G. Gervino, A. Guglielmetti, C. Gustavino, Gy. Gyürky, I. Kochanek, R. Menegazzo, V. Mossa, F. R. Pantaleo, V. Paticchio, R. Perrino, D. Piatti, P. Prati, L. Schiavulli, K. Stöckel, O. Straniero, F. Strieder, T. Szücs, M. P. Takács, D. Trezzi, M. Wiescher, S. Zavatarelli, Journal of Physics G: Nuclear and Particle Physics, **45**, 025203 (2018)
   doi=10.1088/1361-6471/aaa163

8 Conference Proceedings

1. R. Depalo, *Nuclear Astrophysics Deep Underground*, 21st International Conference on Particles and Nuclei (PANIC), Beijing, China
   International Journal of Modern Physics-Conference Series 46 (2018) 1860003

2. R. Depalo, *Latest results from LUNA*, Nuclear Physics in Astrophysics Conference (NPA VII)
   Journal of Physics Conference Series 940 (2018) 012026

3. Thomas Chillery Proton-Induced Reactions of Astrophysical Interest
   European Physical Journal Web of Conferences 184, 02001 (2018)

9   Invited talks

1. M. Aliotta, EuNPC conference, Bologna Italy, 2-7 September 2018

2. M. Aliotta, ChETEC Training School, Bucharest Romania, 10-20 April 2018

3. C.G. Bruno, 41st Symposium on Nuclear Physics, Cocoyoc Mexico, 8-11 January

4. C.G. Bruno, EuNPC conference Bologna Italy, 2-7 September 2018

5. C. Broggini, Frontier Research in Astrophysics, Mondello Italy, 28 May-2 June 2018

6. A. Guglielmetti, 5th international solar neutrino conference, Dresden Germany, 11-14 June 2018

7. A. Guglielmetti, SIF Società Italiana di Fisica, Rende (Cs) Italy, 17-21 September 2018

8. C. Gustavino, 56th International Winter Meeting on Nuclear Physics, Bormio Italy, 23-28 January 2018

9. C. Gustavino, Frontier Objects in Astrophysics and Particle Physics, Vulcano Italy 20-26 May 2018

10. C. Gustavino, 7th Roman Int. Conf. on Astroparticle Physics, Roma Italy, 4-7 September 2018

11. C. Gustavino, DEUS Workshop, IEEE NSS/MIC conference, Sidney Australia, 10-18 November 2018

12. G. Imbriani, 5th International Solar Neutrino Conference, Dresden Germany, 11-14 June 2018

13. P. Prati, NIC XV, Laboratori Nazionali del Gran Sasso, Assergi (Aq.) Italy, 24-29 June 2018

14. O. Straniero, Frontier objects in Astrophysics and Particle Physics, Vulcano Italy, 20-26 May 2018

15. A. Caciolli, 5th International Solar Neutrino Conference, Dresden Germany 11-14 June 2018

16. A. Caciolli, Carpathian Summer School of Physics 2018 Exotic Nuclei and Nuclear/Particle Astrophysics (VII), Physics with small accelerators, Romania, 1-14 July 2018

17. R. Depalo, 13th international conference on nucleus-nucleus collisions, Saitama Japan, 4-8 December 2018

18. G. Imbriani, NUSTAR week, Milano Italy, 24-28 September 2018

10   Contributed talks

1. F. Cavanna, 15th Varenna Conference on Nuclear Reaction Mechanisms, Varenna Italy, 11-15 June 2018

2. F. Cavanna, XXII International Conference on Few-Body Problems in Physics Caen, France 9-13 July 2018

3. T. Chillery, EuNPC conference, Bologna Italy, 2-7 September 2018

4. F. Ferraro, EuNPC conference, Bologna Italy, 2-7 September 2018

5. R. Depalo, 5th International Solar Neutrino Conference Dresden, Germany 11-15 June 2018

6. G.F. Ciani, XXII International Conference on Few-Body Problems in Physics, Caen France 9-13 July 2018

7. V. Mossa, INFN2018, Laboratori Nazionali del Sud Italy, 7-9 November 2018

8. A. Best, NIC XV, Laboratori Nazionali del Gran Sasso, Assergi (Aq.) Italy, 24-29 June 2018

9. S. Zavatarelli, NIC XV, Laboratori Nazionali del Gran Sasso, Assergi (Aq.) Italy, 24-29 June 2018

11   Posters

1. F. Ferraro, NIC XV, Laboratori Nazionali del Gran Sasso, Assergi (Aq.) Italy, 24-29 June 2018

2. G.F. Ciani, NIC XV, Laboratori Nazionali del Gran Sasso, Assergi (Aq.) Italy, 24-29 June 2018

3. V. Mossa, NIC XV, Laboratori Nazionali del Gran Sasso, Assergi (Aq.) Italy, 24-29 June 2018

4. L. Csedreki, NIC XV, Laboratori Nazionali del Gran Sasso, Assergi (Aq.) Italy, 24-29 June 2018

5. A. Caciolli, D. Bemmerer, NIC XV, Laboratori Nazionali del Gran Sasso, Assergi (Aq.) Italy, 24-29 June 2018

6. A. Caciolli, EuNPC conference, Bologna Italy, 2-7 September 2018

12   PhD Theses

The Study of $^{22}Ne(\alpha,\gamma)^{26}Mg$ and $^{6}Li(p,\gamma)^{7}Be$ Reactions at LUNA
Denise Piatti, PhD thesis
Università degli Studi di Padova, December 2018
Supervisor: Dr. Carlo Broggini
Referee: PD. Dr. Daniel Bemmerer, Prof. Pietro Corvisiero

XENON

E. Aprile[a]*, J. Aalbers[b], F. Agostini[c,d], M. Alfonsi[e], F. D. Amaro[f],

M. Anthony[a], F. Arneodo[g], P. Barrow[h], L. Baudis[h], B. Bauermeister[i],

M. L. Benabderrahmane[g], T. Berger[j], P. A. Breur[b], A. Brown[b], E. Brown[j],

S. Bruenner[k], G. Bruno[c], R. Budnik[l], L. Butikofer[m], J. Calvén[i],

J. M. R. Cardoso[f], M. Cervantes[n], D. Chicon[k], D. Coderre[m], A. P. Colijn[b],

J. Conrad[i], J. P. Cussonneau[o], M. P. Decowski[b], P. de Perio[a], P. Di Gangi[d],

A. Di Giovanni[g], S. Diglio[o], E. Duchovni[l], G. Eurin[k], J. Fei[p], A. D. Ferella[i],

A. Fieguth[q], D. Franco[h], W. Fulgione[c,r], A. Gallo Rosso[c], M. Galloway[h],

F. Gao[a], M. Garbini[d], C. Geis[e], L. W. Goetzke[a], L. Grandi[s], Z. Greene[a],

C. Grignon[e], C. Hasterock[k], E. Hogenbirk[b], R. Itay[l], B. Kaminsky[m],

G. Kessler[h], A. Kish[h], A. Kopec[n], H. Landsman[l], R. F. Lang[n], D. Lellouch[l],

L. Levinston[l], M. Le Calloch[o], Q. Lin[a], S. Lindemann[k,m], M. Lindner[k],

J. A. M. Lopes[f], A. Manfredini[l], I. Maris[g], T. Marrodán Undagoitia[k],

J. Masbou[o], F. V. Massoli[d], D. Masson[n], D. Mayani Paras[h], Y. Meng[t],
M. Messina[a], K. Micheneau[o], B. Miguez[r], A. Molinario[c], M. Murra[q],

J. Naganoma[u], K. Ni[p], U. Oberlack[e], S. E. A. Orrigo[f], P. Pakarha[h],

B. Pelssers[i], R. Persiani[o], F. Piastra[h], J. Pienaar[n], M.-C. Piro[j],

V. Pizzella[k], G. Plante[a], N. Priel[l], L. Rauch[k], S. Reichard[n], C. Reuter[n],

A. Rizzo[a], S. Rosendahl[q], N. Rupp[k], R. Saldanha[s], J. M. F. dos Santos[f],

G. Sartorelli[d], M. Scheibelhut[e], S. Shindler[e], J. Schreiner[k], M. Schumann[m],

L. Scotto Lavina[v], M. Selvi[d], P. Shagin[u], E. Shockley[s], M. Silva[f],

H. Simgen[k], M. von Sivers[m], A. Stein[t], D. Thers[o], A. Tiseni[b],

G. Trinchero[r], C. Tunnell[b,s], N. Upole[s], H. Wang[t], Y. Wei[h],

C. Weinheimer[q] J. Wulf[h], J. Ye[p], Y. Zhang[a].

(The XENON Collaboration)

---

*Spokesperson

[a] Physics Department, Columbia University, New York, NY, USA

[b] Nikhef and the University of Amsterdam, Science Park, Amsterdam, Netherlands

[c] INFN-Laboratori Nazionali del Gran Sasso and Gran Sasso Science Institute, L'Aquila, Italy

[d] Department of Physics and Astrophysics, University of Bologna and INFN-Bologna, Bologna, Italy

[e] Institut für Physik & Exzellenzcluster PRISMA, Johannes Gutenberg-Universität Mainz, Mainz, Germany

[f] Department of Physics, University of Coimbra, Coimbra, Portugal

[g] New York University in Abu Dhabi, Abu Dhabi, United Arab Emirates

[h] Physik-Institut, University of Zürich, Zürich, Switzerland

[i] Oskar Klein Centre, Department of Physics, Stockholm University, AlbaNova, Stockholm, Sweden

[j] Department of Physics, Applied Physics and Astronomy, Rensselaer Polytechnic Institute, Troy, NY, USA

[k] Max-Planck-Institut für Kernphysik, Heidelberg, Germany

[l] Department of Particle Physics and Astrophysics, Weizmann Institute of Science, Rehovot, Israel

[m] Physikalisches Institut, Universität Freiburg, 79104 Freiburg, Germany

[n] Department of Physics and Astronomy, Purdue University, West Lafayette, IN, USA

[o] SUBATECH, Ecole des Mines de Nantes, CNRS/In2p3, Université de Nantes, Nantes, France

[p] Department of Physics, University of California, San Diego, CA, USA

[q] Institut für Kernphysik, Wilhelms-Universität Münster, Münster, Germany

[r] INFN-Torino and Osservatorio Astrofisico di Torino, Torino, Italy

[s] Department of Physics & Kavli Institute of Cosmological Physics, University of Chicago, Chicago, IL, USA

[t] Physics & Astronomy Department, University of California, Los Angeles, CA, USA

[u] Department of Physics and Astronomy, Rice University, Houston, TX, USA

[v] LPNHE, Université Pierre et Marie Curie, Université Paris Diderot, CNRS/IN2P3, Paris 75252, France

Abstract

In 2018, the XENON collaboration accumulated the world's first one ton $\times$ year of dark matter search data using liquid xenon. Combined with very low background and excellent background rejection capability, the XENON1T detector achieved a new record upper limit for the WIMP-nucleon interaction cross section down to 4.1×10^{-47} cm^2 for a WIMP mass of 30 GeV/c^2. After upgrading the purification system, testing online radon distillation to reduce the radon background, and deployment of a new ^{37}Ar calibration source, XENON1T data taking was stopped at the end of 2018. The collaboration is currently upgrading the detector to XENONnT with three times more active liquid xenon target and lower backgrounds. Start of operations is planned for late 2019.

1   Introduction

The XENON collaboration operates a series of direct detection experiments at LNGS to search for dark matter particles in our Milky Way. The experiments use dual-phase liquid xenon time-projection chambers (TPCs) which are particularly well-suited to search for one of the most compelling dark matter candidate particle, the Weakly Interacting Massive Particle (WIMP), over a broad range of parameters. Starting with the XENON10 experiment more than a decade ago, the collaboration has successively built larger and more sensitive detectors. The XENON100 experiment was the world's most sensitive direct detection dark matter experiment for a number of years, until late 2013, and the 2018 results from the subsequent XENON1T experiment currently give the most constraining limit on the spin independent WIMP-nucleon cross section of $\sigma_{WN} < 4.1 \times 10^{-47}$ cm^2 for a WIMP mass of 30 GeV/c^2 [5]. XENON1T data taking ended as of late 2018, and the detector is now being upgraded to the next phase of the experiment, XENONnT, which will reach its projected sensitivity of $\sigma_{WN} \sim 2 \times 10^{-48}$ cm^2 for a WIMP mass of 30 GeV/c^2 [2]. The swift experimental upgrade is possible due to already designing much of
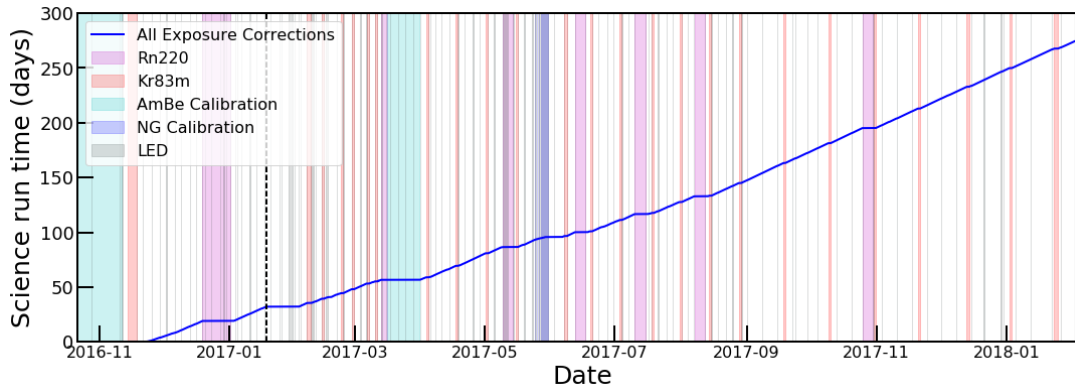
Figure 1: XENON1T data taking, with a total of about 300 live-days of dark matter search data. The experiment is regularly calibrated with ^{220}Rn, ^{83m}Kr, neutron and LED calibration sources.

the XENON1T infrastructure to be compatible with XENONnT, and by beginning portions of the upgrade in parallel to the completion of XENON1T. The progress made in 2018 is presented here.

2 XENON1T

2.1 Operations

XENON1T acquired science data until February 8, 2018 [5], with about 280 live-days of science data (Science Run-1, SR1), in addition to the 34 days acquired during Science Run-0 (SR0). Detector operations had been very stable until the blackout on February 25th, 2018. Thanks to the well-designed XENON1T safety systems, the detector was kept in safe condition during the lab-wide blackout. The dedicated UPS kept the important systems working. The emergency LN2 cooling system automatically started, critical detector parameters could be controlled through the underground slow control touch panels, and the detector parameters were recorded by the logging system. Except for the electron lifetime, the detector came back to the same operational conditions in the week of March 4th, 2018, which culminated in a 1 tonne×year exposure.

The XENON1T data are automatically transferred from LNGS to remote sites for storage and further processing using the computing Grid. Our sophisticated slow control system notifies experts in case detector parameters go out of range. Experts can then often resolve any potential issues remotely.

As shown in Fig.1, the XENON1T detector continuously acquired data since October 2016. By February 2018 we had accumulated 278.8 days total livetime, split into two Science Runs of 32.1 days (SR0) and 246.7 days (SR1). SR0 was collected between October 2016 and January 18, 2017, when an earthquake of magnitude 5.7 caused a two-week downtime. SR1 began immediately afterwards and the new analysis considers the data up to February 8, 2018, while the detector continued to run and collect data. The main operational difference after the earthquake incident (i.e. between the two science runs) is the cathode voltage, which had to be lowered from -12 kV for SR0 to -8 kV for SR1. All key detector parameters were continuously monitored to ensure operational stability. The experiment was regularly calibrated with ^{220}Rn, ^{83m}Kr, neutron and LED calibration sources.
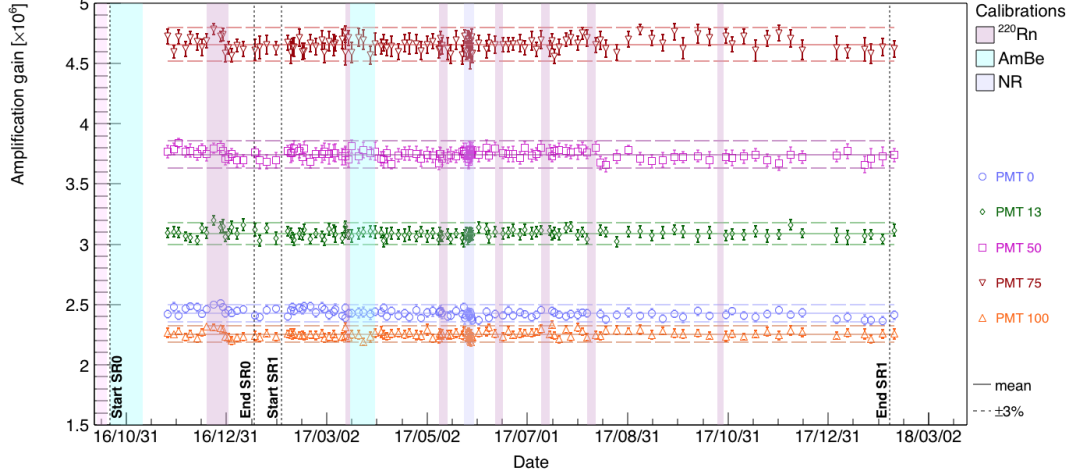
Figure 2: PMT gain evolution, through the whole duration of SR0 and SR1, of randomly selected good (i.e. no leaks) PMTs exhibiting different gain

2.2 Photomultiplier tubes

The photosensors of the XENON1T TPC are in stable operation and their average gain fluctuation, mostly due to the measurement precision, is less than 2% RMS as shown in Figure 2. As reported previously, 35 of the 248 Hamamatsu R11410-21 PMTs were switched off or excluded from analysis of the first science run due to poor performance, e.g. electrical micro-discharges and subsequent photon emission, and deterioration of the amplification gain and quantum efficiency. The rate of PMT losses is greatly reduced now; only one additional PMT had to be removed from the analysis during the last year. The issues have been identified to be related to a production problem, i.e. loss of vacuum, and the faulty units will be replaced under warranty for the XENONnT detector upgrade.

2.3 New science run (SR1)

The detector's effective livetime is reduced by removing periods when the muon veto is either actively triggering or disabled (3.4 days), when leaking PMTs are emitting light (0.6 days), and time after high energy background events that induce photo-ionization and delayed electron extraction activity, reducing the sensitivity to low energy signals (12.3 days). Various internal and external radioactive sources were deployed to calibrate the detector. GXe is flushed through a 83Rb source to introduce 83mKr into the LXe injection line, providing a homogeneous distribution of 9.4 keV and 32.1 keV conversion electrons within the active volume. This data was collected every 2 ± 2.5 weeks to monitor the electron lifetime, S1 and S2 yields, drift field distortion, and charge build-up on the PTFE panels. Low energy electronic recoils (ER) were calibrated with 17.1 days of data taken with an internal 220Rn source, split into 6 periods spread throughout SR1 and 1 period near the middle of SR0. Nuclear recoil (NR) calibration was performed with 30.0 days of exposure to an external AmBe source, about half split between science runs, and 1.9 days of exposure to a D-D neutron generator (NG). The number of low energy NR events found in the inner volume is about the same for each of these datasets. To minimize human bias, the DM search data was blinded in the NR signal region until the analysis was frozen. The blinded region was defined in discrimination (S2/S1) space between the

S2 threshold of 200 PE and the ER lower 2σ quantile. After all selection criteria, signal and background models, and statistical inference procedures were fixed, data was unblinded. No excess signal was observed above the background and results were reported [5] as an upper limit for spin-independent interaction cross section.

2.4 Further Data Acquisition

After the conclusion of the published SR1 data acquisition [5], the XENON collaboration has taken additional calibration data, and tested hardware for XENONnT. The additional calibrations include neutron generator data on different locations, anode voltage scanning with ^{83m}Kr source, and the ^{220}Rn calibrations. We upgraded the purification system by replacing 1/2" lines with 1" lines to reduce the flow resistance, and by replacing three QDrive pumps [4] with a radon-free magnetic pump [6]. By changing the lines, the circulation speed has increased from 50 slpm to 80 slpm, which has resulted in an improvement of the electron lifetime from 650 μs to 1 ms as shown in Fig. 3 (left). Figure 3 (right) shows the achievement of a factor three reduction in the radon concentration, thanks to the magnetic pump and the online radon distillation [3].

In October 2018 the new calibration source 37Ar has been added to the XENON calibration system. This isotope decays into 37Cl by electron capture with a half-life of 35 days, emitting two lines at 2.8 keV and 0.27 keV, thus providing point-like energy deposition in the LXe with low-energy mono-energetic lines. These calibration lines are the lowest energy lines used so far in LXe TPCs, and is thus of prime importance for XENONnT. A first calibration campaign has been performed in October and November 2018; the analysis of the data is ongoing and very promising, see figure 4. In particular, we managed to effectively remove the source via cryogenic distillation.

Additional calibration runs have been acquired with a new 83mKr source as well as with the neutron generator. Data taking for XENON1T has been officially terminated on December 3rd, 2018. One week prior to the recuperation of the entire liquid xenon inventory into the ReStoX vessel, a 'stress test' of the new XENONnT data acquisition system using the XENON1T PMTs as input channels was carried out. The test was successful and will considerably reduce the commissioning time of the final system for XENONnT.

2.5 Physics Analysis

The analysis of 1 ton $\times$ year exposure of XENON1T, accumulated from October 2016 until February 2018, led to the result published in Phys. Rev. Lett. [5]. The XENON1T 1 ton$\times$year data are shown in Fig. 5. No significant excess of spin-independent elastic scattering WIMP signal over background was found. The world leading sensitivity for spin-independent WIMP search has been reached and the most stringent constraint have been set, as shown in Fig. 6.

After the release of the 1 ton$\times$year data and the results of spin-independent WIMP search, the analysis effort switched to testing alternative dark matter models and search for new physics. Three major analysis regimes are being explored. First, with the lowest electromagnetic background in XENON1T, the data are also sensitive to alternative dark matter models, such as inelastic dark matter, dark photon, superWIMPs, etc. With the generalized and refined analysis framework of XENON1T, these studies are progressing rapidly. Second, the analysis team is searching for light WIMPs using data with lower energy threshold than the currently-published one. Various WIMP mass ranges are going to be studied through different scattering channels, such as the inelastic scatter-induced Bremsstrahlung signals, WIMP-electron interaction, and electronic recoils due to the Migdal effect. Third, high energy electronic recoil (ER) data are under study for the search of two-neutrino double electron capture (2νEC) and neutrinoless double
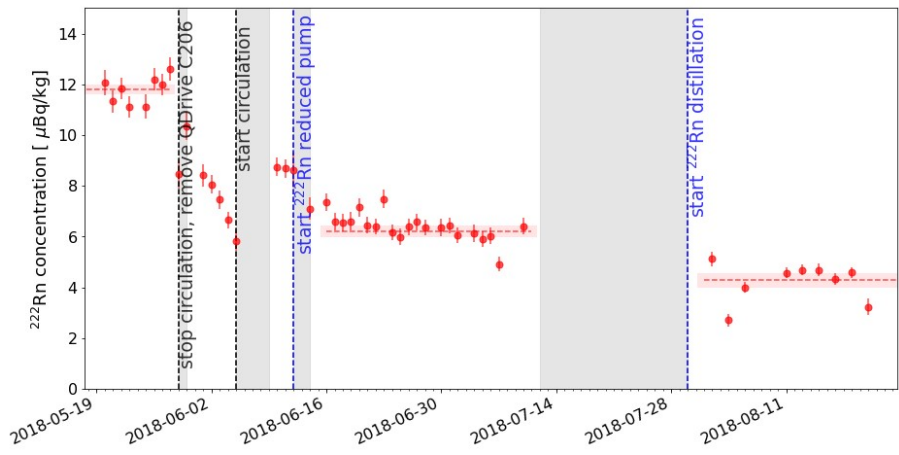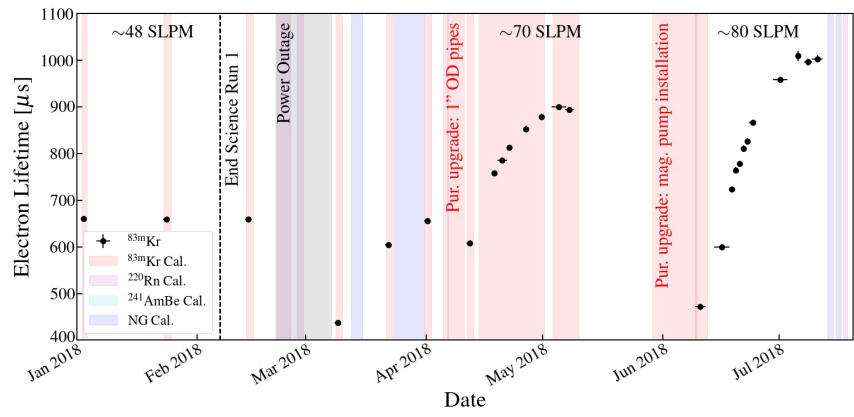
Figure 3: The XENON1T electron lifetime evolution by the upgraded purification system (top) and the ^{222}Rn concentration improvement due to the radon-free magnetic pump and the online radon distillation system (bottom).
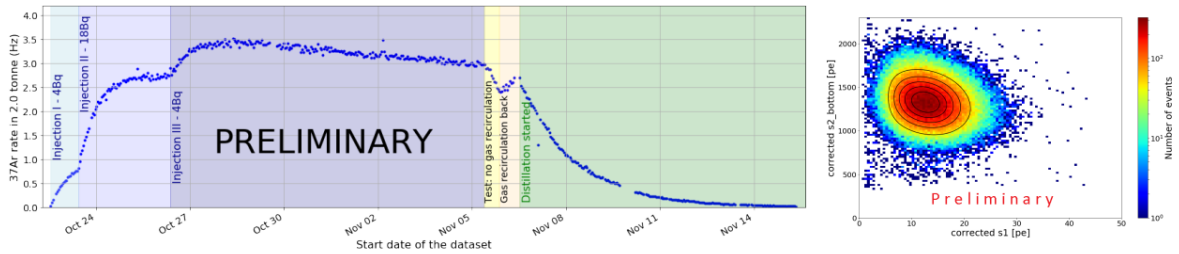
Figure 4: An 37Ar calibration run was performed in fall 2018 to investigate the use of this low-energy source for XENONnT. (left) The isotope has been injected three times and was successfully removed via cryogenic distillation after data-taking. (right) The image shows the clearly visible 2.8 keV line in the charge-vs.-light parameter space.

Figure 5: DM search data in the 1.3 t fiducial mass distributed in (cS2b, cS1) (left) and (cS2b, R2) (right) parameter spaces. The distributions of different background components are marked with different colors. Vertical shaded regions are outside the ROI. Gray lines show iso-energy contours in nuclear recoil energy.
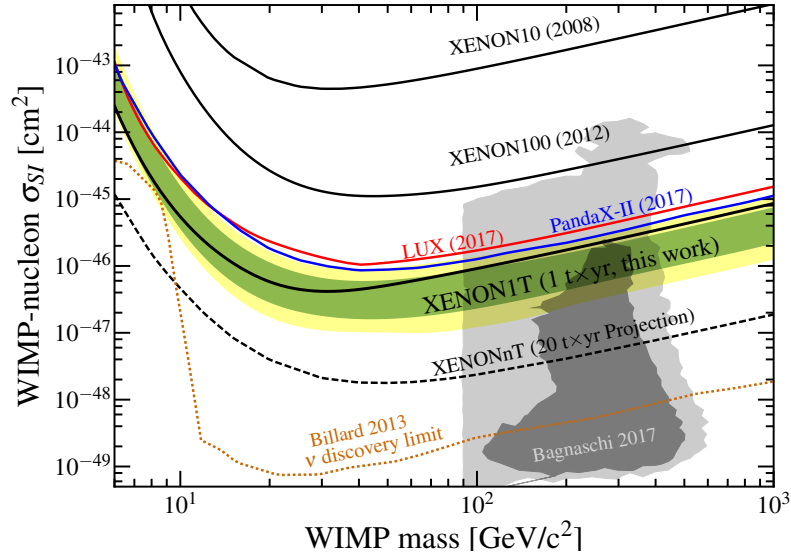
Figure 6: The progress on constraining the WIMP-nucleon spin-independent cross sections from the XENON10, XENON100 and the latest of XENON1T experiment. Results from LUX [1] and PandaX-II [7] are shown for comparison. The expected sensitivity for XENONnT with 20 ton×year of exposure is shown.
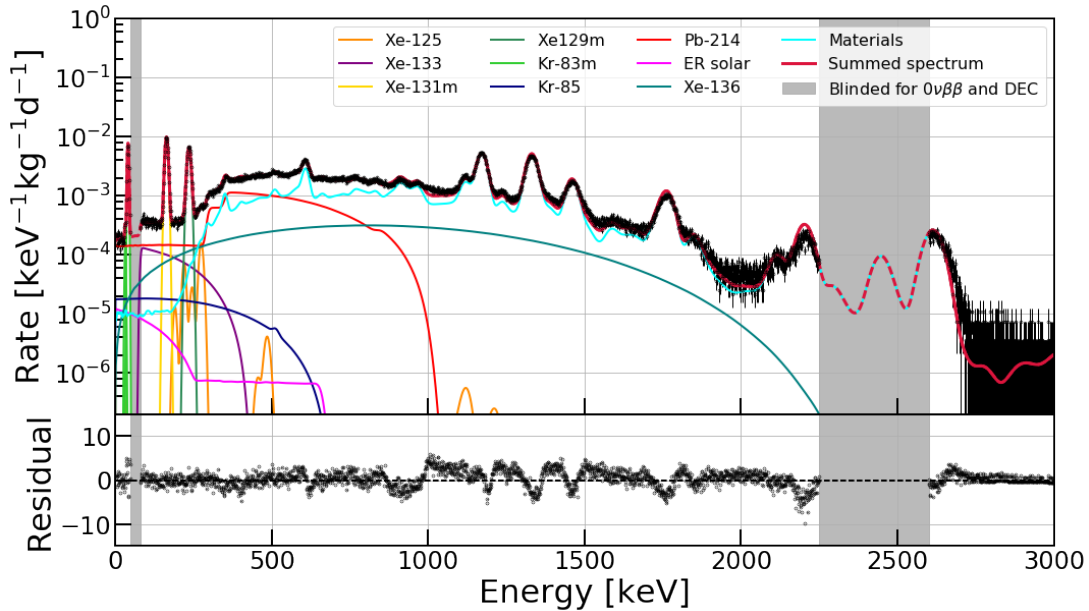

Figure 7: The ER background spectrum of XENON1T (black solid), compared with the Monte Carlo expectation (red solid). The components of the background are shown in different colors as well. The shaded regions are the interested regions for $2\nu EC$ and $0\nu\beta\beta$ searches, which are both blinded.

beta decay ($0\nu\beta\beta$) signals in liquid xenon. Fig. 7 shows the whole ER spectrum of XENON1T. XENON1T signal reconstruction has excellent linearity and energy resolution in both low and high energy region. Both of these ensure good data quality for search of 2νEC and $0\nu\beta\beta$. The regions of interest for 2νEC and $0\nu\beta\beta$ remained blinded until the analysis was completed in 2019.

3 XENONnT

The preparation of the XENONnT phase, aiming at a factor 10 improvement in sensitivity compared to XENON1T, is ongoing. Currently, the design, construction, procurement, production and testing of the various components required for the upgrade is ongoing. The full amount of Hamamatsu R11410-21 PMTs as well as more than 8t of Xenon gas are already in our hands. Many of the low-background materials have already been identified using the screening facilities of the collaboratio. Additional electronics required for XENONnT was mostly purchased already as well.

After submission of the Technical Design Report in Spring of 2018, the collaboration started a focused effort on XENONnT in order to have the upgrade operational by the Fall of 2019. Even
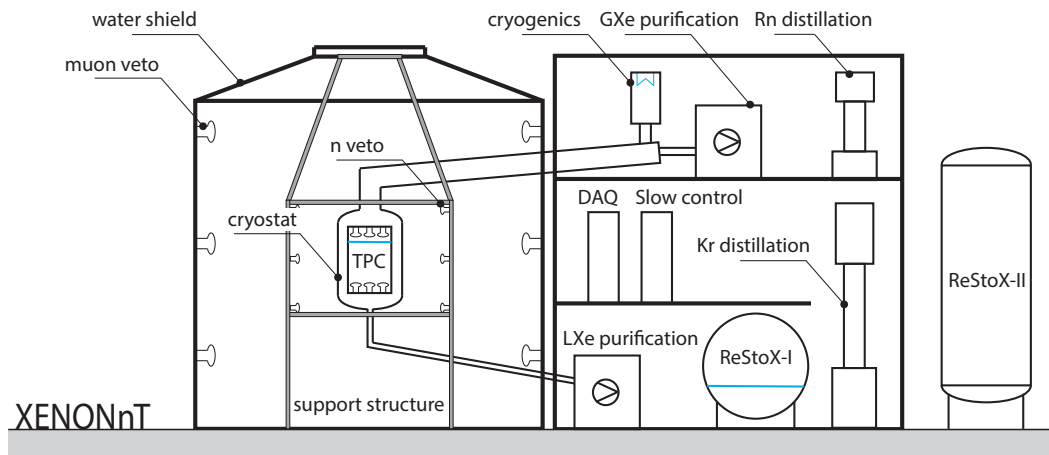

Figure 8: *Overview of the XENONnT experiment.*

though the overall XENONnT detector will look similar in many ways to XENON1T, nearly all of the sub-systems will be improved to some extent, informed by the experience with our previous generation of XENON detectors. An overview of the systems composing the new experiment is presented in Fig. 8. At the same time, preparations for a new larger cleanroom, where we intend to build our new TPC, are ongoing in the Hall di Montaggio. Major improvements with respect to XENON1T are the much larger cryostat to host 8 t of liquid xenon (6 t of which active inside the TPC), a new storage tank (ReStoX2) to store the same amount of xenon, a novel liquid xenon purification system including a radon distillation column, and a neutron veto surrounding the TPC.

The design of the low-background Time Projection Chamber (TPC) that constitutes the heart of XENONnT was nearly finished, most radio-pure materials for detector construction are in hand and have been screened, and production of components was scheduled to start. Important design choices have been validated using full-scale mockups, e.g, for the PMT arrays or the TPC field cage. Compared to XENON1T, we expect that the new design will result in

a superior electrical field configuration. In parallel, the additional photomultiplier tubes have been produced by Hamamatsu and have all been delivered.
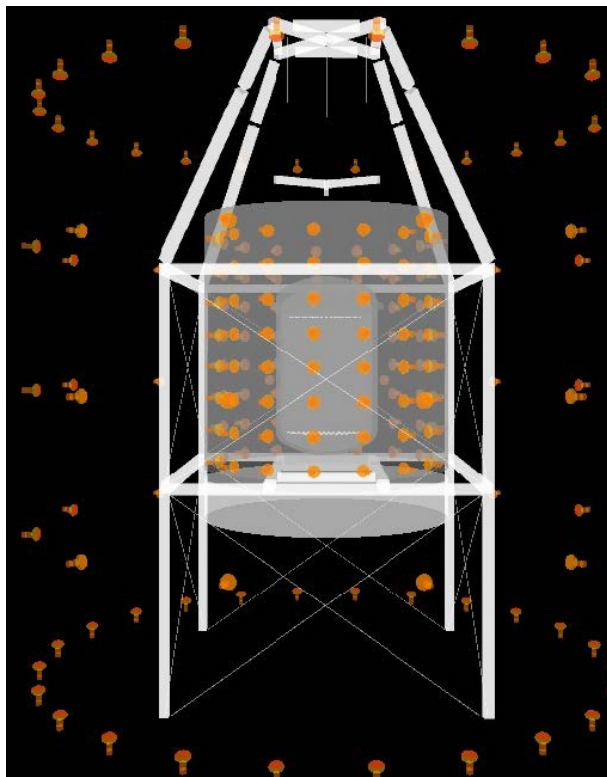

Figure 9: GEANT4 model of the XENONnT neutron veto with Gd-loaded water: in orange the PMTs, and in light gray the Tyvec reflector to contain the Cherenkov light in the neutron veto region outside the cryostat.

A neutron veto composed of Gd-doped liquid scintillator was originally proposed, but safety and environmental concerns discussed extensively with the LNGS technical staff in the last months led us to explore a different solution: Doping the whole water in the Muon Veto with $Gd_2(SO_4)_3$-octahydrate to increase the neutron capture efficiency. This technique has been studied for many years in the EGADS [8] test setup for Super-Kamiokande. Following the successful tests, by 2019 the whole SK detector will be filled with Gd-loaded water. This option has been decided as the final one for the XENONnT neutron veto. Monte Carlo simulations predict that with a 0.2% Gd mass fraction in the water, 120 additional PMTs mounted close to the XENONnT cryostat, and a Tyvec reflector behind them to effectively collect the Cherenkov light ultimately caused by a neutron capture, we can obtain at least 85% rejection rate for neutrons.

4   Publications

We published the following papers in 2018:

1. **"Dark Matter Search Results from a One Ton-Year Exposure of XENON1T"**
   E. Aprile *et al.* [XENON Collaboration].

arXiv:1805.12562 [astro-ph.CO]
Phys. Rev. Lett. **121**, no. 11, 111302 (2018)

2. **"First results on the scalar WIMP-pion coupling, using the XENON1T experiment"**
E. Aprile *et al.* [XENON Collaboration].
arXiv:1811.12482 [hep-ph]
Phys. Rev. Lett. **122**, no. 7, 071301 (2019)

References

[1] DS Akerib, S Alsum, HM Araújo, X Bai, AJ Bailey, J Balajthy, P Beltrame, EP Bernard, A Bernstein, TP Biesiadzinski, et al. Results from a search for dark matter in the complete lux exposure. *Phys. Rev. Lett.*, 118(2):021303, 2017.

[2] E. Aprile et al. Physics reach of the XENON1T dark matter experiment. *JCAP*, 1604(04):027, 2016.

[3] E. Aprile et al. Online^{222} Rn removal by cryogenic distillation in the XENON100 experiment. *Eur. Phys. J.*, C77(6):358, 2017.

[4] E. Aprile et al. The XENON1T Dark Matter Experiment. *Eur. Phys. J.*, C77(12):881, 2017.

[5] E. Aprile et al. Dark matter search results from a one ton-year exposure of xenon1t. *Phys. Rev. Lett.*, 121:111302, Sep 2018.

[6] E. Brown et al. Magnetically-coupled piston pump for high-purity gas applications. *Eur. Phys. J.*, C78:604, 2018.

[7] Xiangyi Cui et al. Dark matter results from 54-ton-day exposure of pandax-ii experiment. *Phys. Rev. Lett.*, 119(18):181302, 2017.

[8] A. Renshaw et al. Research and Development for a Gadolinium Doped Water Cherenkov Detector. *Physics Procedia*, 37:1249, 2012.

Cosmic Silence

L. Satta[a]

E. Bortolin[b], C. De Angelis[b], G. Esposito[b], C. Nuccetelli[b], C. Quattrini[b], M.A. Tabocchini[a,b*]

E. Alesse[c],

M. Balata[d],

G. Carinci[e], O. Frasciello[e], M. Chiti[e]

G. Cenci[a,f], F. Cipressa[a,f], A.Porrazzo[f], A. De Gregorio [f], P. Morciano[f]

[a]Museo Storico della Fisica e Centro Studi e Ricerche Enrico Fermi
[b]Istituto Superiore di Sanità, and INFN-Roma1
[c]L'Aquila University, Department of Biotechnological and Applied Clinical Sciences
[d]INFN - Gran Sasso National Laboratory
[e]INFN - Frascati National Laboratory
[f]'La Sapienza" University of Rome, "C. Darwin"Department of Biology and Biotechnologies

*Spokepersons

Abstract

An overall view on the research activities in deep underground laboratories (DULs) around the world show an increased interest in the last years for underground biology, with dedicated programs, meetings and proposals. LNGS, one of the first underground laboratories to host biology experiments, is where the majority of *in vitro* radiobiological data set have been collected so far. It is also the place where, recently, we obtained the first evidence of a differential response below and above ground at the organism level, using the fruit fly *Drosophila melanogaster* as a model organism. Here, we report the new advancements and the layout planned for the next years. In 2018, an Operative Collaboration for R&D activities in the field of Radiobiology has been established between INFN-LNGS and ISS. In this framework, a three years research proposal, called RENOIR, has been submitted to INFN-CSN5. We are planning to improve our knowledge of the radiation environment and to study in deep the biophysics and molecular mechanisms underlying the phenomena observed in Drosophila.

Introduction

Understanding of how environmental radiation influences living matter is an important dowel to elucidate the biological effects induced by ionizing radiation at low dose/dose rate, an issue that continues to be the major challenge in predicting radiation risk to human health (1-3).

161

Life on the Earth has evolved in the presence of low levels of natural ionizing radiation, referred as natural background. It comes from sources such as cosmic rays and radionuclides present in Earth's crust and it is a constant abiotic factor integrated in metabolism of living organisms that have led organisms to evolve defense mechanisms to maintain their healthy homeostasis.

What happens when you strongly reduced this constant natural stimulus? One of the very exciting areas of low dose radiobiology research is represented by studies performed on living organisms placed in sites where background radiation is strongly reduced (4-13).

Deep underground laboratories (DULs) represent unique places where it is possible to study the effects of strong reduction of natural background radiation. These places, originally built to host particle, astroparticle and nuclear physics experiments, are increasingly involved in underground biology experiments (14-16).

Among DULs, LNGS are one of the first underground laboratories to host biology experiments. Here the majority of *in vitro* radiobiological data set have been collected so far, and the first evidence of a differential response below and above ground at the organism level using the fruit fly *Drosophila melanogaster* as a model organism, has been shown recently (Flyinglow project) (10, reviewed in 14).

LNGS-INFN, always opened to new scientific challenges, in 2018 endorses with ISS, an Operative Collaboration for R&D activities in the field of Radiobiology. In this framework, a three years research proposal, called RENOIR ("Radiation Environment triggers biological Response in flies: physical and biological mechanisms") has been submitted to INFN-CSN5. The purpose of the proposal is to improve our knowledge of the radiation environment and to study in deep the biophysics and molecular mechanisms underlying the response of *Drosophila* to reduced natural background radiation.

Retrospective

In the framework of the Flyinglow project, funded by Centro Fermi, we recently obtained the first evidence of a differential response below and above ground at the organism level using the fruit fly *Drosophila melanogaster* as model organism. We have reported a comparative data set on lifespan, fertility and response to genotoxic stress in different *Drosophila* strains grown in parallel at the LNGS (LRE) and in the reference laboratory at L'Aquila University (RRE) (10). Our study has shown that the permanence in a strongly reduced radiation environment can indeed affect *Drosophila* development and, depending on the genetic background, may affect viability for several generations even when flies are moved back to the reference radiation environment.

We found that the median lifespan of independent populations, consecutively grown and maintained for several generations at LRE, was significantly increased with respect to that of reference (RRE) wild-type populations, indicating that reduction of natural background radiation alters the survival ratio. Interestingly, the positive effect on lifespan was observed as

early as after one generation time (10–15 days) and the extension rate remained constant as well, even after several generations.

While LRE prolongs the life span, it also strongly limits the reproductive capacity of both male and female flies. Fertility tests that were performed on both wild-type male and female adults from the same generation time have indeed shown that LNGS background radiation reduces the fertility of both male and female adults by about 30%. Interestingly, as well as for the lifespan, the fertility reduction was observed in flies as soon as they were grown at the LNGS for two generations, and more importantly the rate of reduced fertility remained almost unchanged for different generations. This latter evidence excluded the possibility that the reduction in fertility was a consequence of the induction of spontaneous mutations that required a much longer time to get fixed in the population. Moreover, these results indicated that a short time of permanence underground was sufficient to obtain a significant effect on the "biology" of *Drosophila*, pointing out that fruit fly is a perfect complex organism for low dose radiobiology experiments (10).

The RENOIR project

So far, all the obtained results in underground studies have consistently show that natural background radiation is necessary to trigger biological response to cope against stressors *in vitro* (4-9) and that reduction of the environmental radiation perturbs basic biological processes such as lifespan and fertility *in vivo* (10). It is not yet known whether all the components of the natural radiation field weigh in the same or in different manner to trigger the observed biological responses. It is therefore mandatory to characterize in detail the environmental radiation field and to understand the contribution of its different components in determining the biological effects.

In 2018, in the framework of the Operative Collaboration for R&D activities in the field of Radiobiology, established between INFN-LNGS and ISS, a three years research proposal (RENOIR) has been submitted to INFN-CSN5. One of the main aim of RENOIR is to improve the knowledge of the radiation field inside the external (reference) and underground laboratories, with dosimetric and spectroscopic measurements and with simulations, and to analyze in details the influence of the gamma component on the observed biological response, As for the biological measurements, with respect to the past, some changes have been made: (a) the Reference Radiation Laboratory, RRE is now located at the LNGS external lab, inside the "Servizio di Chimica e Impianti Chimici"; (b) the underground laboratory, LRE, is the new facility for organisms, named "COSMIC SILENCE", located close to the "PULEX" cell culture facility. It has been provided with temperature and light control systems (as required by *D. melanogaster*), as well as with a ventilation system. In our experiments, hourly and daily variation of indoor radon activity concentration in air is monitored and analyzed by the ALFAGUARD active device, which simultaneously measures other physics parameters such as relative humidity, temperature and pressure.

After the recent upgrading, the ventilation system of the "COSMIC SILENCE" facility works efficiently and keeps the radon concentration at comparable values with respect to the external reference environment RRE, at "Servizio di Chimica e Impianti Chimici", as shown by the latest measurements in Fig. 1.
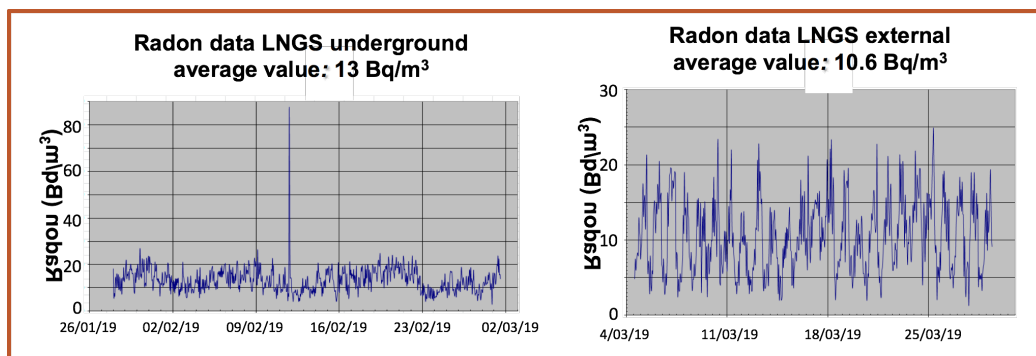

Fig. 1: Output of the ALFAGUARD active device

Besides the careful control of the environmental parameters (presence of Radon, temperature, pressure, relative humidity), the major problem when parallel underground and aboveground experiments are carried out is related to the identification of other possible systematic confounding factors. They have been widely evaluated, specifically for the different biological systems used since the beginning of our investigation. In particular, for cultured cells as well as for fruit flies, all the reagents (culture media, buffers, chemicals, …) used during the sample growth and manipulations were the same. Moreover, for *Drosophila*, the same operator will be in charge for the forthcoming experiments. With this approach we are confident to minimize all the possible sources of variability that, at the best of our knowledge, can affect the experimental results.

For further improving the control of the experimental variables, besides all the precaution already mentioned, we are planning to equip the LRE and RRE laboratories with identical incubators *ad hoc* for *Drosophila*.

In order to characterize the radiation field, we are planning to carry out a semi-quantitative *in-situ* γ-spectroscopic measurements using a high-efficiency commercial portable spectrometer (80% HpGe) (17-18). In particular, we will measure the activity concentration ratios between the radioactive series of [238]U and [232]Th and their decay disequilibrium to evaluate the contributions from the different families of radionuclides to the detected γ-dose rates (19-20). These latter will be measured with organic scintillator dose rate meters, Reuter Stokes high pressure ionization chambers and high sensitivity thermoluminescent detectors (TLD). In particular, TLD-700H will be used to measure the contribution due to the γ-component of the terrestrial radiation in the different sites at the sample position inside the sample holder.

To detect the neutron component, so far we have used a BF3 proportional tube, in particular a Boron trifluoride detector by Centronic (50 mm tube diameter, 1070 mm active length, 70 cm Hg). In this device, boron trifluoride serves as both the target for slow neutron conversion into

secondary particle as well as a proportional gas. We are presently exploring other possibilities.

In order to further characterize the radiation field components and to arrange a suitable dose model inside both the COSMIC SILENCE facility and the reference external laboratory, Monte Carlo simulations do play a crucial role. We will perform extensive simulations by means of MCNP6 and FLUKA or GEANT code. In particular, from the source term point of view, we will consider the literature available data to model the neutron energy spectrum both outside and inside LNGS halls (21-24). Moreover, the source term of the gamma component will be defined based on both our measurements and data available in literature (25).

Given the particle fluxes as the output of simulations, the goal is to predict the γ- and neutron dose rate value to the biological target. To this purpose, a *Drosophila* geometric model will also be implemented in the simulations. Further dosimetric measurements will validate the simulation results.

The identification of the most important component(s) of radiation spectrum able to trigger the biological responses is crucial for the interpretation of the data already collected *in vitro* and *in vivo*. In principle the biological differences observed in RRE and LRE could be due to the differences of both photon and neutron components of the terrestrial contribution since the cosmic rays are almost absent. At this point, we have already a work plan and the tools to reduce or increase the gamma component. We have at our disposal a shield consisting of a 10 cm thick lead hollow cylinder (see Fig. 1) that allows the reduction of gamma component by several hundred times.

Fig. 2: Picture of the shield

The biological sample will be put inside the hollow cylinder equipped with a proper designed ventilation system to prevent the accumulation of radon.

On the other side, to further increase the gamma component, we will use an especially designed "Marinelli beaker" (see Fig. 3), filled with natural building material (tuff and/or pozzolana) and sealed to avoid any radon exposure.

With this approach we are able to increase the gamma component underground by up to a factor of about 10. Starting from a value of 20 nGy/h, that is the gamma dose rate contribution at underground LNGS, we can gradually increase the gamma dose rate value up to external value and even beyond.
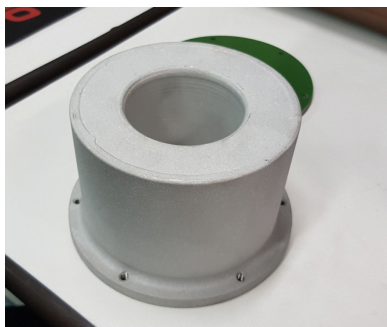

Fig. 3: Picture of "Marinelli" beaker.

We expect to obtain information about the involvement of the different components of the radiation field on biological responses of fruit flies.

Perspectives

The Operative Collaboration for R&D activities in the field of Radiobiology between LNGS-INFN and ISS and the subscribed three years research programme, called RENOIR ("Radiation Environment triggers biological Response in flies: physical and biological mechanisms") enable us for a systematic and consistent future research programme.

Taking advantage of our previous study (10) finding that fertility of both *Drosophila* males and females was reduced underground, we will carry out fertility analysis as a quick and reliable "sentinel" test in our preliminary pilot experiments in different radiation environments obtained with and without shield and using Marinelli beaker filled with tuff and/or pozzolana.

Moreover, our already established multidisciplinary collaboration will make possible to carry out Monte Carlo simulations in the short-term and improve our neutron measurements.

An other important point for future plans is that we would like to undertake a genome wide approach to understand what changes at either proteins and/or RNA levels might occur in flies kept at LRE with respect to RRE.

We are confident that this approach will enable us to shed some lights on the molecular mechanisms of the low radiation background effects and to focus on specific genes/proteins.

References

1. UNSCEAR 2010 Report: "Summary of low-dose radiation effects on health" (https://www.unscear.org/unscear/en/publications/2010.html)
2. UNSCEAR 2012 White Paper: Biological mechanisms of radiation actions at low doses . New York: United Nations Scientific Committee on the Effect of Atomic Radiations (https://www.unscear.org/unscear/en/publications/2012_WP.html)
3. UNSCEAR 2017 Report: Sources, effects and risks of ionizing radiation. New York: United Nations Scientific Committee on the Effect of Atomic Radiations (https://www.unscear.org/docs/publications/2017/UNSCEAR_2017_Report.pdf)
4. Planel G, Soleilhavoup JP, Tixador R, Croute F, Richoilley G. *Demonstration of a stimulating effect of natural ionizing radiation and of very low radiation doses on cell multiplication*. Biological and environmental effects of low-level radiation: v. 1 (IAEA Proceedings Series). Vienna: International Atomic Energy Agency 1976. p. 127–140 *Proceedings of a Symposium 1976. p. 127–140.*
5. Planel H, Soleilhavoup JP, Tixador R, Richoilley G, Conter A, Croute F, et al. Influence on cell proliferation of background radiation or exposure to very low, chronic gamma radiation. Health Phys. 1987; 52: 571–578
6. Carbone MC, Pinto M, Antonelli F, Amicarelli F, Balata M, Belli M, et al. The Cosmic Silence experiment: on the putative adaptive role of environmental ionizing radiation. Radiat. Environ. Biophys. 2009; 48(2): 189-196
7. Castillo H, Schoderbek D, Dulal S, Escobar G, Wood J, Nelson R, Smith G. Stress induction in the bacteria Shewanella oneidensis and Deinococcus radiodurans in response to below-background ionizing radiation. Int. J. Radiat. Biol. 2015; 91(9): 749-756
8. Castillo H and Smith GB. Below-Background Ionizing Radiation as an Environmental Cue for Bacteria. Frontiers in Microbiology 8, Article 177, Feb 2017
9. Fratini E, Carbone C, Capece D, Esposito G, Simone G, Tabocchini MA, Tomasi M, Belli M and Satta L. Low-radiation environment affects the development of protection mechanisms in V79 cells. Radiat. Environ. Biophys. 2015; 54(2): 183–194
10. Morciano P, Iorio R, Iovino D, Cipressa F, Esposito G, Porrazzo A, et al. Effects of reduced natural background radiation on Drosophila melanogaster growth and development as revealed by the FLYINGLOW program. J. Cell Physiol. 2018a; 233(1): 23-29 (doi: 10.1002/jcp.25889).
11. Satta L, Augusti-Tocco G, Ceccarelli R, Esposito A, Fiore M, Paggi P, et al. Low environmental radiation background impairs biological defence of the yeast Saccharomyces cerevisiae to chemical radiomimetic agents. Mutat. Res. 1995; 347(3-4): 129-133
12. Satta L, Antonelli F, Belli M, Sapora O, Simone G, Sorrentino E, et al. Influence of a low background radiation environment on biochemical and biological responses in V79 cells. Radiat. Environ. Biophys. 2002; 41(3): 217-224
13. Smith GB, Grof Y, Navarrette A, Guilmette RA. Exploring biological effects of low level radiation from the other side of background. Health Phys 2011; 100(3): 263-265
14. Morciano P, Cipressa F, Porrazzo A, Esposito G, Tabocchini MA, Cenci G. Fruit flies provide new insights in low radiation background biology at the INFN underground Gran Sasso National Laboratory (LNGS). Radiat. Res. 2018b; 190, 217-225 (doi: 10.1667/RR15083.1)
15. Liu J, Ma T, Liu Y, Zou J, Gao M, Zhang R. History, advancements, and perspective of biological research in deep underground laboratories: A brief review. Environmental International 2018; 120, 207-214

16. Thome C, Tharmalingam S, Pirkkanen J, Zarnke A, Laframboise T, Boreham DR. The REPAIR Project: Examining the Biological Impacts of Sub-Background Radiation Exposure within SNOLAB, a Deep Underground Laboratory. Radiat Res 2017; 188(4.2): 470-474

17. Miller, K.M. A spectral stripping method for a Ge spectrometer used for indoor gamma exposure rate measurements. Report EML-419, 1984. Environmental Measurement Laboratory, USDOE, New York, NY

18. Miller, K.M., Beck, H.L. Indoor gamma and cosmic ray exposure rate measurements using a Ge spectrometer and pressurised ionisation chamber. Radiat. Prot. Dosim. 1984; 7: 185–189

19. Nuccetelli C. In situ gamma spectroscopy in environmental research and monitoring. Applied Radiation and Isotopes 66: 1615– 1618, 2008

20. Bochicchio, F., Campos Venuti, G., Felici, F., Grisanti, A., Grisanti, G., Kalita, S., Moroni, G., Nuccetelli, C., Risica, S., Tancredi, F. Characterisation of some parameters affecting the radon exposure of the population. Radiat. Prot. Dosim. 1994; 56: 137–140

21. Rindi A, Celani F, Lindozzi M, Miozzi S. Underground neutron flux measurement. Nucl. Instr. and Meth. A 1988; 272: 871–874

22. Debicki Z, Jdrzejczaka K, , Karczmarczyka J, Kasztelana M, Lewandowskia R, Orzechowskia J, Szabelskia J, Szeptyckab M, Tokarskia P. Thermal neutrons at Gran Sasso. Nucl. Phys. B 2009 (Proc. Suppl.); 196: 429-432

23. Bonardi M, Aglietta G, Bruno W, Fulgione AA, Bergamini M, Direct measurement of the atmospheric neutron flux in the energy range 10–500 MeV. Astropart. Phys. 2010; 34: 225–229

24. Best A, Görres J, Junker M, Kratz KL, Laubenstein M, Long A, Nisi S, Smith K, Wiescher M. Low energy neutron background in deep underground laboratories. Nucl. Instr. and Meth. A. 2016; 812: 1–6

25. Malczewski D, Kisiel J, Dorda J. Gamma background measurements in the Gran Sasso National Laboratory. J. Radioanal. Nucl. Chem. 2013; 295: 749–754

List of publications and international meetings presentations

P. Morciano, R. Iorio, D. Iovino, F. Cipressa, G. Esposito, A. Porrazzo, L. Satta, E. Alesse, M.A. Tabocchini and G. Cenci. *Effects of reduced natural background radiation on Drosophila melanogaster growth and development as revealed by the FLYINGLOW program.* **Journal of Cellular Physiology 2018**; 233: 23-29 (doi: 10.1002/jcp.25889). [Epub ahead of print March 2017]

P. Morciano, F. Cipressa, A. Porrazzo, G. Esposito, M.A. Tabocchini, G. Cenci. *Fruit flies provide new insights in low radiation background biology at the INFN underground Gran Sasso National Laboratory (LNGS).* **Radiat Res 2018**; 190, 217-225 (doi: 10.1667/ RR15083.1) [Epub ahead of print June 4, 2018]

Graziadio L, Palumbo V, Cipressa F, Williams BC, Cenci G, Gatti M, Goldberg ML, Bonaccorsi S. *Phenotypic characterization of diamond (dind), a Drosophila gene required for multiple aspects of cell division.* **Chromosoma 2018;** Dec;127(4):489-504. (doi: 10.1007/ s00412-018-0680-y.). [Epub 2018 Aug 18]

A. Porrazzo, F. Cipressa, P. Morciano, G. Esposito, C. De Pittà, G. Sales , M.A. Tabocchini, G. Cenci. *Low doses of gamma* irradiation render Drosophila melanogaster resistant to the DNA damage. Italian Drosophila Research Conference **(IRDC)** Padova, 20-22 **June 2018**

G. Esposito, P. Morciano, F. Cipressa, A. Porrazzo, G. Cenci, M.A. Tabocchini. *Drosophila melanogaster come organismo modello per esperimenti radiobiologici in condizioni di fondo ambientale fortemente ridotto presso i Laboratori Nazionali del Gran Sasso (LNGS)*. XVIII Convegno Nazionale della Società Italiana per le Ricerche sulle Radiazioni (**SIRR**), Università degli Studi Roma Tre, 10-13 **September 2018** *(oral)*

F. Cipressa, A. Porrazzo, P. Morciano, G. Esposito, M.A. Tabocchini, G. Cenci. *Low doses of gamma irradiation render Drosophila melanogaster resistant to DNA damage.* 104° Congresso Nazionale della Società Italiana di Fisica **(SIF),** Arcavacata di Rende 17-21 **September 2018**

A. Porrazzo, F. Cipressa, P. Morciano, G. Esposito, C. De Pittà, G. Sales, M.A. Tabocchini, G. Cenci. *Low doses of gamma irradiation render Drosophila melanogaster resistant to the DNA damage.* XV **FISV** Congress, Sapienza University of Rome, 18-21 **September 2018** *(oral)*

G. Esposito, P. Morciano, F. Cipressa, A. Porrazzo, G. Cenci, M.A. Tabocchini. *New Insight in Low-Radiation Background Biology at the INFN Underground Gran Sasso National Laboratory (LNGS)*. **3rd European Radiological Protection Week**, Rovinj, 1-5 **October 2018** *(oral)*

GINGER

G-GranSasso Group
INFN and University of Pisa
Laboratori Nazionali di Legnaro
INFN and University of Naples

Abstract

The G-GranSasso experiment aims at developing an array of ring-laser gyroscopes in order to measure the Lense-Thirring effect on Earth with 1% precision. This project is called GINGER (Gyroscopes IN GEneral Relativity). Lense-Thirring tests are usually performed with space experiments, the measurement is averaged on satellite orbits and requires a very precise map of the gravitational field o f t he Earth. GINGER, instead, provides the measurement as a function of the latitude and does not require the gravitational field m a p. G INGERINO is a ring-laser gyroscope prototype built inside the Gran Sasso Laboratory of INFN (LNGS) in order to validate the site. GINGERINO has already shown the advantages of an underground location as LNGS, which exhibits very high thermal stability and where weather effects are depressed. GINGERINO is the first n on m onolithic g yroscope a ble to run continuously with high duty cycle and high sensitivity. Duty cycle larger than 95% and sensitivity of the order of 0.1nrad/s in 1 second have been already demonstrated. Its location, near an active seismic region, is such that Gingerino data are relevant for seismology; it has detected for the first t ime s trong e arthquakes i n t he n ear fi eld, an d in fall 2018 it has observed for the first t ime t he m icroseismic s ignal from thunderstorms in the Mediterranean sea and in the Atlantic. In the last year GINGERINO has been acquiring data almost continuously and large effort has been devoted to improve the data analysis in order to improve the rejection of the so called back-scatter noise and take into account the laser dynamics.

1 Introduction

The GINGER project requires to improve as much as possible the sensitivity and the long term stability of ring laser gyroscopes (RLGs). Accordingly, since its establishment, the group G-GranSasso is focused on improving the technique and the analysis of high sensitivity RLGs. RLGs are angular rotation inertial sensors based on the Sagnac effect. Let us consider two counter propagating beams circulating inside a closed path. When the frame, which holds the mirrors defining the closed path, rotates with angular velocity Ω, the Sagnac effect states that the time of flight of the two counter-propagating beams is proportional to Ω through a scale factor S, which depends on the geometry of the path. This effect has been applied to develop devices for inertial navigation, with a typical sensitivity of some fractions of the Earth rotation rate. The optical path can consist in a fiber coil, or in a free-space ring resonant cavity; the latter can be passive, when the resonant cavity is interrogated with and external laser source, or active, when an active medium is contained inside the cavity and the Sagnac signal is the beat note between the two counter-propagating laser beams. Large frame RLGs (with ring cavity length larger than 10 m) routinely have sensitivity of prad/s or even better.

GINGERINO is the prototype built inside LNGS in order to validate the site. GINGERINO has shown the advantages of the underground location far from weather disturbances. More than two years of operation has demonstrated a subsidence of underneath basement of the order of μrad. At this level, it has been observed that the operation can be stable for months. This is a very important information for the foreseen installation of a RLG at the maximum Sagnac signal within the frame of the GINGER program, in order to measure the fast variation of the earth rotation rate.

In the following we will describe the work done around GINGERINO, including experimental developments on the prototype GP2 operated in Pisa, the progress in the data analysis for the reduction of the low frequency noise, and advancements in the observation of microseismic signals.

2 The work done for GINGERINO

The apparatus of GINGERINO has been described in previous reports and in ref. [3].

In May 2018 a new set of high quality mirrors has been installed, leading to a factor 3 improvement in ring cavity quality factor.
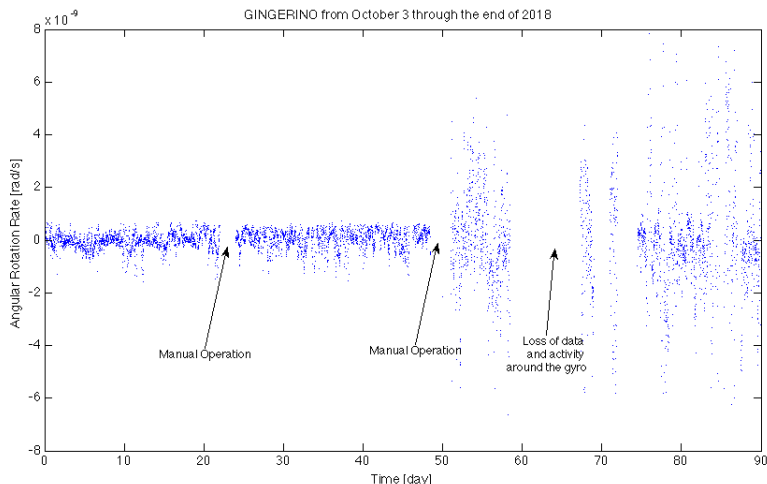
Figure 1: Data of GINGERINO from October 3 up to December 31 2018.

Fig. 1 shows angular rotation rates acquired during three months of operation from October 3 2018 up to the end of 2018. In the summer some shut-downs of electrical power caused the switch-off of the laser and of the acquisition system, requiring manual restarts. In this way we lost data acquired during many days. These troubles in the power supply were fixed in November by substituting the general power differential switching of GINGERINO. Besides, we have developed and tested in Pisa the electronics for remote switching on and power control of the discharge in order to avoid manual operations. Fig. 1 also shows that each time someone enters and works around the apparatus the sensitivity gets deteriorated. In November most of the problems was caused by the activity in the nearby area for restoring the apparatus relative to an array of seismometers. Fortunately, this work has been completed. We have analysed several pieces, for example the 30 days of June 2018, during the LUNA construction.

A test was performed in January in collaboration with prof. Joachim Wassermann of the Ludwig-Maximilian Universität, München, to compare the seismic rotation signal as detected in the same time an same location by our gyroscope, by a co-located high-performance FOG (fiber optical gyroscope) and a seismometer array. Analysis of the recorded data is presently in progress.

In the meantime, we have tested on our smaller gyroscope GP2, installed in Pisa laboratory, the new scheme for the selection of a single transverse

172

mode of the gyro laser emission mentioned in our previous report. Rather than using a narrow discharge capillary as a spatial selector of TEM00 laser emission mode, we have mounted a slightly larger capillary, in order to reduce the interaction of the laser Gaussian profile with the glass, and we selected the single mode operation by inserting in the laser cavity an iris whose diameter and position can be adjusted through electrical commands. We have verified that the transition between TEM00 and higher order modes occurs at the diameter values foreseen by a suitable model that we developed. A paper on this subject is in progress.

Further work on frequency stabilization of the ring laser emission by locking the diagonal length (see previous report) is presently in stand-by, since we are waiting for the arrival of a new iodine-stabilized He-Ne laser reference standard, expected next Fall.

2.1   Analysis taking into account laser dynamics

It is well known that the dynamics of the laser is strongly non linear [1] and that the response of the RLG is affected by such non-linearity. The dominant term is generated by back-scattered light that couples the two counter-traveling waves and eventually locks together their frequencies. The locking can be avoided and frequency shift effect on the Sagnac reduced by increasing the frequency bias between the two beams. In small scale apparatus this is attained by adding a mechanical rotation dithering. Instead, large scale apparatus with perimeter length larger than a few meters does not need dithering, thanks to the natural bias induced by the Earth rotation rate.

However, also in this case the Sagnac signal is affected by a smaller, but always important, frequency shift. We presented a recipe to solve this problem in 2012 by the use of Kalman filters, that was applied to the data collected by G-Pisa with quite good results [2, 4]. Unfortunately the algorithm was rather time consuming, preventing the opportunity of an effective implementation on long streams of data.

Starting from this experience we have developed a new approach for data analysis. The true Sagnac frequency ω_S is evaluated correcting the beat note interference frequency ω_m by using some auxiliary signals acquired in our apparatus: the monobeam signals, i.e. the laser power exiting from the optical cavity in the two opposite directions, and the discharge monitor signal (DM). The theory of this analysis is described in the paper "Analysis of ring laser gyroscopes including laser dynamics", authored by A. Di Virgilio, N. Beverini, G. Carelli, D. Ciampini, F. Fuso, and E. Maccioni, presently submitted to
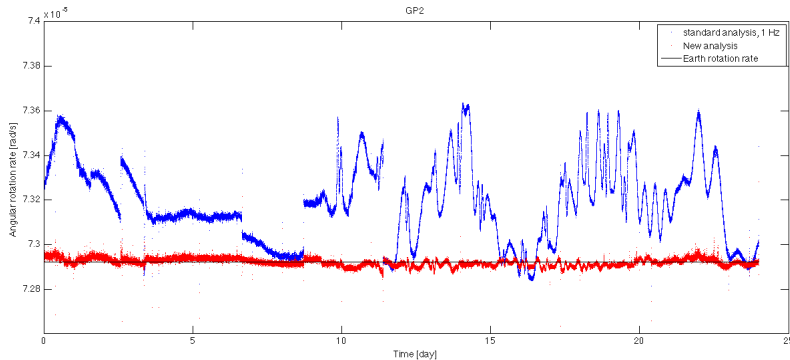
Figure 2: Angular rotation rate of GP2, comparison between the standard and new method of analysis. The old method shows large disturbances induced by back-scatter noise, strongly suppressed in the new one, which, moreover, leads to values closer to the expected angular rotation rate.

EPJC. Fig. 2 shows data of our smaller apparatus, GP2, analysed with the old and new methods. The new approach enables a significant reduction of noise showing that, in principle, an RLG with even smaller size, e.g., of 1 m side length, can reach the nrad/s level of sensitivity provided that data are analysed with the newly developed method.

The analysis says that ω_S can be evaluated as the linear sum of several pieces (each one not linear):

$$\omega_S = \omega_{S0} + \omega_{NS} + \omega_K \tag{1}$$

ω_{S0}, which is the dominant term, corrects the back-scatter effect, ω_{NS} is the null shift term, ω_K is a high frequency resonance of the beat note, and it is not affecting the lower frequency analysis. At present we have evaluated the first two terms, and several attempts to reconstruct ω_K are underway

As an example of the improvements enabled by the new analysis method, we have applied it to data acquired by GINGERINO in a 30 day period heavily affected by the above mentioned disturbances. Fig. 3 shows the histogram of angular rotation rate values obtained from raw data (ω_m) and the ones obtained after correction for back-scatter (ω_{S0}) and null-shift (evaluated ω_S) effects. Improvements are evident: the expected Gaussian distribution shape is recovered after correction for back-scatter, its width is further reduced when null-shift is included. Moreover, the average value of the angular rotation rate recovers in this case the expected value.
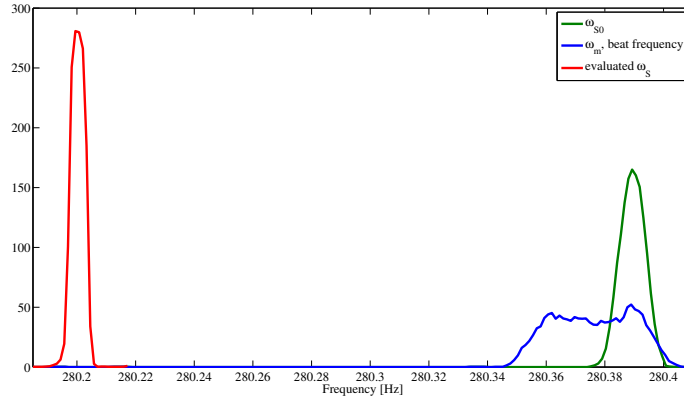
174

Figure 3: Histogram of occurrences for the angular rotation rate as obtained from raw GINGERINO data (ω_m) and after correction for back-scatter (ω_{S0}) and null-shift (evaluated ω_S) effects.
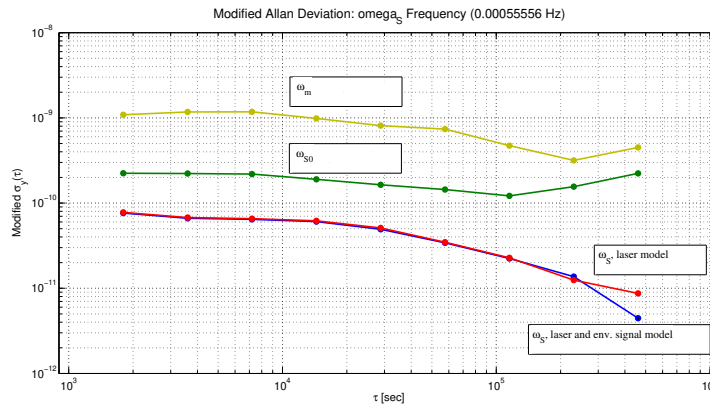

Figure 4: Modified Allan deviation, in units of rad/s, obtained from raw data acquired by GINGERINO (ω_m), after correction for back-scatter (ω_{S0}) and null-shift (ω_S, laser model) effects, and including also in the model the environmental signal (ω_S, laser and env. signal model).

175

Fig. 4 reports the modified Allan deviation computed on raw data acquired by GINGERINO and with different variants of the new method, including also a preliminary attempt to account for environmental monitors such as, temperature, pressure, implemented in the apparatus. Also in this case a clear improvement is achieved demonstrating the ability to reach and even surpass the 10^{-11} rad/s sensitivity for sufficiently long acquisition times.

2.2   DAQ problems

As already stated in previous reports, our DAQ system gave a lot of troubles. At the end of December we acquired a CENTAUR data logger. The CENTAUR is one of the two commercially available recorders developed for seismology, the RLG array ROMY successfully utilizes this kind of recorder. CENTAUR handles absolute timing and writes files in the miniseed format customarily used by seismologists. On-site installation has been done by our young researcher Andrea Simonelli, with the help of Aladino Govoni and Gaetano De Luca (INGV). Presently, it is acquiring data in parallel with the old system. A problem arisen in the communication protocol that does not allow in-time reading of the acquired data, has been reported to the instrument producer and will be solved with his cooperation. Another CENTAUR data logger, provided by INGV, will acquire data of the co-located INGV seismometer, ensuring in this way a correct timing of the data, crucial for geophysical analysis.

Two accesses in March and April 2019 by Enrico Maccioni and Umberto Giacomelli were devoted to optimising the optical alignment of GINGERINO and to installing an electronic system for the remote control of the discharge. This system is very important for switching on again the discharge in case of power interruption and for adjusting the laser operation point close to threshold in optimal conditions without the presence of operators in the lab. Meanwhile, the monobeam detectors have been carefully calibrated and aligned. The intensity of the CW and CCW laser radiation results equal within the errors; also the ring-down times in the two direction were measured and found identical at 0.1%. This is an important information, demonstrating that null-shift (i.e. non-reciprocal effect) in the present conditions of operation is very small.

2.3 Microseism signal observation and collaboration with seismologists

The apparatus of GINGERINO is one of the very few structures in the world, where high-performance seismometers and high sensitivity gyroscopes are co-located, but it is the only RLG placed in a seismically active region. This offers to seismologists the opportunity of studying the correlation of linear and rotational seismic effects in near field condition. Several papers in the field of rotational seismology have been written in collaboration with INGV researchers dating from 2012. In Fall 2018 we could observe the rotational microseismic signal generated by Mediterranean Sea and near Atlantic Ocean in the period bandwidth from 2 to 5 s. In particular, the signal showed up very clearly during a large storm activity between November 25 and November 28, 2018.

Both the spectra of rotation rate (acquired by GINGERINO) and acceleration show a peak around 3.3 s. The signal amplitude is of 8×10^{-10} rad/s and 3×10^{-6} ms^{-2} for rotation rate and for horizontal acceleration, respectively. Correlating rotational and linear data, we could estimate the direction of the source, which in the observation period was consistent with the evolution of two storm systems developing in the South-West part of the Mediterranean sea and near the coasts of Portugal. A paper related to this important observation is in preparation in collaboration with geophysicists.

References

[1] F. Aronowitz and R. J. Collins. Lock-in and intensity-phase interaction in the ring laser,. *Journal of Applied Physics*, 41:1, 1970.

[2] A. Beghi, J. Belfi, N. Beverini, B. Bouhadef, D. Cuccato, A. D. Virgilio, and A. Ortolan. Compensation of the laser parameter fluctuations in large ring-laser gyros: a kalman filter approach. *Appl. Opt.*, 51(31):7518–7528, Nov 2012.

[3] J. Belfi, N. Beverini, F. Bosi, G. Carelli, D. Cuccato, G. De Luca, A. Di Virgilio, A. Gebauer, E. Maccioni, A. Ortolan, A. Porzio, G. Saccorotti, A. Simonelli, and G. Terreni. Deep underground rotation measurements: Gingerino ring laser gyroscope in gran sasso. *Review of Scientific Instruments*, 88(3):034502, 2017.

[4] D. Cuccato, A. Beghi, J. Belfi, N. Beverini, A. Ortolan, and A. D. Virgilio. Controlling the nonlinear inter cavity dynamics of large he-ne laser gyroscopes. *Metrologia*, 51:97–107, 2014.

VIP

C.Curceanu (spokesperson) [a], A. Amirkhani[b], S. Bartalucci[a],

M. Bazzi[a], S. Bertolucci[c], A.M. Bragadireanu[a,d],

M. Cargnelli[a,e], A. Clozza[a], R. Del Grande [a],

J-P Egger[f], C. Fiorini[b], C. Guaraldo[a], M. Iliescu[a],

M. Laubenstein[g], J. Marton[a,e], E. Milotti[h], M. Milucci[a],

L. De Paolis[a], A. Pichler[a,e], D. Pietreanu[a,d],

K. Piscicchia[a,i], A. Scordo[a], H. Shi[a], D. Sirghi[a,d],

F. Sirghi[a,d], L. Sperandio[a], O. Vazquez Doce[j], J. Zmeskal[a,e]

[a] INFN, Laboratori Nazionali di Frascati, CP 13, Via E. Fermi 40,
I-00044, Frascati (Roma), Italy
[b] Politecnico di Milano, Dipartimento di Elettronica,
Informazione e Bioingegneria and INFN Sezione di Milano, Milano, Italy

[c] University and INFN Bologna, Via Irnerio 46, I-40126, Bologna, Italy
[d] "Horia Hulubei"National Institute of Physics and Nuclear Engineering,
Str. Atomistilor no. 407,P.O. Box MG-6, Bucharest - Magurele, Romania
[e] The Stefan Meyer Institute for Subatomic Physics, Boltzmanngasse 3, A-1090 Vienna, Austria
[f] Institut de Physique, Université de Neuchâtel, 1 rue A.-L. Breguet,
CH-2000 Neuchâtel, Switzerland
[g] INFN, Laboratori Nazionali del Gran Sasso, S.S. 17/bis, I-67010 Assergi (AQ), Italy
[h] Dipartimento di Fisica, Università di Trieste and INFN,
Sezione di Trieste, Via Valerio, 2, I-34127 Trieste, Italy
[i] Museo Storico della Fisica e Centro Studi e Ricerche "Enrico Fermi", Roma, Italy
[j] Excellence Cluster Universe, Technische Universität München, Garching, Germany

Abstract

By performing X-rays measurements in the "cosmic silence" of the underground laboratory of Gran Sasso, LNGS-INFN, we test a basic principle of quantum mechanics: the Pauli Exclusion Principle (PEP), for electrons by searching for atomic transitions in copper and lead prohibited by PEP. VIP2 uses Silicon Drift Detectors (SDDs) to measure the X rays emmited in the copper target and a veto system (scintillators read by SiPM) to reduce the background. Within VIP-2 experiment we are also performing feasibility tests of other quantum mechanics processes, such as the collapse of the wave function.

1 The VIP scientific case and the experimental method

Within VIP an experimental test on the Pauli Exclusion Principle is being performed, together with other tests on fundamental physics principles.

The Pauli Exclusion Principle (PEP), a consequence of the spin-statistics connection, plays a fundamental role in our understanding of many physical and chemical phenomena, from the periodic table of elements, to the electric conductivity in metals and to the degeneracy pressure which makes white dwarfs and neutron stars stable. Although the principle has been spectacularly confirmed by the huge number and accuracy of its predictions, its foundation lies deep in the structure of quantum field theory and has defied all attempts to produce a simple proof. Given its basic standing in quantum theory, it is appropriate to carry out high precision tests of the PEP validity and, indeed, mainly in the last 20 years, several experiments have been performed to search for possible small violations. Many of these experiments are using methods which are not obeying the so-called Messiah-Greenberg superselection rule. Moreover, the indistinguishability and the symmetrization (or antisymmetrization) of the wave-function should be checked independently for each type of particles, and accurate tests were and are being done.

The VIP (VIolation of the Pauli Exclusion Principle) experiment, an international Collaboration among 10 Institutions of 6 countries, has the goal to either dramatically improve the previous limit on the probability of the violation of the PEP for electrons, ($P < 1.7$ x 10^{-26} established by Ramberg and Snow: *Experimental limit on a small violation of the Pauli principle*, Phys. Lett. **B 238** (1990) 438) or to find signals from PEP violation.

The experimental method consists in the introduction of electrons into a copper strip, by circulating a current, and in the search for X-rays resulting from the forbidden radiative transition that occurs if some of the new electrons are captured by copper atoms and cascade down to the 1s state already filled by two electrons with opposite spins (Fig. 1.)
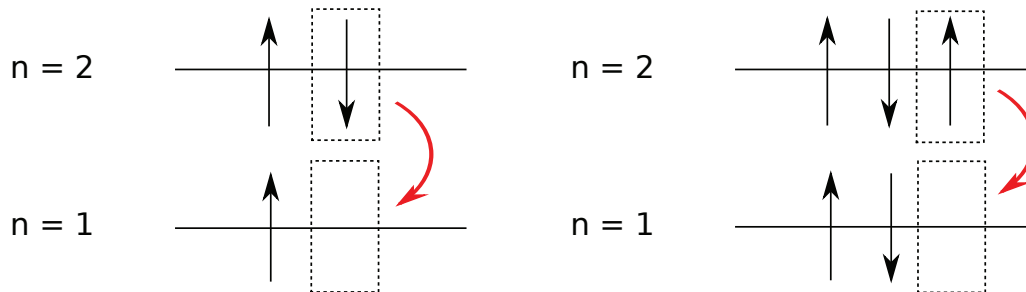

Figure 1: *Normal 2p to 1s transition with an energy around 8 keV for Copper (left) and Pauli-violating 2p to 1s transition with a transition energy around 7,7 keV in Copper (right).*

The energy of $2p \rightarrow 1s$ transition would differ from the normal K_α transition by about 300 eV (7.729 keV instead of 8.040 keV) providing an unambiguous signal of the PEP violation. The measurement alternates periods without current in the copper strip, in order to evaluate the X-ray background in conditions where no PEP violating transitions are expected to occur, with periods in which current flows in the conductor, thus providing "new" electrons, which might violate PEP. The rather straightforward analysis consists in the evaluation of the statistical significance of the normalized subtraction of the two spectra in the region of interest (if no signal is seen). A more complex statistical analysis (such as Bayesian) is also being implemented.

The experiment is being performed at the LNGS underground Laboratories, where the X-ray background, generated by cosmic rays, is reduced.

The VIP group is extending its scientific program to the study of other items of the fundamental physics, such as discrete symmetries and collpase models. Encouraging preliminary results were already obtained.

2 The VIP and VIP2 setups

The VIP setup was realized in 2005, starting from the DEAR setup, reutilizing the CCD (Charge Coupled Devices) as X-ray detectors, and consisted of a copper cylinder, were current was circulated, 4.5 cm in radius, 50 μm thick, 8.8 cm high, surrounded by 16 equally spaced CCDs of type 55.

The CCDs were placed at a distance of 2.3 cm from the copper cylinder, grouped in units of two chips vertically positioned. The setup was enclosed in a vacuum chamber, and the CCDs cooled to 165 K by the use of a cryogenic system. The VIP setup was surrounded by layers of copper and lead to shield it against the residual background present inside the LNGS laboratory, see Fig. 2.

Figure 2: The VIP setup at the LNGS laboratory during installation.

The DAQ alternated periods in which a 40 A current was circulated inside the copper target with periods without current, representing the background.

VIP was installed at the LNGS Laboratory in Spring 2006 and was taking data until Summer 2010. The probability for PEP Violation was found to be: $\beta^2/2 < 4.6 \times 10^{-29}$.

In 2011 we started to prepare a new version of the setup, VIP2, for which a first version was finalized and installed at the LNGS-INFN in November 2015, and with which we will gain a factor about 100 in the probability of PEP violation in the coming years (see Table 1).

In 2018 the VIP2 setup was upgraded with new SDDs and shielding and is presently in data taking.

Table 1: List of expected gain factors of VIP2 in comparison to VIP (given in brackets).

Changes in VIP2	value VIP2(VIP)	expected gain
acceptance	12% (1%)	12
increase current	100A (50A)	2
reduced length	3 cm (8.8 cm)	1/3
total linear factor		8
energy resolution	170 eV(340 eV)	4
reduced active area	6 cm^2(114 cm^2)	-
better shielding and veto		5-10
higher SDD efficiency		1/2
background reduction		200-400
overall gain		**∼120**

3 Activities in 2018

3.1 VIP2 - a new high sensitivity experiment

In order to achieve a signal/background increase which will allow a gain of two orders of magnitude for the probability of PEP violation for electrons, we built a new setup with a new target, a new cryogenic system and we use new detectors with timing capability and an active veto system. As X-ray detectors we use spectroscopic Silicon Drift Detectors (SDDs) which have an even better energy resolution than CCDs and provide timing capability which allow to use anti-coincidence provided by an active shielding.
The VIP2 system is providing:

1. signal increase with a more compact system with higher acceptance and higher current flow in the new copper strip target;

2. background reduction by decreasing the X-ray detector surface, more compact shielding (active veto system and passive), nitrogen filled box for radon radiation reduction.

In the Table 1 the numerical values for the improvements in VIP2 are given which will lead to an expected overall improvement of a factor about 100.

3.2 Status of VIP2 in 2018

In the VIP2 apparatus, in Spring 2018, 4 new SDD arrays with 2×4 SDDs detectors each (with 8×8 cm^2), with a total active area of 20 cm^2 each, were mounted close to the Cu target (see Figure 3). Moreover, an active shielding system (veto) is being implemented, to reduce the background in the energy region of the forbidden transition. This system will play an important role to improve the limit for the violation of the PEP by two orders of magnitude with the new data which are presently coming by running the VIP2 experiment at LNGS.

In November 2018 main part of the lead and cooper shielding were also installed. The data taking, together with data analysis, are undergoing.

Data with 100 Ampere DC current applied to the copper strip was collected together with the data collected without current, representing the background.
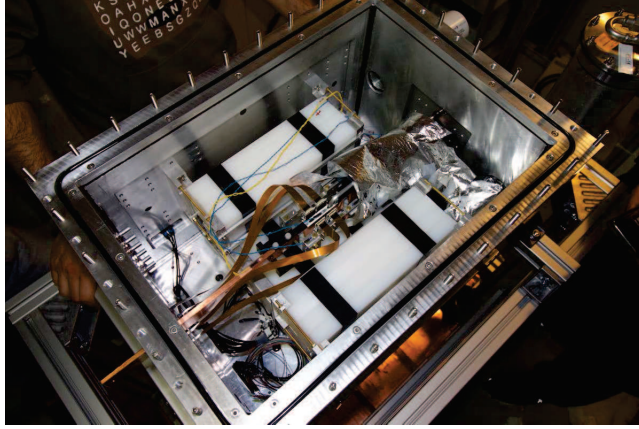
Figure 3: *A picture of the inner part of the VIP-2 setup with the new SDDs installed at LNGS* .

3.3   Preliminary data analyses

A first set of VIP2 data was analysed by using a simultaneous fit of the "signal" and background spectra, in order to use all the information available for the background shape from the data. The obtained spectra are shown in Fig 4, together with the simultaneous fitting functions, from where a limit of the probability of PEP violation was extracted to be:

$$\frac{\beta^2}{2} \leq \frac{3 \times 67}{8.1 \times 10^{30}} = 3.2 \times 10^{-29}. \tag{1}$$

A paper is in preparation describing the new analysis and the obtained results.

3.4   A new data analysis

A new data analysis, considering the electron diffusion in bulk-matter process, was proposed and realised. The result:

$$\frac{\beta^2}{2} \leq 2.6 \times 10^{-40}. \tag{2}$$

was published in Entropy (2018) 20 (7), 515.

Discussions with theoreticians about the interpretation of results are ongoing.

4   X-ray measurements for testing the dynamical reduction models

The aim of the Dynamical Reduction Models (DRM) is to solve the so-called "measurement problem" in Quantum Mechanics (QM). The linear and unitary nature of the Shrödinger equation allows, in principle, the superposition of macroscopic states, but such superpositions are not observed in the measurement process, which is intrinsically non-linear and stochastic [1, 2]. The measurement problem led to the introduction of the wave packet reduction principle which, nevertheless, does not predict the scale at which the quantum-to-classical transition occurs, nor explains the collapse mechanism.
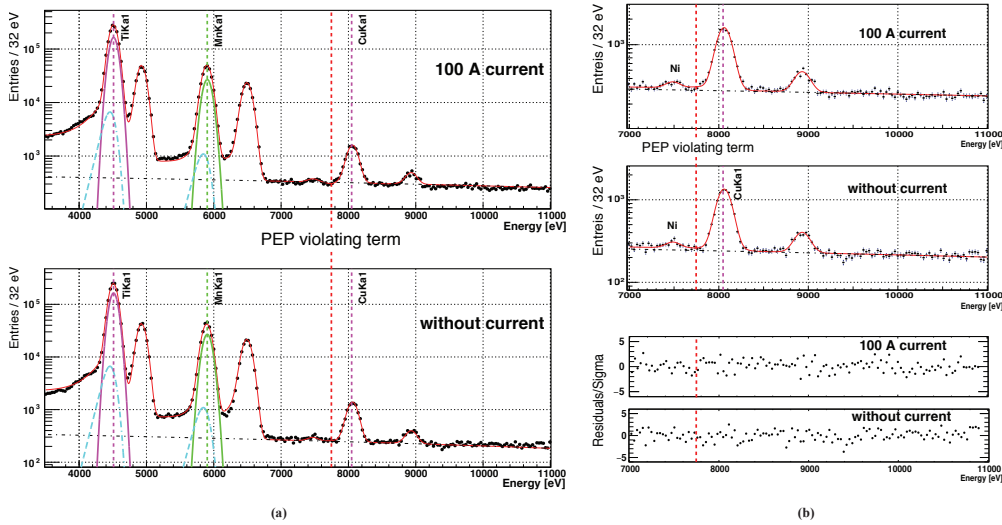
Figure 4: *A global chi-square function was used to fit simultaneously the spectra with and without 100 A current applied to the copper conductor. The energy position for the expected PEP violating events is about 300 eV below the normal copper $K_{\alpha1}$ transition. The Gaussian function and the tail part of the $K_{\alpha1}$ components and the continuous background from the fit result are also plotted. (a) : the fit to the wide energy range from 3:5 keV to 11 keV; (b) : the fit and its residual for the 7 keV to 11 keV range where there is no background coming from the calibration source. See the main text for detail*

The work of Ghirardi, Rimini and Weber [3] lead to the development of a consistent DRM known as Quantum Mechanics with Spontaneous Localization (QMSL). According to the QMSL model each particle of a macroscopic system of n distinguishable particles experiences sudden spontaneous localizations, on the position basis, with a mean rate $\lambda = 10^{-16}$ s^{-1}, and a correlation length $a = 10^{-7}$ m. Between two localizations particles evolve according to the Shrödinger dynamics. The model ensures, for the macroscopic object, the decoupling of the interanl and Center of Mass (CM) motions. The interanl motion is not affected by the localization, whereas the CM motion is localized with a rate $\lambda_{macro} = n\lambda$.

Subsequently, the theory was developed in the language of the non-linear and stochastic Shrödinger equation [4, 5], where besides the standard quantum Hamiltonian, two other terms induce a diffusion process for the state vector, which causes the collapse of the wave function in space. In its final version [6] the model is known as the mass proportional Continuous Spontaneous Localization (CSL).

The value of the mean collapse rate is presently argument of debate. According to CSL λ should be of the order of 10^{-17} s^{-1}, whereas a much stronger value $10^{-8\pm2}$ s^{-1} was proposed by S. L. Adler [8] based on arguments related to the latent image formation and the perception of the eye.

DRM posses the unique characteristic to be experimentally testable, by measuring the (small) predicted deviations with respect to the standard quantum mechanics. The conventional approach is to generate spatial superpositions of mesoscopic systems and examine the loss of interference, while environmental noises are, as much as possible, under control. The present day technology, however, does not allow to set stringent limits on λ by applying this method. The most promising testing ground, instead, is represented by the search for the spontaneous radiation emitted by charged particles when interacting with the collapsing stochastic field [7].

A measurement of the emitted radiation rate thus enables to set a limit on the λ parameter of the models.

The radiation spectrum spontaneously emitted by a free electron, as a consequence of the interaction with the stochastic field, was calculated by Q. Fu [7] in the framework of the non-relativistic CSL model, and it is given by:

$$\frac{d\Gamma(E)}{dE} = \frac{e^2\lambda}{4\pi^2 a^2 m^2 E} \tag{3}$$

in eq. (3) m represents the electron mass and E is the energy of the emitted photon. In the mass proportional CSL model the stochastic field is assumed to be coupled to the particle mass density, then the rate is to be multiplied by the factor $(m/m_N)^2$, with m_N the nucleon mass. Using the measured radiation appearing in an isolated slab of Germanium [9] corresponding to an energy of 11 KeV, and employing the predicted rate eqn. (3), Fu obtained the following upper limit for λ (non-mass poportional model):

$$\lambda < 0.55 \cdot 10^{-16} s^{-1}. \tag{4}$$

In eq. (4) the QMSL value for a ($a = 10^{-7}$ m) is assumed and the four valence electrons were considered to contribute to the measured X-ray emission, since the binding energy is ~ 10 eV in this case, and they can be considered as *quasi-free*. Recent re-analyses of Fu's work [8, 10] corrected the limit to $\lambda < 2 \cdot 10^{-16} s^{-1}$.

We improved the limit on the collapse rate [11] by analysing a set of data collected at LNGS with Ge detectors and an ultra-pure lead target.

A Bayesian model was adopted to calculate the χ^2 variable minimized to fit the X ray spectrum, assuming the predicted (Eq. (3)) energy dependence:

$$\frac{d\Gamma(E)}{dE} = \frac{\alpha(\lambda)}{E}. \tag{5}$$

The preliminary obtained value for λ is:

$$\lambda \leq 5.2 \times 10^{-13} s^{-1}, \tag{6}$$

in the mass proportional CSL assumption. The results was submitted for publication.

By using a similar method, we are considering the idea to perform other dedicated experiments at LNGS which will allow for 1 - 2 orders of magnitude further improvement on the collapse rate parameter λ.

4.1   Workshops organization

In 2018 the following events related to the physics of VIP, and, more generally, to quantum mechanics, were organized:

1. Workshop "New Quantum Horizons: From Foundations to Biology" ", 15-16 November 2018, Frascati, Italy.

2. Workshop Quantum Foundation, "Is quantum theory exact? The quest for the spin-statistics connection violation and related items ", 02-05 July, 2018, Frascati, Italy.

5 Activities in 2019

In 2019 we will be in data taking with VIP2 at LNGS-INFN. The 2016, 2017 and 2018 data analysis will be finalized and published. We are, as well, going to continue the studies on fundamental physics, in particular on the collapse model by measurements of X rays spontaneously emitted in the continuous spontaneous localization (CSL) model.

6 Publications in 2018

1. H. Shi *et al*, Search for the violation of Pauli Exclusion Principle at LNGS, EPJ Web Conf. **182** (2018) 02118.

2. P. Moskal *et al*, Feasibility studies of the polarization of photons beyond the optical wavelength regime with the J-PET detector, Eur.Phys.J. C **78** (2018) no.11, 970.

3. K. Dulski *et al*, Commissioning of the J-PET detector in view of the positron annihilation lifetime spectroscopy, Hyperfine Interact. **239** (2018) no.1, 40.

4. J. Raj *et al*, A feasibility study of the time reversal violation test based on polarization of annihilation photons from the decay of ortho-Positronium with the J-PET detector, Hyperfine Interact. **239** (2018) no.1, 56.

5. P. Kowalski *et al*, Estimating the NEMA characteristics of the J-PET tomograph using the GATE package, Phys.Med.Biol. 63 (2018) 165008.

6. G. Korcyl *et al*, Evaluation of Single-Chip, Real-Time Tomographic Data Processing on FPGA - SoC Devices, DOI: 10.1109/TMI.2018.2837741, e-Print: arXiv:1807.10754 [physics.ins-det].

7. E. Milotti *et al*, On the Importance of Electron Diffusion in a Bulk-Matter Test of the Pauli Exclusion Principle, Entropy **20** (2018) no.7, 515.

8. J. Marton *et al*, Detector setup of the VIP2 Underground Experiment at LNGS, e-Print: arXiv:1807.02182 [physics.ins-det].

9. E. Czerwinski *et al*, Studies of discrete symmetries in decays of positronium atoms, EPJ Web Conf. **181** (2018) 01019.

10. P. Moskal *et al*, Feasibility study of the positronium imaging with the J-PET tomograph, e-Print: arXiv:1805.11696 [physics.ins-det].

11. K. Piscicchia *et al*, Experimental constrains on the Continuous Spontaneous Localization model from spontaneous radiation emission, PoS CORFU2017 (2018) 201, DOI: 10.22323/1.318.0201.

12. A. Gajos *et al*, Feasibility Study of the Time Reversal Symmetry Tests in Decay of Metastable Positronium Atoms with the J-PET Detector, Adv.High Energy Phys. **2018** (2018) 8271280.

13. H. Shi *et al*, Experimental search for the violation of Pauli Exclusion Principle, Eur.Phys.J. C **78** (2018) no.4, 319.

References

[1] Von Neumann J 1932 Mathematische Grundlagen der Quantummechanik (Springer-Verlag). English translation 1955: Mathematical Foundations of Quantum Mechanics (Princeton University Press)

[2] Bassi A and Ghirardi G C 2003 *Phys. Rep.* **379** 257

[3] Ghirardi G C, Rimini A and Weber T 1986 *Phys. Rev. D* **34** 47

[4] Pearle P 1989 *Phys. Rev. A* **39** 2277

[5] Ghirardi G C, Pearle P and Rimini A 1990 *Phys. Rev. A* **42** 78

[6] Pearle P and Squires E 1994 *Phys. Rev. Lett.* **73** 1

[7] Fu Q 1997 *Phys. Rev. A* **56** 1806

[8] Adler S L 2007 *Journal of Physics A* **40** 2935

[9] Miley H S *et al* 1990 *Phys. Rev. Lett.* **65** 3092

[10] Mullin J and Pearle P 2014 *Phys. Rev. A* **90** 052119

[11] Curceanu C, Hiesmayer B C and Piscicchia K 2015 *Journal of Advanced Physics* **4** 1

THE PIERRE AUGER OBSERVATORY

G. A. Anastasi[a,c], D. Boncioli [a,c], A. Condorelli [a,c],
I. De Mitri[a,c], M. Mastrodicasa [a,b], G. Morlino[a,c],
S. Petrera[a,c], V. Rizi[a,b], F. Salamida[a,b], I. Valiño[a,c],
for the Pierre Auger Collaboration

[a] INFN Laboratori Nazionali del Gran Sasso, Assergi (AQ), Italy
[b] INFN and Department of Physical and Chemical Sciences,
University of L'Aquila, L'Aquila, Italy
[c] GSSI, Gran Sasso Science Institute, L'Aquila, Italy

Abstract

The Pierre Auger Project is an international Collaboration involving about 450 scientists from 16 countries, with the objective of studying the highest energy cosmic rays. Recent results from the Collaboration as well as further developments in the detector are presented in this report.

1 Introduction

Ultra-high energy cosmic rays are of intrinsic interest as their origin and nature are unknown. It is quite unclear where and how particles as energetic as $\approx 10^{20}$ eV are accelerated. Over 40 years ago it was pointed out that if the highest energy particles are protons then a fall in the flux above an energy of about 4×10^{19} eV is expected because of energy losses by the protons as they propagate from distant sources through the photon background radiation. At the highest energies the key process is photo-pion production in which the proton loses part of its energy in each creation of a Δ resonance. This is the Greisen–Zatsepin–Kuzmin (GZK) effect. It follows that at 10^{20} eV any proton observed must have come from within about 50 Mpc and on this distance scale the deflections by intervening magnetic fields in the galaxy and intergalactic space are expected to be so small that point sources should be observed. If nuclei are propagated from sources their photo-disintegration in the photon background field plays a role similar to the GZK effect in the depletion of the flux above 10^{20} eV and the limitation of the CR horizon, but the angular correlation with the sources is expected weaker because of the higher charges.

The Pierre Auger Observatory [1] comprises about 1600 10 m^2 × 1.2 m water-Cherenkov detectors deployed over 3000 km^2 on a 1500 m hexagonal grid, plus a sub array, the Infill, with 71 water Cherenkov detectors on a denser grid of 750 m covering nearly 30 km^2. This part of the Observatory (the surface detector, SD) is over-looked by 24 fluorescence telescopes in 4 clusters located on four hills around the SD area which is extremely flat. The surface detectors contain 12 tonnes of clear water viewed by $3 \times 9''$ hemispherical photomultipliers. The fluorescence detectors (FD) are designed to record the faint ultra-violet light emitted as the shower traverses the atmosphere. Each telescope images a portion of the sky of 30° in azimuth and 1°–30° in elevation using a spherical mirror of 3 m^2 effective area to focus light on to a camera of 440×18 cm^2 hexagonal pixels, made of photomultipliers complemented with light collectors, each with a field of view of 1.5° diameter. 3 High Elevation Auger Telescopes (HEAT) located at one of the fluorescence sites are dedicated to the fluorescence observation of lower energy showers. The Observatory also comprises a sub array of 124 radio sensors (AERA, Auger Engineering Radio Array) working in the MHz range and covering 6 km^2, a sub Array of 61 radio sensors (EASIER, Extensive Air Shower Identification with Electron Radiometer) working in the GHz range and covering 100 km^2, and two GHz imaging radio telescopes AMBER and MIDAS.

A review of main results from the Pierre Auger Observatory is presented with a particular focus on the energy spectrum measurements, the mass composition studies, the arrival directions analyses and the search for neutral cosmic messengers. The measurement of the energy spectrum of UHECRs, the inference on their mass composition and the analysis of their arrival directions bring different information, complementary and supplementary one to the other, with respect to their origin. Despite the results reached by Auger, the understanding of the nature of UHECRs and of their origin remains an open science case that the Auger collaboration is planning to address with the AugerPrime project [2] to upgrade the Observatory.

2 Recent results from the Pierre Auger Observatory

2.1 Cosmic Ray Spectrum measurements

The measurement of the flux of UHECRs has been one of the first outcomes of Auger data [3, 4, 5]. Two spectral features have been established beyond doubt: the hardening in the spectrum at about 5×10^{18} eV (the so-called ankle), and a strong suppression of the flux at the highest

energies, starting at about 4×10^{19} eV. The all-particle flux of cosmic rays presented at ICRC 2017 [6] is an update of such measurement, being based on an exposure exceeding 67,000 km^2 sr yr, accumulated since January 2004 until December 2016. Four independent energy spectra (Fig. 1, left) are obtained: two data sets from the SD-1500 m, respectively vertical and horizontal (zenith angles above 60°) events; one from the SD-750 m; the last one from events detected by the FD simultaneously with at least one detector of the SD 1500. The SD-1500 m vertical data are crucial above the energy of full trigger efficiency of 3×10^{18} eV up to the highest energies, with horizontal events contributing above 4×10^{18} eV and providing an independent measurement in this energy range. Data from the SD-750 m allow for the determination of the energy spectrum down to 10^{17} eV. Hybrid data bridge those from the two SDs, between 10^{18} eV and $10^{19.6}$ eV. The four spectra, in agreement within uncertainties, are combined into a unique one (Fig. 1, right) through a likelihood function defined in such a way to fit all the data sets globally. The result is emblematic of the power of using multiple detectors.

The evident features are quantified by fitting a model that describes the spectrum with two power-laws around the ankle, the second of which includes a smooth suppression at the highest energies. The ankle is found to be at $E_{\mathrm{ankle}} = (5.08 \pm 0.06 \pm 0.8) \times 10^{18}$ eV. The spectral slope below the ankle is $\gamma_1 = 3.293 \pm 0.002 \pm 0.05$, and above the ankle is $\gamma_2 = 2.53 \pm 0.02 \pm 0.1$. The energy at which the integral spectrum drops by a factor of two below what would be the expected with no steepening is $E_{1/2} = (22.6 \pm 0.8 \pm 4.0) \times 10^{18}$ eV. The obtained parameters are in good agreement with those previously shown in [7].

2.2 Mass composition studies

The composition of cosmic rays in the energy range of 0.1 to 1 EeV is the key for identifying a possible transition from galactic to extra-galactic sources and for understanding the features in the energy spectrum, such as the ankle and the flux suppression. This study has been addressed by the Collaboration through the measurement of the depth of the shower maximum, X_{max}, one of the most robust mass-sensitive EAS observables. The measurement published in [8] (relying on hybrid events above $10^{17.8}$ eV collected by the standard FD telescopes) has been extended in [9] down to $10^{17.2}$ eV using data collected with HEAT in coincidence with the closest FD, Coihueco (so-called HeCo data set) and updated in the last ICRC conference [10].
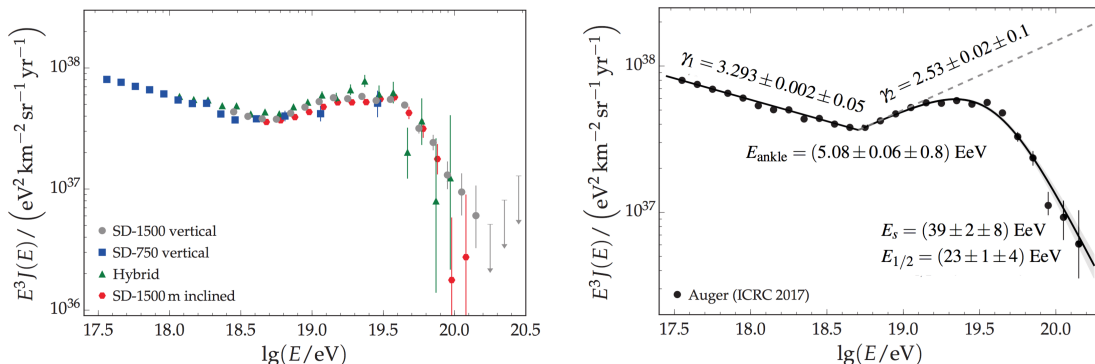

Figure 1: Left: The four energy spectra derived from SD and hybrid data. The systematic uncertainty on the energy scale is 14%. Right: The combined energy spectrum, fitted with a flux model and the related fitting parameters (see text). As in the left panel, only statistical uncertainties are shown. Images from [6].

The determination of the primary composition is performed by comparing the measured X_{max} distributions of EAS with expectations according to high energy hadronic interaction models. The analysis is based on a selected set of hybrid events, recorded during stable runs and good atmospheric conditions. In addition to these selection criteria a set of fiducial FoV cuts are applied to reduce to a minimum the detector effects in the sampled Xmax distributions. The total number of events that passed all cuts (quality and FoV cuts) is 16778 and 25688 for HeCo and Standard-FD data sets respectively.

The resulting $\langle X_{max} \rangle$ and $\sigma(X_{max})$ is shown in Fig. 2, left and right, respectively, as a function of energy. Data are confronted to simulations, for proton and iron primaries, performed using three hadronic interaction models that were found to agree with recent LHC data. Between $10^{17.2}$ and $10^{18.3}$ eV, $\langle X_{max} \rangle$ increases by around (79 ± 1) g cm^{-2} per decade of energy; around $10^{18.3}$ eV, the rate of change of $\langle X_{max} \rangle$ becomes significantly smaller $((26 \pm 2)$ g cm^{-2}/decade). These two values, consistent with those found with FD data alone [8], allow to extend the inferences on the evolution of the average mass composition down to 10^{17} eV. As the first value is larger than the one expected for a constant mass composition (~ 60 g cm^{-2}/decade), it indicates that the mean primary mass is getting lighter all the way from 10^{17} to $10^{18.3}$ eV. Above this energy, the trend inverts and the composition becomes heavier. The fluctuations of X_{max} start to decrease above the same energy $\sim 10^{18.3}$ eV, being rather constant below.

2.3 Photons and neutrinos diffuse search

Both neutrinos and photons are sought for in the flux of UHECRs detected by Auger. The neutrino search is performed by studying very inclined showers and earth-skimming ones [11]. The criteria are based on the characteristics expected for "young" showers initiated by neutrinos, developing deeper in the atmosphere, compared to "old" ones from inclined hadronic showers, having their electromagnetic component fully absorbed before reaching the detectors. Also photon showers develop deep in the atmosphere, but a key difference is the lower average number
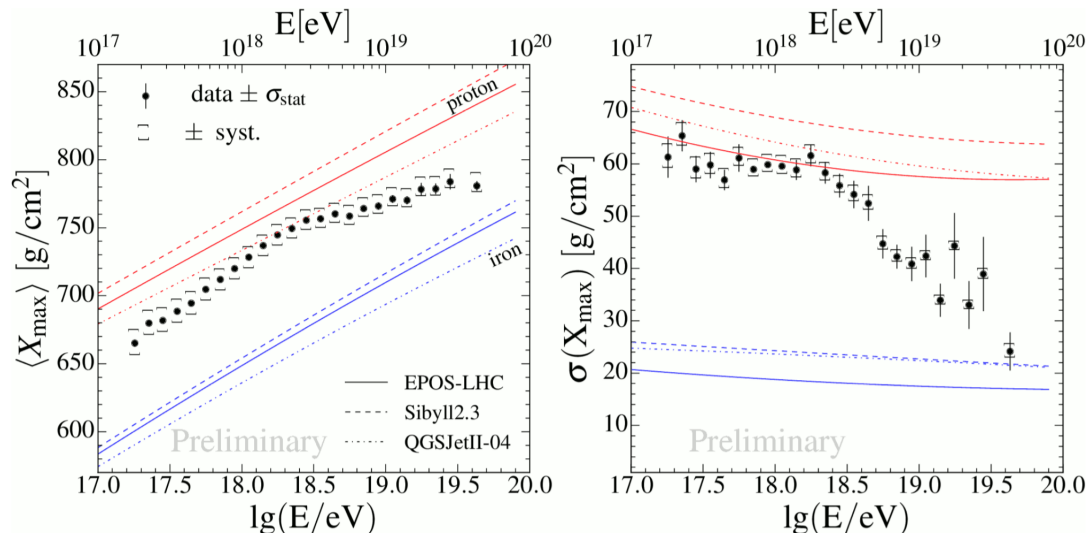

Figure 2: The mean (left) and the standard deviation (right) of the measured X_{max} distributions as a function of energy compared to air-shower simulations for proton and iron primaries. Images from [10].

of muons in photon-induced air showers compared to those initiated by hadrons of the same primary energy.

SD events on the one hand, and hybrid events on the other hand have been analyzed, to cover the energy range above 1 EeV. stringent upper limits to their flux can be derived. The Auger limits on neutrinos (Fig.3 left panel) outperform those from IceCube and ANITA, and also the Waxman-Bahcall limit; in the range 10^{17} - 10^{19} eV they are challenging the contribution from cosmogenic-neutrino models [12]. The limits to the integral photon flux are shown in Fig.3 right panel. So far, the extensive searches for UHE photons at the Pierre Auger Observatory have not yielded an unambiguous detection, but the upper limits on the diffuse flux of photons presented in [13] are the most stringent limits to date, severely constraining top-down models for the origin of UHE cosmic rays.

2.4   Targeted search of neutrinos

The detection of gravitational waves started by the Advanced Ligo Collaboration has triggered a targeted search for coincidence events that would complement these observations. Even if the directionality of the neutrino exposure makes the effectivity of the search quite dependent on the event position, an upper bound to the flux of UHE neutrinos and on the related energy budget can be obtained. These limits help to constrain all kinds of models as part of a multi-messenger approach.

A search [12] has been made for EeV events in the data collected with the Observatory and correlated in time and position with gravitational wave events. In particular, on 2017 August 17 a binary neutron star coalescence candidate (later designated GW170817) was observed through gravitational waves by the Advanced LIGO and Advanced Virgo detectors [14]. Subsequently, ultra-violet, optical, and infrared emission was observed from the merger, consistent with kilonova/macronova emission.

Auger performed a search for UHE neutrinos with its SD in a time window of ± 500 s centered at the merger time of GW170817, as well as in a 14-day period after it. Remarkably, the position of the optical counterpart was visible from Auger in the field of view of the Earth-skimming channel during the whole ± 500 s window as shown in Fig. 4. Inclined showers passing the Earth-
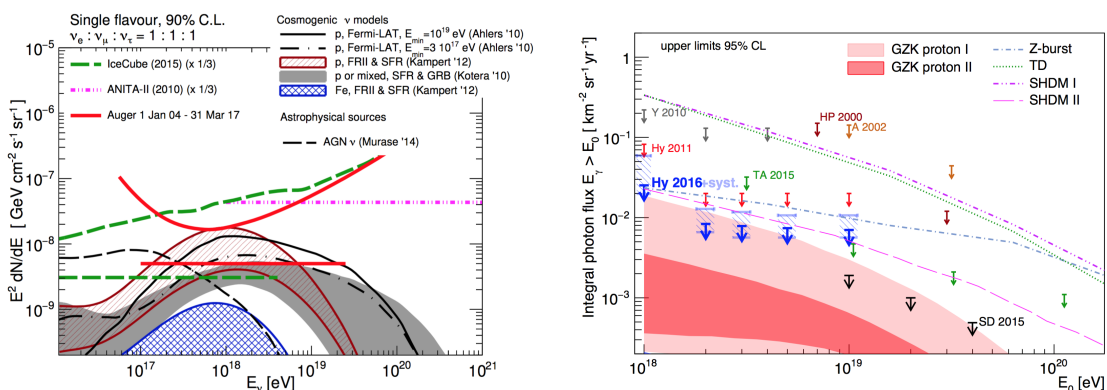

Figure 3: Left: Integral upper limit (at 90% C.L.) for a diffuse neutrino flux, given as a normalization (straight red line) and differential upper limit (see [12] for details). Right: Upper limits on the integral photon flux (95% C.L.) (see [13] for details).

skimming selection (neutrino candidates) were not found in this time window, nor in the 14-day period. However, the absence of candidates allows to constrain the fluence in UHE neutrinos from GW170817 (reported in [15]), assuming they are emitted steadily and with an E^{-2} spectrum.

Figure 4: Localizations and sensitive sky areas at the time of the event GW170817 in equatorial coordinates: GW 90% credible-level localization (red contour), direction of NGC 4993 oprtical counterpart (black plus symbol), directions of IceCube's and ANTARES's neutrino candidates within 500 s of the merger (green crosses and blue diamonds, respectively), ANTARES's horizon separating down-going (north of horizon) and up-going (south of horizon) neutrino directions (dashed blue line), and Auger's fields of view for Earth-skimming (darker blue) and down-going (lighter blue) directions. Image from [15].

2.5 The important role of the Pierre Auger Observatory in the multimessenger astronomy era

Besides the different wavelengths of traditional astronomy, neutrinos, cosmic rays, very high energy gamma rays, and gravitational waves provide complementary information to study the most energetic objects of the Universe. The combined effort of many different experiments marks an unprecedented leap forward in astrophysics revealing many aspects of the Gamma-Ray Burst (GRB) induced by the merger and its subsequent kilonova. More recently an energetic neutrino candidate was detected in IceCube in coincidence with the powerful blazar TXS-0506+056 during a flare in the very-high-energy gamma-ray band, incompatible with a chance of $.3.5\sigma-$ leve. [23] As opposed to cosmic rays, inclined neutrinos can interact deep in the atmosphere because their interaction length exceeds the matter depth of the atmosphere for any zenith angle, θ. For neutrino energies exceeding 100 PeV, the combined conversion and exit probability is maximal for nearly horizontal ("Earth-skimming") directions, showering close and almost parallel to the ground.

Together with that, the detection of gravitational waves from the merging of binary systems has marked the birth of gravitational wave astronomy. They triggered the search for the emission of electromagnetic radiation and neutrinos at neutrino telescopes and at the Pierre Auger Observatory, as you can see in the picture 5. Unfortunately, No neutrinos were found [26] in coincidence with these events and other interesting neutrino events detected at the IceCube telescope.[23]
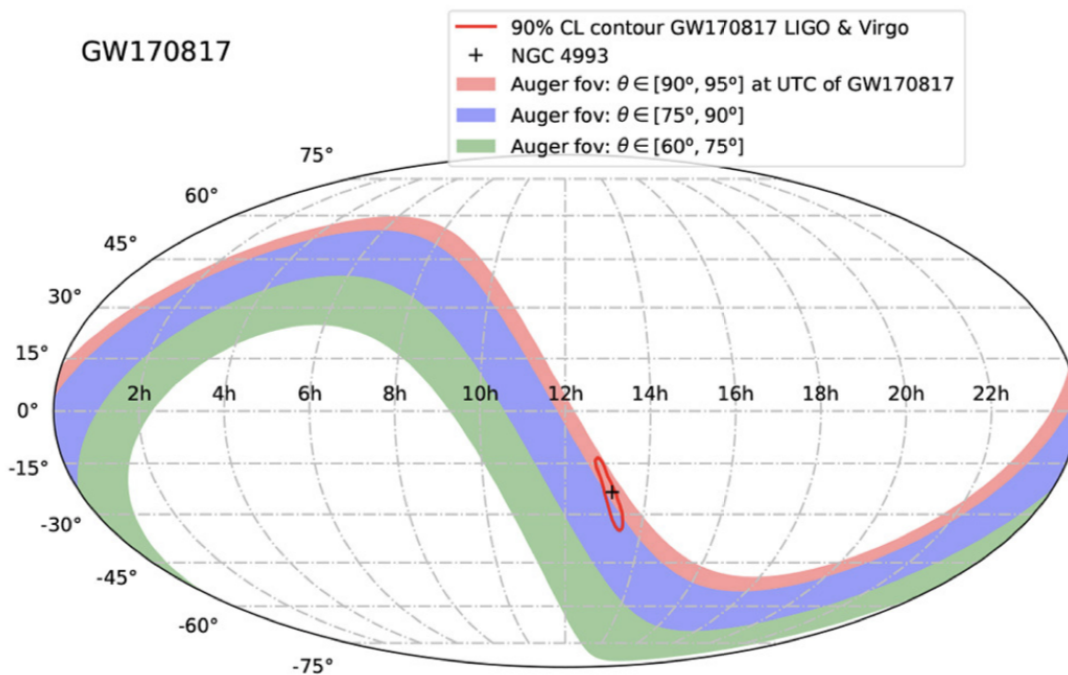

Figure 5: Field of view of the Observatory in Earth-skimming and down-going channels at the instant of the detection of neutron star merger GW170817. The small red contour marks the event localization obtained by the Ligo-Virgo collaborations [24] and the black cross is the position of NGC 4993, later correlated to the event by optical telescopes [25]

As opposed to neutrinos, UHE photons undergo interactions with the extragalactic background light (EBL) inducing electromagnetic cascades; This process makes photons sensitive to the extragalactic environment (e.g., EBL and magnetic fields) but it also limits the volume from which EeV photons may be detected. The search for UHE photon primaries is basically based on the different development and particle content of electromagnetic and hadronic air showers: in fact, the induced electromagnetic cascades develop slower than hadronic ones so that the shower maximum X_{max} is reached closer to the ground. Proton and photon simulated showers have average X_{max} values that differ by about 200 $g \cdot cm^{-2}$ in the EeV energy range.

The observation of photon fluxes from individual sources or from stacked sets of targets would have proved that EeV protons are being accelerated at those considered sources within the galaxy or its neighborhood. Nevertherless, the absence of detectable photon fluxes does not exclude the production of EeV protons within the Galaxy because the derived flux limits are time-averaged values and for this reason EeV photons might be produced in transient sources, such as gamma-ray bursts or supernovae, or be aligned in jets not pointing to us.

2.6 Anisotropy searches

Besides the measurement of the cosmic ray spectrum and the determination of the primary composition, the analysis of the arrival direction distribution provides a crucial handle for the studies about the origin and nature of the ultra-high energy cosmic rays. It is difficult to locate the sources of cosmic rays, as they are charged particles and thus interact with the magnetic fields in our galaxy and the intergalactic medium that lies between the sources and Earth. However, even if particles from individual sources are strongly deflected, it remains possible that anisotropies in the distribution of their arrival directions will be detectable on large angular scales. Previous large-scale studies [16, 17, 18, 19] have been performed down to the lowest energies accessible by the Observatory ($\sim 10^{16}$ eV). Nevertheless, the updated analysis [20, 21] considers showers with energies above 4 EeV, in particular the bins 4 EeV < E < 8 EeV and E $\geq$ 8 EeV (median energies 5.0 EeV and 11.5 EeV). The standard approach to study the
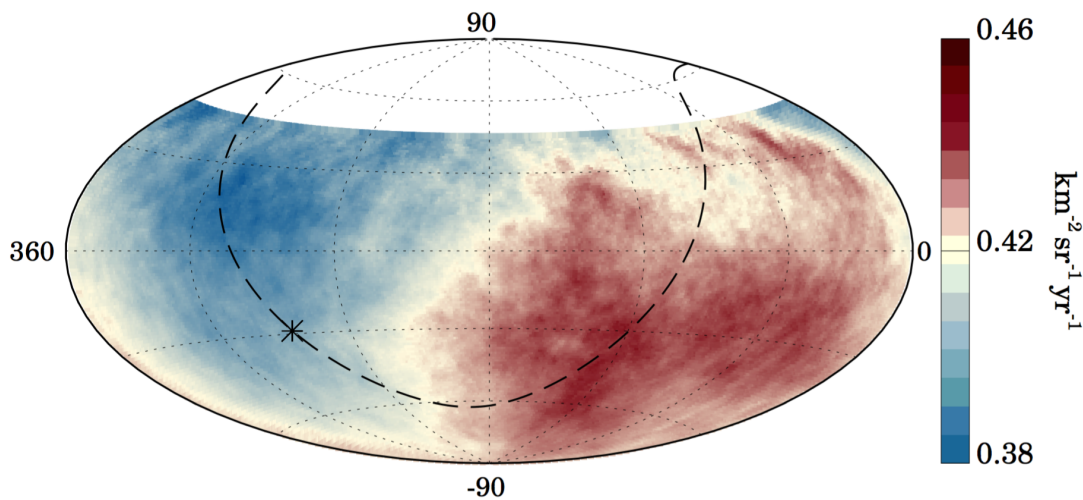

Figure 6: Sky map in equatorial coordinates, using a Hammer projection, of the cosmic-ray flux above 8 EeV smoothed with a 45° top-hat function. The Galactic center is marked with an asterisk and the Galactic plane is shown by a dashed line. Image from [21].

distribution at large angular scales of the arrival directions is to perform a harmonic analysis over the distributions in right ascension (α) and in the azimuthal angle (ϕ). In fact, in the presence of a three-dimensional dipole, the analysis in right ascension is sensitive only to its component orthogonal to the rotation axis of Earth. Instead, the dipole component in the direction of the rotation axis of Earth induces a modulation in the azimuthal distribution of the arrival directions at the array.

For 4 EeV < E < 8 EeV, the dipole amplitude is again not statistically significant; It might also be the result of stronger magnetic deflections at lower energies. For energies above 8 EeV, the total dipole amplitude is d = $6.5^{+1.3}_{-0.9}\%$ This dipolar pattern can be clearly seen in the flux map in Fig. 6. To establish whether the departures from a perfect dipole are just statistical fluctuations or indicate the presence of additional structures at smaller angular scales would require at least twice as the events selected for this analysis.

By comparing the results in [21] with phenomenological predictions, the magnitude and direction of the anisotropy support the hypothesis of an extragalactic origin for the highest-energy cosmic rays, rather than sources within the Galaxy. In general, models proposing a Galactic origin up to the highest observed energies are in increasing tension with observations. In this sense, the constraint obtained here on the dipole amplitude for 4 EeV < E < 8 EeV further disfavors a predominantly Galactic origin. This tension could be alleviated if cosmic rays at a few EeV were dominated by heavy nuclei such as iron, but this would be in disagreement with the lighter composition inferred observationally at these energies. Furthermore, the anisotropy observed in events with E $\geq$ 8 EeV is better explained in terms of an extragalactic origin, since the direction of the three-dimensional dipole determined above 8 EeV lies $\sim$ 125° from the Galactic center. Finally, above 40 EeV, where the propagation should become less diffusive, there are no indications of anisotropies associated with either the Galactic center or the Galactic plane.

3 The Pierre Auger Observatory Upgrade: AugerPrime

To answer many questions still open in the UHECR field, the Observatory has started a major upgrade, called AugerPrime [2]. The main goal of AugerPrime is to improve the mass composition
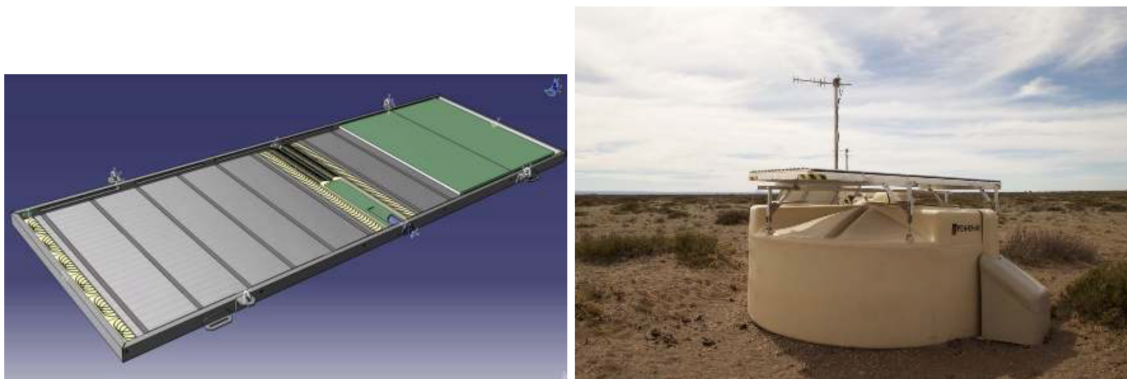

Figure 7: Left: the layout of the Surface Scintillator Detector (SSD); Right: One station of the AugerPrime Engineering Array. Image from [22].

sensitivity of the surface detectors to explore energies above 10^{19} eV where the fluorescence detector is not adequate due to its limited duty cycle ($\sim$15%).

The upgrade program will include more powerful SD electronics, an extension of the dynamic range with an additional PMT installed in the water-Cherenkov detectors and above-all the installation of a new detector above each of the existing tanks. This Surface Scintillator Detector (SSD) consists of a plane of plastic scintillator (a box of area 3.8 m $\times$ 1.3 m) that will be triggered by the larger WCD below it (Fig. 7).

A thin scintillation detector, which is mounted above the larger WCD, provides a robust and well-understood scheme for particle detection that is sufficiently complementary to the water-Cherenkov technique and permits a good measurement of the density of muons. The availability of muon information on an event-by-event basis will permit an estimation of the primary mass and also the selection of a sub-sample of events in the cutoff region enriched with light elements, increasing the capacity of the Observatory to identify potential sources of UHECRs.

The first twelve stations of AugerPrime were assembled in Europe and deployed at the Pierre Auger Observatory in September 2016 [22]. This Engineering Array has been in continuous data taking mode since begin of October 2016 and has collected more that 30000 local triggers. In this way the performance of the upgraded stations has been monitored, producing signals that are in good agreement with expectations.

4 Activity of the L'Aquila–Gran Sasso Group

The activity of the group proceed in the following main lines:

- Development of a Monte Carlo code (*SimProp*) for the propagation of UHECR nuclei in source enviroment and in extragalactic space, and its use for the study of physical observables [27].

- Development and operation of the Raman Lidar system for an enhanced atmospheric test beam within the Pierre Auger Observatory.

- Study of Lorentz invariance violation from the point of view of the effects on UHECR propagation and interactions of particles in atmosphere [28].

- Development of an updated air shower reconstruction procedure based on the paradigm of air shower Universality [29, 30].

- Search of upward-going UHE tau neutrino induced events with the fluorescence detector of the Pierre Auger Observatory.

- Participation to the Auger-Telescope Array joint Spectrum working groups.

4.1 Talks

- <u>S.Petrera</u> for the Pierre Auger Collaboration, ISVHECRI, May 2018, Nagoya, Japan

References

[1] A. Aab *et al.* [Pierre Auger Collaboration], Nucl. Instrum. Meth. A **798** (2015) 172 doi:10.1016/j.nima.2015.06.058 [arXiv:1502.01323 [astro-ph.IM]].

[2] A. Aab *et al.* [Pierre Auger Collaboration], arXiv:1604.03637 [astro-ph.IM].

[3] J. Abraham *et al.* [Pierre Auger Collaboration], Phys. Rev. Lett. **101**, 061101 (2008) doi:10.1103/PhysRevLett.101.061101 [arXiv:0806.4302 [astro-ph]].

[4] J. Abraham *et al.* [Pierre Auger Collaboration], Phys. Lett. B **685**, 239 (2010) doi:10.1016/j.physletb.2010.02.013 [arXiv:1002.1975 [astro-ph.HE]].

[5] A. Aab *et al.* [Pierre Auger Collaboration], JCAP **1508**, 049 (2015) doi:10.1088/1475-7516/2015/08/049 [arXiv:1503.07786 [astro-ph.HE]].

[6] Francesco Fenu, for the Pierre Auger Collaboration, "The cosmic ray energy spectrum measured using the Pierre Auger Observatory", ICRC 2017

[7] I. Valiño, for the Pierre Auger Collaboration, "The flux of ultra-high energy cosmic rays after ten years of operation of the Pierre Auger Observatory", ICRC 2015, [arXiv:1509.03732[astro-ph.HE]].

[8] A. Aab *et al.* [Pierre Auger Collaboration], Phys. Rev. D **90**, no. 12, 122005 (2014) doi:10.1103/PhysRevD.90.122005 [arXiv:1409.4809 [astro-ph.HE]].

[9] A. Porcelli, for the Pierre Auger Collaboration, "Measurements of X_{max} above 10^{17} eV with the fluorescence detector of the Pierre Auger Observatory", ICRC 2015, [arXiv:1509.03732[astro-ph.HE]].

[10] J. Bellido, for the Pierre Auger Collaboration, "Depth of maximum of air-shower profiles at the Pierre Auger Observatory: Measurements above 10 17.2 eV and Composition Implications", ICRC 2017

[11] A. Aab *et al.* [Pierre Auger Collaboration], "Improved limit to the diffuse flux of ultrahigh energy neutrinos from the Pierre Auger Observatory," Phys. Rev. D **91**, no. 9, 092008 (2015) doi:10.1103/PhysRevD.91.092008 [arXiv:1504.05397 [astro-ph.HE]].

[12] E. Zas, for the Pierre Auger Collaboration, "Searches for neutrino fluxes in the EeV regime with the Pierre Auger Observatory : UHE neutrinos at Auger", ICRC 2017

[13] M. Niechciol, for the Pierre Auger Collaboration, "Diffuse and targeted searches for ultra-high-energy photons using the hybrid detector of the Pierre Auger Observatory: Auger photon searches", ICRC 2017

[14] LIGO Scientific and Virgo and Fermi GBM and INTEGRAL and IceCube and IPN and Insight-Hxmt and ANTARES and Swift and Dark Energy Camera GW-EM and Dark Energy Survey and DLT40 and GRAWITA and Fermi-LAT and ATCA and ASKAP and OzGrav and DWF (Deeper Wider Faster Program) and AST3 and CAASTRO and VINROUGE and MASTER and J-GEM and GROWTH and JAGWAR and CaltechNRAO and TTU-NRAO and NuSTAR and Pan-STARRS and KU and Nordic Optical Telescope and ePESSTO and GROND and Texas Tech University and TOROS and BOOTES and MWA and CALET and IKI-GW Follow-up and H.E.S.S. and LOFAR and LWA and HAWC and Pierre Auger and ALMA and Pi of Sky and DFN and ATLAS Telescopes and High Time Resolution Universe Survey and RIMAS and RATIR and SKA South Africa/MeerKAT Collaborations and AstroSat Cadmium Zinc Telluride Imager Team and AGILE Team and 1M2H Team and Las Cumbres Observatory Group and MAXI Team and TZAC Consortium

and SALT Group and Euro VLBI Team and Chandra Team at McGill University, Astrophys. J. **848** (2017) no.2, L12 doi:10.3847/2041-8213/aa91c9 [arXiv:1710.05833 [astro-ph.HE]].

[15] A. Albert *et al.* [ANTARES and IceCube and Pierre Auger and LIGO Scientific and Virgo Collaborations], Astrophys. J. **850** (2017) no.2, L35 doi:10.3847/2041-8213/aa9aed [arXiv:1710.05839 [astro-ph.HE]].

[16] P. Abreu *et al.* [Pierre Auger Collaboration], Astrophys. J. Suppl. **203**, 34 (2012) doi:10.1088/0067-0049/203/2/34 [arXiv:1210.3736 [astro-ph.HE]].

[17] A. Aab *et al.* [Pierre Auger Collaboration], Astrophys. J. **802**, no. 2, 111 (2015) doi:10.1088/0004-637X/802/2/111 [arXiv:1411.6953 [astro-ph.HE]].

[18] A. Aab *et al.* [Telescope Array and Pierre Auger Collaborations], Astrophys. J. **794**, no. 2, 172 (2014) doi:10.1088/0004-637X/794/2/172 [arXiv:1409.3128 [astro-ph.HE]].

[19] I. Al Samarai for the Pierre Auger Collaboration, "Indications of anisotropy at large angular scales in the arrival directions of cosmic rays detected at the Pierre Auger Observatory", ICRC 2015, [arXiv:1509.03732[astro-ph.HE]].

[20] O. Taborda, for the Pierre Auger Collaboration, "Dipolar anisotropy of cosmic rays above 8 EeV", ICRC 2017

[21] A. Aab *et al.* [Pierre Auger Collaboration], Science **357** (2017) no.6537, 1266 doi:10.1126/science.aan4338 [arXiv:1709.07321 [astro-ph.HE]].

[22] D. Martello, for the Pierre Auger Collaboration, "The Pierre Auger Observatory Upgrade", ICRC 2017

[23] Aartsen, M. G., Ackermann, M., Adams, J., Aguilar, J. A., Ahlers, M., Ahrens, M., et al. (2018b). "Neutrino emission from the direction of the blazar TXS 0506+056 prior to the IceCube-170922A alert." Science 361, 147–151. doi: 10.1126/science.aat2890

[24] LIGO-Collaboration (2018). LIGO Document P1800381-v2. Available online at: https://dcc.ligo.org/LIGO- P1800381/public

[25] Coulter, D. A., Foley, R. J., Kilpatrick, C. D., Drout, M. R., Piro, A. L., Shappee, B. J., et al. (2017). Swope supernova survey 2017a (SSS17a), the optical counterpart to a gravitational wave source. Science. 358, 1556–1558. doi: 10.1126/science. aap9811

[26] Alvarez Muniz, J. (2018). Multi-messenger astrophysics at ultra-high energy with the Pierre Auger observatory. Eur. Phys. J. Web of Conf.

[27] A. Aab *et al.* [Pierre Auger Collaboration], JCAP **1704** (2017) no.04, 038 Erratum: [JCAP **1803** (2018) no.03, E02] doi:10.1088/1475-7516/2018/03/E02, 10.1088/1475-7516/2017/04/038 [arXiv:1612.07155 [astro-ph.HE]].

[28] D. Boncioli *et al.*, PoS ICRC **2015** (2016) 521 [arXiv:1509.01046 [astro-ph.HE]].

[29] M. Ave, R. Engel, M. Roth and A. Schulz, Astropart. Phys. **87** (2017) 23. doi:10.1016/j.astropartphys.2016.11.008

[30] M. Ave, M. Roth and A. Schulz, Astropart. Phys. **88** (2017) 46. doi:10.1016/j.astropartphys.2017.01.003

5 List of Publications

1. A. Aab *et al.* [Pierre Auger Collaboration], JCAP **04** (2017)009

2. A. Aab *et al.* [Pierre Auger Collaboration], The Astrophysical Journal Letters, **837**:L25 (7pp), 2017 March 10

3. A. Aab *et al.* [Pierre Auger Collaboration], JINST **12** (2017) P03002

4. A. Aab *et al.* [Pierre Auger Collaboration], JINST **12** P02006 (2017)

5. A. Aab *et al.* [Pierre Auger Collaboration], JCAP **04** (2017) 038

6. A. Aab *et al.* [Pierre Auger Collaboration], Phys. Rev. D **94**, 122007 (2016)

7. A. Aab *et al.* [Pierre Auger Collaboration], PRL **117**, 192001 (2016)

8. A. Aab *et al.* [Pierre Auger Collaboration], Phys. Rev. D **94**, 082002 (2016)

9. A. Aab *et al.* [Pierre Auger Collaboration], Phys.Lett. **B762** (2016) 288-295

10. A. Aab *et al.* [Pierre Auger Collaboration], Phys. Rev. D **93**, 122005 (2016)

11. A. Aab *et al.* [Pierre Auger Collaboration], PRL **116**, 241101 (2016)

12. A. Aab *et al.* [Pierre Auger Collaboration], Phys. Rev. D **93**, 072006 (2016)

13. J. Heinze, D. Boncioli, M. Bustamante and W. Winter, arXiv:1512.05988 [astro-ph.HE].

14. A. Aab *et al.* [Pierre Auger Collaboration], JINST **11**, no. 01, P01018 (2016)

15. D. Boncioli *et al.* [Pierre Auger Collaboration], arXiv:1512.02314 [astro-ph.HE].

16. M. G. Aartsen *et al.* [IceCube and Pierre Auger and Telescope Array Collaborations], JCAP **1601**, no. 01, 037 (2016)

The Pierre Auger Collaboration

A. Aab[77], P. Abreu[68], M. Aglietta[49,48], I. Al Samarai[31], I.F.M. Albuquerque[18], I. Allekotte[1], A. Almela[8,11], J. Alvarez Castillo[64], J. Alvarez-Muñiz[76], G.A. Anastasi[40,42], L. Anchordoqui[83], B. Andrada[8], S. Andringa[68], C. Aramo[46], F. Arqueros[74], N. Arsene[70], H. Asorey[1,26], P. Assis[68], J. Aublin[31], G. Avila[9,10], A.M. Badescu[71], A. Balaceanu[69], F. Barbato[56], R.J. Barreira Luz[68], J.J. Beatty[88], K.H. Becker[33], J.A. Bellido[12], C. Berat[32], M.E. Bertaina[58,48], X. Bertou[1], P.L. Biermann[b], P. Billoir[31], J. Biteau[30], S.G. Blaess[12], A. Blanco[68], J. Blazek[28], C. Bleve[52,44], M. Boháčová[28], D. Boncioli[42,d], C. Bonifazi[24], N. Borodai[65], A.M. Botti[8,35], J. Brack[h], I. Brancus[69], T. Bretz[37], A. Bridgeman[35], F.L. Briechle[37], P. Buchholz[39], A. Bueno[75], S. Buitink[77], M. Buscemi[54,43], K.S. Caballero-Mora[62], L. Caccianiga[55], A. Cancio[11,8], F. Canfora[77], L. Caramete[70], R. Caruso[54,43], A. Castellina[49,48], F. Catalani[18], G. Cataldi[44], L. Cazon[68], A.G. Chavez[63], J.A. Chinellato[19], J. Chudoba[28], R.W. Clay[12], A. Cobos[8], R. Colalillo[56,46], A. Coleman[89], L. Collica[48], M.R. Coluccia[52,44], R. Conceição[68], G. Consolati[55,50], F. Contreras[9,10], M.J. Cooper[12], S. Coutu[89], C.E. Covault[81], J. Cronin[90], S. D'Amico[51,44], B. Daniel[19], S. Dasso[5,3], K. Daumiller[35], B.R. Dawson[12], R.M. de Almeida[25], S.J. de Jong[77,79], G. De Mauro[77], J.R.T. de Mello Neto[24], I. De Mitri[52,44], J. de Oliveira[25], V. de Souza[17], J. Debatin[35], O. Deligny[30], C. Di Giulio[57,47], A. Di Matteo[53,k,42], M.L. Díaz Castro[19], F. Diogo[68], C. Dobrigkeit[19], J.C. D'Olivo[64], Q. Dorosti[39], R.C. dos Anjos[23],

M.T. Dova[4], A. Dundovic[38], J. Ebr[28], R. Engel[35], M. Erdmann[37], M. Erfani[39], C.O. Escobar[f],
J. Espadanal[68], A. Etchegoyen[8,11], H. Falcke[77,80,79], J. Farmer[90], G. Farrar[86], A.C. Fauth[19],
N. Fazzini[f], F. Fenu[58], B. Fick[85], J.M. Figueira[8], A. Filipčič[72,73], O. Fratu[71], M.M. Freire[6],
T. Fujii[90], A. Fuster[8,11], R. Gaior[31], B. García[7], D. Garcia-Pinto[74], F. Gaté[e], H. Gemmeke[36],
A. Gherghel-Lascu[69], P.L. Ghia[30], U. Giaccari[24], M. Giammarchi[45], M. Giller[66], D. Głas[67],
C. Glaser[37], G. Golup[1], M. Gómez Berisso[1], P.F. Gómez Vitale[9,10], N. González[8,35], A. Gorgi[49,48],
P. Gorham[i], A.F. Grillo[42], T.D. Grubb[12], F. Guarino[56,46], G.P. Guedes[20], M.R. Hampel[8],
P. Hansen[4], D. Harari[1], T.A. Harrison[12], J.L. Harton[h], A. Haungs[35], T. Hebbeker[37], D. Heck[35],
P. Heimann[39], A.E. Herve[34], G.C. Hill[12], C. Hojvat[f], E. Holt[35,8], P. Homola[65], J.R. Hörandel[77,79],
P. Horvath[29], M. Hrabovský[29], T. Huege[35], J. Hulsman[8,35], A. Insolia[54,43], P.G. Isar[70], I. Jandt[33],
J.A. Johnsen[82], M. Josebachuili[8], J. Jurysek[28], A. Kääpä[33], O. Kambeitz[34], K.H. Kampert[33],
I. Katkov[34], B. Keilhauer[35], N. Kemmerich[18], E. Kemp[19], J. Kemp[37], R.M. Kieckhafer[85], H.O. Klages[35],
M. Kleifges[36], J. Kleinfeller[9], R. Krause[37], N. Krohm[33], D. Kuempel[37], G. Kukec Mezek[73],
N. Kunka[36], A. Kuotb Awad[35], B.L. Lago[15], D. LaHurd[81], R.G. Lang[17], M. Lauscher[37], R. Legumina[66],
M.A. Leigui de Oliveira[22], A. Letessier-Selvon[31], I. Lhenry-Yvon[30], K. Link[34], D. Lo Presti[54],
L. Lopes[68], R. López[59], A. López Casado[76], Q. Luce[30], A. Lucero[8,11], M. Malacari[90], M. Mallamaci[55,45],
D. Mandat[28], P. Mantsch[f], A.G. Mariazzi[4], I.C. Mariş[13], G. Marsella[52,44], D. Martello[52,44],
H. Martinez[60], O. Martínez Bravo[59], J.J. Masías Meza[3], H.J. Mathes[35], S. Mathys[33], J. Matthews[84],
J.A.J. Matthews[j], G. Matthiae[57,47], E. Mayotte[33], P.O. Mazur[f], C. Medina[82], G. Medina-
Tanco[64], D. Melo[8], A. Menshikov[36], K.-D. Merenda[82], S. Michal[29], M.I. Micheletti[6], L. Middendorf[37],
L. Miramonti[55,45], B. Mitrica[69], D. Mockler[34], S. Mollerach[1], F. Montanet[32], C. Morello[49,48],
M. Mostafá[89], A.L. Müller[8,35], G. Müller[37], M.A. Muller[19,21], S. Müller[35,8], R. Mussa[48], I. Naranjo[1],
L. Nellen[64], P.H. Nguyen[12], M. Niculescu-Oglinzanu[69], M. Niechciol[39], L. Niemietz[33], T. Niggemann[37],
D. Nitz[85], D. Nosek[27], V. Novotny[27], L. Nožka[29], L.A. Núñez[26], L. Ochilo[39], F. Oikonomou[89],
A. Olinto[90], M. Palatka[28], J. Pallotta[2], P. Papenbreer[33], G. Parente[76], A. Parra[59], T. Paul[87,83],
M. Pech[28], F. Pedreira[76], J. Pękala[65], R. Pelayo[61], J. Peña-Rodriguez[26], L. A. S. Pereira[19],
M. Perlín[8], L. Perrone[52,44], C. Peters[37], S. Petrera[40,42], J. Phuntsok[89], R. Piegaia[3], T. Pierog[35],
P. Pieroni[3], M. Pimenta[68], V. Pirronello[54,43], M. Platino[8], M. Plum[37], C. Porowski[65], R.R. Prado[17],
P. Privitera[90], M. Prouza[28], E.J. Quel[2], S. Querchfeld[33], S. Quinn[81], R. Ramos-Pollan[26], J. Rautenberg[33],
D. Ravignani[8], B. Revenu[e], J. Ridky[28], F. Riehn[68], M. Risse[39], P. Ristori[2], V. Rizi[53,42], W. Ro-
drigues de Carvalho[18], G. Rodriguez Fernandez[57,47], J. Rodriguez Rojo[9], D. Rogozin[35], M.J. Roncoroni[8],
M. Roth[35], E. Roulet[1], A.C. Rovero[5], P. Ruehl[39], S.J. Saffi[12], A. Saftoiu[69], F. Salamida[53],
H. Salazar[59], A. Saleh[73], F. Salesa Greus[89], G. Salina[47], F. Sánchez[8], P. Sanchez-Lucas[75],
E.M. Santos[18], E. Santos[8], F. Sarazin[82], R. Sarmento[68], C.A. Sarmiento[8], R. Sato[9], M. Schauer[33],
V. Scherini[44], H. Schieler[35], M. Schimp[33], D. Schmidt[35,8], O. Scholten[78,c], P. Schovánek[28],
F.G. Schröder[35], S. Schröder[33], A. Schulz[34], J. Schumacher[37], S.J. Sciutto[4], A. Segreto[41,43],
M. Settimo[31], A. Shadkam[84], R.C. Shellard[14], G. Sigl[38], G. Silli[8,35], O. Sima[g], A. Śmiałkowski[66],
R. Šmída[35], G.R. Snow[91], P. Sommers[89], S. Sonntag[39], R. Squartini[9], D. Stanca[69], S. Stanič[73],
J. Stasielak[65], P. Stassi[32], F. Strafella[52,44], A. Streich[34], F. Suarez[8,11], M. Suarez Durán[26],
T. Sudholz[12], T. Suomijärvi[30], A.D. Supanitsky[5], J. Šupík[29], J. Swain[87], Z. Szadkowski[67],
A. Taboada[34], O.A. Taborda[1], V.M. Theodoro[19], C. Timmermans[79,77], C.J. Todero Peixoto[16],
L. Tomankova[35], B. Tomé[68], G. Torralba Elipe[76], P. Travnicek[28], M. Trini[73], R. Ulrich[35],
M. Unger[35], M. Urban[37], J.F. Valdés Galicia[64], I. Valiño[76], L. Valore[56,46], G. van Aar[77], P. van
Bodegom[12], A.M. van den Berg[78], A. van Vliet[77], E. Varela[59], B. Vargas Cárdenas[64], G. Varner[i],
R.A. Vázquez[76], D. Veberič[35], C. Ventura[24], I.D. Vergara Quispe[4], V. Verzi[47], J. Vicha[28], L. Vil-
laseñor[63], S. Vorobiov[73], H. Wahlberg[4], O. Wainberg[8,11], D. Walz[37], A.A. Watson[a], M. Weber[36],
A. Weindl[35], L. Wiencke[82], H. Wilczyński[65], M. Wirtz[37], D. Wittkowski[33], B. Wundheiler[8],
L. Yang[73], A. Yushkov[8], E. Zas[76], D. Zavrtanik[73,72], M. Zavrtanik[72,73], A. Zepeda[60], B. Zimmermann[36],

201

M. Ziolkowski[39], Z. Zong[30], F. Zuccarello[54,43]

1 Centro Atómico Bariloche and Instituto Balseiro (CNEA-UNCuyo-CONICET), San Carlos de Bariloche, Argentina

2 Centro de Investigaciones en Láseres y Aplicaciones, CITEDEF and CONICET, Villa Martelli, Argentina

3 Departamento de Física and Departamento de Ciencias de la Atmósfera y los Océanos, FCEyN, Universidad de Buenos Aires and CONICET, Buenos Aires, Argentina

4 IFLP, Universidad Nacional de La Plata and CONICET, La Plata, Argentina

5 Instituto de Astronomía y Física del Espacio (IAFE, CONICET-UBA), Buenos Aires, Argentina

6 Instituto de Física de Rosario (IFIR) – CONICET/U.N.R. and Facultad de Ciencias Bioquímicas y Farmacéuticas U.N.R., Rosario, Argentina

7 Instituto de Tecnologías en Detección y Astropartículas (CNEA, CONICET, UNSAM), and Universidad Tecnológica Nacional – Facultad Regional Mendoza (CONICET/CNEA), Mendoza, Argentina

8 Instituto de Tecnologías en Detección y Astropartículas (CNEA, CONICET, UNSAM), Buenos Aires, Argentina

9 Observatorio Pierre Auger, Malargüe, Argentina

10 Observatorio Pierre Auger and Comisión Nacional de Energía Atómica, Malargüe, Argentina

11 Universidad Tecnológica Nacional – Facultad Regional Buenos Aires, Buenos Aires, Argentina

12 University of Adelaide, Adelaide, S.A., Australia

13 Université Libre de Bruxelles (ULB), Brussels, Belgium

14 Centro Brasileiro de Pesquisas Fisicas, Rio de Janeiro, RJ, Brazil

15 Centro Federal de Educação Tecnológica Celso Suckow da Fonseca, Nova Friburgo, Brazil

16 Universidade de São Paulo, Escola de Engenharia de Lorena, Lorena, SP, Brazil

17 Universidade de São Paulo, Instituto de Física de São Carlos, São Carlos, SP, Brazil

18 Universidade de São Paulo, Instituto de Física, São Paulo, SP, Brazil

19 Universidade Estadual de Campinas, IFGW, Campinas, SP, Brazil

20 Universidade Estadual de Feira de Santana, Feira de Santana, Brazil

21 Universidade Federal de Pelotas, Pelotas, RS, Brazil

22 Universidade Federal do ABC, Santo André, SP, Brazil

[23] Universidade Federal do Paraná, Setor Palotina, Palotina, Brazil

[24] Universidade Federal do Rio de Janeiro, Instituto de Física, Rio de Janeiro, RJ, Brazil

[25] Universidade Federal Fluminense, EEIMVR, Volta Redonda, RJ, Brazil

[26] Universidad Industrial de Santander, Bucaramanga, Colombia

[27] Charles University, Faculty of Mathematics and Physics, Institute of Particle and Nuclear Physics, Prague, Czech Republic

[28] Institute of Physics of the Czech Academy of Sciences, Prague, Czech Republic

[29] Palacky University, RCPTM, Olomouc, Czech Republic

[30] Institut de Physique Nucléaire d'Orsay (IPNO), Université Paris-Sud, Univ. Paris/Saclay, CNRS-IN2P3, Orsay, France

[31] Laboratoire de Physique Nucléaire et de Hautes Energies (LPNHE), Universités Paris 6 et Paris 7, CNRS-IN2P3, Paris, France

[32] Laboratoire de Physique Subatomique et de Cosmologie (LPSC), Université Grenoble-Alpes, CNRS/IN2P3, Grenoble, France

[33] Bergische Universität Wuppertal, Department of Physics, Wuppertal, Germany

[34] Karlsruhe Institute of Technology, Institut für Experimentelle Kernphysik (IEKP), Karlsruhe, Germany

[35] Karlsruhe Institute of Technology, Institut für Kernphysik, Karlsruhe, Germany

[36] Karlsruhe Institute of Technology, Institut für Prozessdatenverarbeitung und Elektronik, Karlsruhe, Germany

[37] RWTH Aachen University, III. Physikalisches Institut A, Aachen, Germany

[38] Universität Hamburg, II. Institut für Theoretische Physik, Hamburg, Germany

[39] Universität Siegen, Fachbereich 7 Physik – Experimentelle Teilchenphysik, Siegen, Germany

[40] Gran Sasso Science Institute (INFN), L'Aquila, Italy

[41] INAF – Istituto di Astrofisica Spaziale e Fisica Cosmica di Palermo, Palermo, Italy

[42] INFN Laboratori Nazionali del Gran Sasso, Assergi (L'Aquila), Italy

[43] INFN, Sezione di Catania, Catania, Italy

[44] INFN, Sezione di Lecce, Lecce, Italy

[45] INFN, Sezione di Milano, Milano, Italy

[46] INFN, Sezione di Napoli, Napoli, Italy

[47] INFN, Sezione di Roma "Tor Vergata", Roma, Italy

[48] INFN, Sezione di Torino, Torino, Italy

[49] Osservatorio Astrofisico di Torino (INAF), Torino, Italy

[50] Politecnico di Milano, Dipartimento di Scienze e Tecnologie Aerospaziali , Milano, Italy

[51] Università del Salento, Dipartimento di Ingegneria, Lecce, Italy

[52] Università del Salento, Dipartimento di Matematica e Fisica "E. De Giorgi", Lecce, Italy

[53] Università dell'Aquila, Dipartimento di Scienze Fisiche e Chimiche, L'Aquila, Italy

[54] Università di Catania, Dipartimento di Fisica e Astronomia, Catania, Italy

[55] Università di Milano, Dipartimento di Fisica, Milano, Italy

[56] Università di Napoli "Federico II", Dipartimento di Fisica "Ettore Pancini", Napoli, Italy

[57] Università di Roma "Tor Vergata", Dipartimento di Fisica, Roma, Italy

[58] Università Torino, Dipartimento di Fisica, Torino, Italy

[59] Benemérita Universidad Autónoma de Puebla, Puebla, México

[60] Centro de Investigación y de Estudios Avanzados del IPN (CINVESTAV), México, D.F., México

[61] Unidad Profesional Interdisciplinaria en Ingeniería y Tecnologías Avanzadas del Instituto Politécnico Nacional (UPIITA-IPN), México, D.F., México

[62] Universidad Autónoma de Chiapas, Tuxtla Gutiérrez, Chiapas, México

[63] Universidad Michoacana de San Nicolás de Hidalgo, Morelia, Michoacán, México

[64] Universidad Nacional Autónoma de México, México, D.F., México

[65] Institute of Nuclear Physics PAN, Krakow, Poland

[66] University of Łódź, Faculty of Astrophysics, Łódź, Poland

[67] University of Łódź, Faculty of High-Energy Astrophysics,Łódź, Poland

[68] Laboratório de Instrumentação e Física Experimental de Partículas – LIP and Instituto Superior Técnico – IST, Universidade de Lisboa – UL, Lisboa, Portugal

[69] "Horia Hulubei" National Institute for Physics and Nuclear Engineering, Bucharest-Magurele, Romania

[70] Institute of Space Science, Bucharest-Magurele, Romania

[71] University Politehnica of Bucharest, Bucharest, Romania

[72] Experimental Particle Physics Department, J. Stefan Institute, Ljubljana, Slovenia

[73] Laboratory for Astroparticle Physics, University of Nova Gorica, Nova Gorica, Slovenia

[74] Universidad Complutense de Madrid, Madrid, Spain

[75] Universidad de Granada and C.A.F.P.E., Granada, Spain

[76] Universidad de Santiago de Compostela, Santiago de Compostela, Spain

[77] IMAPP, Radboud University Nijmegen, Nijmegen, The Netherlands

[78] KVI – Center for Advanced Radiation Technology, University of Groningen, Groningen, The Netherlands

[79] Nationaal Instituut voor Kernfysica en Hoge Energie Fysica (NIKHEF), Science Park, Amsterdam, The Netherlands

[80] Stichting Astronomisch Onderzoek in Nederland (ASTRON), Dwingeloo, The Netherlands

[81] Case Western Reserve University, Cleveland, OH, USA

[82] Colorado School of Mines, Golden, CO, USA

[83] Department of Physics and Astronomy, Lehman College, City University of New York, Bronx, NY, USA

[84] Louisiana State University, Baton Rouge, LA, USA

[85] Michigan Technological University, Houghton, MI, USA

[86] New York University, New York, NY, USA

[87] Northeastern University, Boston, MA, USA

[88] Ohio State University, Columbus, OH, USA

[89] Pennsylvania State University, University Park, PA, USA

[90] University of Chicago, Enrico Fermi Institute, Chicago, IL, USA

[91] University of Nebraska, Lincoln, NE, USA

———

[a] School of Physics and Astronomy, University of Leeds, Leeds, United Kingdom

[b] Max-Planck-Institut für Radioastronomie, Bonn, Germany

[c] also at Vrije Universiteit Brussels, Brussels, Belgium

[d] now at Deutsches Elektronen-Synchrotron (DESY), Zeuthen, Germany

[e] SUBATECH, École des Mines de Nantes, CNRS-IN2P3, Université de Nantes, France

[f] Fermi National Accelerator Laboratory, USA

[g] University of Bucharest, Physics Department, Bucharest, Romania

[h] Colorado State University, Fort Collins, CO

[i] University of Hawaii, Honolulu, HI, USA

[j] University of New Mexico, Albuquerque, NM, USA

[k] now at Université Libre de Bruxelles (ULB), Brussels, Belgium